Engineering Myeloid Cell Phenotype Using Cell Surface-Adhered Microparticles for Therapeutic Applications

by

Neha Kapate

B.S. Chemical Engineering, Additional Major in Biomedical Engineering
Carnegie Mellon University, 2018

Submitted to the department of Harvard-MIT Health Sciences and Technology in partial fulfillment of the requirements for the degree of

Doctor of Philosophy in Medical Engineering and Medical Physics

at the

Massachusetts Institute of Technology

June 2023

Authored by: *Neha Kapate*
Harvard-MIT Health Sciences and Technology
May 1, 2023

Certified by: *Samir Mitragotri, PhD*
Hiller Professor of Bioengineering
Hansjorg Wyss Professor of Biologically Inspired Engineering
Thesis Supervisor

Accepted by: *Collin M. Stultz, MD, PhD*
Director, Harvard-MIT Program in Health Sciences and Technology
Nina T. and Robert H. Rubin Professor in Medical Engineering and Science
Professor of Electrical Engineering and Computer Science

Thesis Supervisor:
Samir Mitragotri, PhD
Hiller Professor of Bioengineering at the John A. Paulson School of Engineering and Applied Sciences, Harvard University

Thesis Committee Chair:
Paula T. Hammond, PhD
Institute Professor and Department Head, Chemical Engineering, MIT

Thesis Readers:
Jennifer Guerriero, PhD
Assistant Professor, Brigham and Women's Hospital and Harvard Medical School

Jeffrey Karp, PhD
Professor of Medicine, Brigham and Women's Hospital and Harvard Medical School

Engineering Myeloid Cell Phenotype Using Cell Surface-Adhered Microparticles for Therapeutic Applications

By Neha Kapate

Abstract

Cell-based therapies present a new frontier for treating previously untreatable diseases. Living cells can innately overcome biological barriers, respond in real-time to biological stimuli, interact with specific cell types, and provide a canvas for further cellular engineering. The crucial role of the innate immune system, and particularly myeloid cells, in the dysregulated biological processes in numerous diseases has come into focus, motivating the development of myeloid cell therapies. The polarization of myeloid cells between classically activated, pro-inflammatory states and suppressive, anti-inflammatory states has myriad effects within the local environment, including metabolic modulation, production of cytokines, and activation of responding adaptive immune cells. As adoptively transferred cells can readily alter their phenotype based on their microenvironments, it is critical to develop a method for controlling cell phenotype *in vivo*.

In this thesis, I develop a biomaterials approach for tuning myeloid phenotype, specifically differentiating monocytes and macrophages, for pre-clinical applications as cell therapy. I investigate how different myeloid cell phenotypes can be engineered and sustained using cell surface-adhered microparticles, termed "backpacks." I delve into designing backpacks that load various drug molecules to promote anti- or pro-inflammatory phenotypes. I assess the effect of these microparticles on durability of phenotypic activation and other cellular functions *in vitro*. Next, I apply this platform to study immune-modulation and therapeutic effect in several disease models. I assess treatment with anti-inflammatory backpacks adhered to monocytes in a mouse model of progressive multiple sclerosis to determine immunomodulatory effects and therapeutic efficacy. Then, I scale up the fabrication of backpack-macrophages and apply this treatment in a clinically relevant porcine model of traumatic brain injury. Finally, I backpack-induced polarization of monocytes into the opposite direction with a pro-inflammatory phenotype, demonstrating the utility of backpacks as a platform technology. I assess treatment of monocytes with pro-inflammatory microparticles in a mouse model of breast cancer to assess tumor microenvironment remodeling and effect on tumor burden. Altogether, this work provides a biomaterials-based approach to tune myeloid cell phenotype *ex vivo*, for precise control of cell phenotype *in vivo*.

Table of Contents

List of Figures

List of Tables

Acknowledgments

I acknowledge Samir for his mentorship and support during my PhD and for all that I have learned from him in this time. For overall backpack development and rich scientific discussions and experiment troubleshooting over the last 5 years, I acknowledge Lily Li-Wen Wang, Ninad Kumbhojkar, and Supriya Prakash for their teamwork. I acknowledge Morgan Goetz, Alex Gottlieb, and Alex Currerri for their friendship, camaraderie, and scientific discussions over the last 5 years. Thanks as well to Bijay Singh, Nadia Selig-Wober, and Claudia Stearns for supporting the daily operations of the lab to allow us to perform our research. Thank you to all past and present lab members for making the Mitragotri Lab an enjoyable place to perform research and spend time with each other.

Thank you to my thesis committee, Prof. Paula Hammond, Prof. Jennifer Guerriero, and Prof. Jeff Karp for their intellectual contributions and sage insights as my dissertation research evolved.

For the MS project, I acknowledge Ninad Kumbhojkar, Supriya Prakash, Lily Li-Wen Wang, Dr. Michael Dunne, Amanda Graveline, Dr. Kyung Soo (Charles) Park, Dr. Vineeth (Vinny) Chandran Suja, Juhee Goyal, Prof. John R. Clegg. I also acknowledge Prof. Jennifer Guerriero, Dr. Jayoung Kim, Dr. Yongsheng Gao, Dr. Kolade Adebowale, and Alex Gottlieb for helpful scientific discussions. I also thank Andyna Vernet, Melinda Sanchez, and Sarai Bardales of the Wyss Institute for assistance with EAE mouse studies.

For the TBI project, I acknowledge Lily Li-Wen Wang, Rick Liao, Ninad Kumbhojkar, Supriya Prakash, Dr. Vineeth (Vinny) Chandran Suja, and Prof. John Clegg. I also acknowledge Dr. Beth Costine-Bartell and her team for their extensive contribution to the pig studies. To help with backpack-macrophage scale up and preparation, I think Suyog Shaha, Morgan Janes, Dr. Kyung Soo (Charles) Park, Dr. Kolade Adebowale, Dania Villafuerte, Mikayla Flanz, and Rojan Rajeev.

For the cancer project, I acknowledge Dr. Michael Dunne and Alex Gottlieb for project execution, and Dr. Kyung Soo (Charles) Park, Ninad Kumbhojkar, and Supriya Prakash for helping scientific discussions.

Throughout my dissertation research, I was fortunate to be supported by the National Science Foundation Graduate Research Fellowship under Grant No. 1122374. I also acknowledge support from the Defense Medical Research and Development Program by the Department of Defense (W81XWH-19-2-0011), Wyss Institute of Biologically Inspired Engineering and John A. Paulson School of Engineering at Harvard University. I acknowledge the Harvard Center for Biological Imaging; the Allston Science and Engineering Complex's Molecular and Cellular Biology Core; and Harvard University Center for Nanoscale Systems, a member of the National Nanotechnology Coordinated Infrastructure Network supported by National Science Foundation ECCS-2025158. I also thank the Dana-Farber/Harvard Cancer Center in Boston, MA, for the use of the Rodent Histopathology Core and its histological section preparation service.

I acknowledge the use of https://www.biorender.com in creating schematics.

Dedication

I would like to dedicate this dissertation to my parents, Chandra and Sunita Kapate, and my sister, Nidhi Kapate. Thank you for your endless support over the last 26 years and counting. This milestone is just as much mine as it is yours. I love you!

1. Chapter 1: Introduction

Cell-based therapies present a paradigm-shifting opportunity to better treat previously untreatable diseases (1, 2). Living cells are able to innately overcome biological barriers (1, 3), respond in real-time to biological stimuli and mediators, interact with specific cell types (3), and provide a canvas for further engineering (such as genetic or surface modifications) (4–6). In my dissertation research, I focus on materials-based modifications of immune cells for application to cell therapies. Specifically, I investigate how myeloid cell phenotype can be engineered using surface-adhered non-spherical microparticles for therapeutic applications. I delve into the design of discoidal microparticles ("backpacks") that load various drug molecules and adhere to the surface of phagocytic immune cells. I focus on modulation of myeloid cell phenotype, comprising monocytes and macrophages, due to their implication in dysregulated biological processes in a variety of diseases, from multiple sclerosis (MS) to traumatic brain injury (TBI) to cancer (7).

In Chapter 2, I discuss the fundamentals of how particle shape influences biological interactions and emerging applications of non-spherical particles in medicine. I provide an overview of fabrication and characterization techniques. I then discuss the relevance of particle shape to drug delivery, starting with cell-particle interactions. This section sets the foundation for the subsequent design of backpacks, as my development of backpacks is based on their ability to evade phagocytosis by immune cells due to their non-spherical shape and high aspect ratio (8). To provide a perspective on the emerging utility of non-spherical particles in disease treatment, I also describe how non-spherical particle geometry influences particle circulation, biodistribution, cell-targeting, and elicitation of an immune responses. I conclude with an outlook on the technology moving forward, with an emphasis on particle manufacturing, quality control, and ongoing clinical trials.

In Chapter 3, I discuss the importance of myeloid cells, including a background on their biology and the therapeutic landscape of myeloid cells. Monocytes and macrophages play a key role in defending against foreign pathogens, healing wounds, and regulating tissue homeostasis. Driving this versatility is their phenotypic plasticity, which enables macrophages to respond to subtle cues in tightly coordinated ways. However, when this coordination is disrupted, macrophages can aid the progression of numerous diseases. The central link between these disorders is aberrant macrophage polarization, which misguides their functional programs, secretory products, and regulation of the surrounding tissue microenvironment. As a result of their important and deterministic roles in both health and disease, macrophages have gained considerable attention as targets and therapeutic modalities for drug delivery.

In Chapter 4, I discuss my project to control myeloid cell phenotype into an anti-inflammatory state for potential treatment to multiple sclerosis (MS). MS is a currently uncurable autoimmune disease with a complex disease pathology. Despite the key role of myeloid cells in the pathophysiology of MS, current treatments do not specifically target myeloid cells or directly make their use for modulating the disease. I propose that immunomodulatory monocytes, upon intravenous injection, can infiltrate into inflamed central nervous system (CNS) and have the potential to mitigate disease progression We control monocyte phenotype through cell surface-adhered microparticles ("backpacks") loaded with interleukin-4 (IL-4) and dexamethasone. Treatment with backpack-laden monocytes elicited local and systemic immunomodulatory effects, culminating in improved motor functions in experimental autoimmune encephalomyelitis mice.

The results reported in this chapter demonstrate the possibility of myeloid cells as a therapy and drug target in MS.

In Chapter 5, I expand the application of IL-4 and dexamethasone backpacks on myeloid cells as an anti-inflammatory cell therapy approach to treat traumatic brain injury (TBI) in a higher order, clinically relevant porcine model. Due to some of the positive roles that inflammation plays in regeneration and recovery after TBI, anti-inflammatory interventions can benefit from therapeutic targeting to contusion sites in the brain, rather than conventional global suppression strategies (9). Macrophages are also implicated in the dysregulated inflammatory response after TBI We demonstrate that backpack-carrying macrophages reduce inflammation at the contusion side in a gyrencephalic porcine model of traumatic brain injury. The results reported in this chapter demonstrate, to the best of our knowledge, the first use of a cell therapy intervention in a large animal model of TBI.

In Chapter 6, I discuss my final project promote myeloid phenotype into the opposite pro-inflammatory, anti-tumor state for application to a breast cancer model. We report the development of a backpack design with stable surface conjugation of interferon gamma (IFNγ), a potent pro-inflammatory cytokine, which maintains pro-inflammatory activation of the carrier monocyte as it differentiates. IFNγ backpacks direct differentiating monocytes towards a pro-inflammatory phenotype both *in vitro* and *in vivo*, remodeling the tumor microenvironment towards a more anti-tumor state. We demonstrate that monocytes carrying IFNγ backpacks are effective in delaying tumor growth and significantly improving survival.

Finally, I conclude my thesis in Chapter 7 with a summary of conclusions drawn from the data and future perspectives.

Permissions and Attributions:

1. Content from Chapter 2 was adapted from Reference (10), published in *Advanced Drug Delivery Reviews*.
2. Content from Chapter 3 was adapted from Reference (11), published in *Advanced Drug Delivery Reviews,* and Reference (2), published in *Bioengineering and Translational Medicine*.
3. Content from Chapter 4 was adapted from Reference (12), published in *Proceedings of the National Academy of Sciences*.
4. Content from Chapter 5 was adapted from "Backpack induced anti-inflammatory macrophages for the treatment of traumatic brain injury," Kapate et al, *submitted*.
5. Content from Chapter 6 was adapted from "Polymer Backpack-loaded Tissue Infiltrating Monocytes for Treating Cancer," Kapate et al, *in preparation*.

2. Chapter 2: Non-Spherical Particles for Therapeutic Applications

2.1. Importance of Particle Shape as a Design Parameter

The therapeutic outcome of particles is closely related to their design parameters including size, shape, and surface charge, among others. Influence of particle size, charge, and surface chemistry on their interactions with cells and tissues has been well studied, particularly as they pertain to drug delivery (3, 13–18). However, particle shape is a parameter that has been less widely studied as a key parameter.

We performed Google Scholar and PubMed searches in 2021, from which we collected a database of empirical studies on non-spherical particles for drug delivery applications. We used the following search terms: particle, anisotropic, non-spherical, shape, drug delivery. Our search returned 156 unique papers (Supplementary Table 1), on which we performed a content analysis. We documented the year of publication, material selection, particle shape(s), particle size(s), characterization method(s), cell line(s) and animal model(s) used in each study. The search results focus mainly on particles composed of materials that been more commonly used for in vivo drug delivery applications (i.e., polymers, lipids, silica). We include some, albeit non-exhaustive, discussion of metal and carbon nanoparticles when applied to drug delivery. We excluded naturally occurring non-spherical particles, such as cells and viruses, from our analysis. Our summary statistics are the first to summarize the current status and trajectory of the particle shape field (**Figure 2-1**).

There has been a steady increase in publications on particle shape over the last 15 years (**Figure 2-1, left**). The focus of over half of these papers is on fundamental aspects, concerning fabrication of non-spherical particles or interactions between cells and non-spherical particles (**Figure 2-1, right**). Recently, scientists have published several proof-of-concept studies that demonstrate unique advantages of non-spherical particles for cancer immunotherapy, anti-inflammatory drug delivery, and vaccination (19–22).

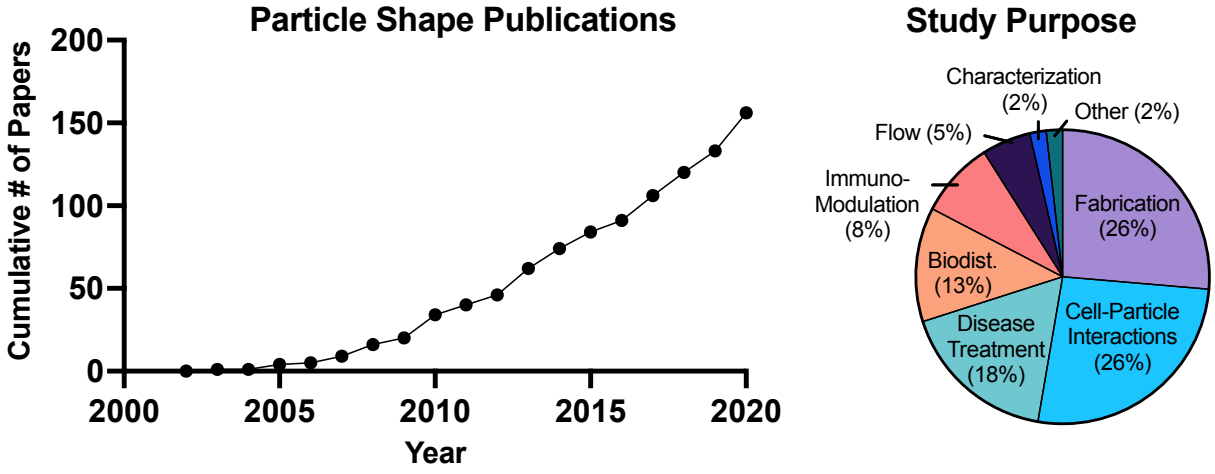

Figure 2-1. Research on the role of particle geometry in drug delivery.
Scientific papers regarding non-spherical particles applied to drug delivery over the past 15 years were gathered by searching a combination of the following terms on Google Scholar and PubMed: "Particle", "anisotropic", "non-spherical", "shape", "drug delivery." Papers were gathered as of December 2020.

2.2. Fabrication of Non-Spherical Particles

Various top-down and bottom-up methods have been proposed to design non-spherical polymeric nanoparticles. These synthesis methods have been extensively reviewed previously (23–30), Here, we provide an overarching summary the fabrication methods. Methods for synthesizing spherical particles, such as liposomes, nanogels, and dendrimers are excluded, although we acknowledge that such nanoscale materials can act as building blocks for design of non-spherical particles. A summary of the prevalence of various fabrication methods in the literature is shown in **Figure 2-2.**

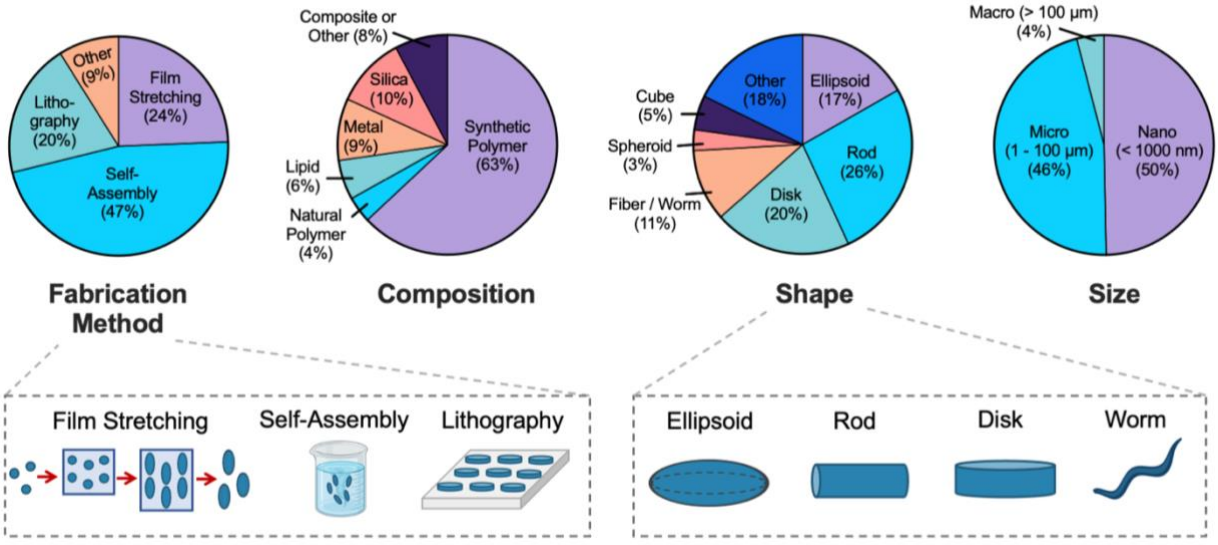

Figure 2-2. Summary statistics for non-spherical particle synthesis and characterization. Each study was binned for its particle fabrication method, composition, shape, and size. Some studies were binned more than once, if more than one non-spherical particle was synthesized or assessed. Summary statistics are provided as a percentage of total.

The most used method for fabricating non-spherical particles is self-assembly (47% of published studies). Self-assembled particles are formed when building blocks (amphiphilic polymers, proteins, peptides) form ordered assemblies (i.e., micelles, fibers, sheets). For biomedical applications, these fibers, particles, and other non-spherical assemblies are designed to achieve stability in aqueous solution. Therefore, the enthalpic gain of complementary hydrophobic and electrostatic interactions, as well as the entropic gain of disrupting of ordered water assemblies around hydrophobic chains, are the main thermodynamic drivers (31, 32). The most common shapes for self-assembled particles are rods, worms, fibers, and other filamentous structures. However, other complex shapes such as spheroids, rhombi, stars, crescents, and wrinkled particles have also been generated (33–36).

Two other common and spontaneous processes for particle formation are precipitation and layer-by-layer polyelectrolyte deposition. Precipitation has been used to form a number of non-spherical particles, including drug particles (e.g. dexamethasone (37), itraconazole (38)) as well as drug-containing calcium carbonate particles. Layer-by-layer deposition has proven useful for

assembling discoidal particles on micropatterned supports (i.e. glass, polydimethylsiloxane (PDMS)), as well as for modifying the surface of charged particles (39, 40).

The second most common method for fabricating non-spherical particles is mechanical deformation, or stretching (24%). This method was used by Mohraz *et al.* and Champion *et al.,* among others, to make particles of various shapes (8, 41). First, nano- or micro-particles are embedded in a polymeric film. The film, typically comprised of poly(vinyl alcohol), serves to contain and separate the embedded particles while they are heated through their glass transition. By stretching the supporting film along multiple axes, the embedded liquified particles are deformed uniformly. After cooling the film below the particles' glass transition temperature, the support film is dissolved, and prolate/oblate ellipsoidal particles are collected.

Non-spherical particles have also been formed by various lithographic techniques (20% of studies). Photolithography allows for the formation of micro- and nano-patterned surfaces with resolution as low as 10 nm (42, 43). Non-spherical particles formed by lithography techniques can be broadly separated into those formed using microfluidic devices, by micro/nano- molding, or by surface contact/printing.

In 48% of identified studies on non-spherical particles, the particle surface was chemically modified. Surface modifications have included coupling of fluorophores, antibodies, proteins, peptides, polymeric stabilizers, and phospholipids. In the most common case, particles are modified through non-covalent assembly at the particle-media interface. For example, a protein corona can be formed at the surface of hydrophobic particles through non-covalent adsorption in aqueous solution. These surface-bound proteins can be useful, not only for stabilization purposes, but also for cell targeting or antigen presentation (44). For charged particles, alternating polyelectrolytes can be deposited layer-by-layer. In addition to binding therapeutic cargo to the particle surface, layer-by-layer deposition was recently used to enhance macrophage-particle interactions for cell attachment (39). One strategy, which has been applied with a lesser frequency but shows future promise, is the assembly of lipid or phospholipid layers around non-spherical particles (45, 46).

Covalent surface modification requires the presence of suitable reactive groups (i.e., acid, amine, thiol, maleimide, etc.) at the particle surface, which could be contributed by either a component of the polymer backbone or its end groups. Covalent tethers of hydrophilic polymers, such as poly(ethylene glycol), have been explored at depth for particle stabilization and stealth behavior (47, 48). Attaching bioactive proteins and peptides to the particle surface is also a common practice (49, 50). When optimizing a new peptide or protein-particle conjugate, it is important to optimize the length of linker molecules and chemical nature of the conjugation reaction, ensuring that bioactivity is conserved (51).

Recently, researchers have synthesized anisotropic particles which switch shape in response to light, temperature, or electric fields (52). Materials that respond to (i.e. swell, degrade) pH, the presence of reducing agents, and enzymes have already been developed for other biomedical applications, such as biosensing and drug delivery (53). As researchers elucidate the role of particle geometry in biological processes, non-spherical particles comprised of responsive materials could be useful for connecting physical and biochemical stimuli to cell and tissue-scale function.

2.3. Characterization

Compared to their spherical counterparts, characterization methods for non-spherical particles have been discussed in the literature to a much lesser extent. Multiple measurements or dimensions are needed to accurately characterize non-spherical particles. Determining the diameter and length is necessary for a rod or fiber. Naming conventions are also important. For example, long cylindrical particles can be described as a "*fiber*" when rigid, and a "*worm*" when deformable. For ellipses, the *aspect ratio (AR),* is equal to the particle length on its major axis, divided by its width along the minor axis. The lower bound of aspect ratio for an ellipsoid is 1 (a sphere). An ellipsoid further needs to be described as either *prolate* (stretched along one axis, rod-like), or *oblate* (stretched along 2 axes, disk-like). In each case, characterization of non-spherical particles is more complex than that for a similar sphere, whose geometry can be described fully by a single "size" or "diameter" parameter.

From an applied technology point-of-view, there is a pressing need for high throughput methods, which can continually monitor the fabrication of non-spherical particles in an industrial setting (54). In the laboratory setting, electron microscopy is the most prevalent method for non-spherical particle characterization. While electron microscopy provides the resolution necessary to properly measure size and shape parameters, it is too low in throughput for continuous monitoring. Light scattering methods, such as static light scattering or dynamic light scattering are effective for continuous or high-throughput monitoring, but do not readily provide shape information. In **Table 9.2-1**, I systematically summarizing the frequency with which different characterization methods have been used to characterize the size and shape of non-spherical particles, with a list of their resolutions, limitations, and throughputs.

Overall, characterization methods for non-spherical particles have been developed and discussed in the literature to a lesser extent compared to spherical particles. Of the limited characterization methods used, most are low throughput, such as SEM, TEM, and confocal microscopy, which is an important consideration for translation. As this field shifts from fundamental investigations to contemporary applications for disease treatment, rigorous characterization will be paramount to study reliability and reproducibility. Standard characterization methods are needed for quality control, while new and highly sensitive methods are needed to determine advanced structure-function relationships.

2.4. Effect of shape on Cell-Particle Interactions

2.4.1. Phagocytosis

Cell-particle interactions make up the main focus area of particle shape papers (26%), along with non-spherical particle fabrication (26%) (**Figure 2-1**). In particular, the discovery that particle shape plays a role in phagocytosis by immune cells was one of the major findings that triggered interest in geometry as a design parameter for drug carriers. Phagocytosis is a two-step process consisting of the attachment and internalization of particles by cells (55). It is one of the primary mechanisms of innate immune defense by various immune cells, including macrophages, monocytes, neutrophils, dendritic cells, and mast cells. The paper by Champion *et al*. in 2006 demonstrated that the local shape of the particle at the point where macrophages attach to the particle's surface dictates whether or not a macrophage began internalization (8). Champion *et al*. tested a range of nonopsonized and IgG-opsonized geometrically anisotropic PS particles with the

same volume, including oblate ellipsoids (major axis 4 μm, AR 4), prolate ellipsoids (major axis 2–6 μm, AR 1.3–3), and elliptical disks (ED) (major axis 3–14 μm, AR 2–4, thickness 400–1,000 nm). Macrophages did not successfully internalize non-spherical particles from the particle's low curvature side (major axis). Accordingly, increasing the particle aspect ratio decreased internalization. Formation of an actin cup around the particle was found to be an important pre-requisite for particle phagocytosis by macrophages (8). When macrophages attached the end of an opsonized ED or sphere, the membrane progressed down the length of the particle and eventually engulfed the particle (**Figure 2-3A, top: #1–2, #5–6**). But when macrophages attached at the flat side of an opsonized ED, the membrane simply spread on the particle (**Figure 2-3A, top: #3–4**). Internalization velocity was found to inversely correlate with the tangent angle of the particle (Ω), which represents the mean direction of tangents drawn to the target contour from the point of initial contact to the center line of the target. When $\Omega<45$ °, macrophages successfully internalized particles *via* forming an actin-cup and ring; when $\Omega>45$ °, macrophages spread on particles but did not internalize them (8).

In a follow-up study, Sharma *et al*. demonstrated that the shape of 1 μm-sized PS particles affects the attachment to and internalization by macrophages separately (56). Ellipsoids exhibit increased attachment to macrophages, but the energy required for actin remodeling limits their internalization and phagocytosis. Reduced internalization of prolate ellipsoid particles compared to oblate ellipsoid particles by macrophages is attributed to the energy requirement for actin remodeling necessary for engulfment of the high aspect ratio particles. Others have validated this finding that sufficiently elongated particles can avoid phagocytosis by macrophages (57, 58).

More recently, phagocytosis of non-spherical particles by other immune cells, specifically neutrophils, has also been explored. There have been reported differences between the interaction of particles with neutrophils compared with other leukocytes. For example, PEGylation of particle surfaces decreases particle phagocytosis by monocytes/macrophages, but increases phagocytosis by neutrophils (59). Neutrophils demonstrated diverging phagocytic responses to non-spherical particles compared to prior observations for mononuclear phagocytes (macrophages, monocytes) (60). While rods exhibit reduced phagocytosis by macrophages, monocytes, and dendritic cells, the association of neutrophils with particles significantly increased for rod-shaped particles, both *in vitro* and *in vivo* (**Figure 2-3A, bottom**) (60). This observed trend of increased phagocytosis of rods by neutrophils was demonstrated with both PLGA and PS particles and validated across a range of human and murine primary and immortalized cells, including primary murine cells from a disease model, experimental autoimmune encephalitis (EAE). Dendritic cells also reside in tissues and are capable of phagocytosis of microbes for antigen presentation to cells of the adaptive immune system. However, the impact of shape on phagocytosis by dendritic cells has not been systematically studied in depth. Some results indicate that dendritic cells have a similar phagocytic response as macrophages (60).

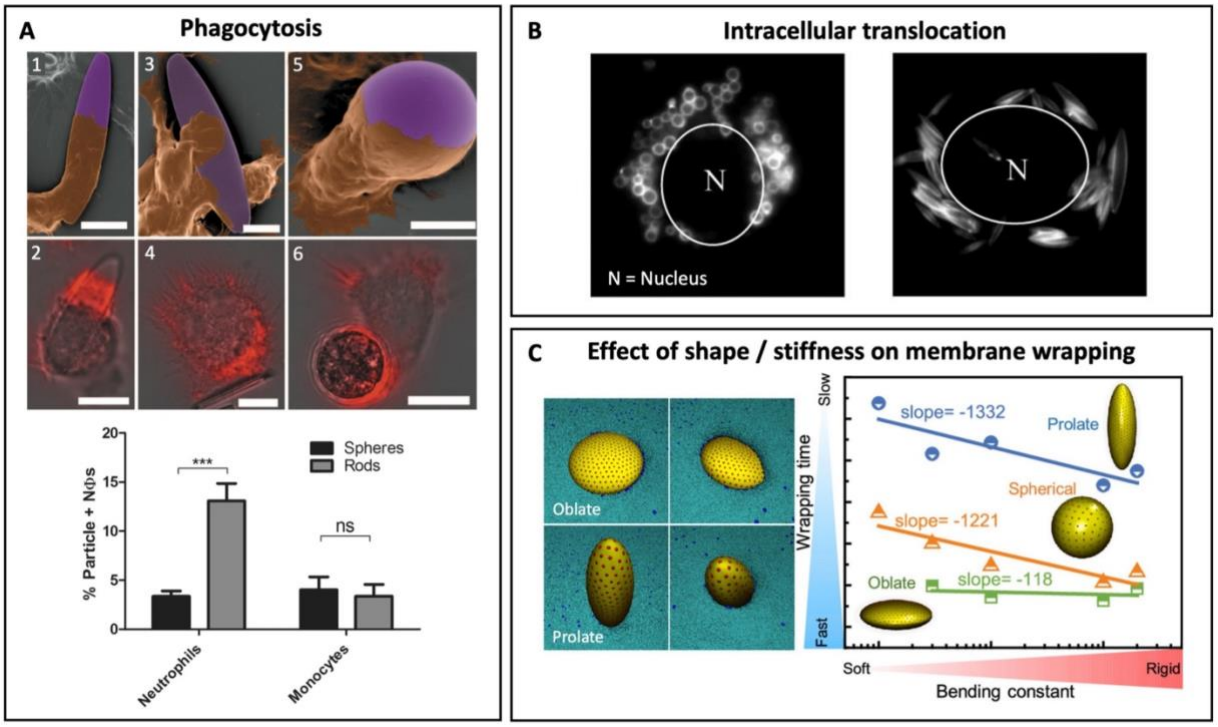

Figure 2-3. Role of particle shape in cell-particle interactions.
(a) *Top: Phagocytosis by macrophages is influenced by particle shape. (#1,3,5) Scanning electron micrographs of macrophages in the presence of various shaped particles shapes revealed the macrophages' ability to engulf microparticles when attached to a sphere or the end of an ellipsoidal particle. Macrophages instead spread on the surface of the ellipsoidal particle when attached to the flat surface of the particle. The microparticles are re-colored in purple for visualization. (#2,4,6) Overlays of bright-field and fluorescent images after fixing the cells and staining for polymerized actin with rhodamine phalloidin, which revealed the macrophages' membrane adhesion to and wrapping around the microparticles. Presence of an actin cup or ring (#2, #6) signals particle internalization after initial attachment. Modified with permission from* (8)*, Copyright 2006, National Academy of Sciences. Bottom: In vivo uptake of the 500nm polystyrene spheres and rods (aspect ratio = 6) of the same volume by mouse neutrophils and monocytes. Rod shaped particles were preferentially internalized by mouse neutrophils in vivo. Reproduced from* (60)*, Copyright 2020, AAAS.* ***(b)*** *Fluorescent images of endocytosed of micron sized PLGA spheres (left) and elliptical disks (right) of the same volume in HUVECs. Both particles accumulated around the nucleus, with disks orienting tangentially with the nuclear membrane. Modified with permission from* (61)*, Copyright 2010, John Wiley & Sons, Inc.* ***(c)*** *Particle internalization for oblate, prolate, and spherical NPs of varying stiffnesses illustrated through wrapping time as a function of bending constant. Soft NPs are less efficiently wrapped than rigid NPs due to their elastic deformation. Prolate NPs are the most sensitive geometry to variation in particle elasticity, followed by sphere, and then oblate ellipsoid, due to increasing contact edge length. Modified with permission from* (62)*, Copyright 2018, American Chemical Society.*

The observed differences between the response of various immune cells may be attributed to the differences in their phagocytic mechanisms. For example, membrane stiffness, surface motility, and receptor phosphorylation affect the energy barrier for actin remodeling and engulfment of particles (63, 64). It is important to systematically assess these interactions so that drug particles may be targeted to specific immune cells and subsequent intra- or extra-cellular locations. When performing these biological characterizations, it is important to use appropriate and robust *in vitro* models, as findings will differ depending on cell species and source. For example, most studies used immortalized human cell lines for cell-particle experiments (44%), with only 13% using primary human cells. However, it is well documented that immortalized cells can demonstrate diverging morphological or functional features from primary cells, with serial passages causing variations in genotype and phenotype, calling into question the physiological relevance of such findings (65, 66). **Figure 2-4** provides a summary of the types of biological evaluation for the 156 particle shape studies analyzed. Further, influence of geometry in conjunction with other parameters, such as size, charge, and surface modification, must also be systematically assessed. One study found that a combination of both an elongated shape and PEGylation had the strongest phagocytosis inhibiting effect for PLGA nanoparticles (48), demonstrating that shape may synergize with other physicochemical properties of the drug carrier.

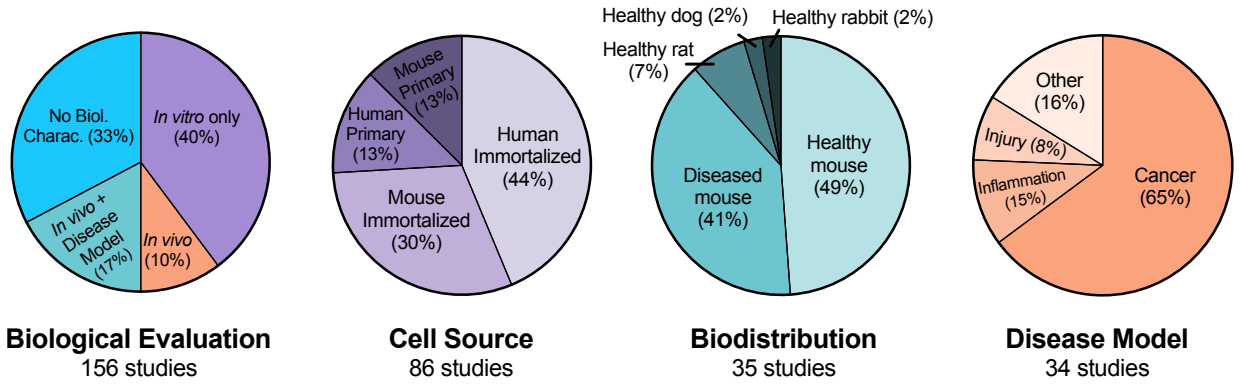

Figure 2-4. Summary statistics for biological evaluation of non-spherical particles.
156 original studies evaluating non-spherical particles for drug delivery were identified. Each study was binned for type of biological evaluation: no biological characterization, in vitro characterization only, in vivo characterization without a disease model (i.e. biodistribution), and in vivo characterization as applied to a disease model. For studies that included in vitro experiments (86 studies total), the source of cells for in vitro evaluation was analyzed. For studies that included in vivo experiments, type of biodistribution model (35 studies) and disease model (34 studies) were analyzed. Some studies were binned more than once, if more than one cell source, biodistribution experiment or disease model was assessed. Summary statistics are provided as a percentage of total.

2.4.2. Mechanism of non-spherical particle internalization

Scientists have used biophysical principles and molecular simulations to infer the mechanisms underlying interactions between the cell membrane and non-spherical particles (13). Agarwal *et al*. proposed that nanoparticle internalization is a complex manifestation of three shape– and size–dependent parameters: (i) particle surface-to-cell membrane contact area, (ii) strain energy for membrane deformation, and (iii) sedimentation or local particle concentration at the cell membrane (67). Huang *et al*. used an efficient coarse-grained molecular dynamics (CGMD) model to simulate

endocytosis. They determined that, for spherocylindrical nanoparticles with an initial upright docking position on the membrane plane, endocytosis proceeds through a laying-down-then-standing- up sequence (68). Free energy analysis revealed that nanoparticle size primarily determines whether endocytosis can proceed to complete particle wrapping. Nanoparticle shape determines the endocytic pathway and the angle of entry, as non-spherical geometries break the symmetry of membrane curvature and pose an energetic barrier to membrane wrapping (68).

On top of shape and size, particle stiffness also influences the extent and favorability of membrane wrapping (62). Membrane wrapping efficiency of particles during endocytosis results from competition between the kinetics of receptor recruitment (affected by the contact edge length between the nanoparticle and membrane) and thermodynamic driving force to drive particles into the cell (62). Shen *et al.* demonstrated a difference in wrapping efficiency between soft and rigid spherical nanoparticles because soft nanoparticles are less efficiently wrapped to a full extent due to their elastic deformation. This difference in wrapping efficiency is exacerbated with increasing size (25 – 100 nm). Prolate ellipsoid is the most sensitive geometry to variation in particle elasticity due to its small contact edge length, followed by sphere, and then oblate ellipsoid, which has the largest contact edge length (**Figure 2-3C**). When considering kinetics of endocytosis, Jin *et al.* developed a quantitative model to correlate endocytosis rate with nanoparticle geometry. They found that shape contributed to a difference in the endocytosis rate constant, but not exocytosis rate constant, for tubes (130 – 660 nm) vs. spherical nanoparticles across distinct cell lines (69). Of note, these models focused on non-spherical nanoparticles. Thus, it is unclear if these findings can be reliably extrapolated to non-spherical particles in the micron size range.

2.4.3. Intracellular translocation

Particle geometry also modulates intracellular translocation. Hinde *et al*. synthesized polymeric nanoparticles with different shapes (micelles, vesicles, rods and worms), but identical surface chemistries. Pair correlation microscopy analysis showed that shape differences led to different rates of intracellular transport (70). High aspect ratio nanoparticles (i.e., rods and worms, but not micelles and vesicles) crossed the nuclear envelope, delivering more doxorubicin into the nucleus than spherical nanoparticles. The non-spherical, drug-loaded particles crossed cell barriers to different extents (i.e., cell membrane, endosomes, nuclear envelope), generating different intracellular concentration gradients, which ultimately determined the site of drug release. This demonstrated that particle shape can be a useful parameter for defining the intracellular site of drug delivery. For example, ellipsoidal nanocarriers functionalized with invasive protein InvA497 demonstrated intracellular delivery of anti-infective agents, leading to killing of intracellular bacterial (71).

The material and mechanical properties of internalized particles also affect cell physiology. Needle-shaped polymeric particles (4.4 μm in length, stretched from 1 μm spheres) induced transient disruption of cell membranes, resulting in contraction of cells but recovery over 48 hours (72). In comparison, spheres (1 μm) and elliptical disks (2.91 μm x 0.71 μm, stretched from 1 μm spheres) did not have an impact on cell spreading and motility. When needle-shaped PLGA-PEG fibers of differing stiffness were tested (3-6 μm in length), fibers with a high apparent Young's modulus (average apparent modulus 246 - 872 kPa) maintained their original shape upon phagocytosis, while fibers with low Young's modulus (average apparent modulus 56 – 142 kPa) curled in cells, resulting in abnormal intracellular actin translocation and absence of lysosome/phagosome fusion in macrophages (73).

2.5. Effect of Shape on Particle Distribution

2.5.1. Biodistribution

Particle geometry influences biodistribution independent of particle volume and composition. Compared to spherical nanocarriers, aspherical nanocarriers that show reduced phagocytosis generally exhibit reduced liver accumulation, thus demonstrating increased accumulation in other organs. This phenomenon has been observed for multiple nanoparticle shapes, such as nanochains (74), disks (75), and rods (36, 76–79). Silica disks 1.6 μm in diameter were injected intravenously and accumulated in the lungs and heart to a significant degree, with a smaller degree of accumulation in the liver compared to spheres (75). When injected intravenously, PEGylated gold rods in the nano-size range were taken up to a lesser extent by the liver than their spherical counterparts (77). Similarly, long mesoporous silica nanorods (AR = 5) accumulated to a greater extent in the spleen and a lesser extent in the liver, as compared to similar short-rods (AR = 1.5) (76). Mesoporous silica nanorods of both aspect ratios have a higher content in the lung after PEG modification (76). After oral administration, with the increase of AR, mesoporous silica nanorods demonstrate decreased liver distribution and urinal excretion (36, 79). Mesoporous silica nanorods also had a longer residence time in the gastrointestinal tract compared with spherical nanoparticles (36). Based on pharmacokinetic analysis, nifedipine-loaded long rods had higher availability than nifedipine-loaded short rods and spheres (36).

2.5.2. Targeted Delivery

In conjunction with using shape to alter biodistribution, non-spherical particles may be functionalized with antibodies (50, 78, 80, 81), peptides (43,55,56), or other ligands, including transferrin (86), albumin (86), sialyl Lewis a (sLe^a) (78) to achieve more specific organ targeting. Disks functionalized with anti-ICAM-1 showed lower uptake by the liver and specific targeting to the lungs, compared to non-specific pulmonary targeting by IgG disks (80). Tjandra *et al*. functionalized ellipsoidal polymersomes with an in-house phage-display cell-targeting peptide to target a medulloblastoma cell line *in vitro* (84). They tuned the peptide density to modulate association with medublastoma cells while lowering association with primary human phagocyte. Wang *et al*. modified nanodisks with a targeting peptide to recognize extracellular matrix fibronectin and its complexes specifically expressed on the walls of tumor vessels and in tumor stroma (85). This allowed for higher drug accumulation at prostate tumor sites compared to conventional nanospheres and superior anti antitumor efficacy when loaded with drug compared to unmodified disks and nanospheres. Namdee *et al*. showed that 2μm rods coated with sLe^a and anti-VCAM antibody significantly accumulated in the lungs compared to coated spheres (500nm or 2μm diameter), while uncoated rods had accumulated in the liver (78).

More recently, biological phenomena have been mimicked or exploited for targeting of non-spherical drug carriers. Platelet-like nanoparticles (PLNs) have been developed that mimic four key attributes of platelets, (i) discoidal morphology, (ii) mechanical flexibility, (iii) biophysically and biochemically mediated aggregation, and (iv) heteromultivalent presentation of ligands (87). *In vivo* murine studies demonstrated that PLNs accumulate at the wound site and induce ~65% reduction in bleeding time, effectively mimicking and improving the hemostatic functions of natural platelets.

In general, of the 156 original papers gathered, 22% made use of disease models. These models are important for more thoroughly understanding particle behavior in the body, as biodistribution

of non-spherical particles in disease states used to be less well studied (25). For example, in a murine model of atherosclerosis, microrods targeted developing plaques more efficiently than microspheres, with microparticles displayed better targeting than nanoparticles, regardless of shape (78). Cancer is the most studied disease state, comprising 65% of disease models. A number of studies have shown that nanocarriers with non-spherical shapes demonstrate enhanced tumor targeting and accumulation, such as nanotubes, filomicelles, rods, and disks (30, 81, 82, 88–93).

2.6. Effect of Shape on Elicitation of Immune Responses

2.6.1. Particle shape as a design consideration for targeting immune cells

Particle shape can influence the host immune response by evading or exhibiting preference for specific immune cells. Wibroe *et al.* demonstrated that disk and rod shaped particles (500 nm) evade uptake by macrophages in pigs *in vivo* (94). Administration of non-spherical particles (i.e., rods, disks) led to a reduced extent of cardiopulmonary distress, as compared to spherical particles of the same dose. This stressor was diminished when pulmonary intravascular macrophages were depleted, suggesting that macrophage uptake within minutes of administration was the underlying cause of adverse effects. In a similar study discussed earlier in this review, Safari *et al.* demonstrated that rod shaped PS microparticles, as compared to spheres of the same volume, were preferentially taken up by human and mouse neutrophils in whole blood (60). This suggests that particle shape could be leveraged to target neutrophils and treat inflammatory conditions.

In addition to the flow behaviors discussed above, geometry can alter particle biodistribution by changing the nature of interactions with tissue-resident immune cells. For example, the combination of PEGylation and non-spherical geometry extended the lung retention of PRINT particles following pulmonary delivery (95, 96). This extended retention, achieved by evading uptake by alveolar macrophages and preventing an inflammatory response, presents an opportunity for drug and gene delivery to the lung. Enhanced particle uptake by dendritic cells, as a result of particle geometry, presents an opportunity to simultaneously deliver an antigen and adjuvant for vaccination (19, 97).

2.6.2. Non-spherical particles as immune adjuvants

Scientists have explored non-spherical synthetic particles as immune adjuvants, in an effort to expand the existing repertoire for vaccination. For example, Kumar *et al.* stretched 193 nm and 521 nm spherical PS nanoparticles into rods, and conjugated ovalbumin to the particle surfaces (49). *In vitro* studies with dendritic cells suggested that both the spherical and rod-shaped particles were internalized, leading to intracellular delivery of ovalbumin. Small (193 nm) spherical and large (1530 nm length) rod particles with bound ovalbumin generated a Th1-biased immune response *in vivo.* In a similar study, Garapaty *et al.* stretched 3 μm PS spheres into rods with an aspect ratio of 2.5. They coated both rods and control spheres with protein ligands (ovalbumin, BSA, IgG) (98). Rod shaped particles increased the inflammatory response of J774 murine macrophages, as determined by secreted TNFα. While this result was promising, further studies are needed to determine the extent to which this inflammatory response is therapeutically useful.

From an application point-of view, many non-spherical particle adjuvants have been reported. Tazaki *et al.* developed a gold nanorod-based adjuvant for intranasal inactivated influenza vaccines (99). Shukla *et al.* reported that icosahedral nanoparticles derived from cowpea mosaic virus were more effective than filamentous particles from potato virus X at enhancing lymph node trafficking,

immune cell interactions, and HER-2 antigen presentation for cancer immunotherapy (100). Galloway *et al.* used cylindrical PLGA nanoparticles fabricated by PRINT, with a surface immobilized flu vaccine, to enhance IgG titers to influenza hemagglutinin in mice (101). While each of these studies produced interesting, applied technology, particle size and geometry were not probed with sufficient experimental or statistical rigor to determine the influence of geometry on adjuvant safety or efficacy.

Recently, Moon et al. developed synthetic high-density lipoprotein nanodiscs coupled with adjuvants and antigen peptides that markedly improve antigen/adjuvant co-delivery to lymphoid organs and generate robust and specific T cell responses (22, 102–104). They have demonstrated application of this cancer immunotherapy technology in a number of tumor models. Furthermore, Moore *et al.* fabricated resiquimod-loaded acetylated dextran filaments called "microconfetti" by electrospinning and homogenization (19). The microconfetti were internalized by bone marrow-derived dendritic cells in a size-specific manner, facilitating intracellular co-delivery of encapsulated and adsorbed payloads **(Figure 2-5A)**. Ovalbumin-coated microconfetti stimulated an inflammatory cytokine response in bone marrow derived dendritic cells, as well as antigen presentation and a Th1-skewed immune response *in vivo*. The authors suggested that these microconfetti can act as an injectable platform technology for vaccine delivery. One limitation, however, was that the experimental design did not control for particle geometry. Therefore, it is unclear the extent to which the microconfetti geometry was responsible for specific and useful biological properties (i.e., uptake, antigen presentation, cytokine production).

2.6.3. Non-spherical particles as components of immunomodulatory constructs

Non-spherical geometry can also result in useful properties (i.e., injectability, persistence in the extracellular space, cell modulation) for immunotherapy or tissue regeneration applications. Lu *et al.* developed injectable, cube-shaped PLGA microparticles which encapsulate a stimulator of interferon genes (STING) agonist (20). Their shape specific PLGA microparticles consisted of a drug core and a solid polymer shell, formed by soft lithography. These constraints prevented drug release from the particle core for several days, while allowing pulsatile drug release upon hydrolysis of the PLGA shell **(Figure 2-5B)**. By forming particles with different PLGA formulations, and administering a particle suspension containing three unique polymers, the authors delivered pulsatile doses of STING agonist intratumorally in mice. STING agonist delivery via this pulsatile release system increased the number of both infiltrating innate immune cells and circulating IFNγ+CD8+ memory T cells, inhibiting distant tumor growth and preventing metastasis.

Scientists have also explored the use of biomimetic, non-spherical particles as artificial antigen presenting cells (aAPCs). These aAPCs can engage T cells for immunotherapy applications. Sunshine *et al.* synthesized aAPCs comprised of a prolate ellipsoidal PLGA microparticle with surface-immobilized major histocompatibility complex-immunoglobulin dimers (44). aAPCs exhibited enhanced activity with increased particle AR (up to AR = 6.6), as determined by T cell association and CD8+ T cell expansion. Subcutaneous injection of optimized aAPCs further demonstrated efficacy by reducing tumor size and enhancing survival in a B16 murine melanoma model.

In contrast to cancer immunotherapy applications, non-spherical injectables and implants eluting anti-inflammatory cargo have been developed for wound healing and tissue regeneration **(Figure**

2-5C). For example, laponite is a discoidal nanoclay that sequesters cationic cytokines for days to weeks, due to the high density of negative charges on the disk face. Koshy *et al.* demonstrated that Laponite encapsulation within alginate hydrogels leads to the sequestration and sustained delivery of GM-CSF or murine IL-2 (21). Spiller *et al.* and others have shown that shifting macrophages from a pro-inflammatory (M1) to tissue-remodeling (M2) phenotype, which can be achieved through cytokine delivery, is critical to vascularization and wound healing (11, 105–107).

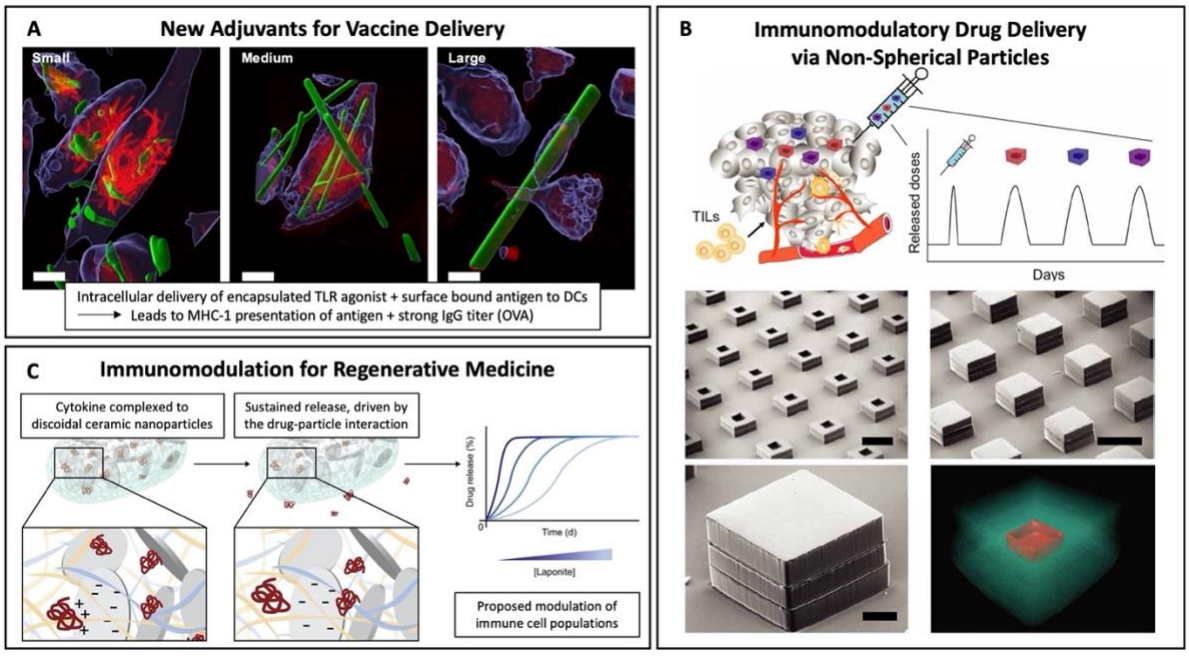

Figure 2-5. Design and evaluation of non-spherical immunomodulatory particles.
(a) Uptake of filamentous "microconfetti" by bone marrow derived dendritic cells (Blue = membrane, Red = cytoskeleton, Green = particle). Modified with permission from (19)*, Copyright 2020, American Chemical Society. (b) Fabrication of pulsatile-delivery PLGA particles by additive manufacturing. Particle morphology was assessed by SEM, and the encapsulation of a model drug is shown by high resolution x-ray computed tomography (Blue = PLGA particle, Red = encapsulated drug). Modified with permission from* (20)*, Copyright 2020, AAAS. (c) Cytokines (GM-CSF, IL-2) complexed with discoidal Laponite nanoclay exhibited a sustained elution from hydrogel depots. This sustained release profile can be useful for immune modulation and tissue regeneration. Modified with permission from* (21)*, Copyright 2018, Elsevier.*

2.7. Non-spherical Particles in the Clinic

Although the advances in technology discussed for non-spherical particles demonstrate potential, there are few clinical trials involving these particles, indicating that this research has largely remained in the preclinical space. Of the trials that do exist, a number are from Liquidia Corporation, which uses PRINT technology to fabricate non-spherical drug particles in a highly precise and controlled fashion. One product, LIQ861, is an inhaled dry powder formulation of Treprostinil with a pollen-like shape for ideal aerodynamic properties for deep-lung delivery to treat pulmonary arterial hypertension (PAH) and was granted tentative approval by the FDA. LIQ865, an injectable, hexagonal-shaped sustained-release formulation of bupivacaine for the

management of local post-operative pain, is being investigated in NCT02982889 (Phase 1). There are currently no non-spherical particles that have been FDA-approved for clinical use.

A number of barriers to translation still remain. To aid in scale up and commercialization, there is a need for methods that are highly reproducible and ensure narrow size distribution and uniform topology. This must be accompanied by rigorous yet facile characterization to allow for high throughput quality control. A limited number of characterization methods are being used currently, and the popular ones are low throughput, which must be considered for translational purposes. Further, there is a need for more rigorous biological evaluation when it comes to preclinical testing. Of the 156 original papers gathered, 26% included *in vivo* studies, while 33% of studies did not include biological evaluation and 40% included only *in vitro* studies (Figure 4). As cellular phenotype varies with species, cell source, and disease induction, it is necessary to perform robust *in vitro* experiments that are supplemented by *in vivo* studies. Most of these therapies have been applied to cancer, while there is room to treat other disorders, such as inflammatory or autoimmune diseases. As many soluble mediators may be upregulated in these disease states, non-spherical particles comprised of responsive materials that recognize biochemical stimuli may be able to better target sites of interest or selectively release drug.

3. Chapter 3: Use of Myeloid Cells as Cell Therapy Modality

3.1. Background of Myeloid Cells

Myeloid cells are derived from the common myeloid progenitor in the bone marrow during hematopoiesis (108). The myeloid lineage comprises the first line of defense against infection in the innate immune system. The myeloid lineage includes many differentiated cell types, including megakaryocytes, erythrocytes, mast cells, myeloblasts, which give rise to granulocytes like basophils, neutrophils, and eosinophils, and monoblasts, which serve as progenitors for monocytes, macrophages, and dendritic cells (108). During lineage commitment, transcription factors play important roles at different differentiation branches (109). For general myeloid-lineage commitment, PU.1, an Ets family transcription factor, is believed to play the key role (110). At later stages of myeloid cell maturation, soluble cytokines secreted by stromal cells such as G-CSF and M-CSF are important to maintain the homeostatic myelopoiesis (111). MafB, c-Maf, and Egr-1 are suggested to promote monocytic differentiation, rather than granulopoiesis (112).

3.2. Monocyte Biology

Upon differentiation from mononuclear phagocyte cells, the expression of various chemokine receptors and cell adhesion molecules at on the monocyte surface allows monocytes to exit the bone marrow into the blood and to be subsequently recruited from the blood into tissues (113, 114). Monocytes circulate in the blood for a few hours to days before being recruited into the tissue (115, 116). While they are circulating in the blood, monocytes, along with neutrophils, are able to initiate generalized responses at faster rates compared to lymphocytes. Monocytes possess the unique ability to enter tissues and terminally differentiate into macrophages (117). Monocytes may also differentiate into dendritic cells (DC) in lymphoid organs and Langerhans cells in skin, which function as professional antigen presenting cells (108). Monocytes and other leukocytes migrate across endothelial barriers, including the blood-brain barrier, by a multi-stage process known as diapedesis (118). The immune cell transiently tethers to and rolls along the endothelial cells, ultimately firmly attaching to the endothelial cells and transmigrating through interactions between integrins (α4β1), endothelial adhesion molecules (VCAM-1 and ICAM-1), and selectin molecules (P-selectin glycoprotein-1) (119–123). The immune cell then generates actin-containing structures such as lamellipodia to extend into the endothelial cells. These protrusions, paired with an invagination of the endothelial cell, eventually leads to the immune cell tunneling through the endothelial cell (119–121, 124).

3.3. Macrophage Biology

When monocytes are differentiating into macrophages in various tissues, they may show a unique, tissue-dependent morphology and specific functions (117). Examples are the Kupffer cells in the liver, alveolar macrophages in the lungs, microglia in the brain, and mesangial macrophages in the kidneys. Macrophages are crucial for maintaining homeostasis in their respective tissue compartments (125). When maintaining homeostasis, macrophages control metabolic regulation and tissue surveillance. When homeostasis is disrupted, macrophages, given their role as professional phagocytes, respond by taking up apoptotic cells and debris, which initiates inflammatory pathways, thereby amplifying tailored immune responses through the recruitment and activation of other immune cells (126). When moving towards homeostasis, macrophages undertake functions pertaining to wound-healing processes, which encompasses hindering immune activity, supporting proliferation, neovascularization, and cellular differentiation. In a number of diseases, as macrophages unsuccessfully strive toward reaching homeostasis, their phenotypic plasticity triggers a cycle of inflammation and regeneration, aiding the progression of malignancies (126).

Macrophages are important regulators of inflammation, as they can adopt a range of phenotypes in a manner that is dynamic, reversible, and dependent on their environment **(Figure 1)**. Macrophages become activated when triggered by a stimulus, which produces distinctive patterns of gene and protein expression (127, 128). Activated macrophages are sometimes described by an ostensible M1/M2 dichotomy, suggesting that macrophages are "polarized" to possess either pro-inflammatory or anti-inflammatory phenotypes. In reality, macrophage activation is non-binary (129). In certain diseases, populations of both M1 and M2 macrophages are present (130–132). Similarly, macrophages may express both M1 and M2 markers simultaneously, and to different extents, reflecting intermediate activation states (133, 134). For this reason, I note that the M1/M2 language sometimes used in this dissertation is out of preservation of the referenced literature as a shorthand description for macrophage activation.

Generally, M1 macrophages are pro-inflammatory, characterized by the secretion of pro-inflammatory cytokines, reactive nitrogen intermediates (RNIs), and reactive oxygen species (ROS), all of which act to clear pathogens and damage unhealthy tissues. However, macrophages with sustained M1 phenotypes have been shown to promote autoimmune diseases due to chronic secretion of Th1 response elements, iNOS-dependent RNIs, chemokines, and cytokines such as IFN-1β, IL-12, IL-23, and TNF-α (135). M1 macrophages are also characterized by low expressions of IL-10. Conversely, M2 macrophages are usually anti-inflammatory, characterized by high expressions of scavenging molecules, mannose and galactose receptors, ornithine, and polyamines. Yet, macrophages with M2 phenotypes in neoplastic tissues have been linked to tumor growth and metastasis (136). The M2 phenotype has several sub-types (M2a, M2b, and M2c) that have distinct physiological roles. M2 macrophages are generally characterized by increased secretion of IL-10 and decreased secretion of IL-12 and IL-23 (135), promoting tissue remodeling and healing, extracellular matrix (ECM) deposition, responses to fungal infections *via* decreased autophagy, and regulation of other immune cells, particularly Th2 responses, in a highly adaptable manner (137).

The balance of pro-inflammatory and anti-inflammatory macrophage programs is often key to the outcome of many diseases (138). Accordingly, drugs and drug delivery strategies that target macrophages are gaining traction as a means to treat diseases characterized by aberrant macrophage function.

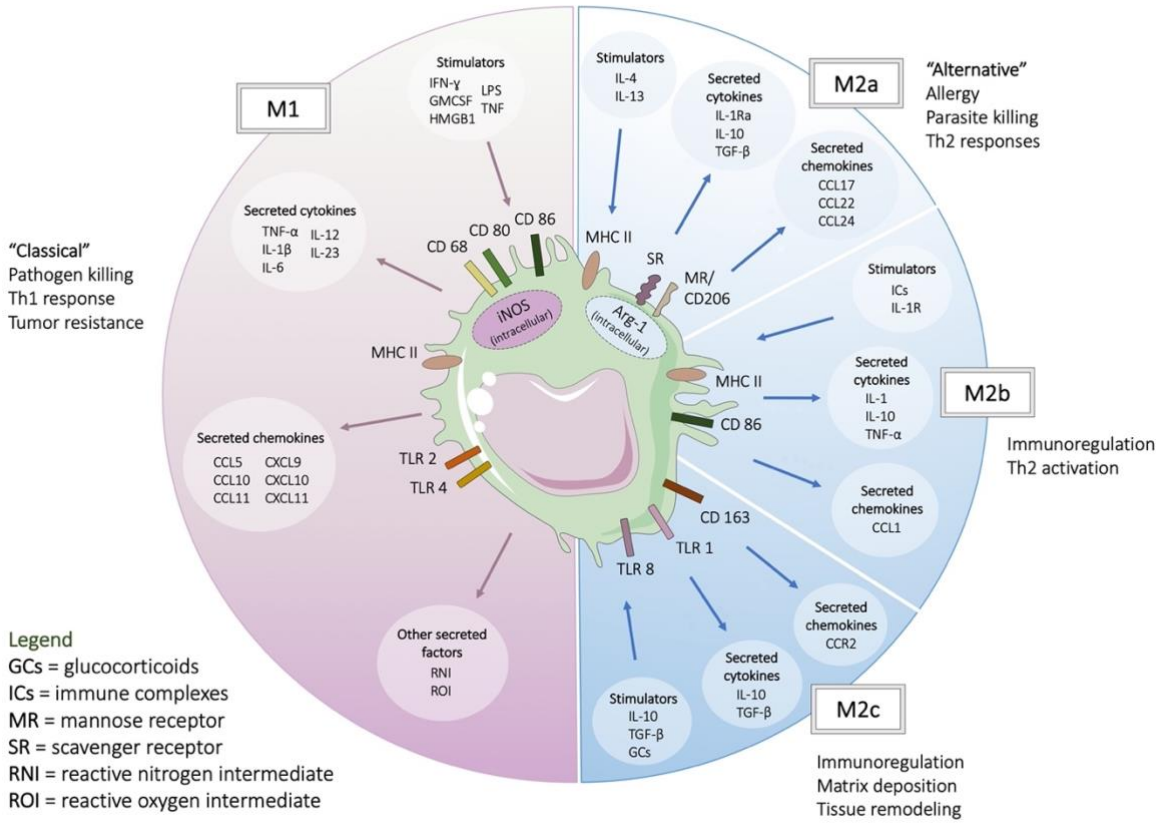

Figure 3-1. Spectrum of macrophage activation and corresponding stimulators, markers, and secretory outputs.
Macrophage polarization is best characterized by a multidimensional spectrum, but it is often simplified into inflammatory (M1) and anti-inflammatory (M2) phenotypes. The inflammatory responses of M1 macrophages (classically activated) encompass pathogen killing, Th1 activation, and tumor resistance. The anti-inflammatory response of M2 macrophages (alternatively activated) can be further categorized as M2a (allergy, parasite killing, Th2 responses), M2b (immunoregulation, Th2 activation), and M2c (immunoregulation, matrix deposition, tissue remodeling). Although the corresponding stimulators, cytokines, and chemokines serve as general hallmarks for each activation state, macrophages may express a mix of these markers, regardless of function. Adapted from Martinez and Gordon (128).

3.4. Clinical Landscape of Myeloid Cells

Compared to the other cell types, such as T cells and stem cells,, there are fewer clinical trials monocytes and macrophages (2). When considering mononuclear cells, comprising monocytes Macrophages, bone marrow mononuclear cells (BMMC), or peripheral blood mononuclear cells (PBMC), a majority of trials focus on BMMCs and PBMCs. The most common indications are cardiovascular disease(39%) and cancer (29%), with some applications for trauma (14%) (2). These trials are almost evenly distributed across Phase 1 (38%), Phase 2 (33%), and Phase 3 (30%)). Most (89%) of these trials use autologous cells (2).

There are many preclinical studies that use monocytes and macrophages as therapies, therapeutic targets, or both, most often for the treatment of cancer, autoimmune diseases, and other inflammatory diseases. However, translation to the clinic has been limited. For monocytes, two trials are indicated for central nervous system (CNS) disorders, while one trial is indicated for cancer. Notably, there are anumber of studies where monocytes are separated via leukapheresis and subsequently differentiated into DCs for re-injection. Due to their highly plastic nature, monocytes are well-suited for ex vivo conditioning, which is used to induce phenotypic changes before re-injection (NCT02948426). While many trials use macrophage populations as a target for imaging agents or as an indicator of clinical outcomes, these cells are not currently being infused as an intervention. BMMCs and PBMCs were also included in the clinical trial analysis. These groups are clinically useful because they invoke pleiotropic mechanisms, owing to the variety of distinct cell populations that are included. This allows, for example, the secretion of various remodeling factors to facilitate wound healing and regeneration. Similar to monocytes/macrophages*, ex vivo* conditioning allows for the induction of phenotypic changes (NCT02948426). It is also possible to enrich or deplete these mononuclear cells of certain cell populations, such as naïve T cells (NCT02942173) or B cells (NCT03939585). Other modifications include transfection with small interfering RNA(siRNA) (NCT03087591) and induction of specific receptors before re-infusion (NCT01697527). Combination therapies with stem cells are also being investigated (NCT03943940). Though the trial space for mononuclear cells is in its early stages, the multifunctional properties of these cells make them an attractive avenue for a diverse array of future therapies.

4. Chapter 4: A Backpack-based Myeloid Cell Therapy for Multiple Sclerosis

4.1. Introduction

Multiple Sclerosis (MS) is a currently uncurable autoimmune disease characterized by inflammation and demyelination, leading to progressive neurodegeneration (139, 140). While adaptive immune cells are ultimately responsible for demyelination in MS (141), myeloid cells are known to play an important role in the initiation and exacerbation of MS (142). Myeloid cells constitute the largest population of CNS-resident immune cells, comprising primarily of tissue-resident microglia and circulating monocytes that infiltrate and differentiate into macrophages (143). Not surprisingly, macrophages and microglia are the predominant inflammatory cells in active MS lesions (144–146). Myeloid cells also produce several inflammatory cytokines, free radicals, and other mediators that augment the inflammatory milieu, which in turn contributes to axonal injury (142, 147).

Current MS treatments are based largely on systemic immunomodulators, including interferon-β injections, oral glatiramer acetate and oral fingolimod (11, 139, 148). These treatments are primarily aimed at reducing flares, rather than preventing disease, for relapsing MS and are ineffective for progressive MS. Corticosteroids are also often used as a supplementary option for reduction of flares (149). All these treatments mediate their effect through systemic immunosuppression, with little to no direct impact at the target site due to the ineffective delivery of these drugs into the central nervous system (CNS) (139, 140, 148). In particular, treatments for progressive MS are limited by lack of drug access to the compartmentalized innate immune response in the CNS (150). Current experimental therapies are dominated by systemically delivered small molecules and monoclonal antibodies, with a majority constituting currently approved immunomodulators for other indications or new dosing regimens. Some examples of new experimental therapeutic modalities include Bruton's tyrosine kinase inhibitors (Evobrutinib, Fenebrutinib, Tolebrutinib), phosphodiesterase inhibitor (ibudilast), statins (Simvastatin), antisense oligonucleotide for CD49d (ATL1102), and allogeneic Epstein Barr virus T cells (ATA188), all delivered systemically (151–153).

Despite their key role in the pathophysiology of MS, current treatments do not specifically target pro-inflammatory myeloid cells or make their use for modulating the disease. There is growing recognition, however, that the therapeutic activity of current MS therapies that target the adaptive immune system is actually indirectly mediated through myeloid cells (142, 154). Taking advantage of the ability of circulating monocytes to infiltrate into the CNS, here we report an anti-inflammatory myeloid cell therapy for the treatment of progressive MS. Specifically, we propose that immunomodulatory monocytes, upon intravenous injection, can infiltrate into the inflamed CNS and elicit an anti-inflammatory phenotype to mitigate disease progression. To control the therapeutic phenotype of injected cells *in vivo*, disk-shaped particles ("backpacks"), containing interleukin-4 (IL-4) and dexamethasone were designed, synthesized, and attached to monocytes. Backpack-laden monocytes exhibited infiltration into the CNS of mice with autoimmune encephalomyelitis (EAE), and modulated both the local and systemic immune response, thereby improving disease burden.

4.2. Materials and Methods

4.2.1. Materials

PLGA resomer 502H, dexamethasone, PVA, heparin RPMI 1640 media, fetal bovine serum, penicillin and streptomycin, PBS, UltraComp eBeads compensation beads and LIVE/DEAD Blue dye were purchased from Sigma-Aldrich. PLGA-rhodamine was obtained from PolySciTech Akina. Recombinant murine IL-4, recombinant murine macrophage colony-stimulating factor (MCSF), and murine IL-4 ELISA kits were obtained from PeproTech. Sylgard 184 Silicone Elastomer kit was purchased from Dow. DiR 750 Fluorescent Cell Labeling Dye was obtained from PerkinElmer. MOG_{35-55}/CFA Emulsion kits for EAE induction were obtained from Hooke Laboratories. Debris removal solution and tissue dissociation kits were obtained from Miltenyi Biotec. Cell staining buffer and Legendplex Mouse Inflammation Panel and Mouse Macrophage/Microglial Panel kits were purchased from Biolegend. All fluorescent probe-conjugated antibodies for immune cell staining were purchased from BioLegend, Invitrogen, or R&D Systems. Cell fixation/permeabilization kits were obtained from BD Biosciences.

4.2.2. Animals

Female C57BL/6J mice (6 to 11 weeks of age) were purchased from Charles River Laboratories and Jackson Laboratories. All animal experiments were performed according to approved protocols by the Institutional Animal Care and Use Committee (IACUC) of the Faculty of Arts and Sciences, Harvard University and the IACUC of the Longwood Medical Area, Harvard University.

4.2.3. Backpack Fabrication

Polydimethylsiloxane (PDMS) templates were prepared as described previously (39). Briefly, silicon wafers were fabricated with patterned photoresist in an array of 8μm holes. PDMS mixed in a 10:1 base to crosslinker ratio from the Sylgard 184 kit was poured onto silicon wafers in petri dishes. The PDMS was de-gassed and cured at 65°C overnight and cut away from the silicon wafers. A solution of 80 mg/mL PLGA and 15mg/mL dexamethasone in acetone was prepared, with a 2:1 ratio of PLGA (7 to 17 kDa; Resomer 502 H) and PLGA-PEG-Maleimide (10 kDa PLGA; 5 kDa PEG). For fluorescently labelled backpacks, PLGA-rhodamine B was incorporated at a ratio of 100:1 fluorescent to nonfluorescent PLGA. 220uL of PLGA solution was spin coated onto each PDMS quadrant at 2000 rpm for 35s (at a 200 rpm/s ramp). Quadrants were plasma-ashed with O_2 for 60 s. A solution of 0.5 wt% PVA (146 to 186 kDa, 99 + % hydrolyzed) and 0.5 wt% heparin in phosphate-buffered saline (PBS) was prepared with IL-4 (25 ug/ml). Immediately after plasma treatment, 50uL of PVA/IL-4 solution was spread onto each quadrant. Quadrants were dried in a desiccator and then a second PLGA layer was deposited using the same procedure as the first. Backpacks were then stamped onto PVA-coated dishes by microcontact printing, as described previously (39). For blank backpacks, dexamethasone was omitted from the PLGA layers and IL-4 was omitted from the PVA layer. To collect backpacks, PVA-coated dishes were washed twice with 3mL of PBS. The solution was filtered through 20μm cell strainers, centrifuged at 2000g for 5 minutes, and then incubated with a solution of CD45 F(ab') for 15 minutes to functionalize the backpacks. CD45 F(Ab') fabrication process described in *Appendix 9.1.3*. Backpacks were washed, pelleted, and resuspended in media of choice.

4.2.4. Backpack Characterization

To quantify drug release, backpacks were harvested from dishes and resuspended in RPMI + 0.1% BSA. Backpacks were incubated at 37°C while rotating, and supernatant samples were taken at various time points. IL-4 release was quantified via ELISA and dexamethasone release was

quantified via HPLC-MS, as described in *Appendix 9.1.1*. AFM (JPK Nanowizard, Bruker) was used to characterize the topology and stiffness of backpacks as described in *Appendix 9.1.2*.

4.2.5. Primary Monocyte Culture

Bone marrow cells were harvested by flushing the femurs and tibias of donor mice. The collected cells were filtered through 40um cell strainers and centrifuged at 350g for 7.5 minutes. Then, the bone marrow cells were resuspended in RPMI supplemented with 20ng/mL M-CSF and plated at a density of $1x10^6$ cells/mL in 6-well ultra-low attachment plates for differentiation into monocytes (155, 156). For studies with human monocytes, primary blood-derived monocytes were purchased from STEMCELL.

4.2.6. Preparation and Characterization of Backpack-Monocytes

Monocytes were harvested from culture, counted, and seeded in 50ul aliquots with $1x10^6$ cells per well in a U-bottom 96 well plate. Backpacks were harvested and counted and added at a 3:1 backpack:cell ratio in 50uL aliquots. Monocytes and backpacks were incubated for 30-60 minutes at 37°C, 5% CO_2 to allow attachment to occur. Then, the backpack-monocytes were harvested from the wells, pelleted at 300g for 5 minutes, and resuspended in media of choice for subsequent use. Backpack adhesion was quantified via flow cytometry (Cytek Aurora) and confocal microscopy (Zeiss OIC LSM 900). For viability studies, backpack-monocytes were stained using LIVE/DEAD Blue (Biolegend) at 1 hour (after backpack-monocyte preparation) and 24 hours and analyzed via flow cytometry (Cytek Aurora). For shear studies, backpack-monocytes were loaded in a 1mL syringe fitted with a 27g blunt capillary needle (McMaster Carr #75165A688, 75165A763). The syringe was fixed on a syringe pump and dispensed with predetermined flow rates to subject backpack-monocytes to hydrodynamic shear stresses. Backpack-monocytes were subsequentially quantified for attachment by flow cytometry. For migration studies, human umbilical vein endothelial cells (EA.hy926) were seeded on 5μm Transwell inserts, and media containing 10ng/mL CCL2 was added to the lower chamber. 200k monocytes or backpack-monocytes were added into the upper chamber. The number of monocytes or backpack-monocytes in the lower chamber after 24 hours was counted.

4.2.7. In vitro phenotyping of backpack-monocytes.

Monocytes or backpack-monocytes were prepared and cultured in non-tissue cultured treated 24-well plates with 200,000 cells suspended in 750uL of growth media or growth media supplemented with 2ng/mL IFNγ. To determine activation status and viability, cells were cultured for 48 hours, harvested, blocked with CD16/CD32 (BioLegend), and stained using LIVE/DEAD Blue (BioLegend), anti-F4/80-BV510 (BioLegend), anti-CD11b-BV785 (BioLegend), anti-CD80-Pe-Cy5 (BioLegend), anti-MHCII-Spark Blue 550 (BioLegend), anti-CD86-BV605 (BioLegend), and anti-CD206-AlexaFluor700 (BioLegend) antibodies. Samples were then fixed and permeabilized and stained using anti-Arg1-eFluor 450 (Invitrogen), anti-IL-10-APC-Cy7 (BioLegend), anti-iNOS-PE-Cy7 (Invitrogen), anti-IFNγ-AlexaFluor647 (Invitrogen) antibodies. To determine chemokine receptor expression, backpack-monocytes or monocytes were cultured in 500uL growth media at 100,000 cells per well in non-tissue culture treated 48-well plate. At 1 hour and 24 hours, cells were harvested, blocked with CD16/CD32 (BioLegend), and stained using LIVE/DEAD Blue (BioLegend), F4/80-BV510 (BioLegend), CD11b-BV711 (BioLegend), Ly6C-Pacific Blue (BioLegend), CCR2-FITC (BioLegend), and CX3CR1-APC (BioLegend). Cytek Aurora analyzer was used, and data were analyzed with FlowJo V10. To determine cytokine excretion, monocytes or backpack-monocytes were seeded at 200k cells per well in non-tissue

culture treated U-bottom 96 well plates. After 24 hours, the plate was centrifuged, and the supernatant was harvested. LEGENDplex™ Mouse Inflammation Panel (13-plex) and LEGENDplex™ Mouse Macrophage/Microglia Panel (13-plex) were used to assay the supernatant samples, following vendor instructions.

4.2.8. EAE model establishment.

EAE was induced in female C57BL/6J mice (Jackson Laboratories) at 9-14 weeks using the EK-2110 kit (Hooke Laboratories), with myelin oligodendrocyte glycoprotein 35-55 (MOG_{35-55}) and Complete Freund's Adjuvant emulsion and pertussis toxin injections as described in *Appendix 9.1.4*. EAE severity was assessed using an established disease score rubric (157). Scoring was performed by an investigator blinded to the treatment groups, as described in *Appendix 9.1.5*. Mice were randomly assigned to different experimental treatments.

4.2.9. Biodistribution study.

Female C57BL6 mice were induced with EAE. 11 days after EAE induction, when mice began showing clinical signs, $3x10^6$ monocytes, backpacks, or backpack-monocytes were administered intravenously via tail vein. Backpacks were labeled with rhodamine and monocytes were labeled with CellTrace Far Red (ThermoFisher) or IVISense DiR 750 (PerkinElmer) depending on the readout. 24 hours, 2 days, or 5 days after administration, blood was drawn, and the mice were euthanized and perfused with saline. For a subset of the mice, the spinal columns were extracted, fixed in formalin for tissue sectioning, and submitted to Hooke Laboratories (Lawrence, MA) for sectioning and DAPI staining of the spinal cord. Tissue sections were imaged with Zeiss Axioscan. For a subset, the major organs, including brain, spinal cord, lungs, heart, liver, spleen, and kidneys, were extracted, and imaged by in vivo imaging system (PerkinElmer IVIS Spectrum). For the final subset of mice, the brain and spinal cord was harvested and digested into single cell suspension as described in the SI. To track the injected cells in the CNS, the single cell suspensions were blocked with anti-CD16/CD32 antibody (BioLegend) and stained using LIVE/DEAD Blue (Biolegend), anti-CD11b-BV711 (BioLegend), and anti-CD45-FITC (BioLegend) antibodies. Cytek Aurora analyzer was used, and data were analyzed with FlowJo V10.

4.2.10. Single Cell Suspension Processing.

For blood samples, the samples were lysed with ACK lysis buffer (3–5-minute incubation with 10-20x blood sample volume at room temperature) and the cells were collected by centrifugation at 300g for 5 minutes. For brain and spinal cord samples, the organs were minced and incubated with enzyme solution from Multi Tissue Dissociation Kit 1 (Miltenyi) following vendor instructions for 60 minutes at 37°C. The suspension was triturated through 70μM cells strainers with cold PBS and pelleted at 300g for 10 minutes. Myelin and other debris were removed using density gradient separation with debris removal solution (Miltenyi) following manufacturer's instructions to yield the final myelin-free single cell suspension.

4.2.11. Antibodies used for In Vivo Studies.

Cells were stained with the following antibodies for *in vivo* studies. Some samples were stained anti-CD45-Pacific Blue (BioLegend), anti-Ly6G-PeCY7 (BioLegend), anti-CD3- BUV737 (Invitrogen), anti-CD11b-APC-Fire 750 (BioLegend), anti-Ly6C-BV570 (BioLegend), anti-F4/80-AlexaFluor488 (BioLegend), and anti-CD19-BV750 (BioLegend) antbodies. Other samples were stained with anti-CD45-AlexaFluor700 (BioLegend), anti-CD3-APC/Cy7 (BioLegend), anti-CD4-BV510 (BioLegend), anti-CD8a-PeCy7 (BioLegend), anti-CD25-AF647 (BioLegend), anti-

CD69, BV785 (BioLegend), anti-IL-17A-BV605 (BioLegend), anti-Tbet-BV421 (BioLegend), anti-FoxP3-PE-CY5 (BioLegend), anti-RORyT-AlexaFluor488 (R&D Systems), anti-IFNγ–BUV737 (Invitrogen) antibodies. Other samples were stained with anti-CD45-PerCP-Cy5.5 (BioLegend), anti-F4/80-BV510 (BioLegend), anti-CD11b-BV750, (BioLegend), anti-CD80-Pacific Blue (BioLegend), anti-MHCII-APC (BioLegend), anti-CD86-BV605 (BioLegend), anti-CD206-PeCy7 (BioLegend), anti-Arg1–eFluor 450 (Invitrogen), anti-iNOS Pe-Cy7 (Invitrogen), anti-IL-10–APC-Cy7(BioLegend), and anti- IFNγ -BUV737 (Invitrogen) antibodies.

4.2.12. Characterization of immune responses induced by backpack-monocytes.

Female C57BL6 mice were induced with EAE. 11 days after EAE induction, when mice began showing clinical signs, $3x10^6$ backpacks, backpack-monocytes, monocytes with blank backpacks, or saline were administered intravenously via tail vein. Monocytes with empty backpacks were used because it has been shown that backpacks alone can affect the carrier cell (Appendix Fig. 9.3-5 *B*)(39). A second dose was administered 3 days later. 24 hours after the second dose, the mice were perfused with saline and euthanized. The blood, brain, and spinal cord were harvested and processed into single cell suspensions, as described in Section 4.2.10. The samples were blocked with anti-CD16/CD32 (BioLegend), stained with LIVE/DEAD Blue (BioLegend), stained for surface markers, fixed and permeabilized, and stained for intracellular markers, as detailed in Section 4.2.11. Cytek Aurora analyzer was used, and data were analyzed with FlowJo V10. Infiltrating myeloid cells and resident myeloid cells were defined based on differential CD45 expression for $CD11b^+$ cells ($CD45^{high}CD11b^+$ for resident myeloid cells, $CD45^{low}CD11b^+$ for infiltrating myeloid cells) (158, 159). Serum and organ suspension supernatant were collected, assayed with LEGENDplex™ Mouse Inflammation Panel (13-plex) and LEGENDplex™ Mouse Macrophage/Microglia Panel (13-plex), and analyzed with the Cytek Aurora.

4.2.13. Therapeutic efficacy of backpack-monocytes.

Female C57BL6 mice were induced with EAE. 11 days after EAE induction, when mice began showing clinical signs, and 14 days after induction, $3x10^6$ monocytes, backpack-monocytes, or saline were administered intravenously via tail vein. Body weight and clinical score were monitored for 25 days by an investigator blinded to the treatment groups. On Day 25, blood was draw and mice were perfused with saline, euthanized, and major organs were harvested. For a portion of the mice, the brain, spinal cord, and blood was digested to yield a single cell suspension for flow cytometry analysis. The organ suspension supernatant was saved, along with a portion of the blood was saved for serum processing. These samples were assayed with LEGENDplex™ Mouse Inflammation Panel (13-plex) and LEGENDplex™ Mouse Macrophage/Microglia Panel (13-plex) and analyzed with the Cytek Aurora. Hematoxylin and eosin (H&E) staining was performed on the non-CNS major organs (Harvard Medical School Rodent Histology Core Facility). For a portion of the mice, the spinal column was extracted and submitted to Hooke Laboratories (Lawrence, MA) for H&E and anti-myelin basic protein (MBP) staining of serial sections of the lumbar, thoracic, and cervical spinal cord. Tissue sections were imaged with Zeiss Axioscan. Immune cell infiltration was measured using QuPath v0.3.2 (160). Eight circular regions of interest, each equal to 23000 um^2, were drawn on each H&E-stained image. The positive cell count analysis tool was used to measure the number of eosin-stained cells in the regions of interest. All analyses were conducted blind to the treatment administered. Blood and serum samples were submitted to IDEXX BioAnalytics (North Grafton, MA) for hematological and serum chemistry analysis.

4.2.14. Statistical Analysis.

All statistical analyses were carried out using GraphPad Prism 8 software. As described in figure captions, unpaired student's t test and one-way or two-way ANOVA with Tukey's HSD (honestly significant difference) test were used to determine significance. The n and P values are indicated in the legends. Flow cytometry analyses were carried out using FlowJo V10.

4.3. Results

4.3.1. Design and characterization of backpack-monocytes.

We designed disk-shaped, microparticles ("backpacks") that carry drug molecules and reproducibly adhere to primary monocytes. Backpacks were prepared from poly-lactic-co-glycolide (PLGA) and *poly(vinyl alcohol)* (PVA) by spin coating in a layer-by-layer fashion, allowing for design modularity. Backpacks consisted of a layer of PLGA/dexamethasone, a layer of PVA/heparin/IL-4, and a final layer of PLGA/dexamethasone (Fig. 4-1 *A*). The PLGA layers were composed of a 2:1 polymer blend of PLGA and PLGA-PEG-maleimide. Heparin was used in the PVA layer to stabilize IL-4 and improve loading (161) (Appendix Fig. 9.3-1 *A*). After micro-contact printing, backpacks were resuspended and functionalized with CD45 F(ab') to functional maleimide groups on the backpack surface via thiol-maleimide click chemistry. Backpacks displayed an average diameter of 7.75 ± 0.25μm, an average thickness of 505.03 ± 43.1 nm, and an average stiffness of 7.37 ± 0.15 GPa, as determined by atomic force microscopy (AFM) (Appendix Fig. 9.3-1 *B*). Backpacks retained their morphology when resuspended in aqueous solution (Appendix Fig. 9.3-1 *C*). Backpack-monocyte complexes were prepared by mixing primary monocytes and backpacks at optimized incubation parameters (Fig. 4-1*B*). A backpack:monocyte ratio of 3:1 during incubation was determined to promote substantial adhesion of CD45-functionalized backpacks to monocytes, while minimizing cell aggregation (Appendix Fig. 9.3-2A). CD45 F(ab')-backpacks exhibited excellent adhesion to murine bone-marrow derived monocytes, with 60.5% of monocytes attached to at least one backpack, compared to 12.9% for unmodified backpacks (Fig. 4-1*C*). Backpack adhesion to monocytes was further confirmed and visualized using confocal microscopy (Fig. 4-1*D,* Appendix Fig. 9.3-2B). We also confirmed that backpacks efficiently attached to primary human blood-derived monocytes (Appendix Fig. 9.3-2 *C*). To verify whether backpacks remained adhered to monocytes under physiological disturbances, backpack-carrying monocytes were exposed to physiologically relevant shear stresses (162). Across increasing shear conditions (2, 6, and 20 Pa), backpacks remained adhered to monocytes (Fig. 41*E*). Furthermore, backpacks did not adversely impact the viability of carrier monocytes (Fig. 4-1*F*). In fact, drug-loaded backpacks led to improved viability compared to untreated monocytes and monocytes treated with free drugs for 72 hours (Appendix Fig. 9.3-2 *D*). This could be due to monocytes being exposed to gradual drug release, compared to a bolus dose of free drug at once.

Dexamethasone and IL-4 were chosen as therapeutic payloads due to their potency in stimulating anti-inflammatory functions, such as tissue repair, phagocytosis, and reactive species processing (associated with biomarkers CD206 (11) and arginase-1 (Arg1) (163)) while dampening pro-inflammatory functions, such as antigen presentation and co-stimulation (associated with biomarkers MHCII (164) and CD80 (11)). By investigating the expression of these biomarkers, we found that dexamethasone and IL-4 acted synergistically on macrophages and achieved a unique phenotype that was only observed upon exposure to both drugs (Appendix Fig. 9.3-2 *E*). The potent effect of IL-4 and dexamethasone on macrophages makes them excellent candidates

for prolonged cell stimulation using backpacks. Backpacks released dexamethasone and IL-4 for at least 5 days (Fig. 4-1*G*). The total drug loading was 37.42 ± 1.68 µg dexamethasone per 10^6 backpacks and 183.1 ± 15.2 ng IL-4 per 10^6 backpacks (Fig. 4-1*G*).

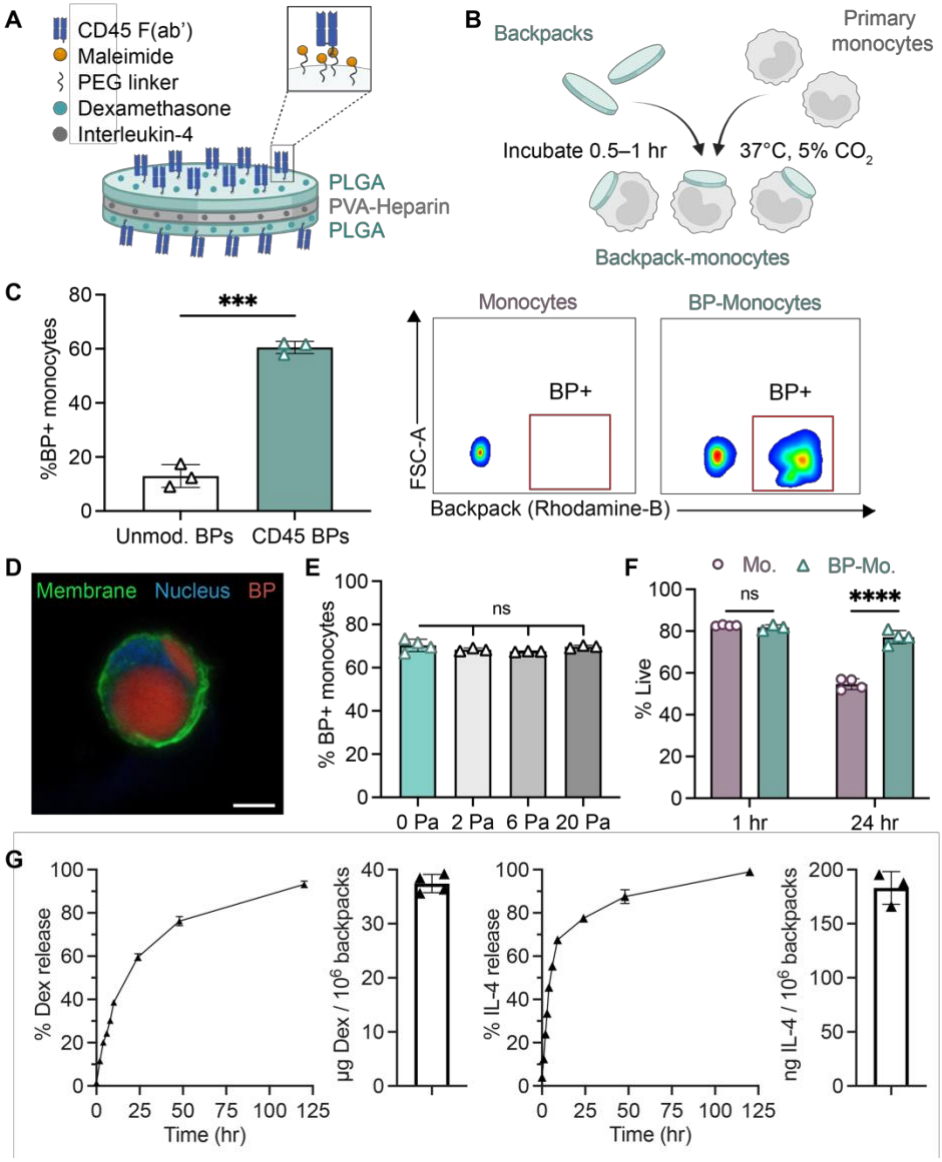

Figure 4-1. Design and characterization of backpack-carrying monocytes.
A) Schematic of backpack (BP) design, including dexamethasone and IL-4 loading and CD45 F(ab') functionalization. B) Schematic of backpack attachment to primary monocytes. C) Percentage of monocytes with >1 backpack (determined by flow cytometry); mean ± SD (n=3). Representative flow cytometry gating of control monocytes vs. backpack-adhered monocytes. D) Confocal micrograph of monocyte (membrane: green, nucleus: blue) with backpack (red). Scale bar = 5µm. E) Percentage of monocytes with backpacks attached following shear studies (determined by flow cytometry); mean ± SD (n=3-4). F) Percentage of live cells at 1 hour and 24 hours for monocytes (Mo.) and backpack monocytes (BP-Mo.) (determined by flow cytometry); mean ± SD (n=3-4). G) Left, release and loading of dexamethasone over time, quantified by HPLC.

*Dexamethasone loading was determined by degrading backpacks post-fabrication via chemical dissolution and quantifying dexamethasone content. Right, release and loading of IL-4 over time, quantified by ELISA. IL-4 loading calculated by cumulative release from backpacks after 14 days, at which point apparent drug release ceased. Mean ± SD (n=3-4). For C, data were analyzed by two-tailed student's t test, ***P<0.001. For E, data were analyzed by one-way ANOVA with Tukey's HSD test; ns, not significant. For F, data were analyzed by two-way ANOVA with Sidak's correction. ****P<0.0001.*

4.3.2. Backpacks induce anti-inflammatory myeloid phenotype.

IL-4 and dexamethasone backpacks induced a strong anti-inflammatory myeloid phenotype, as indicated by reduced expression of pro-inflammatory markers (MHCII, CD80, CD86, *inducible nitric oxide synthase (*iNOS)) and increased expression of anti-inflammatory markers (CD206, Arg1, IL-10) after backpack-laden monocytes were cultured and allowed to differentiate for 48 hours (Fig. 4-2*A,* Appendix Fig. 9.3-3). Compared to control monocytes, backpack-carrying monocytes demonstrated significantly decreased MHCII expression (0.42-fold), CD80 expression (0.22-fold), and iNOS expression (0.81-fold). Backpack-carrying monocytes also demonstrated significantly increased CD206 expression (5.60-fold), Arg1 expression (12.5-fold), and IL-10 expression (1.89-fold). Monocyte activation by backpacks was durable, as seen by phenotype maintenance when backpack-carrying monocytes were cultured in pro-inflammatory media (Appendix Fig. 9.3-*4*), which is expected to resemble *in vivo* conditions. To characterize the effect of backpacks on the local biochemical environment, cytokine production from backpack-carrying monocytes was assessed 24 hours after backpack attachment (Fig 4-2*B*). Backpack-monocytes demonstrated significantly decreased secretion of pro-inflammatory cytokines (i.e., IL-6 and TNFα), and significantly increased secretion of relevant anti-inflammatory and wound healing cytokines (i.e., IL-10 and TGFβ).

As monocytes respond to chemotactic gradients to migrate from circulation to sites of inflammation, it is vital that backpack-monocytes retain chemokine receptor expression. Chemokine receptors CCR2 and CX3CR1 have been implicated in the extravasation and transmigration of monocytes under inflammatory conditions, including MS (165, 166). Our data suggest that CCR2 and CX3CR1 expression of monocytes was not affected by the backpack attachment (Fig. 4-2*C*). In fact, a significant increase in CCR2 and CX3CR1 expression was observed in the backpack-containing subset of backpack-monocytes (Appendix Fig. 9.3-5 *A*). Monocytes with blank backpacks also displayed increased CCR2 and CX3CR1 expression, demonstrating that the backpack itself may impact the cell (Appendix Fig. 9.3-5 *B*). Further, backpack attachment did not influence trans-endothelial migration of murine monocytes, as assessed *ex vivo* (Fig. 4-2*D*). Similar observations were made for primary human monocytes (Appendix Fig. 9.3-5 *C*). Backpack-laden monocytes maintained their ability to differentiate into macrophages, as quantified by F4/80 expression after 48 hours (Fig. 4-2*E*).

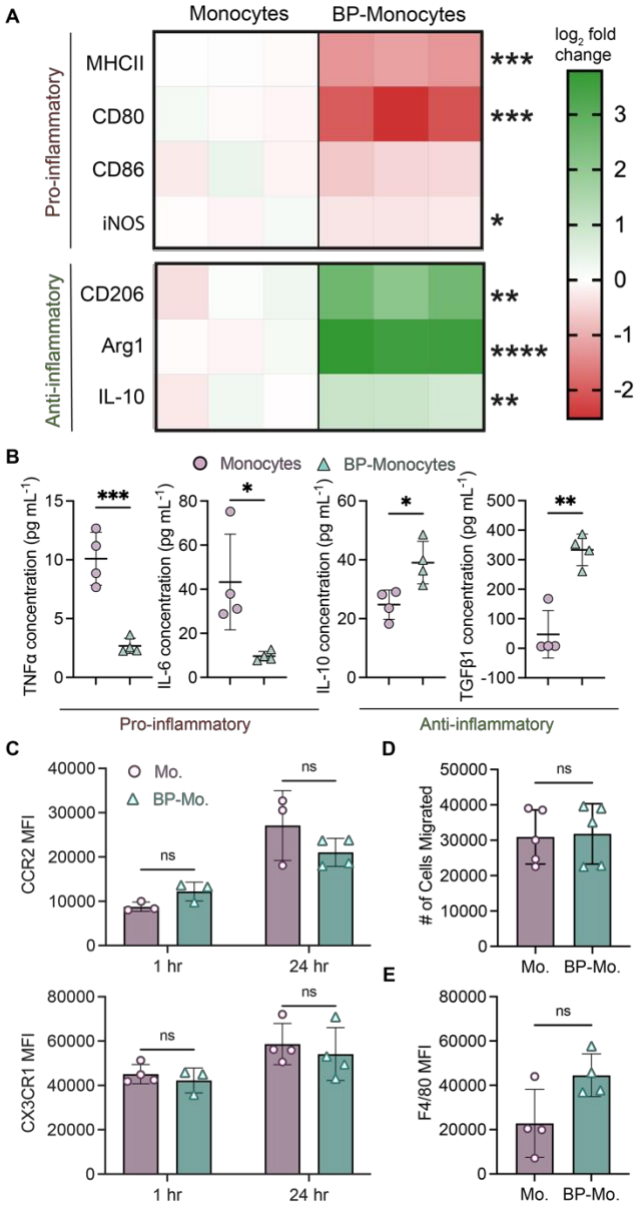

Figure 4-2. Backpacks induce anti-inflammatory phenotype in differentiating monocytes.
A) Monocytes or backpack-monocytes were cultured for 48 hours and analyzed for expression of pro-inflammatory (MHCII, CD80, CD86, and iNOS) and anti-inflammatory (CD206, Arg1, IL-10) markers. Heatmap columns show data from individual replicates (n = 3), reported as log2 fold change in expression compared to the average value of the monocyte group. Raw data are in Appendix Fig. 9.3-*3. B). Cytokine excretion from monocytes or backpack-monocytes after 24 hours; mean ± SD (n=3). C) Chemokine receptor expression of monocytes (Mo.) and backpack-monocytes (BP-Mo.) at 1 hour and 24 hours, quantified by flow cytometry; mean ± SD (n=3-4). D) Migration was assessed using a Transwell assay, with endothelial cells seeded on 5µm inserts, and media containing 10ng/mL CCL2 added to the lower chamber. 200k monocytes or backpack-monocytes were added into the upper chamber. The number of monocytes or backpack-monocytes in the lower chamber after 24 hours was counted; mean ± SD (n=5). E) Monocytes or backpack-*

*monocytes were plated and differentiated for 48 hours. F4/80 expression was quantified via flow cytometry; mean ± SD (n=4). For A, B, D, E, data were analyzed by two-tailed student's t test; ns, not significant, *P<0.05, **P<0.01, ***P<0.001, ****P<0.0001. For C, data were analyzed by two-way ANOVA with Sidak's correction; ns, not significant.*

4.3.3. Backpack-carrying monocytes traffic and accumulate in the CNS

Experimental autoimmune encephalomyelitis (EAE) is a murine model of progressive MS that shares many clinical, histopathological, and immunological characteristics with MS (167, 168) and hence was chosen to assess the therapeutic efficacy of backpack-carrying monocytes. Intravenously injected backpack-carrying monocytes, administered at the onset of disease signs, accumulated in the CNS of EAE mice (Fig. 4-3*A*-*C*). In fact, the percent relative dose of backpack-monocytes that infiltrated the CNS after 24 hours was 1.59%, which was significantly greater than in the case of monocytes alone, 0.96% (Fig. 4-3*C*). The overall organ accumulation at 24 hours of backpack-monocytes was quantified via in vivo imaging system (IVIS) (Appendix Fig. 9.3-6). We observed that backpack-monocytes persist in the CNS of EAE for up to 5 days (Fig**.** 3 *D*). Although the greatest proportion of backpack-monocytes were present in the brain and spinal cord 24 hours after administration, backpack-monocytes could be visualized in the CNS 2 days and 5 days after administration (Fig**.** 4-3*D,* Appendix Fig. 9.3-7). The overall organ accumulation at 2 and 5 days after administration was also quantified (Appendix Fig. 9.3-8).

By analyzing single cell suspensions of the CNS, we found that backpack-carrying monocytes exhibited higher infiltration into the spinal cord (120,756 cells/g organ) compared to control monocytes (50,240 cells/g) (Fig. 4-3*E*). No significant difference was observed between the number of control monocytes (6,901 cells/g organ) and backpack-carrying monocytes (11,455 cells/g) in the brain (Fig. 4-3E). Blood concentrations of control monocytes (2,351 cells/100uL blood) and backpack-carrying monocytes (2,479 cells/100uL blood) were also comparable (Fig. 4-3*E*). Importantly, when free backpacks were administered, only 339 backpacks/g organ and 122 backpacks/g extravasated into the spinal cord and brain, respectively, which was 356-fold and 93-fold lower than quantity of backpack-monocytes that infiltrated into the respective CNS components (Appendix Fig. 9.3-9).

Backpacks remained attached to the carrier monocytes as monocytes infiltrated into the CNS (Figure 4-3*F*). Backpack adhesion stability, quantified as proportion of monocytes tracked *in vivo* carrying backpacks compared to monocytes carrying backpacks pre-injection, was 79.9% for the brain and 81.1% for the spinal cord. Fluorescence imaging confirmed that monocytes and backpacks were co-localized in the spinal cord parenchyma (Fig. 4-3*B*).

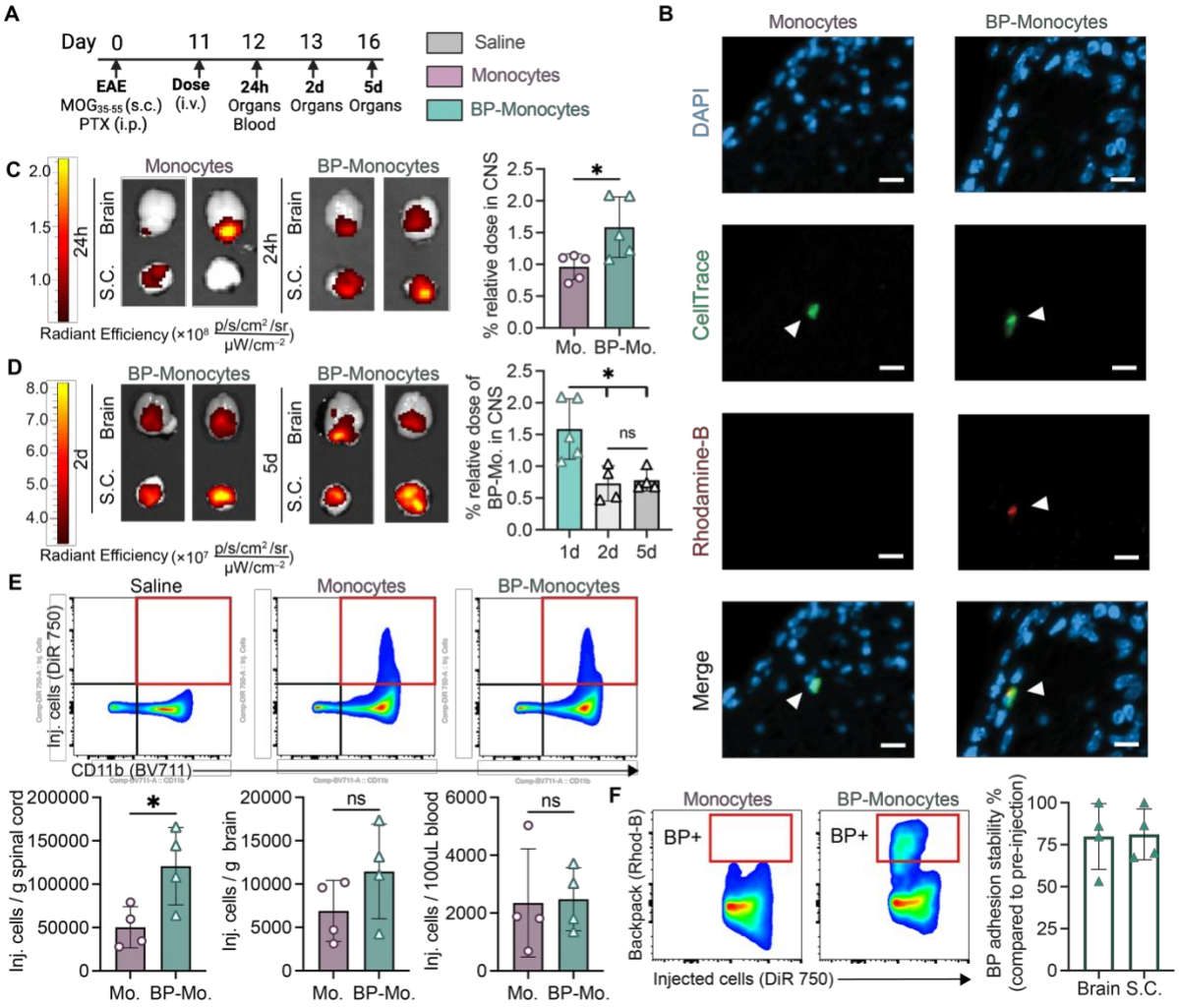

Figure 4-3. Backpack-carrying monocytes migrate to the CNS of EAE mice.
EAE was induced in female C57BL/6J mice. A) Mice were treated with 3×10⁶ monocytes or backpack-monocytes or saline 11 (i.v., tail vein) at the onset of clinical signs on day 11, with the adoptively transferred cells stained with DiR 750 or CellTrace Far Red. The mice were sacrificed after 1, 2, or 5 days, and the CNS and blood were harvested for ex vivo imaging and single cell suspension processing. B) Fluorescence imaging of lumbar spinal cord stained for DAPI (nucleus, blue), Cell Trace (adoptively transferred cells, green), and Rhodamine-B (backpacks (BP), red). Scale bar represents 10µm. C) Representative in vivo system imaging (IVIS) of brain and spinal cord (S.C.) displaying DiR 750 signal 24 hours after monocyte (Mo.) or BP-monocyte (BP-Mo.) administration. Fluorescence quantification of relative dose accumulated in the CNS (cumulative brain and spinal cord signal) for monocytes and backpack-monocytes; mean ± SD (n=5). D) Representative IVIS images of brain and spinal cord displaying DiR 750 signal 2 days and 5 days hours after BP-monocyte (BP-Mo.) administration. Fluorescence quantification of relative dose accumulated in the CNS (cumulative brain and spinal cord signal); mean ± SD (n=4). E) Representative gating for tracking injected cells (DiR 750) after 24 hours in the single cell suspension of the spinal cord; flow cytometry quantification of adoptively transferred cells in the single cell suspensions of the spinal cord, brain, and blood; mean ± SD (n=4). F) Representative

*flow cytometry gating and quantification for backpack attachment to adoptively transferred cells in spinal cord single cell suspension. Adhesion stability is quantified as percent of adoptively transferred monocytes with a backpack adhered as compared to pre-injected backpack-monocyte adhesion; mean ± SD (n=5). For C, D, E, data were analyzed using two-tailed student's t test; ns, not significant, *P<0.05.*

4.3.4. Backpack-monocytes impact immune cell profiles in the CNS.

Treatment with backpack-carrying monocytes elicited changes in the myeloid cell profile of the CNS, compared to the control groups (Figure 4-4*A*, *B*). Although the abundances of general immune cells were similar across groups (Appendix Fig. 9.3-10), among the infiltrating myeloid cells in the spinal cord, there was a significant decrease in iNOS+ infiltrating myeloid cells compared to saline and control monocytes with blank backpacks (Figure 4-4 *A*, *B i*). A significant increase in Arg1+ infiltrating myeloid cells was also observed for the backpack-carrying monocytes compared to the other groups (Figure 4 *B i*). Among the resident myeloid cells of the spinal cord, there was a significant decrease in $MHCII^{high}$ and $CD80^{+}$ resident myeloid cells for backpack-carrying monocytes compared to saline (Figure 4-4 *B ii*). These changes correspond to decreased inflammatory hallmarks typically associated with pro-inflammatory myeloid cells. A significant increase was observed in IFNβ levels, an EAE-resolving mediator, and a significant decrease was observed in IL-6 and IFNγ levels, EAE-exacerbating mediators after treatment with backpack-carrying monocytes (Figure 4*C*) (169, 170). Additional organ cytokine analysis can be found in Appendix Fig. 9.3-11.

Further analysis of the systemic immune response revealed significant decreases in TNFα, IL-17A, and IL-12p70 levels in the serum, common pro-inflammatory mediators (Figure 4-4*D*) (171). Expanded cytokine analysis in the serum is included in Appendix Fig. 9.3-12. Finally, we assessed if there was crosstalk between the myeloid and lymphoid arms of disease by analyzing T cell subsets, as pro-inflammatory myeloid cells can induce T_H1 and T_H17 responses, two drivers of disease pathology (149). On Day 15, within the spinal cord, there was a significant decrease in $IFN\gamma^{+}CD4^{+}$ T cells in the backpack-monocyte treated group, signifying a decrease in T_H1 cells, and a significant increase in $ROR\gamma T^{+}CD4^{+}$ T cells within the control monocyte group, signifying an increase in T_H17 cells (Figure 4-4*E*). This effect on the adaptive immune system was maintained at Day 25, where a decrease in $IL\text{-}17A^{+}$ $CD4^{+}$ T cells in the blood was seen after treatment with backpack-monocytes, demonstrating a decrease in pathogenic T_H17 cells (Figure 4-4*F*). No significant differences were seen in the general immune cell population at this time point in the CNS or blood (Appendix Fig. 9.3-13). Overall, treatment with backpack-monocytes elicited changes in the immune milieu by reducing inflammation through local anti-inflammatory activation of myeloid cells and secretion of inflammation-resolving mediators. Treatment with drug-loaded backpacks alone, the relevant drug dosage control, demonstrated negligible effects on the local and systemic immune environment.

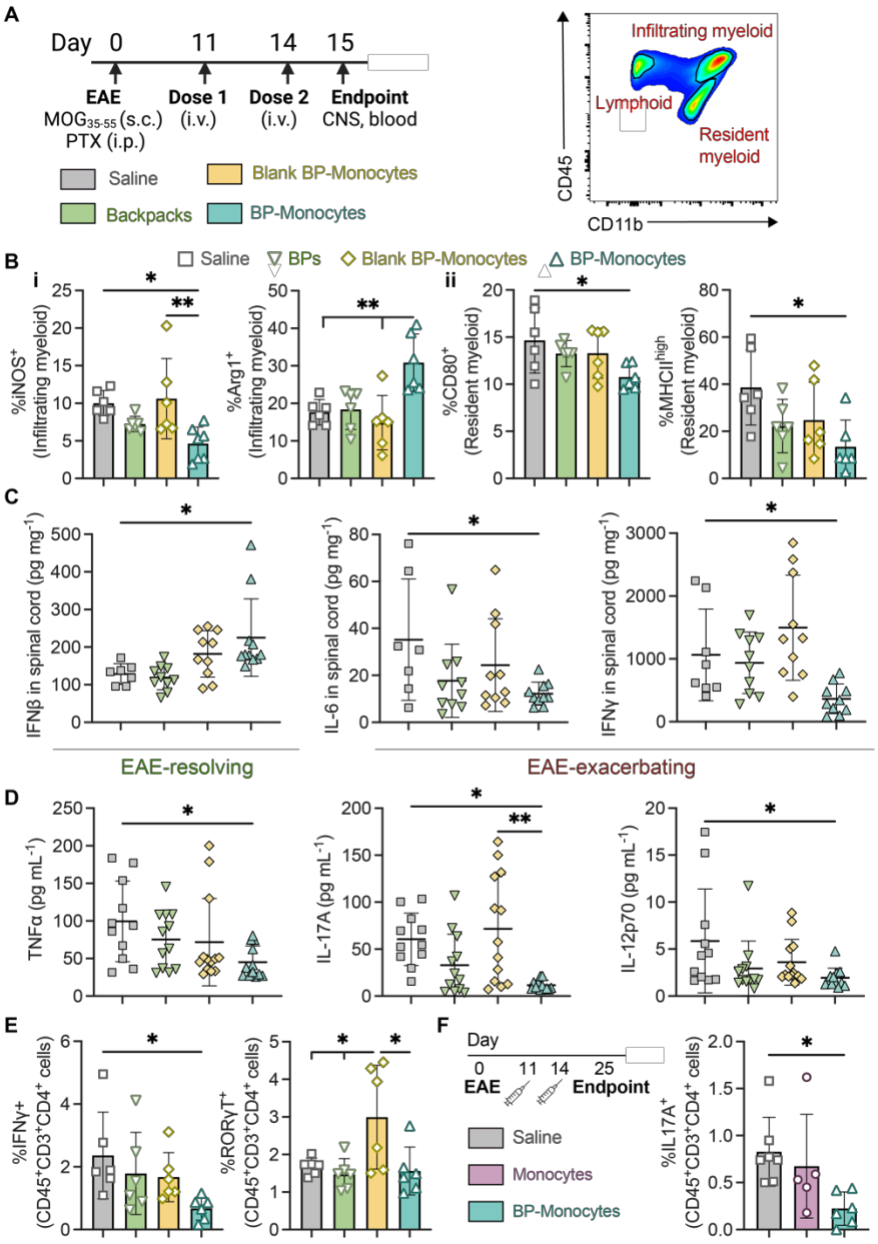

Figure 4-4. Backpack-laden monocytes modulate the CNS immune microenvironment.
EAE was induced in female C57BL/6J mice. A) Mice were treated with 3×10^6 backpacks (BPs), blank backpack-monocytes, backpack-monocytes, or saline on days 11 and 14 (i.v., tail-vein). Mice were sacrificed 24 hours after the second dose. Representative flow cytometry gating for distinguishing tissue resident and infiltrating myeloid cells. B) The spinal cord was processed into single cell suspensions and analyzed via flow cytometry to profile the i) infiltrating and ii) tissue-resident myeloid cell populations; mean ± SD (n=5). C) Concentrations of anti-/pro-inflammatory mediators from spinal cord homogenate at day 15; mean ± SD (n=10-11). D) Serum concentrations of pro-inflammatory mediators at day 15; mean ± SD (n=10-11). E) IFNγ$^+$ and RORγT$^+$ CD4 T cell populations in the spinal cord at day 15; mean ± SD (n=5). F) EAE was induced, and mice were treated with 3×10^6 monocytes or BP-monocytes or saline at days 11 and

*14. At day 25, the IL-17A$^+$ T_H17 population of the blood was analyzed; mean ± SD (n=7). For B, C, D, E, F, data were analyzed using one-way ANOVA with Tukey's HSD test; ns, not significant, *P<0.05, **P<0.01.*

4.3.5. Backpack-monocytes confer therapeutic benefit in a mouse model of progressive MS.

Treatment with backpack-carrying monocytes, dosed therapeutically at onset of disease signs, led to a significant decrease in disease score over time compared to monocytes alone or saline (Fig. 4-5*A, B*). Treatment with backpack-monocytes reversed disease progression to a presentation of limp tail, compared to complete hind limb paralysis in the control groups, and overall diminished cumulative score (Fig. 4-5*B, C*). Furthermore, we report a significant decrease in maximum disease score for the backpack-monocyte group compared to monocytes or saline (Fig. 4-5*D)*. When comparing day of onset of maximum score, the maximum score occurred at a similar time across groups (Fig. 4-5*E*), demonstrating that treatment with backpack-monocytes dampened disease severity, rather than delayed disease progression. Histopathology analyses of the lumbar spinal cord on Day 25 showed reduced inflammatory immune cell infiltration in mice treated with backpack-monocytes, compared to treatment with monocytes or saline (Fig. 4-5*F, G)*. Treatment with backpack-monocytes resulted in a survival benefit, where all mice dosed with backpack-monocytes survived to the end of the study (Fig. 4-5*H*). The biocompatibility of backpack-monocytes was assessed by body weight, hematological analysis, blood chemistry, and blinded histological evaluation of major organs. Hematological analysis and blood chemistry data suggested that backpack-monocytes did not lead to significant changes in the tested markers as compared to the untreated group (Appendix Fig. 9.3-14). Similarly, H&E analysis of the major organs was normal for the treated groups compared to untreated (Appendix Fig. 9.3-15). Given the limitations of dosing (172), half-life (173), and inability to cross the blood-brain barrier (174–176), free drug combination was not tested in the survival study.

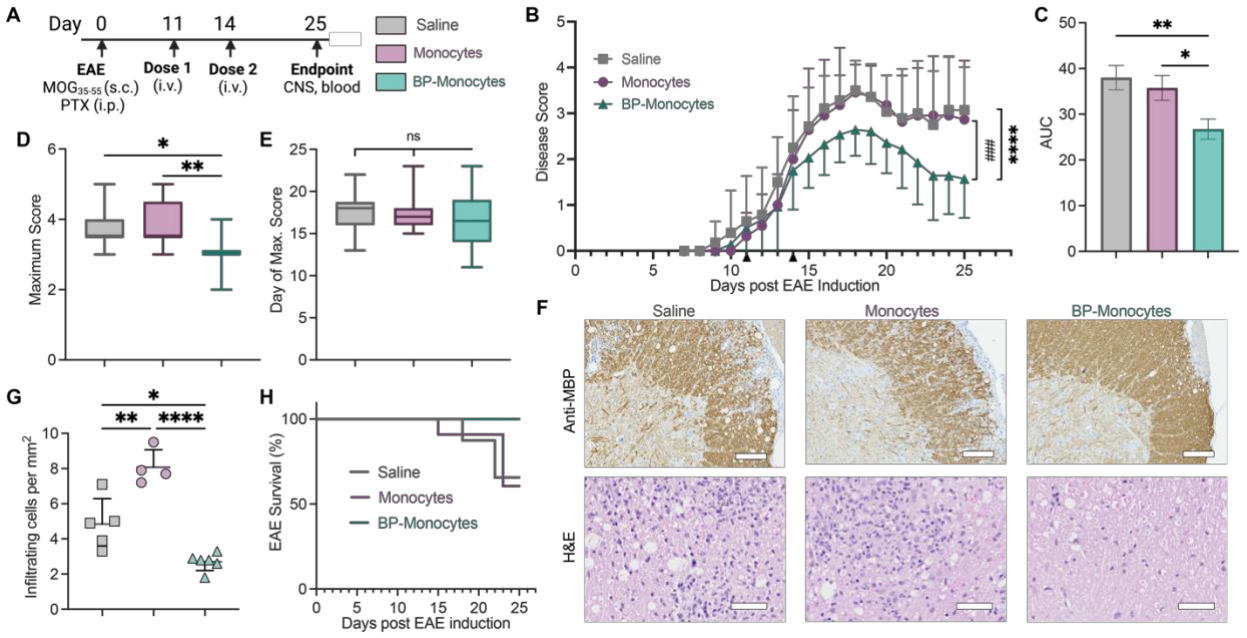

Figure 4-5. Backpack-monocytes are therapeutically effective.
*EAE was induced in female C57BL/6J mice. A) Mice were treated with monocytes, backpack-laden monocytes (BP-monocytes), or saline on days 11 and 14 (i.v., tail-vein). Mice were scored until Day 25. B) Disease score over time; mean ± SE (n=11-14). C) Area under the curve (AUC) of disease score; mean ± SD (n=11-14). D) Maximum disease score; mean ± SD (n=11-14). E) Day of onset of maximum score; mean ± SD (n=11-14). F) Representative anti-myelin basic protein (MBP) staining, revealing areas of demyelination, and hematoxylin and eosin (H&E) staining, revealing inflammatory infiltrates, for lumbar spinal cord sections of mice from (B) (n=5). Anti-MBP scale bar represents 100µm. H&E scale bar represents 50 µm. G) Inflammatory infiltrating cells per mm^2 from lumbar spinal cord sections from (F); mean ± SD (n=4-6). H) EAE survival percentage from mice in (B). (n=11-14). For B, data were analyzed by two-way ANOVA with Bonferroni's multiple comparison; ****P < 0.0001 comparing saline and backpack-monocytes; ###P < 0.001 comparing monocytes and backpack-monocytes. For C and E, data were analyzed using one-way ANOVA with Tukey's HSD test; ns, not significant, *P<0.05, **P<0.01.*

4.4. Discussion

Myeloid cell therapy presents an untapped opportunity for the treatment of MS. Delivery of monocytes alone, however, is not a viable option since phenotype-controlling supporting therapies, such as cytokines, are necessary to maintain immune cell function. Systemic delivery of supporting therapies often results in off-target side effects (2). Cell-adhering backpacks address this challenge by providing a high local drug dose while minimizing systemic drug dose. We designed and characterized backpacks adhered to monocytes for modulating myeloid cell phenotype into an anti-inflammatory state. Backpacks were synthesized using PLGA and PVA and were loaded with IL-4 and dexamethasone. IL-4 and dexamethasone were chosen for their potency, in combination, for stimulating anti-inflammatory, regulatory functions (i.e. phagocytic activity (177), oligodendrogenesis (178)), while dampening pro-inflammatory functions (i.e. antigen presentation (179), cytokine secretion (180)) to achieve a unique, therapeutically-relevant cell phenotype. As IL-4 and dexamethasone are both pleiotropic molecules, loading them into cell-associated

backpacks allows for localization of drug activity to the desired therapeutic site with minimal systemic exposure.

Backpacks persistently activated myeloid cells to an anti-inflammatory, regulatory phenotype. In EAE, CNS myeloid cells, including tissue-infiltrating macrophages and resident microglia, demonstrate upregulated antigen presentation, reflecting interactions with CNS-invading T cells (143). Backpack-carrying monocytes demonstrated significant decreases in MHCII and CD80 expression, correlating to decreased antigen presentation and co-stimulation. Backpack-carrying monocytes demonstrated significant decrease in iNOS expression and increase in Arg1 expression, correlating to processing of reactive oxygen and nitrogen species, mediators of tissue injury and neurodegeneration (181). Finally, backpack-carrying monocytes demonstrated significant increases in CD206 expression, relevant for phagocytosis and processing of myelin debris, and IL-10, relevant for pleiotropic wound-healing effects. These cellular phenotype changes were accompanied by increased secretion of anti-inflammatory cytokines (i.e., IL-10, TGFβ1) and decreased secretion of pro-inflammatory cytokines (i.e., IL-6, TNFα), allowing backpack-laden monocytes to modulate the lesion microenvironment.

In EAE mice, backpack-carrying monocytes migrated to the inflamed CNS with superior trafficking abilities compared to control monocytes. Significantly more backpack-carrying monocytes extravasated into the spinal cord compared to monocytes, which could be attributed to inflammation being initiated in the spinal cord in EAE (139). We hypothesize that the improved trafficking by backpack-monocytes is due to increased chemokine receptor expression of backpack-containing monocytes, increasing the propensity of backpack-carrying monocytes to respond to soluble chemokine cues and migrate to inflamed tissues.

Backpack-carrying monocytes conferred therapeutic benefit in EAE mice, as quantified by improved motor function. Treatment with backpack-carrying monocytes was administered at the onset of disease signs, which is more clinically relevant than studies with prophylactic treatment. The magnitude of measured therapeutic benefit reported here with only 2 doses is on par with reported therapeutic treatment with the standards of care fingolimod (dosed daily) and methylprednisolone (dosed every other day) (182). Since the monocyte therapy reported here focuses on the myeloid arm of the disease, it leads to the possibility that treating both arms of the disease in conjunction may lead to synergistic benefit. Indeed, many current MS therapies that target the adaptive immune system, primarily T cells and B cells, also affect myeloid cells, which are being recognized for their contribution to efficacy of these treatments (142).

Studies reported here show that treatment with backpack-carrying monocytes modulated both the local and systemic immune responses. Within the CNS, backpack-monocytes regulated both the resident and infiltrating myeloid cell compartments in the brain and spinal cord. This is necessary, as macrophages and microglia are the predominant inflammatory cells in active MS lesions (144–146). Our approach is based on findings that suggest the initial proinflammatory polarization of myeloid phagocytes needs to be prevented when treating inflammatory CNS diseases (183). After treatment with backpack-monocytes, resident myeloid cells demonstrated reduced antigen presentation and co-stimulation, which may promote antigen-specific suppression of autoreactive T cells. Infiltrating myeloid cells demonstrated increased Arg1 expression and decreased iNOS expression, reminiscent of the relevant myeloid phenotype during disease remission (184).

Systemically, there was a decrease in relevant pro-inflammatory cytokines in the serum (171). Additionally, we observed a crosstalk by the myeloid and lymphoid branches of the disease, evidenced by effects on T_H1 and T_H17 populations, important drivers of disease pathology. As bidirectional communication between T cells and myeloid cells can shape effector responses (141, 149, 150), these studies demonstrate the pleiotropic effects of myeloid cell therapy for curtailing the inflammatory milieu.

Overall, the studies reported here demonstrate a myeloid cell-based strategy to improve disease outcome in a mouse model of progressive MS. The use of backpack-monocytes offers a biomaterials approach to precisely modulate cell phenotype by providing prolonged cues to persist cellular phenotype *in vivo*. Currently, there are well established methods for harvesting autologous monocytes from patients, involving leukapheresis and rapid monocyte purification, that take less than 3 hours (185–187). Importantly, this approach is antigen-free and does not require genetic engineering. These are vital considerations for translatability, given lack of knowledge regarding the antigens for MS initiation and poor success of antigen-based approaches in the clinic, along with regulatory and manufacturing hurdles for genetically modified cells. Disease treatment could be improved in combination with other medications that target the adaptive immune system, such as fingolimod, which sequesters lymphocytes in the lymph nodes. Taking into consideration the significant role of myeloid cells in disease initiation and progression, our findings support the potential of myeloid cells as a therapeutic modality and target in MS.

4.5. Conclusions

Multiple sclerosis (MS) is an incurable autoimmune disease and is currently treated by systemic immunosuppressants with off-target side effects. Although aberrant myeloid function is often observed in MS plaques in the central nervous system (CNS), the role of myeloid cells in therapeutic intervention is currently overlooked. Here, we developed a myeloid cell-based strategy to reduce the disease burden in experimental autoimmune encephalomyelitis (EAE), a mouse model of progressive MS. We developed monocyte-adhered microparticles ("backpacks") for activating myeloid cell phenotype to an anti-inflammatory state through localized interleukin-4 and dexamethasone signals. We demonstrate that backpack-laden monocytes infiltrated into the inflamed CNS and modulated both the local and systemic immune response. Within the CNS, backpack-carrying monocytes regulated both the infiltrating and tissue-resident myeloid cell compartments in the spinal cord for functions related to antigen presentation and reactive species production. Treatment with backpack-monocytes also decreased the level of systemic pro-inflammatory cytokines. Additionally, backpack-laden monocytes induced modulatory effects on T_H1 and T_H17 populations in the spinal cord and blood, demonstrating crosstalk between the myeloid and lymphoid arms of disease. Backpack-carrying monocytes conferred therapeutic benefit in EAE mice, as quantified by improved motor function. The use of backpack-laden monocytes offers an antigen-free, biomaterials-based approach to precisely tune cell phenotype *in vivo*, demonstrating the utility of myeloid cells as a therapeutic modality and target.

5. Chapter 5: Backpack-induced Anti-inflammatory Macrophages for the Treatment of Traumatic Brain Injury

5.1. Introduction

Traumatic brain injury (TBI) afflicts 3 million people in the United States annually, with around 55,000 fatal cases (188). Despite decades of research, there are no clinically approved therapeutics for the treatment of TBI. The primary brain injury results in the immediate death of neurons and other cells, leading to the extracellular release of pro-inflammatory damage-associated molecular patterns. While a moderate acute inflammatory response after TBI is desired to promote debris clearance and regeneration, excessive inflammation contributes to secondary brain injury. Inflammatory activation of microglia, the brain-resident macrophages, and astrocytes leads to further production and secretion of pro-inflammatory cytokines, along with oxidative stress, local hypoxia, and excitotoxicity (189–191). Furthermore, with blood-brain barrier impairment and production of chemokines, peripheral myeloid cells, such as monocytes and neutrophils, infiltrate from circulation into the injured brain tissue, providing additional sources of inflammation. Infiltrating monocytes differentiate into macrophages and can remain in the contusion site for weeks after the primary injury, contributing to ongoing chronic neuroinflammation (192). Rampant inflammation after TBI contributes to expansion of the lesion, and increases the risk of downstream development of post-traumatic epilepsy, deficits in sensorimotor and memory function, depression, and dementia (188, 193). Thus, managing the inflammatory cascade is vital for ameliorating TBI sequelae.

While some benefits of anti-inflammatory therapeutic strategies for TBI are clear, such strategies should specifically target the damaged brain regions rather than exert global immunosuppression to prevent inadvertent side effects. Cell therapies potentially offer a targeted therapy solution due to the intrinsic ability of cells to chemotactically home to injured tissues. However, cell therapies have found limited use in treating TBI so far. Some preclinical studies have used stem cells for neuro-regeneration, but the use of immune cells, and more specifically macrophages, is a relatively new frontier. Given the role of macrophages and microglia in the dysregulated inflammatory response after TBI, targeting macrophages holds substantial promise. Macrophages perform vital roles of debris clearance in the lesion core and produce growth factors conducive for neurogenesis and angiogenesis (194–196). Accordingly, we hypothesize that delivery of anti-inflammatory macrophages to the lesion microenvironment after injury may confer therapeutic benefits by mitigating damage and promoting tissue repair.

Adoptively transferred macrophages can infiltrate into the brain following the chemotactic gradients generated by TBI-induced inflammation and tissue damage. However, the excessively pro-inflammatory TBI microenvironment can force infiltrating macrophages to undergo pro-inflammatory phenotype switch, which can further exacerbate inflammation. It is critical that adoptively transferred macrophages maintain their anti-inflammatory phenotype *in vivo*, amidst the pro-inflammatory TBI milieu. To prevent pro-inflammatory repolarization and retain anti-inflammatory macrophage phenotype *in vivo*, we use discoidal microparticles, termed backpacks (6, 39), which encapsulate a mixture of two anti-inflammatory agents: interleukin-4 (IL-4) and dexamethasone. Owing to their discoidal shape, backpacks remain adhered to the macrophage surface without internalization and deliver the anti-inflammatory drug cocktail to the carrier macrophage, thereby maintaining it in an anti-inflammatory phenotype. The results reported here demonstrate, to the best of our knowledge, the first use of a cell therapy intervention in a large animal model of TBI. In a clinically relevant, gyrencephalic porcine cortical impact model of TBI, we demonstrate that treatment with anti-inflammatory backpack-macrophages results in a 56%

reduction in lesion volume. Furthermore, we demonstrate potential remodeling of the peri-contusion microenvironment into an anti-inflammatory state. Overall, anti-inflammatory agent-releasing backpacks are an effective strategy for extending anti-inflammatory phenotype of the carrier macrophage, resulting in enhanced therapeutic efficacy against TBI neuroinflammation.

5.2. Materials and Methods

5.2.1. Materials.

PLGA Resomer 502H, dexamethasone, PVA, heparin, RPMI 1640 media, Dipotassium ethylenediaminetetraacetic acid (K_2EDTA), fetal bovine serum (FBS), penicillin and streptomycin (P/S), phosphate buffered saline (PBS), and LIVE/DEAD Blue dye were purchased from Sigma-Aldrich. PLGA-rhodamine B was obtained from PolySciTech Akina. Recombinant murine macrophage colony stimulating factor (M-CSF) was obtained from PeproTech. Recombinant porcine IL-4 was obtained from ThermoFisher. Porcine TNFa and GFAP ELISA kits were purchased from RayBioTech and MyBioSource, respectively. Sylgard 184 Silicone Elastomer kit was purchased from Dow. All primary antibodies for immune cell staining were purchased from Invitrogen, Novus Biologicals, and R&D Systems. All secondary antibodies were purchased from Invitrogen. Cell staining buffer was purchased from BioLegend. Cell fixation/permeabilization kits were obtained from BD Biosciences.

5.2.2. Animals.

Male, Yorkshire piglets aged 30 days were used (n = 24; 8-11 kg; Parsons Farm, Hadley, MA). All protocols used were approved by the Massachusetts General Hospital Institutional Animal Care and Use Committee and the Animal Care and Use Review Office of the United States Army Medical Research and Development Command and adhere to the guidelines of the NIH Guide for the Care and Use of Laboratory Animals. Every effort was made to reduce animal number and animal discomfort and suffering.

5.2.3. Backpack fabrication.

Polydimethylsiloxane (PDMS) templates were prepared as described previously (39)]. Briefly, silicon wafers were fabricated with patterned photoresist in an array of 8 μm holes. PDMS mixed in a 10:1 base to crosslinker ratio from the Sylgard 184 kit was poured onto silicon wafers in petri dishes in 20 g aliquots. The PDMS was de-gassed and cured at 65°C overnight and cut away from the silicon wafers. A solution of 80 mg/mL PLGA Resomer 502H (7 to 17 kDa) and 15 mg/mL dexamethasone in acetone was prepared. For fluorescently labelled backpacks, PLGA-rhodamine B was incorporated at a ratio of 100:1 fluorescent to nonfluorescent PLGA. 220 μL of PLGA solution was spin-coated onto each PDMS quadrant at 2000 rpm for 35 s (at a 200 rpm/s ramp). Quadrants were plasma-ashed with O_2 for 60s. A solution of 0.5 wt% PVA (146 to 186 kDa, 99+ % hydrolyzed) and 0.5 wt% heparin in PBS was prepared with IL-4 (25 μg/ml). Immediately after plasma treatment, 50 μL of PVA/IL-4 solution was spread onto each quadrant. Quadrants were dried in a desiccator for 1h and then a second PLGA layer was deposited using the same procedure as the first. Backpacks were then stamped onto PVA-coated dishes by microcontact printing, as described previously(39). To collect backpacks, PVA-coated dishes were washed twice with 3mL of PBS. The solution was filtered through 20 μm cell strainers and pelleted at 2000g for 5 min. Backpacks were resuspended in media of choice.

5.2.4. Backpack characterization.

Backpacks were harvested from dishes and centrifuged at 2500g for 5 min and resuspended in RPMI + 0.1% bovine serum albumin (BSA). To assess drug release, backpacks were incubated at 37°C while rotating, and supernatant samples were taken at various time points. IL-4 release was quantified via ELISA and dexamethasone release was quantified via HPLC-MS (Agilent 1290 Infinity II), using a similar method as previously reported (197). Atomic force microscopy (AFM, JPK Nanowizard, Bruker) was used to characterize the topology and stiffness of backpacks. Backpacks were adhered to glass slides, mounted on the AFM (JPK Nanowizard, Bruker) and imaged in Qi (single point contact) mode using All-In-One-Al cantilever D with a stiffness of ~40 Nm^{-1}. 10 μm X 10 μm regions were scanned for quantifying backpack topography, followed by a 2 μm X 2 μm scan on backpack surface for probing stiffness. Topography and stiffness were recovered using JPK DP data processing software. Stiffness was obtained by fitting corrected deflection curves to a Hertz model assuming a pyramid tip.

5.2.5. Yorkshire porcine bone marrow cell (BMC) extraction

Prior to PBS and formalin perfusion, the rib cage was collected from 4-6 week old piglets (detailed above) and stored on ice until bone marrow extraction. The surface of the rib cage was cleaned in 70% ethanol and dried prior to transfer into a sterile biosafety cabinet. All media and surgical instruments used were sterile. Surgical scissors and tweezers were used to cut and remove the adipose and muscle tissue from the rib cage, yielding individual ribs. Exposed ribs were cleaned in 70% ethanol and dried once more. To ensure sterility, ~0.5 cm of the end of the exposed bones and the costal cartilage on the opposite end of the rib were cut and removed. Subsequently, the bone marrow was flushed out in 4°C bone marrow extraction media (BMEM: RPMI 1640 with 5 mM K_2EDTA) with a 21 G syringe needle and collected into a sterile 50mL falcon tube. Once the ends of the bones were thoroughly flushed, the bone was cut ~2 cm for subsequent flushing until the bone marrow from the entire rib was extracted. After BMCs from all the ribs were extracted, the BMEM solution was passed through a 40 μm cell strainer into a new sterile 50 mL falcon tube to remove debris. The filtered BMEM solution was centrifuged at 300 g for 10 min, aspirated, resuspended in 4°C PBS, combined into one tube media, and again underwent centrifugation and aspiration. BMCs were then resuspended in 5 mL of ACK lysing buffer for 2 minutes at room temperature, resuspended to 50 mL with 4°C PBS, followed by centrifugation and aspiration. BMCs underwent resuspension in 50 mL of 4°C PBS, centrifugation, and aspiration once more to wash away lysed red blood cells. BMCs were resuspended in 4°C macrophage media (MM-: RPMI 1640 with 1% P/S and 10% FBS) with 10% DMSO at a concentration of 40 million cells/mL, transferred to cryovials and frozen overnight in a Mr. Frosty container at -80°C. The next day, cryovials were transferred to liquid nitrogen for storage until culturing.

5.2.6. Yorkshire porcine bone marrow-derived macrophage culturing

Cryovials were thawed in a metal bead bath until a small ice crystal remained. The cryovials were collected with 4°C MM- at a volume ratio of 1:3 into 50 mL falcon tubes, followed by centrifugation at 300g for 10 min and supernatant aspiration. BMCs were then resuspended in pre-warmed MM+ (MM- with 20 ng/mL murine M-CSF) and counted. BMCs were seeded in TC-treated 100 mm dishes at ~$10x10^6$ BMCs/dish in 12 mL MM+ and placed into an incubator at 37°C and 5% CO_2. To promote cell attachment to the 100 mm dish surface, extreme caution was taken throughout culturing to not disturb the plates. After 6 days of incubation, media was gently aspirated, followed by gentle addition of 12 mL of pre-warmed MM+. On day 9 after seeding,

BMCs had matured into bone marrow-derived macrophages (BMMs) and were ready for subsequent experiments.

5.2.7. Backpack attachment to porcine macrophages

Backpacks were harvested from dishes and centrifuged at 2500g for 5 min and resuspended in media. Backpacks were counted using a hemocytometer and added in the pre-determined ratio (0.75:1 to 3:1 backpacks to macrophages) to each well of the 24-well plate. Plates were then centrifuged at 300g for 7.5 min to allow backpacks to settle on the bottom of the plate. Plates were then placed in a cell culture incubator for 1-1.5h to allow macrophages to bind to backpacks. To harvest the backpack-macrophage complexes, the media from the wells was collected, 4°C PBS was added and collected, and then a 4°C solution of 5mM K_2EDTA in PBS was added. The plates were placed in 37°C incubator for 15 min. The plates were then removed and aggressively tapped to dislodge adherent cells, and the K_2EDTA solution was collected. 4°C PBS was added to the wells, the plates were tapped, and the PBS solution was collected. Further PBS washes and cell scraping were performed as necessary. Cells were centrifuged and pellets were resuspended in media or buffer of choice for downstream use.

For *in vivo* studies, porcine macrophages were plated in non-tissue culture treated 100 mm^2 dishes. Backpacks were harvested, pelleted, and resuspended in media at a concentration of 3-4 million backpacks/mL. 1 mL of media was removed from the macrophage dishes, and 1mL of backpack solution was added per dish and the dishes were swished to disperse the backpacks. Dishes were then placed in a cell culture incubator for 1-1.5h to allow macrophages to bind to backpacks. To harvest the backpack-macrophage complexes, the media was collected as described above using 4°C PBS and K_2EDTA solution with 5 mL per step per 100 mm^2 dish. Cells were centrifuged and pellets were resuspended in 10-20 mL saline for *in vivo* injections.

5.2.8. Phenotyping of backpack-macrophage complexes

For *in vitro* studies, porcine macrophages were matured and replated in non-tissue cultured treated 24-well plates with 150,000-175,000 cells suspended in 500 uL of growth media. Backpacks were harvested, pelleted, resuspended in media, and added at a 2:1 ratio to seeded macrophages. The plates of macrophages were centrifuged at 300 g for 5 minutes and incubated for 1 h in a cell culture incubator. After incubation, the growth media was replaced with unstimulated growth media (MM+), unstimulated growth media containing free porcine IL-4/dexamethasone, or inflammatory media supplemented with 1 ng/mL IFN-γ. To determine activation status longitudinally, cells were cultured and harvested at 1, 4, and 7 days. During the harvesting steps, cells were collected as described previously, and stained using LIVE/DEAD Blue (BioLegend). Samples were washed and blocked with Anti-Pig CD16 (BioRead) in a solution of either 1% goat serum (samples for surface staining) or 1% donkey/chicken serum (samples for intracellular staining). For surface staining, samples were stained with primary antibodies anti-CD80-SuperBright600 (Invitrogen) and anti-CD206 (Novus Biologicals) and secondary antibodies anti-rat-AlexaFluor488 (Invitrogen). For intracellular staining, samples were fixed, permeabilized, stained with primary antibodies anti-iNOS (Life Technologies) and anti-Arg1 (Life Technologies), and stained with secondary antibodies anti-rabbit-AlexaFluor647 (Invitrogen) and anti-goat-AlexaFluor488 (Invitrogen). Samples were resuspended in stain buffer and assayed on the Cytek Aurora analyzer. Data were analyzed with FlowJo V10. The expression of each biomarker was normalized to macrophages alone for each respective day.

5.2.9. Surgical procedures

Piglets were sedated with an intramuscular injection of Telazol (0.5 mg/kg), xylazine (1-2.2 mg/kg), and atropine (0.04 mg/kg) or midazolam (0.05 mg/kg), xylazine, and atropine. Anesthesia was induced by inhaled isoflurane with a snout mask. Surgical sites were clipped and scrubbed. Piglets were draped. Buprenorphine (0.02 mg/kg) was administered at least 15 minutes prior to the incision for analgesia. A Bair hugger blanket with forced hot air was used to maintain core body temperature between 37 and 39°C as body temperature influences lesion size after TBI(198). An ear IV was placed and propofol (0.5-2 mg/kg) was used as an adjunct for anesthetic induction. The piglet was intubated and anesthesia was maintained with isoflurane and mechanically ventilated. Oxygen saturation, heart rate, blood pressure, respiration rate (via mechanical ventilation), end-tidal CO_2, and core body temperature as recorded with a nasal temperature probe was monitored continuously and recorded every 5 min. Ventilation was adjusted to maintain end-tidal CO_2 within 35-45 mmHg. Prior to injury, animals were switched from ventilation with oxygen to ventilation with room air, to parallel TBI in humans. Prophylactic cefazolin (20 mg/kg) was administered intravenously. Local anesthetic bupivacaine (1.5-2.5 mg/kg) was administered subcutaneously at the incision sites prior to incision.

The external jugular vein was catheterized to allow venous access for backpack-macrophages or saline delivery and was tunneled under the skin for exit near the back of the neck. The incision site was closed. Venous blood (5-7 mL) was collected prior to injury for later analysis. The catheter was flushed with heparinized saline (1 to 3 cc, 10 units/mL) if not actively infused with saline.

A straight incision was made approximately 15 cm long, running down the sagittal midline of skull from above the snout to the crown of the head. The intersection of the right coronal and sagittal suture is exposed, and a craniectomy is performed resulting in a 2 cm window over the rostral gyrus, which is the somatosensory cortex for the snout(199). This cortical impact model is well-characterized resulting in a clinically silent, pathoanatomic contusion. The dura was cut in a stellate manner and pulled back. The stand for the indentor was screwed on securely to the skull such that the indentor was perpendicular to the cortical surface. The spring-loaded device was screwed into the stand until contacting the dura. The spring-loaded indentor tip was deployed and the indentor device was removed. No sham animals were used. The skull was not replaced. The cortical surface was gently irrigated with saline. Both incision sites were closed with interrupted subcutaneous suture (2-0 PDS2) followed by a running subcuticular suture (3-0 Monocryl).

5.2.10. Recovery from anesthesia and post-surgical care

Swine were fitted with a vest (SAI Infusion Technologies, Lake Vila, IL) to secure and protect the external jugular catheter and a fentanyl patch (2- 3 ug/kg/hour for 72 h) was applied. Piglets were lightly sedated for the 1 h post-injury blood collection then were placed back on 100% oxygen, removed from mechanical ventilation, and encouraged to start breathing on their own and extubated while on the OR table.

Piglets were serially assigned to receive treatment or saline. The backpack-macrophages or saline were infused with an IV pump (278 mL/hour) in a 10-20 mL volume. In a subset of piglets (n = 1 treated, n=1 saline), cells with backpacks or saline were infused at 1 h post-injury while still in the operating room. In the remaining piglets (n = 20), backpack-macrophages or saline was

administered 4 h post-injury. Initially, piglets (n = 16) were re-anesthetized at this time point with brief exposure to isoflurane mixed with 100% oxygen delivered via snout mask. At the same time, piglets received a second dose of buprenorphine (0.02 mg/kg) to provide analgesia until the fentanyl from the patch was absorbed. However, after some piglets were apneic during the second bout of anesthesia, the last 4 piglets remained awake for their blood collection and administration of backpack-macrophages or saline. In this case, backpack-macrophages or saline was administered by hand slowly over 1-2 minutes instead of using an IV pump for logistical reasons.

Seven days after cortical impact, piglets were anesthetized with an intramuscular injection of ketamine and xylazine, anesthetized with isoflurane (2%) and intubated. Cerebrospinal fluid (CSF; 2-4 mL) was collected from the cisterna magna with an 18-gauge spinal needle. Piglets were deeply anesthetized (4-5% isoflurane). The chest cavity was opened, and the ribs were removed. In a subset of piglets, ribs were put on ice for harvest of bone marrow cells. Piglets were then perfused through the heart with PBS followed by 10% formalin. The brain was collected as well as samples from the liver, spleen, kidney, and lung. Organs were post-fixed in 10% formalin for 3-5 days before being moved to PBS. One treated piglet underwent the above steps 6 days after cortical impact, due to surgical room availability.

5.2.11. Indentor devices

Two indentor devices were machined in November 2021 for this study. Each is a spring-loaded device previously described(198, 200). Deployment characteristics were analyzed in one indentor ("A"; green) by a biomechanical engineering lab. The uncocked indentor tip was positioned 150 mm away from the top of the laser displace sensor. The indentor was cocked and deployed 5 times with data sampled at 10,000 Hz with a data acquisition system (Labview Signal Express 2015, National Instruments, Austin, TX). A custom MATLAB script was written to analyze the data. A fourth order Butterworth low pass filter with a cut-off frequency of 150 Hz was used on each data set. The region of interest was identified, and the impact velocity was calculated using the last half of the displacement data and polyfit to calculate the slope (velocity) of the line. The impact velocity data location was chosen to eliminate the edge effects (getting the mass up to speed at the start; metal on metal and the resulting rebound at the end). The indentor was found to operate within expected limits: velocity at impact of 1.597 m/s, a time to deploy of 3.5 ms. Indentors were alternated so that a similar number of saline and treated piglets received the same indentor.

5.2.12. Histology

Brains were photographed and cut into 5 mm slabs in a standardized manner separating hemispheres ipsilateral and contralateral to the unilateral cortical impact. Brains were paraffin embedded and 5 μm slices were sectioned, mounted, and baked for 30 minutes at 60°C. The majority of sectioning, H&E, and all of the immunohistochemistry was performed by Comparative Pathology and Genomics Shared Resource at Tufts University Cummings School of Veterinary Medicine. Some sectioning and hematoxylin and eosin (H&E) staining were performed in the Brain Trauma Lab as well as the MGH Pathology Core at Charlestown Navy Yard.

For immunohistochemistry for Iba-1 and CD80, sections were deparaffinized and hydrated. Antigen retrieval was accomplished by heating in a pressure cooker for 25 minutes in citrate buffer then cooled for 20 min at room temperature. Sections were rinsed twice in distilled water (rinses were in distilled water unless specified), loaded onto IntelliPATH FLX automated IHC staining

system (BioCare Medical, Pacheco, CA) and flooded with TBS Auto Wash Buffer ("Buffer"; BioCare Medical) with 3% hydrogen peroxide, 2 changes, 5 minutes each, rinsed twice with Buffer. Sections were blocked for 10 min (Background Punisher, BioCare Medical). Without rinsing, primary antibodies (Iba-1: anti-Iba-1 1:2k, Polyclonal Rabbit, Wako, FujuFilm 019-19741; CD80: anti-CD80 1:50, Polyclonal Rabbit, Invitrogen PAS83990/E3585469) or a universal negative were applied and incubated for 60 min at room temperature. Slides were rinsed twice in Buffer and the secondary HRP-antibody was applied (Mach2 Rabbit HRP-Polymer, BioCareMedical) for 30 min at room temperature. Sections were rinsed twice in Buffer and DAB chromagen was applied and incubated at 4 min at room temperature and rinsed. Sections were counterstained with hematoxylin 1:1 for 4 min, rinsed twice, and exposed bluing reagent for two minutes, rinsed twice, removed from IntelliPATH FLX, rinsed again, and dehydrated 2 changes each 95% ethanol, 100% ethanol, xylene, and were coverslipped.

5.2.13. Microscopic evaluation of backpacks

For backpack quantification, sections were deparaffinized, hydrated, and were coverslipped with soft set mounting medium containing DAPI (VECTASHIELD Antifade, Vector Laboratories). Backpacks were tagged with rhodamine B a fluorescent probe that emits at 568 nm.

The number of backpacks was determined in the peri-contusion region or the analogous region on the rostral gyrus in treated piglets. Some backpack-like signals were detected in saline piglets via the automated analysis due to red blood cell presence at the contusion site from hemorrhage. Red blood cells exhibit autofluorescence and are similar in size as the backpacks. The area was brought into focus using the DAPI/405 nm filter then switched to the red/595 nm filter. A set of qualitative photos were taken of both backpacks (595 nm filter) and DAPI (405 nm filter) and merged. The protocol was tested with piglets that did and did not receive macrophage-backpacks to ensure few false positives. Additionally, backpack density was determined in the kidney, liver, lung, and spleen in 4-5 piglets per group. 5 standardized images using Zen Microscopy image acquisition software were obtained with the 20x objective (ZEISS, Germany; 3200K white balance, X-cite at 50% for photos in red and 20% for blue/DAPI; exposure time for DAPI photos 400 ms; 494/red 3800 ms with the contrast adjusted using the "black" at 35). Only structurally intact tissue was evaluated to focus attention on potentially salvageable tissue and avoid red blood cells. Fields photographed avoided hemorrhages or cavitations in the tissue, which were filled with cells and cell debris.

Backpack counting was automated using the ImageJ Auto count plug in. The threshold was adjusted until only backpacks were highlighted in red, binarized, watershed, and then the erode function was used if the image contained extremely small points. The processed image was saved and then analyzed using the analyze particles function. Background signal displayed in Figure Appendix Figure 9-21.

5.2.14. Microscopic evaluation of lesion volume

The lesion was marked on one section from 4-5 blocks (5 mm thick; Fig. S5A-B) spanning the lesion or the comparable location in sections stained with H&E. Areas that were marked as lesion included pyknotic and vacuolized neurons, hemorrhage, and areas where there was loss of structure of tissue with either cavitations and or the beginnings of a glial scar (disorganized white or gray matter). (Fig. S9). White matter was designated as lesion when there was loss of tightly packed

fibers resulting in rarefaction and/or contained hemorrhage. However, white matter that demonstrated mild edema, including swelling of oligodendrocytes, which is often fixation artifact, was not included as it is non-specific and/or might resolve.
The marked slide was then photographed with a ruler and the lesion area was determined with the ruler tool, paint can tool, and polygonal lasso tool adding layers in Photoshop. The volume of lesion was calculated by multiplying lesion area on each section multiplied by the slice thickness (5 mm) and calculating the sum. Alternatively, the area of lesion as a percent of the contralateral hemisphere was calculated to allow comparison to future studies that might test the effect of age, scaling by brain size. The ratio of the lesion to the contralateral hemisphere was multiplied by 100 and averaged among sections. The lesion size as a percent area was very similar in pattern between groups to lesion volume estimates (Fig. S10).

5.2.15. Macroscopic evaluation of lesion volume

To evaluate differences in swelling and/or edema in addition to microscopic lesion, similar to what might be measured via T2 MRI imaging, macroscopic lesion volume was calculated via photographs of the coronal 5 mm slabs exhibiting visual abnormalities. The area of lesion was marked in Photoshop and volume calculated as described above (microscopic evaluation of lesion volume). Marked areas included hemorrhage, dusky or dark areas of cortex, as well as areas of swelling that were asymmetric from the uninjured, contralateral hemisphere. Both lesion volume and lesion area as a percent of the uninjured hemisphere were calculated as described above. Similarly, areas of hemorrhage only were marked in Photoshop and volume calculated.

5.2.16. Microscopic evaluation of Iba-1 and CD80

Whole brain hemispheres were scanned under brightfield at 20x magnification on the ZEISS Axio Scan-Z1 Slide Scanner to obtain .czi files. Five subset fields were obtained for analysis per slide. Fields randomly sampled the gray matter in the peri-contusion area of the rostral gyrus and ranged in size from 3.7-6.2x10^6 μm^2. Fields were analyzed via ImageJ analysis macros developed in-house. The authors were blinded to whether fields corresponded to saline or treated piglets and ipsilateral or contralateral hemispheres when developing the ImageJ analysis macro. The .czi files were imported into ImageJ as RGB images.

For Iba-1 analysis (Appendix Figure 9-29), after duplicating the Blue channel from the original RGB image, the Blue channel was binarized via *Yen auto-threshold* and converted to mask. The mask then underwent the *Analyze Particles* function with 1300 minimum pixel size, outputting the object count per field representing the number of Iba1+ cells, and the circularity of each object. The fields were separately processed to obtain the area. Microglia cell density was calculated with Equation (1):

$$Microglia\ cell\ density = \frac{Microglia\ cell\ count}{Field\ area\ (mm^2)}$$

Circularity was calculated with Equation (2):

$$Circularity = \frac{4\pi A}{P^2}$$

Where A and P are the individual microglial cell areas and perimeters.

For CD80 analysis (Appendix Figure 9-30), after duplicating the Blue channel from the original RGB image, the Blue channel was binarized via *Otsu auto-threshold* and converted to mask. The mask was then inverted and underwent *Create Selection* to add the cell bodies to the ROI manager. The mask then underwent the *Analyze Particles* function to create a new mask with 1300 minimum pixel size and 0.4-1.0 circularity to remove dark signals from debris and nuclei without CD80 positivity. The new mask underwent *Create Selection* to obtain an ROI of CD80+ objects. This ROI was superimposed onto a duplicate of the Red channel, underwent the *Clear Outside* function, was binarized via *Isodata auto-threshold*, converted to mask, inverted, and underwent *Create Selection* to obtain CD80+ objects without dark nuclei centers. The mask was then inverted and underwent *Create Selection* for a new ROI. This new ROI was then superimposed onto a duplicate of the Blue channel, underwent the *Clear Outside* function, and was binarized via *Isodata auto-threshold* and converted to mask to remove light nuclei centers. The mask was then inverted and underwent *Analyze Particles* with 200 minimum pixel size to add an ROI of each individual object containing the soma of CD80+ cells without nuclei. The pixel intensity of each individual object ROI was then measured on a duplicate of the Red channel.

To obtain the mean background pixel intensity per field (Appendix Figure 9-31), after duplicating the Red channel from the original RGB image, the Red channel was binarized via *Otsu auto-threshold*, converted to mask, inverted, and underwent *Create Selection* to add cell bodies ROI. The cell bodies ROI was then superimposed onto a duplicate of the Red channel and underwent the *Clear Outside* function to remove the cell bodies. A duplicated Red channel without cell bodies was then binarized via *Yen auto-threshold*, converted to mask, and underwent *Create Selection* to add the void white spaces ROI. This void white space ROI was superimposed onto the Red channel without cell bodies and underwent *Clear Outside* function to yield background only, which was measured for pixel intensity.

Individual object pixel intensity (IPI) and field background pixel intensity (FPI) were subtracted from 255 to obtain an inverted pixel intensity value, where 0 represents no signal, and 255 represents fully saturated signal. The CD80 pixel intensity increase was calculated with Equation (3):

$$CD80\ Pixel\ Intensity\ Increase = \frac{Inverted\ IPI - Inverted\ FPI}{Inverted\ FPI} \times 100\%$$

5.2.17. Inflammatory marker analysis of serum and CSF

Blood was obtained from an external jugular vein catheter from swine at -1h pre-injury, and 1, 4, 24, and 168 h post-injury. Blood was stored for 15-30 min at room temperature to allow for clotting, followed by centrifugation at 1,000 g for 10 minutes at 4°C for collection of the serum supernatant. CSF was obtained via lumbar puncture at 168 h post-injury. Serum and CSF were prepared in 120 µL aliquots and stored at -80°C. Serum and CSF samples were transferred from -80°C to 4°C to thaw overnight. The porcine TNF-α ELISA kit (RayBioTech) and porcine glial fibrillary acidic protein (GFAP) ELISA Kit (MyBioSource) were performed following the manufacturer's instructions. Samples were diluted 2-fold in assay diluent prior to running the ELISAs. Porcine TNF-α concentration was measured at 450 nm based on TMB substrate colorimetric detection, and porcine GFAP concentration was measured at 450 nm based on HRP substrate colorimetric detection system on a BioTek Synergy H1 microplate reader. TNF-α and GFAP concentrations were normalized to the -1h pre-injury concentrations of each individual respective piglet to obtain the biomarker baseline percentage with Equation (3).

$$Baseline\ \%_{\ TNF-\alpha\ or\ GFAP} = \frac{Concentration_{TNF-\alpha\ or\ GFAP}}{-1h\ Concentration_{TNF-\alpha\ or\ GFAP}} \times 100\%$$

5.2.18. Transparency and Reproducibility

In this first attempt at determining the efficacy of a cell-based therapy to treat TBI, only male piglets were used and both a 1 h and 4 h delay to treat was chosen. Due to initiation of the coordination and logistics of producing the large volume of engineered cells, piglets were not randomized but treatment was alternated. If there was an issue in the batch of cells where infusion was not attempted, then both piglets scheduled that day were assigned to receive saline that day. Our previous lesion size data after cortical impact in 1 month old male piglets was used for a power analysis. We calculated that 10 piglets per group would detect a 78% difference in lesion size at an alpha level of 0.10 and a power of 95%. All tissue analyses were performed by those blinded to treatment. A total of 5 piglets were excluded from lesion analyses (Table S4). Two piglets were excluded as they did not finish the experiment. An additional 3 piglets were excluded due to problematic backpack-macrophages: piglets were excluded if the culture media was acidic (n = 2) and one piglet was excluded that received backpack-macrophage count >1 standard deviation from the mean count of backpack-macrophages. The piglet excluded for low macrophage-backpack count was included in the data to test a correlation between macrophage-backpack number administered and lesion size. Data generated here will inform our future power tests to detect a 50% reduction of lesion volume at an alpha level of 0.05. A total of 19 piglets were in the study: 11 in the saline group, 8 in the backpack-macrophage group. No individual data points were excluded.

5.2.19. Statistics

For *in vitro* assessments concerning backpack-macrophage binding and viability, data were tested via one-way ANOVA with Tukey's HSD test (*$p < 0.05$, **$p < 0.01$, ***$p < 0.005$). The main effects of treatment and hemisphere and the interaction on backpack density at the contusion site was tested via two-way ANOVA followed by Tukey's HSD test. The main effects of treatment, organ, and the interaction on backpack density in the kidney, liver, lung, and spleen were tested via two-way ANOVA followed by Sidak post-hoc testing. A reduction from treatment with backpack-macrophages was tested in macroscopic and microscopic lesion volume or lesion area as a ratio of the contralateral hemisphere via one-sided, unpaired students t-test. One-sided Pearson Correlation between backpack-macrophage number and lesion volume was determined. Because of the variability intrinsic to large animal, outbred species and of the porcine cortical impact model in this study, *$p < 0.1$ was considered significant for *in vivo* assessments: backpack counts, lesion analysis, and serum/CSF biomarker concentrations. A Chi-square test was performed to detect differences in complications in saline vs. treated piglets.

5.3. Results

5.3.1. Backpacks adhere to porcine macrophages.

Backpacks were designed to adhere to the surface of macrophages. The high aspect ratio of backpacks is a key design feature that allows them to avoid phagocytosis and remain on the cell surface(8). Backpacks comprised three layers: the two outer layers comprised of dexamethasone in poly(lactic-co-glycolic acid) (PLGA) and the middle layer comprised of IL-4 in poly(vinyl

alcohol) (PVA). (Fig. 5-1A). The combination of dexamethasone and IL-4 has been shown to induce synergistic effect in induction of anti-inflammatory macrophage phenotype (12). Backpacks were prepared through serial spin coating steps, as described previously (12). Backpacks possessed an average radius of 8.2 µm, thickness of 914 nm, and stiffness of 7.57 GPa (Appendix Fig. 9-16).

Porcine macrophages were cultured and differentiated from bone marrow and pre-stimulated with IL-4 (Appendix Fig. 9-17). Backpack-macrophage complexes were prepared by incubating backpacks with plate-adhered macrophages to allow backpack attachment to the macrophage surface. Flow cytometry confirmed that backpacks adhered reproducibly to porcine macrophages, with 33.9% of macrophages attached to at least one backpack at a backpack:macrophage incubation ratio of 3:1 (Fig. 5-1B). Adhesion of backpacks to human macrophages was also confirmed with 35.15% of human macrophages differentiated from blood-derived human monocytes attached to at least one backpack, as quantified by flow cytometry (Fig. 5-1C). Confocal microscopy confirmed that backpacks remained adhered to the macrophage surface without internalization (Fig. 5-1D). Backpacks remained adhered to macrophages when exposed to physiologically relevant shear stress conditions (2, 6, and 20 Pa) (Fig. 5-1E). Physiological shear stress ranges from in 0.1-7 Pa in the vasculature (162, 201).

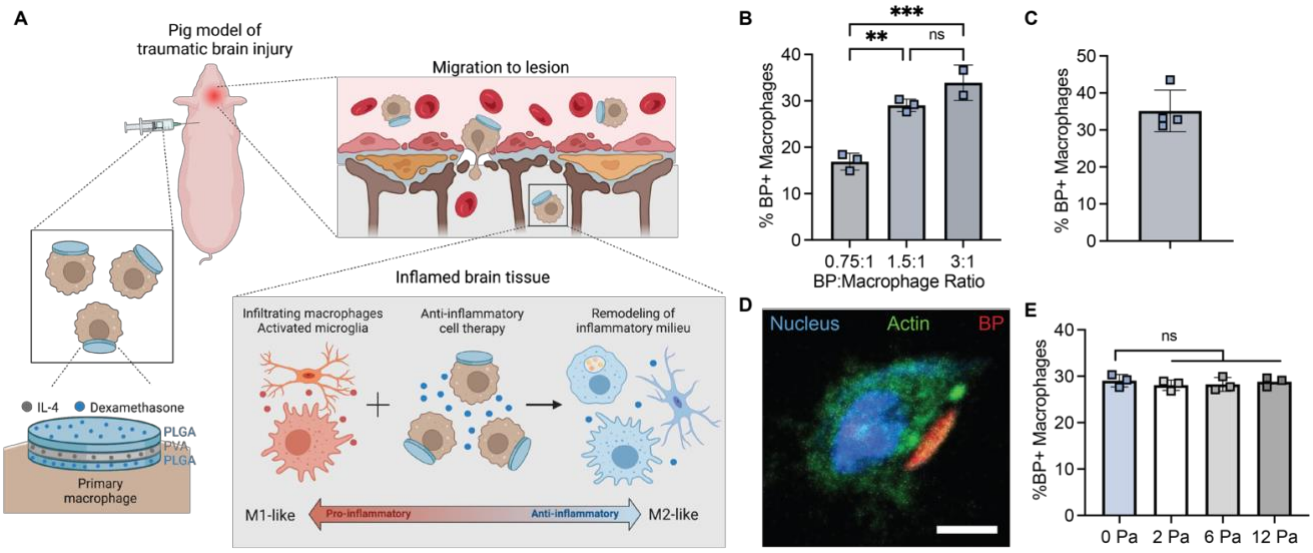

Figure 5-1. Backpacks reproducibly adhere to porcine macrophages.
A) Schematic of concept shows that backpacks loaded with IL-4 and dexamethasone are adhered to porcine macrophages. Upon intravenous infusion, backpack-macrophages respond to inflammatory cues to traverse through the disrupted blood-brain barrier. Backpack-macrophages extravasate into inflamed brain lesion to remodel the inflammatory milieu. B) Percentage of porcine macrophages with ≥1 backpack (BP), as determined by flow cytometry (mean ± SD, n = 2-3). C) Percentage of human macrophages with ≥1 backpack as determined by flow cytometry (mean ± SD, n = 4). D) Confocal micrograph of porcine macrophage (Actin: green, nucleus: blue) with backpack (red). Scale bar = 5 µm. E) Percentage of macrophages with backpacks attached following shear studies as determined by flow cytometry (mean ± SD, n = 3). For B, E, data were

*analyzed by one-way ANOVA with Tukey's HSD test (ns = not significant, **p < 0.01, ***p < 0.005).*

5.3.2. Backpacks induce durable phenotype shifts in porcine macrophages.

Backpacks induced a durable shift in polarization *in vitro* as assessed by the expression of key pro-inflammatory (iNOS, CD80) and anti-inflammatory (Arg1, CD206) markers. The expression of each biomarker was normalized to macrophages alone. In both unstimulated and inflammatory media, backpacks decreased the expression of pro-inflammatory biomarkers iNOS and CD80 and increased the expression of anti-inflammatory biomarkers Arg1 and CD206 to a level comparable or greater than that induced by an equivalent dose of a free drug bolus dose over 7 days (Fig. 5-2A, B). Furthermore, backpacks did not adversely impact the viability of carrier macrophages (Fig. 5-2C). Backpacks did not induce aggregation of macrophages as confirmed by analysis of singlets via flow cytometry (Fig. 5-2D). Backpacks undergoing one freeze-thaw cycle also adhered to macrophages with a minimal loss in adhesion efficiency compared to that of freshly prepared backpacks (Fig. 5-2E).

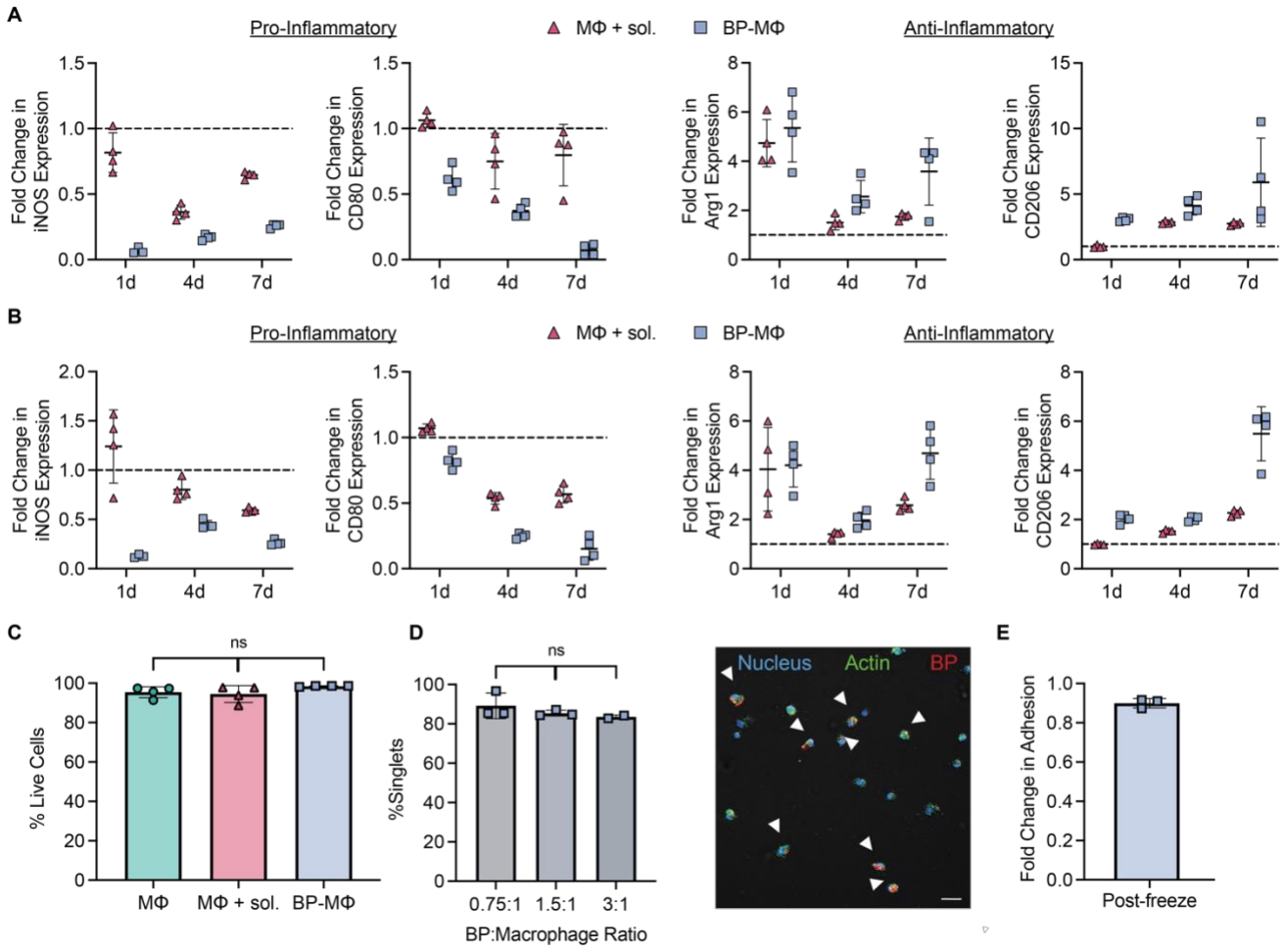

Figure 5-2. Backpacks promote a robust anti-inflammatory phenotype in porcine macrophages.

Macrophages (MΦ), macrophages with soluble IL-4/Dexamethasone (MΦ + sol), or backpack-macrophages (BP-MΦ), were cultured for up to 7 days in A) unstimulated media or B) inflammatory media (supplemented with 1 ng/mL IFN-γ). Cells were analyzed for expression of pro-inflammatory (iNOS, CD80) and anti-inflammatory (Arg1, CD206) markers. Expression of each marker was normalized to the average expression by macrophages alone. Complete data for A show in Appendix Figure 9-18. Complete data for B shown in figure Appendix Figure 9-19. C) Percentage of live cells at 24 h for macrophages (MΦ), macrophages with soluble drug (MΦ + sol.), and backpack-macrophages (BP-MΦ), as determined by flow cytometry (mean ± SD, n = 4). D) Left: Percent of singlets of cells as a function of backpack (BP):macrophage ratio, as determined by flow cytometry (mean ± SD, n = 2-3). Right: Confocal micrograph of porcine macrophages (ActinGreen488: green, NucBlue: blue) with backpacks (rhodamine B: red). White arrows denote backpack-macrophage complexes. Scale bar = 20 μm). E) Fold change in backpack adhesion, as quantified by flow cytometry, for freeze-thaw backpacks compared to freshly printed backpacks (mean ± SD, n = 3). For C and D, data were analyzed by one-way ANOVA with Tukey's HSD test (ns = not significant).

5.3.3. Backpack-macrophage scale-up for in vivo porcine cortical impact studies.

A workflow for high-throughput scale-up of backpack-macrophage production was established to enable studies in porcine cortical impact studies. We began bone marrow cell maturation 9 days before the surgery day, in preparation of on average 141 million macrophages per treated piglet (84-262 million, Table S1). We reproducibly printed 2.4 x 10^6 backpacks per PDMS template (Appendix Figure 9-20) and adhered backpacks to porcine macrophages cultured in 100 mm dishes. For treated piglets, 17.75% of macrophages had ≥1 backpack on average (Appendix Table 9-2).

5.3.4. Backpacks accumulate at the site of the contusion in an outbred, gyrencephalic porcine model of TBI.

Seven days after backpack-macrophage intravenous administration in pigs subjected to cortical impact, backpacks were observed in the lesion penumbra in treated subjects (Fig. 5-3A-C). Some DAPI-labelled cells were adhered to multiple backpacks (Fig. 5-3C magnified inset). For treated subjects, backpacks penetrated healthy appearing tissue adjacent to the penumbra. Backpack density was greater in the lesion penumbra (~80 backpacks/20x field) compared to analogous regions in the contralateral hemisphere (~25 backpacks/20x field) of treated piglets (Fig. 5-3D). Among other organs, backpacks exhibited higher accumulation in the lung and the spleen compared to the kidney and liver (Fig. 5-3E, see Appendix Figure 9-21 for analysis of background signal in pigs administered saline).

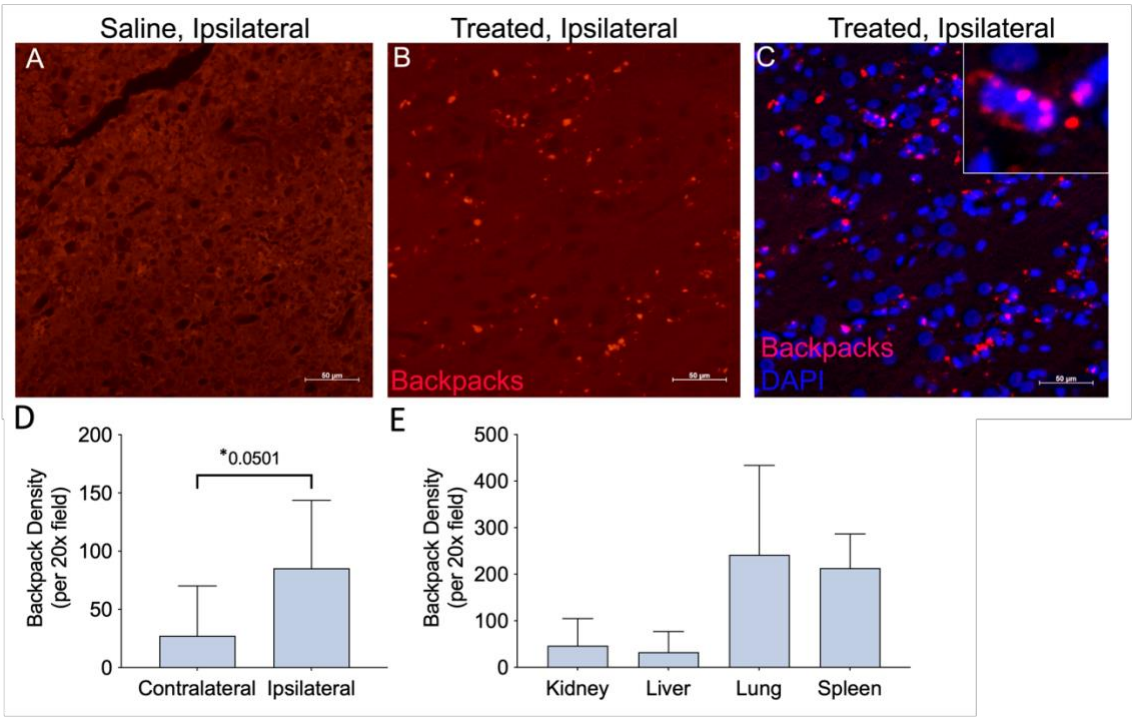

Figure 5-3. Macrophage-backpacks home to the lesion penumbra and accumulate in the lung and spleen.

*Backpacks were tagged with fluorescent rhodamine B (red) and 568 nm signal was visualized in the peri-contusion area of the rostral gyrus in A) saline and B) treated piglets. C) Backpacks were co-visualized with cell nuclei (DAPI nuclei: blue). Scale bar = 50 µm. D) Backpack density in the peri-contusion area of ipsilateral vs. contralateral hemisphere (mean ± SD, *p < 0.1, Welch's t-test) (n = 8 treated). E) Backpack density in organs in treated subjects (n = 5 treated). Because of the variability intrinsic to large animal, outbred species and of the porcine cortical impact model in this study, *p < 0.1 was considered significant for in vivo assessments.*

5.3.5. Backpack-macrophages show promise in reducing lesion size.

The lesion resulting from cortical impact was assessed via macroscopic and microscopic analysis. The macroscopic lesion volume reflects differences in both permanent tissue damage and potentially resolvable swelling similar to lesion volume estimates via T2 MRI (Fig. 5-4A). Treatment with backpack-macrophages reduced total macroscopic lesion volume by 56% compared to that of subjects receiving saline (196 vs. 86 mm^3, Fig. 4B). Lesion volume was inversely correlated to the number of backpack-macrophages administered (Appendix Figure 9-22). As the difference in hemorrhage between the groups was visually striking (Appendix Figure 9-23), the volume of hemorrhage alone was also estimated macroscopically (Fig. 5-4C). Treatment with backpack-macrophages decreased the volume of hemorrhage.

The microscopic lesion volume is an assessment of permanent tissue damage (Fig. 5-4D, Appendix Figure 9-24). Compared to saline administration, backpack-macrophage treatment reduced lesion volume by 51% (94 vs. 50 mm^3) (ns, $p = 0.1571$) when assessed microscopically (Fig. 5-4E). Though the microscopic lesion volume was heterogenous with two of the treated subjects having larger lesions, overall, subjects receiving backpack-macrophages had fewer large lesions (lesions > 20 mm^3, Fig. 5-4F). Calculating lesion area per section analyzed and expression as a ratio to the

contralateral hemisphere, a helpful metric when evaluating treatments among different developmental stages, resulted in a similar pattern (Appendix Figure 9-25). The two indentor devices used to induce cortical impact were alternated between subjects in each group exhibited no difference between indentor and lesion volume (Appendix Figure 9-26).

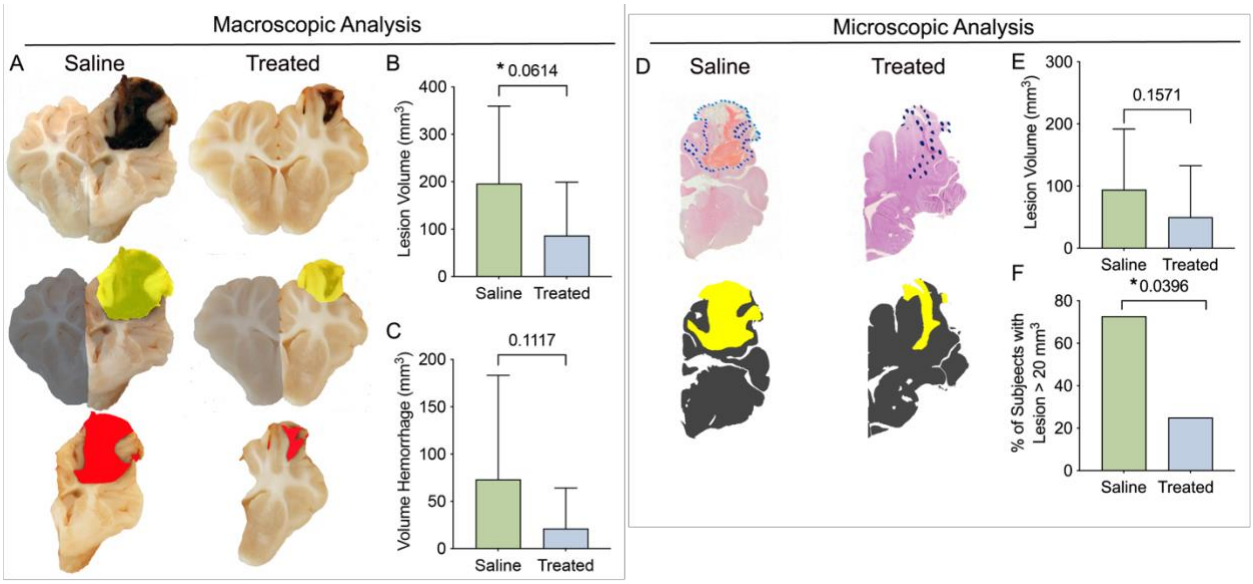

Figure 5-4. Backpack-macrophages show promise in reducing lesion size in an outbred, gyrencephalic model of TBI.
*1-month old Yorkshire piglets received a cortical impact to the rostral gyrus and either treatment with backpack-macrophages or saline 1 or 4 h post-impact. A) Coronal sections demonstrate the lesion 7 days after cortical impact in those that received saline (left column) or treatment (right column). On each coronal slab for the entire brain, areas of hemorrhage, dusky tissue, and swelling (middle, yellow) or hemorrhage alone (bottom, red) were outlined, multiplied by the slice thickness (5 mm), and added together to determine B) macroscopic lesion volume similar to lesion volume determined via T2 MRI and C) hemorrhage volume (mean ± SD). D) The areas of lesioned tissue viewed microscopically were outlined (top, purple dots), filled in (bottom, yellow), multiplied by the slice thickness (5 mm), and added together to determine E) microscopic lesion volume. F) Percent of subjects with microscopic lesion volume less than 20 mm^3 (chi-square test). All comparisons were made with a one-sided, unpaired, student's t-test, *$p < 0.1$.*

5.3.6. Backpack-macrophages reduce inflammation locally and systemically.

Microglia in the intact peri-contusion area was assessed while areas of the cavitation or tissue loss were avoided so that potentially salvageable tissue was analyzed instead of the necrotic lesion core/cellular debris (Appendix Figure 9-27). While Iba1 stains positively for not only microglia, but also infiltrating peripheral macrophages, here we refer to Iba1 count as an indicator of microglia density. Backpack-macrophages reduced the density of Iba1+ cells in the peri-contusion region. Microglia density in the peri-contusion area was lower in subjects treated with backpack-macrophages (322.9 Iba1+/mm^2) compared to that of saline subjects (541.3 Iba1+/mm^2) (Fig. 5-5A). As expected, microglia density at the peri-contusion site was greater than microglia density at the comparable location on the rostral gyrus in the contralateral hemisphere for both treated and saline groups (Appendix Figure 9-28). The morphology of Iba1+ cells was evaluated, where

greater circularity indicates a greater inflammatory phenotype. The Iba1+ cells at the peri-contusion site in subjects receiving backpack-macrophages (0.214) had a 3.91% reduction in circularity compared to that of the saline group (0.223). Furthermore, as percentage increase of CD80 brightfield pixel intensity to background pixel intensity, CD80 pixel intensity increase was lower in the peri-contusion area in subjects treated with backpack-macrophages (6.86%) compared to that of the saline group (9.03%).

Peripheral markers of inflammation, tumor necrosis factor alpha (TNF-α) and glial fibrillary acidic protein (GFAP), were analyzed in the serum and CSF. Post-injury analyte concentrations are presented as percentages, normalized to the baseline analyte concentration of each subject at -1h pre-injury. Serum TNF-α % at 24h post-injury was less in treated subjects (82.7%) vs. that of piglets receiving saline (117.5%) (Fig. 5B). Serum GFAP % at 7 days was less in treated (75.2%) vs. saline (158.4%) groups. Despite exhibiting a consistent trend of reduced concentrations of TNF-α and GFAP in both the serum and CSF of treated piglets at 24 h and 7 days post-injury, there were no other significant differences between the groups (Fig. 5-5C).

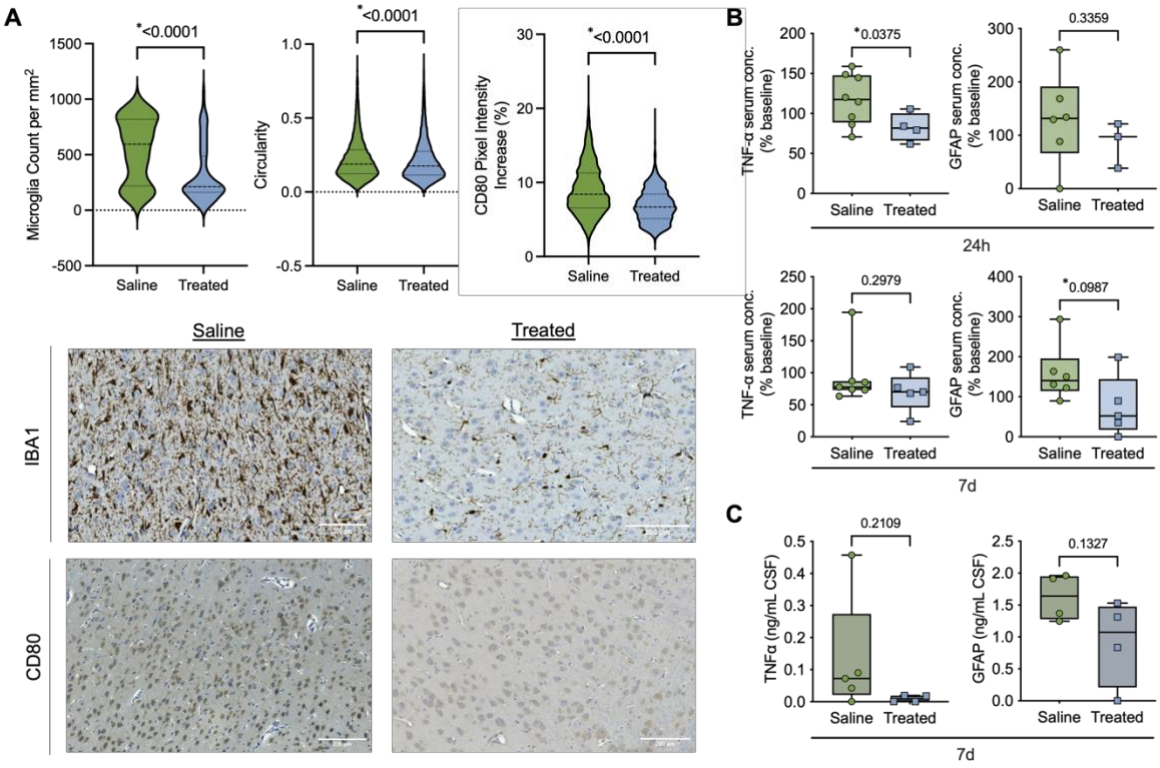

Figure 5-5. Backpack-macrophages reduce inflammation locally and systemically after TBI. *A) Images of peri-contusion regions were analyzed to determine Iba1+ microglia count per field (saline n = 35, treated n = 89), individual Iba1+ microglia circularity (saline n = 11084, treated n = 15590), and CD80 pixel intensity increase (saline n = 2484, treated n = 1664). Data were analyzed by one-way ANOVA with Tukey's HSD test. Full data is reported in Fig. S9. B) Brightfield 20x microphotographs depict representative field images of Iba1 and CD80 expression for the ipsilateral hemisphere of saline and treated groups. C) TNF-α and GFAP concentrations were assessed in serum at 24 h post-injury, in serum at 7 days post-injury, and in CSF at 7 days*

*post-injury via ELISA. Box and whisker plot reported as median with whiskers from minimum to maximum. Data were analyzed by Welch's t-test (*p < 0.1, ****p < 0.0001).*

5.3.7. Backpack-macrophages are safe.

Clinically, the rate of adverse events for treated piglets did not differ from that of piglets receiving saline (Appendix Table 3, see for detailed description of adverse events). Issues with scours occurred pre-surgically/pre-treatment in both groups and resolved with administration of probiotics. Both groups had an equivalent rate of post-surgical swelling at the catheter incision site at the neck, which resolved with cold compression. No piglet had any clinically concerning symptoms in the days following infusion of backpack-macrophages. The kidneys, liver, lung, and spleen were evaluated for signs of toxicology. The rate of specific pathologic findings was not different between groups and within range of farm-derived piglets (Appendix Table 4, see for detailed description of adverse events).

5.4. Discussion

Despite their potential benefits, cell therapies have not been extensively explored for treating TBI, with the exception of stem cells(202–205). Combination of cell therapies with engineered materials such as backpacks can further modulate and enhance cell functions(6). Owing to their discoidal geometry, backpacks exhibit a unique ability to remain adhered to macrophage surfaces without internalization and control macrophage phenotype with controlled release of loaded cargo (39, 55). Backpacks loaded with interferon-γ have been shown to retain an anti-tumoral macrophage phenotype in the anti-inflammatory tumor microenvironment, resulting in a reduction in tumor volume and improvement in survival in mice with 4T1 mammary carcinomas(39). Backpacks loaded with IL-4 and dexamethasone have also been shown to adhere to monocytes and maintain them in an anti-inflammatory state to treat multiple sclerosis in a mouse model of experimental autoimmune encephalomyelitis (12). Here, we demonstrate an anti-inflammatory backpack-macrophage therapy in a clinically relevant porcine model of TBI, where anti-inflammatory backpacks maintain the anti-inflammatory phenotype of adoptively transferred macrophages against the pro-inflammatory TBI microenvironment.

We demonstrate that IL-4 and dexamethasone loaded backpacks can efficiently and durably adhere to primary bone-marrow derived porcine macrophages. Previously, backpack attachment to monocytes required backpack functionalization with anti-CD45 for effective binding (12). In contrast, backpack attachment to macrophages did not require an adhesive coating due to the enhanced phagocytic nature of macrophages, simplifying the backpack design. Backpacks effectively maintain porcine macrophage anti-inflammatory phenotype for up to 7 days in both unstimulated and inflammatory media conditions. After undergoing a freeze-thaw cycle, backpacks still retain adhesive ability to macrophages, making our backpack technology amenable to material storage logistical constraints that would be encountered in translation. Backpack-macrophages can be produced at scale, as evidenced by our preparation of over 200 million backpacks and over 100 million macrophages per treated piglet for this study. Considering the translational potential of this cell therapy approach, the high-throughput scale-up processes reported here are readily translatable to the magnitude of cells and materials necessary for human clinical trials.

Despite significant efforts and pre-clinical data, no therapies have yielded success in clinical trials of TBI. Results from rodent models typically do not translate to larger animals with higher-order cognitive abilities such as pigs and non-human primates, and ultimately to humans. While TBI research in rodents has advanced the field's understanding of the disease, rodents are anatomically different from humans. The rodent cortex is lissencephalic, the hippocampus is located in close proximity to the cortex, and TBI results in a lesion cavity, while the human cortex is gyrencephalic, the hippocampus is embedded deep within the temporal lobe, and a TBI lesion retains its volume in the brain with the formation of a glial scar. The porcine cortical impact model of TBI addresses these weaknesses of rodent models with brain anatomy and TBI pathophysiology that more closely resembles that of humans. Accordingly, the studies reported here demonstrate efficacy of backpack-macrophage therapy in a higher-order porcine model, offering promise for eventual clinical translation.

In response to inflammation after brain injury, microglia undergo proliferation as well as transition into a more circular amoeboid morphology instead of a ramified healthy state(206–208). Image analysis of microglia morphology reliably quantifies microglia activation state and inflammatory phenotype(207, 209). Similarly, CD80 is a pro-inflammatory marker of both microglia and peripheral macrophages(177). CD80 is also expressed on activated B cells, T cells, and dendritic cells(210), but their acute presence after TBI is minimal(211). For microglia, an increase in Iba1 cell density and an increase in CD80 expression correlate to a greater pro-inflammatory environment. For studying the expansion or resolution of inflammation, we focused on microglia in the peri-contusion grey matter. The core lesion that has already undergone neuronal death cannot be rescued by therapeutics. Importantly, the peri-contusion regions are the brain tissues of interest that are capable of salvation with therapeutic interventions to prevent expanding secondary injury. Elevated microglia density and pro-inflammatory phenotype in the lesion-adjacent tissue corresponds to inflammation and damage that is expanding into the neighboring regions(207). For backpack-macrophage treated piglets, as indicated by microglia density, circularity, and CD80 expression, the presence of healthier, less abundant, and less inflamed microglia in the peri-contusion regions of treated piglets suggests that inflammation is resolving compared to that of the saline group.

TNF-α and GFAP are being increasingly studied as biomarkers of TBI severity. TNF-α is one of the most potent pro-inflammatory cytokines and plays a vital role in exacerbating inflammation, oxidative stress, and excitotoxicity(212). GFAP is a cytoskeletal marker of astrocytes and increases expression due to astrocyte proliferation in response to inflammation(206). In the hours and days after TBI, TNF-α and GFAP originating from the brain leaks into the CSF and blood serum(213, 214). Both TNF-α and GFAP levels in CSF and serum correlate to extent of injury after TBI and in other neurological diseases in rodent, porcine, and clinical studies(213, 214). Reduced TNF-α serum concentration at 24 h post-injury for backpack-macrophage treated piglets is indicative of an ameliorated acute inflammatory response. Reduced GFAP serum concentration at 7 days post-injury for treated piglets signifies that ongoing astrocyte activation for formation of a glial scar was reduced. Reduced GFAP serum levels may indicate that the brain has already undergone glial scar formation for lesion isolation and began healing, or that TBI damage was reduced to an extent that less scarring was required(213). Furthermore, TNF-α and GFAP concentrations exhibited a trend of lower concentration in CSF and serum at all timepoints measured for the treated group compared to that of the saline group. In combination with Iba1 and

CD80 image analysis, TNF-α and GFAP levels further supports evidence of reduced local inflammation following backpack-macrophage treatment.

While the findings reported here offer a snapshot of lesion size and serum inflammation markers at 7 days after injury, ongoing rampant neuroinflammation can lead to an expansion in the lesion size beyond 7 days. The dampening of the microglial inflammation in the peri-contusion regions demonstrated in these studies suggests that the therapeutic efficacy of backpack-macrophages may be even more pronounced at later timepoints with a greater relative reduction in lesion size. Furthermore, our work does not assess other potential long-term positive impacts of backpack-macrophage interventions, as reduced acute TBI damage correlates to reduced elevated risk of mental health disorders and dementia. Potential areas of future exploration include investigating the effects of varying backpack-macrophage doses, percentages of macrophages with adhered backpacks, administration time, and measuring lesion size and other metrics at earlier and later timepoints.

5.5. Conclusions

TBI is a debilitating disease resulting in an array of post-TBI sequelae with no current treatments besides clinical management strategies. Cell therapies provide a unique opportunity to leverage chemotactically guided migration to overcome barriers to brain delivery and achieve accumulation at the target site in the brain. We demonstrate that IL-4- and dexamethasone-loaded backpacks can be adhered to porcine macrophages and promote an anti-inflammatory phenotype for at least 7 days. We produced backpack-macrophages at scale and safely infused them into piglets after cortical impact. Backpack-macrophages trafficked to the lesion site in the brain and remodeled the local and systemic inflammatory milieu, evidenced by decreased microglia activation in peri-contusion regions and decreased systemic concentrations of pro-inflammatory biomarkers. These immunomodulatory effects contributed to a 56% decrease in lesion volume. The results reported here demonstrate, to the best of our knowledge, the first use of a cell therapy intervention for a large animal model of TBI.

6. Chapter 6: Polymer Backpack-loading Tissue Infiltrating Monocytes for Treating Cancer a Monocyte-based Therapy against Cancer

6.1. Introduction

Adoptive cell therapies are revolutionizing cancer treatment (215). Six chimeric antigenic receptor T cell (CAR-T cell) therapies have been approved by the Food and Drug Administration (FDA) since 2017, thereby meaningfully improving outcomes for patients diagnosed with leukemia, lymphoma, and myeloma (216–220). However, the efficacy of CAR-T cells in treating solid tumors remains low, in part due to their poor penetration into the tumor and in part due to the immunosuppressive tumor microenvironment (221). Tumor cells induce immune evasion by restricting T cell migration and activation (222). Cytokines including interleukin-6 (IL-6) and tumor necrosis factor-a (TNFα) play a crucial role in adhesion and penetration of T cells into tumors (223), however, their expression is downregulated in solid tumors, thus reducing T cell infiltration. Local factors such as transforming growth factor β (TGFβ) also adversely impact tumor infiltration of T cells.

The limitations of T cell therapies have brought other cell types, especially macrophages, into focus for treating cancer (224–227). Macrophages offer the advantage of antigen-independence, which is beneficial when the tumor antigens are unknown. The phenotypic plasticity of macrophages, however, poses a significant hurdle in their therapeutic utility (128, 228). The immunosuppressive microenvironment within the tumor polarizes macrophages into an anti-inflammatory phenotype, which has pro-tumorigenic effects (7, 229, 230). Despite this challenge, adoptive macrophage therapies have advanced to clinic for the treatment of colorectal, ovarian, renal and non-small-cell lung cancer (231). In these clinical studies, blood monocytes were collected from patients by leukapheresis, differentiated *ex vivo* and activated into an anti-tumor M1 phenotype using interferon gamma (IFNγ) or lipopolysaccharide to address the challenge of phenotypic plasticity, and transfused back into the patients (232). Transfused M1 macrophages exhibited some accumulation at the tumor site based on the radiographic imaging, but they did not yield a favorable clinical outcome. Recently, genetically engineered CAR macrophages, CAR-M, have been developed to incorporate tumor antigen specificity with the intent of enhancing the potency of macrophages in treating cancer, and they have recently shown some therapeutic efficacy in pre-clinical model, however, their efficacy in humans has not been reported (233). In addition to the challenges posed by their phenotypic plasticity, macrophages also experience transport limitations within the tumor. Specifically, recent *ex vivo* studies have shown that the permeability of M1 macrophages into tumors is substantially lower than that of naïve M0 macrophages (234). These challenges have collectively limited the impact of myeloid cells on cancer therapies.

Here, we report on the use of tissue infiltrating monocytes, which retain the key advantages of myeloid cells, but address the limitation posed by macrophages, for cancer treatment. Circulating monocytes readily infiltrate into tissues following chemokine gradients and differentiate into dendritic cells or macrophages (235). Taking advantage of their superior tissue-infiltration ability, we built a cell therapy against cancer using primary monocytes. We use primary monocytes and control their differentiation *in vivo* into macrophages by attaching polymer backpacks *ex vivo*. The backpack surface was modified with anti-CD11b Fab to promote backpack adhesion to monocytes and with IFNγ to promote and control monocyte differentiation into pro-inflammatory macrophages. Adoptively transferred monocytes exhibited extensive tumor infiltration in 4T1

breast cancer tumors. Backpack-laden monocytes remodeled the tumor microenvironment to a pro-inflammatory state and led to substantial reduction in tumor burden.

6.2. Materials and Methods

6.2.1. Materials.

Sylgard 184 polydimethylsiloxane (PDMS) was purchased from Dow Chemical (Midland, MI). Resomer RG 502 H, Poly acid terminated, PLGA (MW = 7,000-17,000) and Polyvinyl alcohol (PVA; MW = 13-23k) were purchased from Sigma (St. Louis, MO). PLGA-polyethylene glycol-maleimide (PLGA-PEG-mal; MW =10k, 5k) was purchased from Nanosoft Polymers. PLGA-rhodamine B and PLGA-Cy5 were purchased from Akina PolySciTech. Murine recombinant IFNγ and macrophage colony stimulating factor was purchased from Peprotech. XenoLight™ CF680 and IVISense DiR 750 were purchased from PerkinElmer (Waltham, MA). LEGENDplex Mouse Inflammation Panel 13-plex was purchased from BioLegend. All fluorescent probe-conjugated antibodies for immune cell staining were purchased from BioLegend, Invitrogen, or BD. 4T1 cells were ordered from ATCC. Lipids (DSPC, cholesterol, PEG-DSPE) were purchased from Avanti Polar Lipids (Alabaster, AL).

6.2.2. Backpack fabrication.

Backpacks were prepared using previously described techniques (12, 39)with changes noted below in order to produce stable IFNγ-conjugated backpacks. Briefly, silicon wafers were manufactured by standard photolithographic technique as previously described with 8 μm circular holes with a 16 μm pitch (39, 236). PDMS molds (with 8 μm cylindrical posts) were prepared by mixing PDMS at a 10:1 (wt:wt) elastomer:crosslinker ratio pouring onto the silicon wafers. PDMS was cured at 65 °C overnight and detached from the silicon wafers. PLGA, PLGA-PEG-mal, and PLGA-rhodamine B were co-dissolved in dicholoromethane (DCM) at 56 mg/mL, 24 mg/mL, 0.2 mg/mL, respectively. 220uL of polymer solution was deposited on the surface of the PDMA molds by spin coating at 2000 rpm for 35s (at a 200 rpm/s ramp) and residual DCM was evaporated. Backpacks were microcontact printed onto plastic dishes coated with PVA. Backpacks were resuspended from PVA dishes in phosphate-buffered saline solution (PBS; 150 mM, pH 7.4). IFNγ and CD11b antibody F(ab)' with exposed thiol groups were quickly added to conjugate to available maleimide sites, as described previously (12).

6.2.3. Backpack characterization.

Successful backpack production was characterized using several techniques. Fluorescence microscopy was used to visually confirm backpack morphology at various steps in the fabrication process. Flow cytometry (Cytek Aurora) was used to confirm the presence of IFNγ on the backpack surface via labelling with eFLuor 450 anti-murine IFNγ antibody. Four backpack formulations were prepared: +/- PLGA-PEG-maleimide and +/- IFNγ in order to confirm conjugation of the IFNγ molecule via the maleimide functional group on the surface of the backpack. Release of IFNγ from backpacks was measured by enzyme-linked immunosorbent assay (ELISA). One million backpacks were suspended in PBS containing 50 mg/mL bovine serum albumin at 37 °C. At specified time-points, free IFNγ and backpacks were separated by centrifugation at 2000 x *g* for 10 minutes at 4 °C.

6.2.4. Primary monocyte and macrophage culture.

Bone marrow cells were harvested by flushing the femurs and tibias of donor mice. The collected cells were filtered through 40um cell strainers and centrifuged at 350g for 7.5 minutes. For monocyte culture, the bone marrow cells were resuspended in RPMI supplemented with 20ng/mL M-CSF and plated at a density of $1x10^6$ cells/mL in 6-well ultra-low attachment plates for differentiation into monocytes(155, 156). For macrophage culture, the bone marrow cells were resuspended in DMEM F12 supplemented with 10% FBS, 1% Pen Strep, and 5% ml of 200 mM GlutaMAX and 20 ng/mL MCSF and plated in $10cm^2$ non-tissue culture treated dishes. Additional media was added to the flasks on day 3 and macrophages were harvested on Day 7 with Accumax as described previously (39).

6.2.5. Preparation of backpack-monocytes

Monocytes were harvested from culture, counted, and seeded in 50ul aliquots with $1x10^6$ cells per well in a U-bottom 96 well plate. Backpacks were harvested and counted and added at a 3:1 backpack:cell ratio in 50uL aliquots. Monocytes and backpacks were incubated for 30-60 minutes at 37°C, 5% CO_2 to allow attachment to occur. Then, the backpack-monocytes were harvested from the wells, pelleted at 300g for 5 minutes, and resuspended in media of choice for subsequent use. Backpack adhesion was quantified via flow cytometry (Cytek Aurora).

6.2.6. In vitro characterization of myeloid cell phenotype.

Differentiated bone marrow macrophages were seeded at 100,000 cells/per well in non-TC 24 well plate in unstimulated growth media or 4T1 media. IFNγ backpacks were added to some cells, and 1ng/mL or 10 ng/mL free IFNγ to other cells. To determine activation status and cytokine excretion, cells were cultured for 24 hours and the supernatant was harvested. LEGENDplex™ Mouse Inflammation Panel (13-plex) was used to assay the supernatant samples, following vendor instructions. To determine activation status, cells were harvested, blocked with CD16/CD32 (BioLegend), and stained using LIVE/DEAD Blue (BioLegend), anti-CD11b-BV785(BioLegend), anti-MHCII-BUV737 (BioLegend), anti-CD80–PE/Cy5 (BioLegend), anti-CD86–APC/Fire750 (BioLegend), anto-CD40–Super Bright 436 (BioLegend). Samples were then fixed and permeabilized and stained using anti-iNOS–AF488 (Invitrogen), anti-CD206–BV605 (BioLegend), anti-HIF1a–PE (BioLegend), anti-VEGF–PECy7 (Invitrogen) and analyzed using the Cytek Aurora. Data were analyzed with FlowJo V10.

6.2.7. Animal studies.

All animal studies were approved by the Harvard Institutional Animal Care and Use Committee. All studies were conducted in female BALB/c mice bearing orthotopic murine 4T1 tumors. 4T1 cells were grown in RPMI-1640 medium with 10% (v/v) FBS and 1% penicillin/streptomycin. Tumors were initiated by injection of 200,000 4T1 cells in the inguinal mammary fat pad. Tumor volumes were measured by caliper in the longest direction (L) and perpendicular to that (w) and estimated according to the formula $V=\pi*w^2*L/6$.

6.2.8. Biodistribution.

To track the biodistribution of adoptively transferred monocytes and macrophages, bone marrow derived cells were labelled *in vitro* with either XenoLight™ CF680 or IVISense DiR 750 according

to the manufacturer's protocol. Labelled macrophages and monocytes were co-injected intravenously and mice underwent anaesthetized live fluorescent imaging using the IVIS Spectrum (Perkin Elmer) at 8, 24, and 48 h. A subset of mice was sacrificed at each timepoint, cardiac perfusion was performed, and major organs were resected and imaged. Fluorescent dye concentrations in resected organs and tumor were quantified by mechanical homogenization, liquid-liquid fluorophore extraction, and fluorometer (Photon Technology International PTI QuantaMaster Fluorescence/Luminescence Spectrometer) measurement.

6.2.9. Therapeutic efficacy.

Orthotopic 4T1 tumors were, with 7 mice per treatment group. All studies commenced when tumors had reached ~80 mm^3 on day 5 following tumor cell injection. Mice were administered $4x10^6$ monocytes, free backpacks, monocyte-backpacks, or saline intravenously via tail-vein. Therapeutic efficacy was determined by daily caliper measurement of tumors until they reached a length of 15 mm in any direction. Mice were weighed daily.

6.2.10. Materials.

Changes in cellular and cytokine composition in tumor and blood were assessed using methods similar to those employed for *in vitro* samples, specifically flow cytometry for immune cell profiling and bead-based ELISA for cytokine analysis. Saline, monocytes, free backpacks, or IFNγ-backpack-monocytes were administered on day five and seven following tumor cell injection and cell and cytokine concentrations were assessed on day eleven. Blood was removed via cardiac puncture and animals were perfused with 20 mL of PBS. Tumors were resected and single cell suspensions were prepared using Miltenyi tissue dissociation kit according to the manufacturer's instructions. The blood was lysed and processed into single cell suspensions. The samples were blocked with anti-CD16/CD32 (BioLegend), stained with LIVE/DEAD Blue (BioLegend), stained for surface markers, fixed and permeabilized, and stained for intracellular markers. Cytek Aurora analyzer was used, and data were analyzed with FlowJo V10. Cytokine levels in blood and tumor were determined by reserving the supernatant from the original single cell suspensions and assayed using the LEGENDplex Mouse Inflammation Panel 13-plex bead-based immunoassay as above.

6.2.11. Toxicity.

Gross toxicity was assessed daily by measuring changes in body weight and behavior. A weight loss limit of 20% was established while behavioral monitoring included grooming and activity levels. Toxicity was compared for the saline control and mice receiving two standard doses of monocytes labelled with IFNγ backpacks. Cytokine analysis was performed in the serum.

6.3. Results

6.3.1. Monocytes efficiently migrate to the tumor.

The ability of monocytes to migrate to tumors was assessed in a 4T1 mouse breast cancer model using fluorescently labelled primary murine Bone Marrow Derived Monocytes (BMDMs, VivoTrack680). To compare the tumor infiltration potential of monocytes with macrophages, fluorescently labeled macrophages differentiated from BMDMs *ex vivo* (labeled with VivoTrack 750) were used. Further, to minimize the impact of tumor and experimental variability on this comparison, macrophages and monocytes were co-injected in the same animals intravenously (**F**ig 6-1). Monocytes demonstrated superior infiltration into the tumor at 8 hours, as demonstrated by accumulation of 26.3% relative dose per gram organ, compared to 3.66% in the case of

macrophages (Fig 6-1A). This represents a 7.2-fold higher infiltration of monocytes compared to macrophages. Macrophages preferentially accumulated in the spleen at 8 hours, with 49.3% relative dose per g organ. Monocytes persisted in the tumor for at least 48 hours (Fig. 6-1B), and the tumor to liver accumulation ratio decreased over time (1.69 at 8 hours, 0.73 at 24 hours, and 0.54 at 48 hours). Representative IVIS images for adoptively transferred monocytes in organs of interest over time shown in Appendix Figure 9-32.

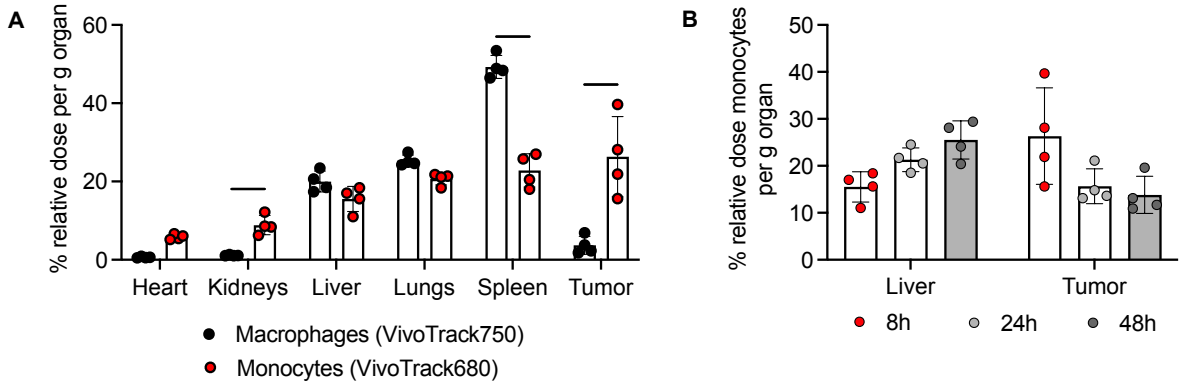

Figure 6-1 Comparison of monocyte and macrophage tumor trafficking abilities.
*Tumors were inoculated with 4T1 in the mammary fat pad and mice were administered fluorescently labeled macrophages (VivoTrack 750) and monocytes (VivoTrack680) intravenously via tail vein. (A) Biodistribution data for fluorescently labelled macrophages and monocytes injected intravenously five days following 4T1 tumor inoculation. Animals were sacrificed at 8 hours following monocyte injection. Organs were resected and adoptively transferred cell concentration determined by fluorescent imaging. (B) Liver and tumor accumulation data for fluorescently labelled monocytes at 8 hours, 24 hours, and 48 hours. For A, data were analyzed by two-way ANOVA with Sidak's test; *P<0.05, ****P<0.0001.*

6.3.2. Engineering IFNγ backpacks to adhere to monocytes.

Backpacks were fabricated by spin-coating and microcontact printing of a blend of poly(lactic-co-glycolic acid) (PLGA) and PLGA-PEG-maleimide (PLGA-PEG-Mal) using the procedures described previously (12, 39). Unlike previous designs of backpacks, which encapsulated IFNγ within the bulk backpack for sustained release, the backpacks described here deployed covalent conjugation of IFNγ on the backpack surface through click conjugation of the terminal cysteine of murine IFNγ to the maleimide functional group on the surface of the backpack. This design modification was done to minimize the release and potential off-target effects of IFNγ. Anti-CD11b Fab was also conjugated to the surface of backpacks through thiol-maleimide click reaction to facilitate backpack adhesion to monocytes. (Fig. 6-2A). Flow cytometry assessment via anti-IFNγ antibody labelling confirmed that IFNγ was conjugated on the backpack surface for PLGA-PEG-Mal backpacks, compared to PLGA backpacks with free, unconjugated IFNγ (Fig 6-2B).

Backpack-monocyte complexes were synthesized by incubating IFNγ- and anti-CD11b Fab-modified backpacks with primary BMDMs. Backpacks demonstrated excellent adhesion to BMDMs, with about 40% of monocytes attaching to at least 1 backpack (Fig. 6-2C). Backpacks

decorated with only IFNγ did not substantially adhere to monocytes, indicating that the presence of anti-CD11b Fab was necessary for adhesion (Fig. 6-2C). Backpacks without surface decoration with anti-CD11b Fab exhibited minimal adhesion to monocytes (Fig 4-1C).

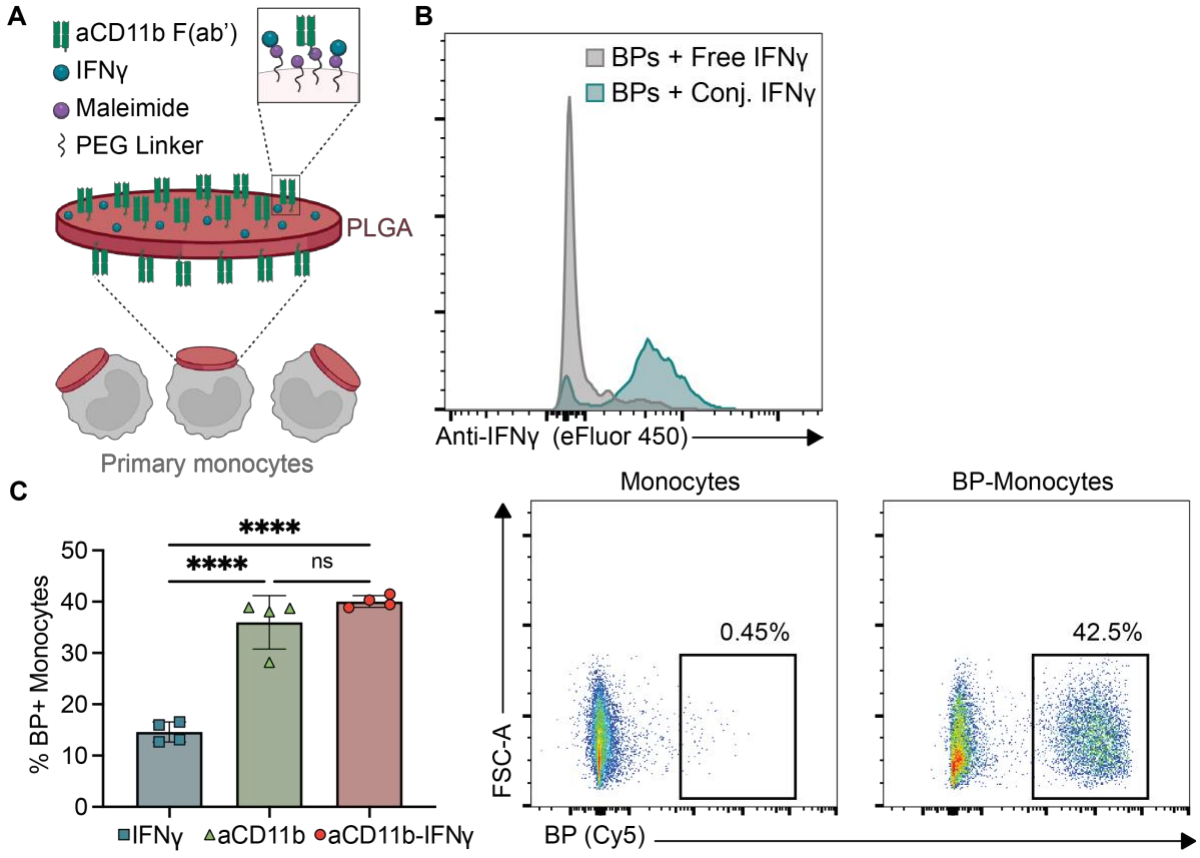

Figure 6-2. Engineering IFNγ backpacks to adhere to primary monocytes.
(*A) Schematic of system. (B) Histogram comparing anti- IFNγ labeling of backpacks with free IFNγ s vs. backpacks with conjugated IFNγ. Obtained via flow cytometry (C) Percentage of monocytes with >1 backpack (determined by flow cytometry); mean ± SD (n=4). Representative flow cytometry gating of control monocytes vs. backpack-adhered monocytes. For C, data were analyzed by one-way ANOVA with Tukey's HSD test; ns, not significant, ****P<0.0001.*

6.3.3. Backpacks durably control myeloid cell phenotype towards an anti-tumor phenotype.

CD11b/IFNγ backpacks were adhered to macrophages and differentiated for 24 hours in unstimulated media (Fig 6-3A). The expression of various surface and intracellular markers were assessed by flow cytometry, including anti-tumor/pro-inflammatory markers MHCII, CD80, CD86, and CD40, and pro-tumor/anti-inflammatory markers CD206, HIF1a, and VEGF. After 24 hours, backpack-macrophages demonstrated enhancements in expression of anti-tumor markers that were comparable to macrophages incubated with 1ng/mL and 10ng/mL of free IFNγ, with negligible increases in pro-tumor markers (Fig. 6-3A). Full data shown in Fig Appendix Figure 9-33. Interestingly, even the backpack -ve population within the backpack-monocyte group, those

monocytes that did not attach to backpacks, yielded significant increase in expression of MHCII, CD80, CD86, and CD40 compared to macrophages alone, demonstrating a paracrine effect of backpacks on other cells in the local microenvironment (Appendix Figure 9-34).

Backpacks continued to display excellent control over myeloid cell phenotype even in the immunosuppressive 4T1 cell media (Fig. 6-3B). The changes elicited by backpacks were comparable to those elicited by free IFNγ alone (Appendix Figure 9-35). Even in the presence of 4T1 media, backpack -ve population within the backpack-monocyte group demonstrated significant enhancements in the expression of anti-tumor, pro-inflammatory markers, demonstrating a paracrine effect (Appendix Figure 9-36).

To further elucidate the paracrine effect on the local environment, the cytokine excretion from backpack-monocytes was assessed. Anti-CD11b Fab decorated backpacks attached to monocytes were also used in this study to identify the contributions of IFNγ in backpack design. Backpacks without anti-CD11b (that is, only with IFNγ) were not included in this study due to poor adhesion to monocytes (Fig. 6-2D). Backpacks without IFNγ elicited increase in CXCL1, but not TNFα, IL-6, or IL-12p40 (Fig 6-3C). However, aCD11b-IFNγ backpacks elicited more potent cytokine excretion, with significant increases in TNFα (5.6-fold), IL-6 (3.7-fold), IL-12p40 (2.8-fold), and CXCL1 (2.8-fold) (Fig 6-3C). Both backpacks without and with IFNγ elicited a significant decrease in IL-10 levels (0.29-fold and 0.22-fold, respectively) (Fig. 6-3D).

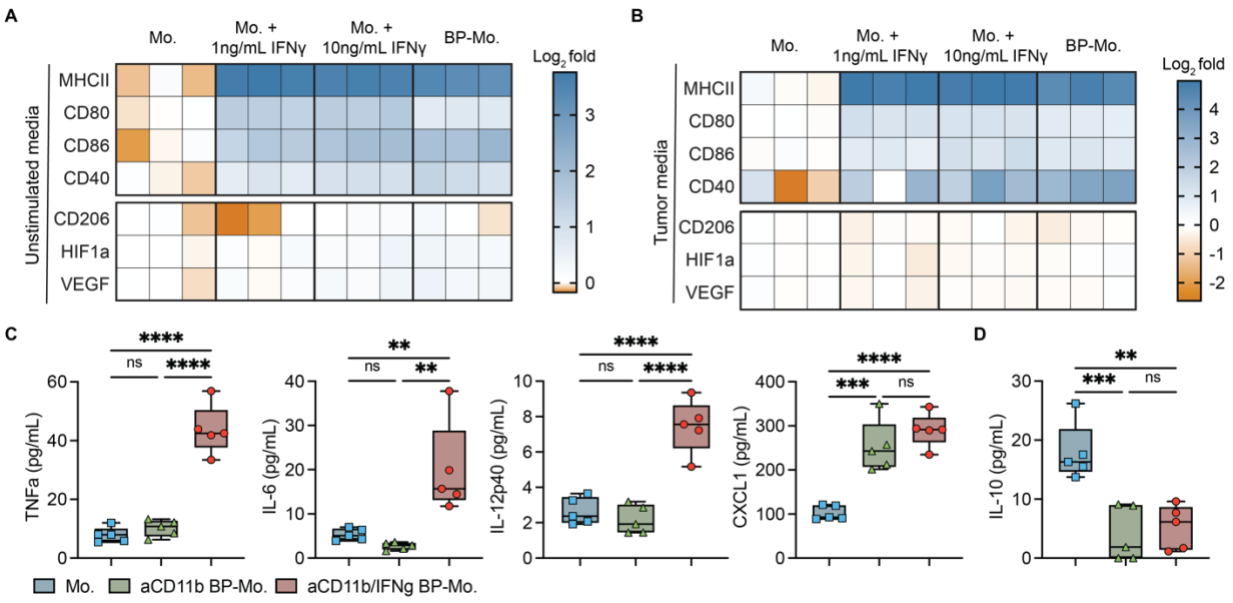

Figure 6-3. IFNγ backpacks confer a robust anti-tumor phenotype to myeloid cells.
Macrophages, macrophages with 1ng/mL IFNγ *or 10 ng/mL* IFNγ *or backpack-macrophages were cultured for 24 hours in A) unstimulated media and B) 4T1 tumor-mimicking media and analyzed for expression of anti-tumor (MHCII, CD80, CD86, and CD40) and pro-tumor (CD206, HIF1a, VEGF) markers. Heatmap columns show data from individual replicates (n = 3), reported as log2 fold change in expression compared to the average value of the macrophage group. Raw data are in Appendix Figure 9-33 for A and Appendix Figure 9-35). C) Cytokine excretion from monocytes,*

*monocytes with aCD11b-backpacks, or monocytes with aCD11b/IFNγ backpacks after 24 hours for pro-inflammatory, anti-tumor mediators; mean ± SD (n=4). D) Cytokine excretion from monocytes, monocytes with CD11b-backpacks, or monocytes with aCD11b/ IFNγ backpacks after 24 hours for anti-inflammatory, pro-tumor mediators; mean ± SD (n=4). For C and D, data were analyzed by one-way ANOVA with Tukey's HSD test; ns, not significant, **P<0.01, ***P<0.001, ****P<0.0001.*

6.3.4. IFNγ BP-monocytes control tumor growth.

A murine therapeutic efficacy tumor bearing mice confirmed that backpack-monocytes controlled the growth of orthotopic 4T1 tumors to a significantly greater extent compared to saline control, free monocytes, or anti- backpacks (Fig 6-4A) ($p<0.0001$). Specifically, at day 11 when the first control mouse reached the endpoint of the study, tumors in mice treated with backpack-monocytes were less than half as large as the other treatment groups (387 mm^3 vs 877, 808 and 861 mm^3, full tumor growth curves displayed in Appendix Figure 9-37). This reduction in tumor growth resulted in a statistically significant increase in median survival of 25 days for the mice receiving backpack-monocytes compared to 12, 13, and 14 days for the mice treated with saline, monocytes, and free backpacks, respectively ($p<0.001$) (Fig 6-4B, individual tumor curves displayed in Fig 6-4C).

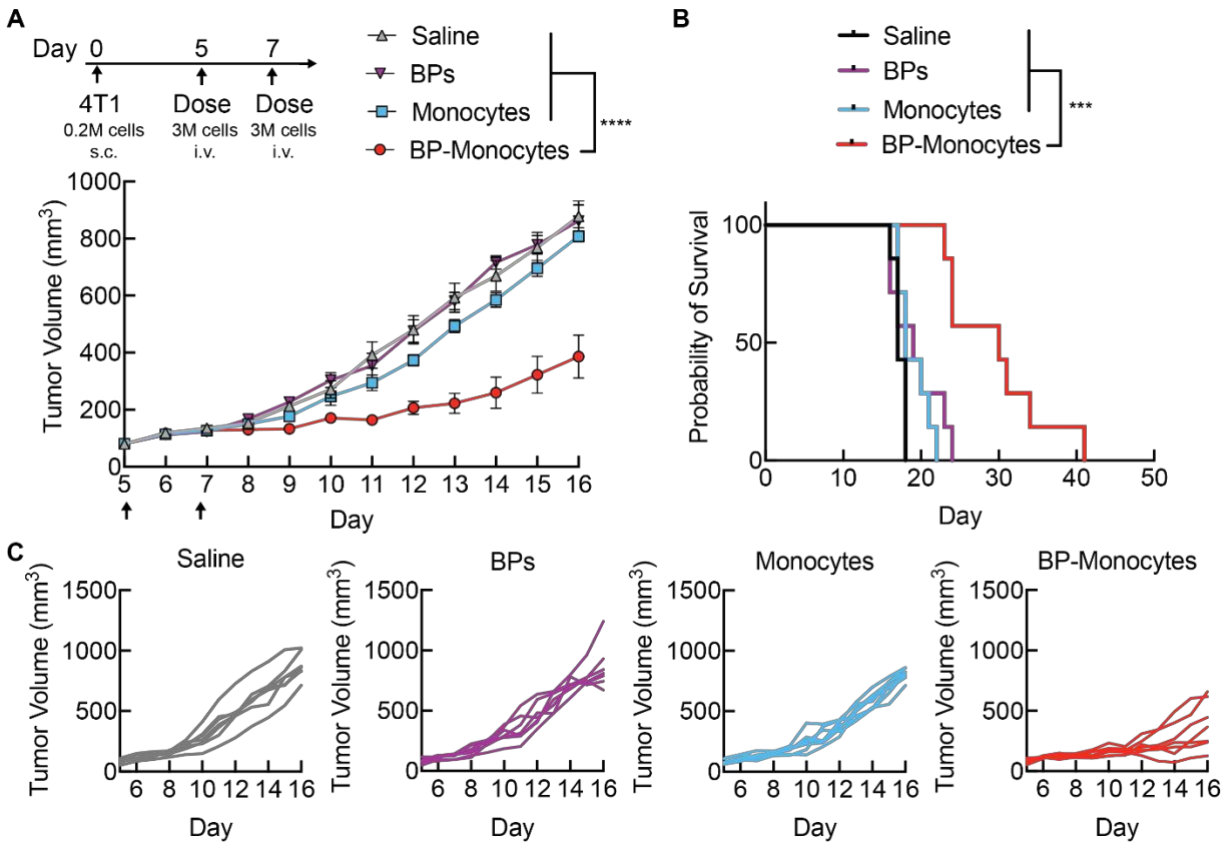

Figure 6-4. Attachment of IFNγ backpacks to monocytes elicits therapeutic efficacy.
(A) Tumors were inoculated with 4T1 in the mammary fat pad and mice were administered 4x10^6 IFNγ BP-monocytes, monocytes alone, free backpacks, or saline intravenously via tail vein on

*Days 5 and 7. Tumor volume was monitored. Data shown represents mean ± SEM with n=7 mice per group (B) Survival data depicting the time until mice reached ethical endpoints for the same cohort of mice represented in panel A. Displayed by by Kaplan–Meier curves. (C) Plots of individual tumor growth curves for the mice depicted in panels A and B. For A, data were analyzed by one-way ANOVA with Tukey's HSD; ****p<0.0001. For B, statistical analysis was performed using Mantel–Cox tests; ***p<0.001.*

6.3.5. Backpack-monocytes remodel the tumor microenvironment.

Treatment with backpack-monocytes enhanced overall immune infiltration into tumors, with a notable increase in macrophage and conventional type I dendritic cells (cDC1) accumulation (Fig. 6-5A). cDC1 are a specialized DC subset that efficiently cross-present extracellular antigens to prime and sustain the activation of CD8 T cells, and their presence within the tumor correlates with the efficacy of immunotherapy and patient prognosis (237, 238). Monocyte-backpack treatment, but not monocyte-only treatment, elicited a robust increase in the concentration of intratumoral GM-CSF, a key cytokine for the recruitment, survival, and maturation of dendritic cells (Fig. 6-5B).

The shifts in the myeloid compartment were accompanied by corresponding changes to the lymphoid cells found in the tumor, significantly enhancing the accumulation of CD8+ T cells and decreasing the CD4/CD8 T cell ratio – a key prognostic indicator(239) (Fig. 6-5C). Further, a greater proportion of intratumoral NK cells expressed KLRG1, a marker for their maturation (Fig 6-5C). These changes demonstrate remodeling of the tumor microenvironment from cold to hot. Corresponding changes in the T cell population of the blood shown in Appendix Figure 9-38.

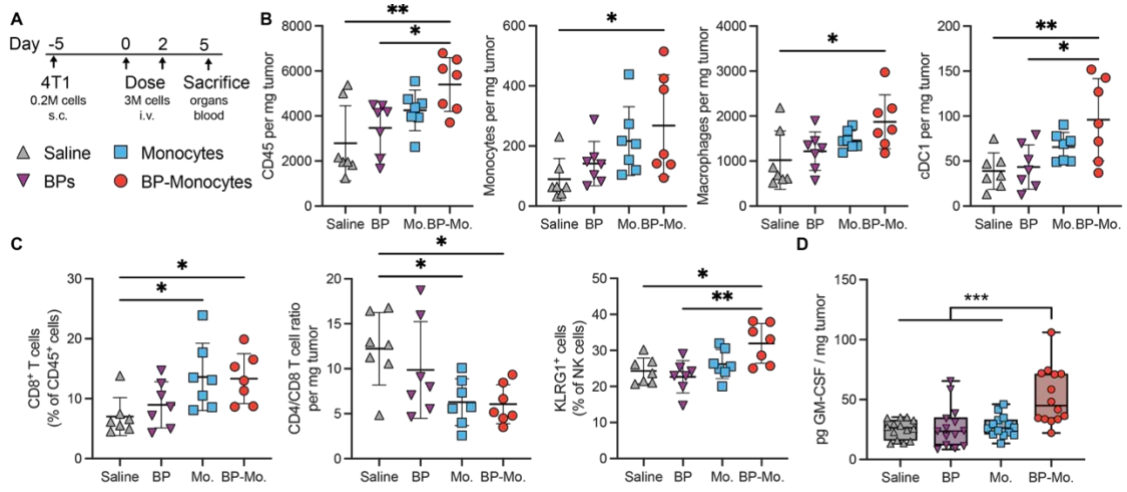

Figure 6-5. IFNγ backpack-monocytes remodel the tumor microenvironment.
A) Mice were inoculated with 0.2 million 4T1 cells subcutaneously (s.c.) and dosed at Days 5 and 7 with 4x10^6 backpack-monocytes, monocytes, free backpacks, or salin intravenously (i.v.) vial tail vein. Mice were sacrificed 3 days after the second dose. The tumor was processed into single cell suspensions and analyzed via flow cytometry to profile the B) myeloid cell profile and B) lymphoid cell profile; mean ± SD (n=7). C) Concentrations of pro-inflammatory mediators from tumor homogenate; mean ± SD (n=14). D) Blood was processed into single suspensions and the T cell

*profile of the blood was analyzed; mean ± SD (n=7). For B, C, D, data were analyzed using one-way ANOVA with Tukey's HSD test; ns, not significant, *P<0.05, **P<0.01, ***P<0.001.*

6.3.6. IFNγ BP-monocytes are safe.

There was no statistically significant difference in the change in body weight at any timepoint for 4T1 tumor bearing mice receiving saline, monocytes, free backpacks, or IFNγ backpack-adhered monocytes (Fig. 6-6A). All mice steadily gained weight over the course of the study and no behavioral changes were observed. Additionally, there was no difference in serum cytokine analysis of tumor-bearing mice receiving saline or IFNγ -adhered monocytes (Fig. 6-6B).

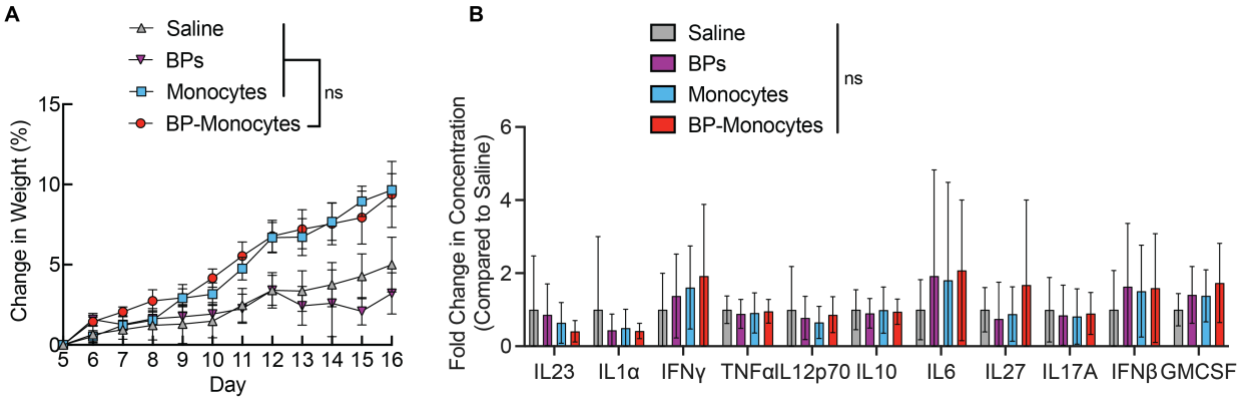

Figure 6-6. IFNγ backpacks-monocytes have a safe toxicity profile.
(A) Change in weight of 4T1 tumor bearing mice treated with saline, free IFNγ *backpacks, naïve monocytes, or* IFNγ *backpacks adhered to monocytes. Mice received treatment on days 0 and 2 and were weighed daily. Data is shown as mean ± SEM. (B) Serum cytokine analysis for mice 4 days after second dose, as displayed in Figure 5. For A, data were analyzed with one-way ANOVA with Tukey's HSD; ns, not significant. For B, data were analyzed using two-way ANOVA with Tukey's correction; ns, not significant.*

6.4. Discussion

The studies presented here demonstrate a novel cancer treatment using tumor infiltrating monocytes. We engineered a strategy of controlling differentiation and phenotype of subsequent macrophages using polymer backpacks. The design uniqueness of backpacks is in their surface conjugation with anti-CD11b Fab to promote monocyte adhesion and IFNγ to control the monocyte with very limited release of IFNγ. IFNγ has pleiotropic effects that are unpredictable in individual patients(240). The ability to minimize systemic exposure and produce a stable IFNγ backpack that influences myeloid cell phenotype represents a major advance.

We have previously reported the therapeutic efficacy of IFNγ-loaded backpacks attached to macrophages after intra-tumoral injection (39). However, direct intra-tumoral injection is not a suitable treatment strategy for many cancers, including those in difficult to access locations, residual disease following surgery, and metastatic disease. Indeed, the majority of cancer deaths

are attributable to metastases (241). The strategy described here offers significant advance by enabling intravenous injections. Intravenously administered monocytes displayed superior trafficking to the immunosuppressive tumor, demonstrating 7-fold tumor accumulation compared to intravenously administered macrophages.

Our studies present a cell therapy approach in delaying the growth of an extremely aggressive solid tumor. Orthotopic 4T1 breast tumors are highly immunosuppressive and are associated with checkpoint inhibitor resistance, tumor metastasis, lack of tumor-specific antigens, and presence of non-responders making them challenging targets for current therapies (230, 242, 243). Delivery of pro-inflammatory backpack-monocytes enables control over tumor growth by enhancing macrophage and cDC1 infiltration into the tumor and increasing intra-tumoral GM-CSF levels. Significant increases in accumulation of CD8+ T cells and mature NK cells are also correlated with stronger anti-tumor immunity. These changes demonstrate potential remodeling of the solid tumor microenvironment from cold to hot, which may enable heterogenous tumor compositions to be treated.

Safety is a critical aspect for cell therapies, due to concerns of off-target or pleiotropic effects. The studies reported here demonstrate an excellent safety profile for the backpack-monocyte system, with serum analytes in normal ranges and normal histology in major organs. The approach described here localizes IFNγ to the carrier monocyte and circumvents the need for co-administration of supporting therapies to sustain the activity of adoptively transferred cells, as is required with currently approved T cell therapies. This further improves the safety of the approach. Cytokine release syndrome (CRS) commonly refers to the acute systemic inflammatory reaction resulting in rapid release of cytokines (244). CRS is the most common form of toxicity associated with CAR T cell therapies, necessitating management with anti-IL-6 (245). This is not ideal as IL-6 has pleiotropic effects, notably related to immune response and hematopoiesis (246). Treatment with anti-IL-6 therapy dampens the pro-inflammatory response beneficial to many cancer treatments. In addition to CAR T cell therapies, CRS is associated with several antibody-based therapeutics and chemotherapies (247). It is therefore notable that the therapeutic strategy employed in this study does not increase systemic levels of cytokines associated with inflammation, including IL-6.

Current CAR T cell therapies approved for the treatment of cancer have limitations on the indications. CAR T cell therapies are only approved for the treatment of acute lymphoblastic leukemia (ALL), non-Hodgkin lymphoma (NHL), follicular lymphoma (FL), mantle cell lymphoma (MCL), and multiple myeloma (MM) (248). FL and MCL are subtypes of NHL, implying that of the expected American cancer diagnoses in 2023, only the 6450 ALL patients, 35,730 MM patients, and 80,550 NHL patients have any chance of receiving CAR T cell therapy (244). This represents just 6.27% of the 1,958,310 Americans expected to be diagnosed with cancer in 2023. More than 90% of the remaining expected cancer diagnoses for which no cell therapies have been approved by the FDA are solid tumors. This represents a major unmet need.

The studies reported here demonstrate an antigen-free, genetic engineering-free approach to cell therapy for solid tumor treatment. This overcomes the cumbersome, centralized model used for CAR therapies (249). CAR T cell and macrophage therapies require genetic engineering of cells in order to express CARs (233, 245). This process adds to the complexity and time required to

prepare treatments. Added complexity increases the financial burden associated with CAR T cell therapy, limiting the number of patients that are treated each year (250). Furthermore, genetically-modified products such as cell therapies undergo greater regulatory scrutiny compared to those that are unmodified (251, 252). Conversely, the cellular engineering strategy proposed in this manuscript is antigen independent, with cells rapidly labelled with backpacks and ready for administration. There are well established methods for separating monocytes from peripheral blood, and myeloid cells are gaining traction by companies for their use in cell therapies. Further improvements will involve developing an allogeneic, off-the-shelf approach to cell therapies to eliminate complexity involved with personalized therapy, as well as developing ways to modify the cells of interest *in vivo*. Future challenges will also involve improving translation in regions lacking required infrastructure for receipt and storage of cryo-preserved materials.

6.5. Conclusions

Adoptive cell therapies are revolutionizing cancer treatment. However, treatment of solid tumors remains a major unmet need, in part due to cell adoptive cell infiltration into the tumor and in part due to the immunosuppressive tumor microenvironment. The heterogeneity of tumors and presence of non-responders also calls for antigen-independent approaches to tumor treatment. Here, we report impressive trafficking of adoptively transferred monocytes into the immunosuppressive 4T1 tumor. To control monocyte plasticity in the tumor microenvironment, we developed backpacks modified with IFNγ to promote differentiation of monocytes into macrophages and maintenance in a pro-inflammatory phenotype. Backpack-laden monocytes remodeled the tumor microenvironment into a pro-inflammatory state, demonstrating a cold to hot transition. Treatment with backpack-monocytes led to substantial reduction in tumor burden and significant increase in survival.

7. Conclusions

7.1. Conclusions

Cell-based therapies are gaining traction as the next frontier of medicine. Living cells can overcome biological barriers, demonstrate plasticity in response to stimuli, and interact with specific cell types. Cells also provide a canvas for further engineering, through implantation in scaffolds or through genetic modifications. In this dissertation, I focus on using biomaterials to tune cell phenotype. I delve into the design of discoidal microparticles that adhere to the surface of phagocytic immune cells, due to particle shape and aspect ratio, allowing for engineering of the cell surface. I expand on the role of shape as a particle design parameter in Chapter 2.

Myeloid cells are gaining more awareness for their implication in the dysregulated biological cascades in numerous diseases, motivating the development of myeloid cell therapies. In Chapter 3, I discuss the importance of myeloid cells, including a background on their biology and the therapeutic landscape of myeloid cells. I focus on the key role of monocytes and macrophages in defending against foreign pathogens, healing wounds, and regulating tissue homeostasis. As a result of their important and deterministic roles in both health and disease, macrophages have gained considerable attention as targets and therapeutic modalities for drug delivery.

In the subsequent chapters, I delve into preclinical applications of microparticles adhered to monocytes and macrophages to promote anti- or pro-inflammatory phenotypes. I assess the effect of these microparticles on durability of phenotypic activation and other cellular functions *in vitro*. I apply this platform to study immune-modulation and therapeutic effect in several disease models. In Chapter 4, I discuss treatment with anti-inflammatory microparticles adhered to monocytes in a mouse model of progressive multiple sclerosis to determine immunomodulatory effects and therapeutic efficacy. In Chapter 5, I discuss scale-up of this treatment modality for application in a gyrencephalic porcine model of traumatic brain injury to reduce inflammation at the contusion site. Finally, in Chapter 6, I report on treatment with pro-inflammatory microparticles adhered to monocytes in a model of murine mammary carcinomas to assess tumor microenvironment remodeling and effect on tumor burden.

Altogether, this work provides a biomaterials-based approach to tune myeloid cell phenotype *ex vivo*, for precise control of cell phenotype *in vivo* for cell therapy applications. Safety is a critical aspect for cell therapies, due to concerns of off-target or pleiotropic effects. The studies reported here demonstrate an excellent safety profile for the backpack-monocyte/macrophage system, with analytes in blood in normal ranges and normal histology in major organs. Considering clinical translation, the studies reported here demonstrated an antigen-free, genetic engineering-free approach to cell therapy. By decreasing complexity, we hope to decrease the financial burden associated with cell therapies, thereby increasing the potential number of patients that may eventually be treated (250).

7.2. Future Directions

7.2.1. Other cell types for engineering with backpacks.

Backpacks and surface-associated microparticles may be engineered to activate and improve the longevity of control over other cell types, including stem cells, T cells, neutrophils, and NK cells. Current clinical trials for cell therapies are dominated by T cells and stem cells (2). T cells are

adaptive immune cells capable of directly eliminating mutated or infected host cells, activating other immune cells, and producing cytokines to regulate immune responses. Backpacks may be engineering to durably activate T cells to bring about anti-tumor functions, for example. The same could be said for NK cells, which destroy tumor cells and virally infected cells via release of lytic molecules from granules and rapid production of pro-inflammatory cytokines. When considering stem cells, such as hematopoietic stem cells and mesenchymal stem cells, backpacks could theoretically be employed to provide sustained cues in vivo to promote differentiation.

7.2.2. Combination therapy.

Due to the disease heterogeneity and presence of non-responders, many disease treatments are multi-pronged and consists of combination therapies (249). For example, in Chapter 6 we demonstrated synergistic effect of myeloid cell therapy and traditional neoadjuvant chemotherapy (Appendix Figure 9-40). Although myeloid cell therapies focus on the innate immune system and demonstrate some crosstalk with the adaptive immune system, we hypothesize this crosstalk can be improved by administering therapies with complementary mechanisms of actions. For example, the anti-inflammatory myeloid cell therapy for MS discussed in Chapter 4, could be improved in combination with other medications that target the adaptive immune system, such as fingolimod, which sequesters lymphocytes in the lymph nodes.

7.2.3. In vivo attachment of backpacks to cells of interest.

In aid in translation to the clinic, a strategy to adhere backpacks and other microparticles *in situ* would be desirable, preventing this approach from being labeled as a cellular therapy product, which would aid in regulatory hurdles. I have previously shown that functionalized backpacks are able to specifically bind to immune cells of interest in whole blood *ex vivo* (Appendix Figure 9-41). However, I demonstrated that intravenous or subcutaneous injection of free functionalized backpacks does not result in *in vivo* binding with target immune cells. This suggests that backpacks need to be further engineered for *in situ* / *in vivo* binding with target circulating immune cells. Another approach could be to draw blood from the patient and introduce backpacks for binding in the blood *ex vivo*, for the blood to then be reinfused.

7.2.4. Outlook.

The cellular engineering strategy proposed in this dissertation is genetic engineering free and antigen independent, with cells rapidly labelled with backpacks and ready for administration. There are well established methods for separating monocytes from peripheral blood, and myeloid cells are gaining traction by many companies for their use in cell therapies. Further improvements will involve developing an allogeneic, off-the-shelf approach to cell therapies to eliminate complexity involved with personalized therapy. Future challenges will also involve improving translation in regions lacking required infrastructure for receipt and storage of cryo-preserved materials.

8. References

1. M. A. Fischbach, J. A. Bluestone, W. A. Lim, Cell-Based Therapeutics: The Next Pillar of Medicine. *Sci. Transl. Med.* **5** (2013).
2. L. L. W. Wang, *et al.*, Cell therapies in the clinic. *Bioeng. Transl. Med.* **6**, 1–36 (2021).
3. Z. Zhao, A. Ukidve, J. Kim, S. Mitragotri, Targeting Strategies for Tissue-Specific Drug Delivery. *Cell* **181**, 151–167 (2020).
4. D. T. Riglar, P. A. Silver, Engineering bacteria for diagnostic and therapeutic applications. *Nat. Rev. Microbiol. 2018 164* **16**, 214–225 (2018).
5. S. R. Bailey, M. V. Maus, Gene editing for immune cell therapies. *Nat. Biotechnol. 2019 3712* **37**, 1425–1434 (2019).
6. K. Adebowale, *et al.*, Materials for Cell Surface Engineering. *Adv. Mater.*, 2210059 (2023).
7. J. L. Schultze, A. Schmieder, S. Goerdt, Macrophage activation in human diseases. *Semin. Immunol.* **27**, 249–256 (2015).
8. J. A. Champion, S. Mitragotri, Role of target geometry in phagocytosis. *Proc. Natl. Acad. Sci.* **103**, 4930–4934 (2006).
9. . J C Mcgann, *et al.*, Inflammatory neuroprotection following traumatic brain injury. *Science (80-.).* **353**, 783–785 (2016).
10. N. Kapate, J. R. Clegg, S. Mitragotri, Non-spherical micro- and nanoparticles for drug delivery: Progress over 15 years. *Adv. Drug Deliv. Rev.* **177**, 113807 (2021).
11. W. He, N. Kapate, C. W. Shields, S. Mitragotri, Drug delivery to macrophages: A review of targeting drugs and drug carriers to macrophages for inflammatory diseases. *Adv. Drug Deliv. Rev.* (2019) https:/doi.org/10.1016/j.addr.2019.12.001.
12. N. Kapate, *et al.*, A backpack-based myeloid cell therapy for multiple sclerosis. *Proc. Natl. Acad. Sci. U. S. A.* (2023).
13. S. Prakash, N. Kumbhojkar, J. R. Clegg, S. Mitragotri, Cell-bound Nanoparticles for Tissue Targeting and Immunotherapy: Engineering of the Particle-Membrane Interface. *Curr. Opin. Colloid Interface Sci.* (2020) https:/doi.org/10.1016/j.cocis.2020.101408.
14. Z. Zhao, A. Ukidve, V. Krishnan, S. Mitragotri, Effect of physicochemical and surface properties on in vivo fate of drug nanocarriers. *Adv. Drug Deliv. Rev.* (2019) https:/doi.org/10.1016/j.addr.2019.01.002.
15. Z. Shen, M. P. Nieh, Y. Li, Decorating nanoparticle surface for targeted drug delivery: Opportunities and challenges. *Polymers (Basel).* (2016) https:/doi.org/10.3390/polym8030083.
16. G. Sanità, B. Carrese, A. Lamberti, Nanoparticle Surface Functionalization: How to Improve Biocompatibility and Cellular Internalization. *Front. Mol. Biosci.* (2020) https:/doi.org/10.3389/fmolb.2020.587012.
17. Y. V Pathak, *Surface Modification of Nanoparticles for Targeted Drug Delivery* (2019) https:/doi.org/10.1007/978-3-030-06115-9.
18. M. J. Mitchell, *et al.*, Engineering precision nanoparticles for drug delivery. *Nat. Rev. Drug Discov.* (2021) https:/doi.org/10.1038/s41573-020-0090-8.
19. K. M. Moore, *et al.*, Injectable, Ribbon-Like Microconfetti Biopolymer Platform for Vaccine Applications. *ACS Appl. Mater. Interfaces* (2020) https:/doi.org/10.1021/acsami.0c10276.
20. X. Lu, *et al.*, Engineered PLGA microparticles for long-term, pulsatile release of STING

agonist for cancer immunotherapy. *Sci. Transl. Med.* **12**, 1–16 (2020).
21. S. T. Koshy, D. K. Y. Zhang, J. M. Grolman, A. G. Stafford, D. J. Mooney, Injectable nanocomposite cryogels for versatile protein drug delivery. *Acta Biomater.* **65**, 36–43 (2018).
22. R. Kuai, L. J. Ochyl, K. S. Bahjat, A. Schwendeman, J. J. Moon, Designer vaccine nanodiscs for personalized cancer immunotherapy. *Nat. Mater.* (2017) https:/doi.org/10.1038/NMAT4822.
23. J. J. Moon, B. Huang, D. J. Irvine, Engineering Nano- and microparticles to tune immunity. *Adv. Mater.* (2012) https:/doi.org/10.1002/adma.201200446.
24. O. Mhatre, S. Sodha, Pharmaceutical feasibility and flow characteristics of polymeric non-spherical particles. *Nanomedicine Nanotechnology, Biol. Med.* (2019) https:/doi.org/10.1016/j.nano.2019.03.002.
25. J. A. Champion, Y. K. Katare, S. Mitragotri, Particle shape: A new design parameter for micro- and nanoscale drug delivery carriers. *J. Control. Release* **121**, 3–9 (2007).
26. S. L. Tao, T. A. Desai, Microfabricated drug delivery systems: From particles to pores. *Adv. Drug Deliv. Rev.* (2003) https:/doi.org/10.1016/S0169-409X(02)00227-2.
27. S. Nejati, E. Mohseni Vadeghani, S. Khorshidi, A. Karkhaneh, Role of particle shape on efficient and organ-based drug delivery. *Eur. Polym. J.* (2020) https:/doi.org/10.1016/j.eurpolymj.2019.109353.
28. E. Blanco, H. Shen, M. Ferrari, Principles of nanoparticle design for overcoming biological barriers to drug delivery. *Nat. Biotechnol.* **33**, 941–951 (2015).
29. J. Wang, J. D. Byrne, M. E. Napier, J. M. Desimone, More effective nanomedicines through particle design. *Small* (2011) https:/doi.org/10.1002/smll.201100442.
30. N. P. Truong, M. R. Whittaker, C. W. Mak, T. P. Davis, The importance of nanoparticle shape in cancer drug delivery. *Expert Opin. Drug Deliv.* **12**, 129–142 (2015).
31. J. R. Clegg, *et al.*, Modular fabrication of intelligent material-tissue interfaces for bioinspired and biomimetic devices. *Prog. Mater. Sci.* (2019) https:/doi.org/10.1016/j.pmatsci.2019.100589.
32. A. J. Metherell, W. Cullen, N. H. Williams, M. D. Ward, Binding of Hydrophobic Guests in a Coordination Cage Cavity is Driven by Liberation of "High-Energy" Water. *Chem. - A Eur. J.* (2018) https:/doi.org/10.1002/chem.201704163.
33. Z. Vatankhah, E. Dehghani, M. Salami-Kalajahi, H. Roghani-Mamaqani, One-step fabrication of low cytotoxic anisotropic poly(2-hydroxyethyl methacrylate-co-methacrylic acid) particles for efficient release of DOX. *J. Drug Deliv. Sci. Technol.* (2019) https:/doi.org/10.1016/j.jddst.2019.101332.
34. Y. Geng, *et al.*, Shape effects of filaments versus spherical particles in flow and drug delivery. *Nat. Nanotechnol.* **2**, 249–255 (2007).
35. P. V. Devarajan, *et al.*, Particle shape: A new design parameter for passive targeting in splenotropic drug delivery. *J. Pharm. Sci.* **99**, 2576–2581 (2010).
36. Y. Zhao, *et al.*, A comparison between sphere and rod nanoparticles regarding their in vivo biological behavior and pharmacokinetics. *Sci. Rep.* **7**, 1–11 (2017).
37. M. Li, *et al.*, Silk-coated dexamethasone non-spherical microcrystals for local drug delivery to inner ear. *Eur. J. Pharm. Sci.* (2020) https:/doi.org/10.1016/j.ejps.2020.105336.
38. J. D. Engstrom, J. M. Tam, M. A. Miller, R. O. Williams, K. P. Johnston, Templated open flocs of nanorods for enhanced pulmonary delivery with pressurized metered dose

inhalers. *Pharm. Res.* (2009) https:/doi.org/10.1007/s11095-008-9707-z.
39. C. W. Shields, *et al.*, Cellular Backpacks for Macrophage Immunotherapy. *Sci. Adv.* (2020).
40. A. J. Swiston, *et al.*, Surface functionalization of living cells with multilayer patches. *Nano Lett.* (2008) https:/doi.org/10.1021/nl802404h.
41. A. Mohraz, M. J. Solomon, Direct visualization of colloidal rod assembly by confocal microscopy. *Langmuir* (2005) https:/doi.org/10.1021/la046908a.
42. J. Dong, J. Liu, G. Kang, J. Xie, Y. Wang, Pushing the resolution of photolithography down to 15nm by surface plasmon interference. *Sci. Rep.* (2014) https:/doi.org/10.1038/srep05618.
43. J. del Barrio, C. Sánchez-Somolinos, Light to Shape the Future: From Photolithography to 4D Printing. *Adv. Opt. Mater.* (2019) https:/doi.org/10.1002/adom.201900598.
44. J. C. Sunshine, K. Perica, J. P. Schneck, J. J. Green, Particle shape dependence of CD8+ T cell activation by artificial antigen presenting cells. *Biomaterials* **35**, 269–277 (2014).
45. R. A. Meyer, *et al.*, Anisotropic biodegradable lipid coated particles for spatially dynamic protein presentation. *Acta Biomater.* **72**, 228–238 (2018).
46. M. L. Bookstaver, K. L. Hess, C. M. Jewell, Self-Assembly of Immune Signals Improves Codelivery to Antigen Presenting Cells and Accelerates Signal Internalization, Processing Kinetics, and Immune Activation. *Small* (2018) https:/doi.org/10.1002/smll.201802202.
47. J. L. Perry, *et al.*, PEGylated PRINT nanoparticles: The impact of PEG density on protein binding, macrophage association, biodistribution, and pharmacokinetics. *Nano Lett.* (2012) https:/doi.org/10.1021/nl302638g.
48. R. Mathaes, G. Winter, A. Besheer, J. Engert, Influence of particle geometry and PEGylation on phagocytosis of particulate carriers. *Int. J. Pharm.* **465**, 159–164 (2014).
49. S. Kumar, A. C. Anselmo, A. Banerjee, M. Zakrewsky, S. Mitragotri, Shape and size-dependent immune response to antigen-carrying nanoparticles. *J. Control. Release* **220**, 141–148 (2015).
50. A. Da Silva-Candal, *et al.*, Shape effect in active targeting of nanoparticles to inflamed cerebral endothelium under static and flow conditions. *J. Control. Release* **309**, 94–105 (2019).
51. J. F. Stefanick, J. D. Ashley, T. Kiziltepe, B. Bilgicer, A systematic analysis of peptide linker length and liposomal polyethylene glycol coating on cellular uptake of peptide-targeted liposomes. *ACS Nano* (2013) https:/doi.org/10.1021/nn305663e.
52. J. W. Yoo, S. Mitragotri, Polymer particles that switch shape in response to a stimulus. *Proc. Natl. Acad. Sci. U. S. A.* **107**, 11205–11210 (2010).
53. H. R. Culver, J. R. Clegg, N. A. Peppas, Analyte-Responsive Hydrogels: Intelligent Materials for Biosensing and Drug Delivery. *Acc. Chem. Res.* (2017) https:/doi.org/10.1021/acs.accounts.6b00533.
54. L. Peltonen, Practical guidelines for the characterization and quality control of pure drug nanoparticles and nano-cocrystals in the pharmaceutical industry. *Adv. Drug Deliv. Rev.* (2018) https:/doi.org/10.1016/j.addr.2018.06.009.
55. J. A. Champion, A. Walker, S. Mitragotri, Role of particle size in phagocytosis of polymeric microspheres. *Pharm. Res.* **25**, 1815–1821 (2008).
56. G. Sharma, *et al.*, Polymer particle shape independently influences binding and internalization by macrophages. *J. Control. Release* **147**, 408–412 (2010).
57. J. A. Champion, S. Mitragotri, Shape induced inhibition of phagocytosis of polymer

particles. *Pharm. Res.* **26**, 244–249 (2009).
58. D. M. Richards, R. G. Endres, How cells engulf: a review of theoretical approaches to phagocytosis. *Rep. Prog. Phys.* **80**, 126601 (2017).
59. W. J. Kelley, C. A. Fromen, G. Lopez-Cazares, O. Eniola-Adefeso, PEGylation of model drug carriers enhances phagocytosis by primary human neutrophils. *Acta Biomater.* **79**, 283–293 (2018).
60. H. Safari, *et al.*, Neutrophils preferentially phagocytose elongated particles-An opportunity for selective targeting in acute inflammatory diseases. *Sci. Adv.* **6** (2020).
61. J. W. Yoo, N. Doshi, S. Mitragotri, Endocytosis and intracellular distribution of PLGA particles in endothelial cells: Effect of particle geometry. *Macromol. Rapid Commun.* **31**, 142–148 (2010).
62. Z. Shen, H. Ye, X. Yi, Y. Li, Membrane Wrapping Efficiency of Elastic Nanoparticles during Endocytosis: Size and Shape Matter. *ACS Nano* **13**, 215–228 (2019).
63. V. Heinrich, Controlled One-on-One Encounters between Immune Cells and Microbes Reveal Mechanisms of Phagocytosis. *Biophys. J.* (2015) https:/doi.org/10.1016/j.bpj.2015.06.042.
64. R. C. May, L. M. Machesky, Phagocytosis and the actin cytoskeleton. *J. Cell Sci.* (2001).
65. R. E. Unger, V. Krump-Konvalinkova, K. Peters, C. James Kirkpatrick, In vitro expression of the endothelial phenotype: Comparative study of primary isolated cells and cell lines, including the novel cell line HPMEC-ST1.6R. *Microvasc. Res.* (2002) https:/doi.org/10.1006/mvre.2002.2434.
66. C. Pan, C. Kumar, S. Bohl, U. Klingmueller, M. Mann, Comparative proteomic phenotyping of cell lines and primary cells to assess preservation of cell type-specific functions. *Mol. Cell. Proteomics* (2009) https:/doi.org/10.1074/mcp.M800258-MCP200.
67. R. Agarwal, *et al.*, Mammalian cells preferentially internalize hydrogel nanodiscs over nanorods and use shape-specific uptake mechanisms. *Proc. Natl. Acad. Sci. U. S. A.* **110**, 17247–17252 (2013).
68. C. Huang, Y. Zhang, H. Yuan, H. Gao, S. Zhang, Role of nanoparticle geometry in endocytosis: Laying down to stand up. *Nano Lett.* **13**, 4546–4550 (2013).
69. H. Jin, D. A. Heller, R. Sharma, M. S. Strano, Size-dependent cellular uptake and expulsion of single-walled carbon nanotubes: Single particle tracking and a generic uptake model for nanoparticles. *ACS Nano* **3**, 149–158 (2009).
70. E. Hinde, *et al.*, Pair correlation microscopy reveals the role of nanoparticle shape in intracellular transport and site of drug release. *Nat. Nanotechnol.* **12**, 81–89 (2017).
71. A. Castoldi, *et al.*, Aspherical and Spherical InvA497-Functionalized Nanocarriers for Intracellular Delivery of Anti-Infective Agents. *Pharm. Res.* **36**, 1–13 (2019).
72. N. Doshi, S. Mitragotri, Needle-shaped polymeric particles induce transient disruption of cell membranes. *J. R. Soc. Interface* **7** (2010).
73. B. Zhang, *et al.*, Cellular fate of deformable needle-shaped PLGA-PEG fibers. *Acta Biomater.* **112**, 182–189 (2020).
74. P. M. Peiris, *et al.*, Enhanced delivery of chemotherapy to tumors using a multicomponent nanochain with radio-frequency-tunable drug release. *ACS Nano* **6**, 4157–4168 (2012).
75. P. Decuzzi, *et al.*, Size and shape effects in the biodistribution of intravascularly injected particles. *J. Control. Release* **141**, 320–327 (2010).
76. X. Huang, *et al.*, The shape effect of mesoporous silica nanoparticles on biodistribution, clearance, and biocompatibility in vivo. *ACS Nano* **5**, 5390–5399 (2011).

77. Arnida, M. M. Janát-Amsbury, A. Ray, C. M. Peterson, H. Ghandehari, Geometry and surface characteristics of gold nanoparticles influence their biodistribution and uptake by macrophages. *Eur. J. Pharm. Biopharm.* **77**, 417–423 (2011).
78. K. Namdee, *et al.*, In vivo evaluation of vascular-targeted spheroidal microparticles for imaging and drug delivery application in atherosclerosis. *Atherosclerosis* **237**, 279–286 (2014).
79. L. Li, *et al.*, Biodistribution, excretion, and toxicity of mesoporous silica nanoparticles after oral administration depend on their shape. *Nanomedicine Nanotechnology, Biol. Med.* **11**, 1915–1924 (2015).
80. S. Muro, *et al.*, Control of endothelial targeting and intracellular delivery of therapeutic enzymes by modulating the size and shape of ICAM-1-targeted carriers. *Mol. Ther.* **16**, 1450–1458 (2008).
81. S. Barua, *et al.*, Particle shape enhances specificity of antibody-displaying nanoparticles. *Proc. Natl. Acad. Sci. U. S. A.* **110**, 3270–3275 (2013).
82. J. H. Park, *et al.*, Systematic surface engineering of magnetic nanoworms for in vivo tumor targeting. *Small* **5**, 694–700 (2009).
83. G. Wang, *et al.*, High-relaxivity superparamagnetic iron oxide nanoworms with decreased immune recognition and long-circulating properties. *ACS Nano* **8**, 12437–12449 (2014).
84. K. C. Tjandra, *et al.*, Modulating the Selectivity and Stealth Properties of Ellipsoidal Polymersomes through a Multivalent Peptide Ligand Display. *Adv. Healthc. Mater.* **2000261**, 1–11 (2020).
85. L. Wang, *et al.*, Novel fibronectin-targeted nanodisk drug delivery system displayed superior efficacy against prostate cancer compared with nanospheres. *Nano Res.* **12**, 2451–2459 (2019).
86. J. Cao, *et al.*, Development of PLGA micro- and nanorods with high capacity of surface ligand conjugation for enhanced targeted delivery. *Asian J. Pharm. Sci.* **14**, 86–94 (2019).
87. Anselmo Aaron C, *et al.*, Platelet-like nanoparticles: mimicking shape, flexibility, and surface biology of platelets to target vascular injuries. *ACS Nano* **8**, 11243–11253 (2014).
88. V. P. Chauhan, *et al.*, Fluorescent nanorods and nanospheres for real-time in vivo probing of nanoparticle shape-dependent tumor penetration. *Angew. Chemie - Int. Ed.* **50**, 11417–11420 (2011).
89. Z. Liu, *et al.*, In vivo biodistribution and highly efficient tumour targeting of carbon nanotubes in mice. *Nat. Nanotechnol.* **2**, 47–52 (2007).
90. B. J. Harris, P. Dalhaimer, Particle shape effects in vitro and in vivo. *Front. Biosci. (Schol. Ed).* **4**, 1344—1353 (2012).
91. A. L. Van De Ven, *et al.*, Rapid tumoritropic accumulation of systemically injected plateloid particles and their biodistribution. *J. Control. Release* **158**, 148–155 (2012).
92. B. Godin, *et al.*, Discoidal porous silicon particles: Fabrication and biodistribution in breast cancer bearing mice. *Adv. Funct. Mater.* **22**, 4225–4235 (2012).
93. K. S. Chu, *et al.*, Plasma, tumor and tissue pharmacokinetics of Docetaxel delivered via nanoparticles of different sizes and shapes in mice bearing SKOV-3 human ovarian carcinoma xenograft. *Nanomedicine Nanotechnology, Biol. Med.* **9**, 686–693 (2013).
94. P. P. Wibroe, *et al.*, Bypassing adverse injection reactions to nanoparticles through shape modification and attachment to erythrocytes. *Nat. Nanotechnol.* (2017) https:/doi.org/10.1038/nnano.2017.47.
95. R. A. Roberts, *et al.*, Analysis of the Murine Immune Response to Pulmonary Delivery of

Precisely Fabricated Nano- and Microscale Particles. *PLoS One* (2013) https:/doi.org/10.1371/journal.pone.0062115.
96. T. W. Shen, *et al.*, Distribution and Cellular Uptake of PEGylated Polymeric Particles in the Lung Towards Cell-Specific Targeted Delivery. *Pharm. Res.* (2015) https:/doi.org/10.1007/s11095-015-1701-7.
97. M. A. Collier, *et al.*, Saquinavir Loaded Acetalated Dextran Microconfetti – a Long Acting Protease Inhibitor Injectable. *Pharm. Res.* (2016) https:/doi.org/10.1007/s11095-016-1936-y.
98. A. Garapaty, J. A. Champion, Shape of ligand immobilized particles dominates and amplifies the macrophage cytokine response to ligands. *PLoS One* **14**, 12–14 (2019).
99. T. Tazaki, *et al.*, Shape-dependent adjuvanticity of nanoparticle-conjugated RNA adjuvants for intranasal inactivated influenza vaccines. *RSC Adv.* (2018) https:/doi.org/10.1039/c8ra01690a.
100. S. Shukla, *et al.*, Plant viral nanoparticles-based HER2 vaccine: Immune response influenced by differential transport, localization and cellular interactions of particulate carriers. *Biomaterials* (2017) https:/doi.org/10.1016/j.biomaterials.2016.12.030.
101. A. L. Galloway, *et al.*, Development of a nanoparticle-based influenza vaccine using the PRINT® technology. *Nanomedicine Nanotechnology, Biol. Med.* (2013) https:/doi.org/10.1016/j.nano.2012.11.001.
102. A. Hassani Najafabadi, *et al.*, Cancer Immunotherapy via Targeting Cancer Stem Cells Using Vaccine Nanodiscs. *Nano Lett.* (2020) https:/doi.org/10.1021/acs.nanolett.0c03414.
103. R. Kuai, *et al.*, Robust Anti-Tumor T Cell Response with Efficient Intratumoral Infiltration by Nanodisc Cancer Immunotherapy. *Adv. Ther.* (2020) https:/doi.org/10.1002/adtp.202000094.
104. L. Scheetz, *et al.*, Synthetic High-density Lipoprotein Nanodiscs for Personalized Immunotherapy against Gliomas. *Clin. Cancer Res.* (2020) https:/doi.org/10.1158/1078-0432.CCR-20-0341.
105. K. L. Spiller, *et al.*, Sequential delivery of immunomodulatory cytokines to facilitate the M1-to-M2 transition of macrophages and enhance vascularization of bone scaffolds. *Biomaterials* (2015) https:/doi.org/10.1016/j.biomaterials.2014.10.017.
106. K. L. Wofford, B. S. Singh, D. K. Cullen, K. L. Spiller, Biomaterial-mediated reprogramming of monocytes via microparticle phagocytosis for sustained modulation of macrophage phenotype. *Acta Biomater.* **101**, 237–248 (2020).
107. M. H. Hettiaratchi, M. S. Shoichet, Modulated Protein Delivery to Engineer Tissue Repair. *Tissue Eng. - Part A* (2019) https:/doi.org/10.1089/ten.tea.2019.0066.
108. H. Kawamoto, N. Minato, Myeloid cells. *Int. J. Biochem. Cell Biol.* **36**, 1374–1379 (2004).
109. V. S. Wacleche, C. L. Tremblay, J. P. Routy, P. Ancuta, The Biology of Monocytes and Dendritic Cells: Contribution to HIV Pathogenesis. *Viruses* **10** (2018).
110. R. P. DeKoter, H. Singh, Regulation of B lymphocyte and macrophage development by graded expression of PU.1. *Science* **288**, 1439–1441 (2000).
111. D. Metcalf, Lineage commitment and maturation in hematopoietic cells: the case for extrinsic regulation. *Blood* **92**, 345–7; discussion 352 (1998).
112. A. D. Friedman, Transcriptional regulation of granulocyte and monocyte development. *Oncogene* **21**, 3377–3390 (2002).
113. F. Geissmann, *et al.*, Development of monocytes, macrophages, and dendritic cells.

Science **327**, 656–661 (2010).
114. N. V. Serbina, T. Jia, T. M. Hohl, E. G. Pamer, Monocyte-mediated defense against microbial pathogens. *Annu. Rev. Immunol.* **26**, 421–452 (2008).
115. L. Ziegler-Heitbrock, Monocyte subsets in man and other species. *Cell. Immunol.* **289**, 135–139 (2014).
116. A. A. Patel, *et al.*, The fate and lifespan of human monocyte subsets in steady state and systemic inflammation. *J. Exp. Med.* **214**, 1913–1923 (2017).
117. A. C. Anselmo, *et al.*, Monocyte-mediated delivery of polymeric backpacks to inflamed tissues: A generalized strategy to deliver drugs to treat inflammation. *J. Control. Release* **199**, 29–36 (2015).
118. D. S. Hersh, *et al.*, Evolving Drug Delivery Strategies to Overcome the Blood Brain Barrier. *Curr. Pharm. Des.* **22**, 1177–1193 (2016).
119. R. Lyck, B. Engelhardt, Going against the tide--how encephalitogenic T cells breach the blood-brain barrier. *J. Vasc. Res.* **49**, 497–509 (2012).
120. L. Liu, *et al.*, From Blood to the Brain: Can Systemically Transplanted Mesenchymal Stem Cells Cross the Blood-Brain Barrier? *Stem Cells Int.* **2013**, 435093 (2013).
121. N. A. Pawlowski, G. Kaplan, E. Abraham, Z. A. Cohn, The selective binding and transmigration of monocytes through the junctional complexes of human endothelium. *J. Exp. Med.* **168**, 1865–1882 (1988).
122. T. Gerhardt, K. Ley, Monocyte trafficking across the vessel wall. *Cardiovasc. Res.* **107**, 321–330 (2015).
123. S. Nourshargh, R. Alon, Leukocyte Migration into Inflamed Tissues. *Immunity* **41**, 694–707 (2014).
124. W. A. Banks, From blood-brain barrier to blood-brain interface: New opportunities for CNS drug delivery. *Nat. Rev. Drug Discov.* **15**, 275–292 (2016).
125. S. P. Nobs, M. Kopf, Tissue-resident macrophages: guardians of organ homeostasis. *Trends Immunol.* **42**, 495–507 (2021).
126. D. J. Kloosterman, L. Akkari, Macrophages at the interface of the co-evolving cancer ecosystem. *Cell*, 1–25 (2023).
127. P. J. Murray, T. A. Wynn, Protective and pathogenic functions of macrophage subsets. *Nat. Rev. Immunol.* **11**, 723–737 (2011).
128. F. O. Martinez, S. Gordon, The M1 and M2 paradigm of macrophage activation: Time for reassessment. *F1000Prime Rep.* **6**, 1–13 (2014).
129. V. Piccolo, *et al.*, Opposing macrophage polarization programs show extensive epigenomic and transcriptional cross-talk. *Nat. Immunol.* **18**, 530–540 (2017).
130. S. Mellor-Pita, *et al.*, Monocytes and T lymphocytes contribute to a predominance of interleukin 6 and interleukin 10 in systemic lupus erythematosus. *Cytometry B. Clin. Cytom.* **76**, 261–270 (2009).
131. J. Godsell, *et al.*, Clinical associations of IL-10 and IL-37 in systemic lupus erythematosus. *Sci. Reports 2016 61* **6**, 1–10 (2016).
132. O. Jin, *et al.*, Lymphocyte apoptosis and macrophage function: Correlation with disease activity in systemic lupus erythematosus. *Clin. Rheumatol.* **24**, 107–110 (2005).
133. D. Y. S. Vogel, *et al.*, Macrophages in inflammatory multiple sclerosis lesions have an intermediate activation status. *J. Neuroinflammation* **10**, 1–12 (2013).
134. S. Soldano, *et al.*, Increase in circulating cells coexpressing M1 and M2 macrophage surface markers in patients with systemic sclerosis. *Ann. Rheum. Dis.* **77**, 1842–1845

(2018).
135. S. Arora, K. Dev, B. Agarwal, P. Das, M. A. Syed, Macrophages: Their role, activation and polarization in pulmonary diseases. *Immunobiology* **223**, 383–396 (2018).
136. C. Lee, *et al.*, Targeting of M2-like tumor-associated macrophages with a melittin-based pro-apoptotic peptide. *J. Immunother. cancer* **7** (2019).
137. S. Abid, *et al.*, CCR2/CCR5-mediated macrophage-smooth muscle cell crosstalk in pulmonary hypertension. *Eur. Respir. J.* **54** (2019).
138. A. Sica, A. Mantovani, Macrophage plasticity and polarization: In vivo veritas. *J. Clin. Invest.* (2012) https:/doi.org/10.1172/JCI59643.
139. C. A. Dendrou, L. Fugger, M. A. Friese, Immunopathology of multiple sclerosis. *Nat. Rev. Immunol.* **15**, 545–558 (2015).
140. , Landmark Study Estimates Nearly 1 Million in the U.S. Have Multiple Sclerosis. *Natl. Mult. Scler. Soc.*, 1 (2019).
141. K. E. Attfield, L. T. Jensen, M. Kaufmann, M. A. Friese, L. Fugger, The immunology of multiple sclerosis. *Nat. Rev. Immunol.* **22**, 1–17 (2022).
142. M. K. Mishra, V. Wee Yong, Myeloid cells-targets of medication in multiple sclerosis. *Nat. Rev. Neurol.* (2016) https:/doi.org/10.1038/nrneurol.2016.110.
143. D. Mrdjen, *et al.*, High-Dimensional Single-Cell Mapping of Central Nervous System Immune Cells Reveals Distinct Myeloid Subsets in Health, Aging, and Disease. *Immunity* **48**, 380-395.e6 (2018).
144. C. Lucchinetti, *et al.*, Heterogeneity of multiple sclerosis lesions: implications for the pathogenesis of demyelination. *Ann. Neurol.* (2001) https:/doi.org/https://doi.org/10.1002/1531-8249(200006)47:6<707::AID-ANA3>3.0.CO;2-Q (November 29, 2022).
145. J. W. Prineas, *et al.*, Immunopathology of secondary-progressive multiple sclerosis. *Ann. Neurol.* **50**, 646–657 (2001).
146. O. W. Howell, *et al.*, Activated microglia mediate axoglial disruption that contributes to axonal injury in multiple sclerosis. *J. Neuropathol. Exp. Neurol.* **69**, 1017–1033 (2010).
147. M. Strachan-Whaley, S. Rivest, V. W. Yong, Interactions between microglia and T cells in multiple sclerosis pathobiology. *J. Interferon Cytokine Res.* **34**, 615–622 (2014).
148. A. J. Thompson, S. E. Baranzini, J. Geurts, B. Hemmer, O. Ciccarelli, Multiple sclerosis. *Lancet* **391**, 1622–1636 (2018).
149. M. Filippi, *et al.*, Multiple sclerosis. *Nat. Rev. Dis. Prim.* **4**, 1–27 (2018).
150. C. Baecher-Allan, B. J. Kaskow, H. L. Weiner, Multiple Sclerosis: Mechanisms and Immunotherapy. *Neuron* **97**, 742–768 (2018).
151. , MS Trial Alerts | National Multiple Sclerosis Society (December 3, 2022).
152. , Explore treatments in trials | MS Society (December 3, 2022).
153. , NIH ClinicalTrials.gov (December 4, 2022).
154. K. Biber, T. Möller, E. Boddeke, M. Prinz, Central nervous system myeloid cells as drug targets: Current status and translational challenges. *Nat. Rev. Drug Discov.* **15**, 110–124 (2016).
155. M. Wagner, *et al.*, Isolation and Intravenous Injection of Murine Bone Marrow Derived Monocytes. *J. Vis. Exp.*, 52347 (2014).
156. A. Francke, J. Herold, S. Weinert, R. H. Strasser, R. C. Braun-Dullaeus, Generation of Mature Murine Monocytes from Heterogeneous Bone Marrow and Description of Their Properties. *J. Histochem. Cytochem.* **59**, 813 (2011).

157. , Hooke - Protocols - EAE Induction by Active Immunization in C57BL/6 Mice (2022) (March 4, 2023).
158. S. M. Agrawal, C. Silva, W. W. Tourtellotte, V. W. Yong, EMMPRIN: a novel regulator of leukocyte transmigration into the CNS in multiple sclerosis and experimental autoimmune encephalomyelitis. *J. Neurosci.* **31**, 669–677 (2011).
159. G. Casella, *et al.*, Oligodendrocyte-derived extracellular vesicles as antigen-specific therapy for autoimmune neuroinflammation in mice. *Sci. Transl. Med.* **12** (2020).
160. P. Bankhead, *et al.*, QuPath: Open source software for digital pathology image analysis. *Sci. Rep.* **7**, 1–7 (2017).
161. L. Schirmer, P. Atallah, C. Werner, U. Freudenberg, StarPEG-Heparin Hydrogels to Protect and Sustainably Deliver IL-4. *Adv. Healthc. Mater.* **5**, 3157–3164 (2016).
162. C. Mondadori, *et al.*, Advanced Microfluidic Models of Cancer and Immune Cell Extravasation: A Systematic Review of the Literature. *Front. Bioeng. Biotechnol.* **8**, 907 (2020).
163. A. D. Greenhalgh, *et al.*, Arginase-1 is expressed exclusively by infiltrating myeloid cells in CNS injury and disease. *Brain. Behav. Immun.* **56**, 61–67 (2016).
164. V. Steimle, C. A. Siegrist, A. Mottet, B. Lisowska-Grospierre, B. Mach, Regulation of MHC class II expression by interferon-gamma mediated by the transactivator gene CIITA. *Science* **265**, 106–109 (1994).
165. H. X. Chu, *et al.*, Role of CCR2 in Inflammatory Conditions of the Central Nervous System. *J. Cereb. Blood Flow Metab.* **34**, 1425–1429 (2014).
166. S. Rivest, CX3CR1 in multiple sclerosis. *Oncotarget* **6**, 19946 (2015).
167. T. M. Rivers, D. H. Sprunt, G. P. Berry, Observations on attempts to produce acute disseminated encephalomyelitis in monkeys. *J. Exp. Med.* **58**, 39–52 (1933).
168. J. M. Fletcher, S. J. Lalor, C. M. Sweeney, N. Tubridy, K. H. G. Mills, T cells in multiple sclerosis and experimental autoimmune encephalomyelitis. *Clin. Exp. Immunol.* **162**, 1–11 (2010).
169. M. Kocur, *et al.*, IFNβ secreted by microglia mediates clearance of myelin debris in CNS autoimmunity. *Acta Neuropathol. Commun.* **3**, 20 (2015).
170. Z. Jiang, J. X. Jiang, G. X. Zhang, Macrophages: A double-edged sword in experimental autoimmune encephalomyelitis. *Immunol. Lett.* **160**, 17 (2014).
171. A. J. Jahan-Abad, *et al.*, Serum pro-inflammatory and anti-inflammatory cytokines and the pathogenesis of experimental autoimmune encephalomyelitis. *Neuropathology* **40**, 84–92 (2020).
172. J. Nam, T. K. Koppinen, M. H. Voutilainen, MANF Is Neuroprotective in Early Stages of EAE, and Elevated in Spinal White Matter by Treatment With Dexamethasone. *Front. Cell. Neurosci.* **15**, 1–13 (2021).
173. P. J. Conlon, S. Tyler, K. H. Grabstein, P. Morrissey, Interleukin-4 (B-cell stimulatory factor-1) augments the in vivo generation of cytotoxic cells in immunosuppressed animals. *Biotechnol. Ther.* **1**, 31–41.
174. B. A. Duffy, K. P. Chun, D. Ma, M. F. Lythgoe, R. C. Scott, Dexamethasone exacerbates cerebral edema and brain injury following lithium-pilocarpine induced status epilepticus. *Neurobiol. Dis.* **63**, 229–236 (2014).
175. O. C. Meijer, *et al.*, Penetration of dexamethasone into brain glucocorticoid targets is enhanced in mdr1A P-glycoprotein knockout mice. *Endocrinology* **139**, 1789–1793 (1998).

176. S. Mori, P. Maher, B. Conti, Neuroimmunology of the Interleukins 13 and 4. *Brain Sci.* **6** (2016).
177. B. A. Durafourt, *et al.*, Comparison of polarization properties of human adult microglia and blood-derived macrophages. *Glia* **60**, 717–727 (2012).
178. O. Butovsky, *et al.*, Induction and blockage of oligodendrogenesis by differently activated microglia in an animal model of multiple sclerosis. *J. Clin. Invest.* **116**, 905–915 (2006).
179. N. Schweingruber, S. D. Reichardt, F. Lühder, H. M. Reichardt, Mechanisms of glucocorticoids in the control of neuroinflammation. *J. Neuroendocrinol.* **24**, 174–182 (2012).
180. D. A. Joyce, J. H. Steer, L. J. Abraham, Glucocorticoid modulation of human monocyte/macrophage function: Control of TNF-α secretion. *Inflamm. Res.* **46**, 447–451 (1997).
181. E. Kamma, W. Lasisi, C. Libner, H. S. Ng, J. R. Plemel, Central nervous system macrophages in progressive multiple sclerosis: relationship to neurodegeneration and therapeutics. *J. Neuroinflammation* **19**, 1–27 (2022).
182. , Hooke Laboratories - EAE - MOG/CFA-Induced EAE in C57BL/6 Mice (November 29, 2022).
183. G. Locatelli, *et al.*, Mononuclear phagocytes locally specify and adapt their phenotype in a multiple sclerosis model. *Nat. Neurosci.* **21**, 1196–1208 (2018).
184. D. A. Giles, *et al.*, Myeloid cell plasticity in the evolution of central nervous system autoimmunity. *Ann. Neurol.* **83**, 131–141 (2018).
185. D. Blumenthal, *et al.*, Pre-clinical development of CAR Monocytes (CAR Mono) for solid tumor immunotherapy (2022) (December 3, 2022).
186. S. Kim, *et al.*, Monocyte enrichment from leukapheresis products by using the Elutra cell separator https:/doi.org/10.1111/j.1537-2995.2007.01470.x (December 18, 2022).
187. A. Faradji, *et al.*, Large scale isolation of human blood monocytes by continuous flow centrifugation leukapheresis and counterflow centrifugation elutriation for adoptive cellular immunotherapy in cancer patients. *J. Immunol. Methods* **174**, 297–309 (1994).
188. A. B. Peterson, L. Xu, J. Daugherty, M. J. Breiding, Surveillance report of traumatic brain injury-related emergency department visits, hospitalizations, and deaths, United States, 2014 (2019) (April 7, 2023).
189. F. Di Virgilio, A. C. Sarti, R. Coutinho-Silva, Purinergic signaling, DAMPs, and inflammation. *Am. J. Physiol. Cell Physiol.* **318**, C832–C835 (2020).
190. S. J. Hewett, N. A. Jackman, R. J. Claycomb, Interleukin-1β in Central Nervous System Injury and Repair. *Eur. J. Neurodegener. Dis.* **1**, 195–211 (2012).
191. T. T. Postolache, *et al.*, Inflammation in Traumatic Brain Injury. *J. Alzheimers. Dis.* **74**, 1–28 (2020).
192. R. Beschorner, *et al.*, CD14 expression by activated parenchymal microglia/macrophages and infiltrating monocytes following human traumatic brain injury. *Acta Neuropathol.* **103**, 541–549 (2002).
193. H. M. Bramlett, W. D. Dietrich, Long-Term Consequences of Traumatic Brain Injury: Current Status of Potential Mechanisms of Injury and Neurological Outcomes. *J. Neurotrauma* **32**, 1834 (2015).
194. M. V. Russo, L. L. Latour, D. B. McGavern, Distinct myeloid cell subsets promote meningeal remodeling and vascular repair after mild traumatic brain injury. *Nat. Immunol.* **19**, 442 (2018).

195. D. J. Loane, A. Kumar, Microglia in the TBI brain: The good, the bad, and the dysregulated. *Exp. Neurol.* **275 Pt 3**, 316–327 (2016).
196. H. Neumann, M. R. Kotter, R. J. M. Franklin, Debris clearance by microglia: an essential link between degeneration and regeneration. *Brain* **132**, 288–295 (2009).
197. W. Gong, S. Liu, P. Xu, M. Fan, M. Xue, Simultaneous Quantification of Diazepam and Dexamethasone in Plasma by High-Performance Liquid Chromatography with Tandem Mass Spectrometry and Its Application to a Pharmacokinetic Comparison between Normoxic and Hypoxic Rats. *Molecules* **20**, 6901–6912 (2015).
198. S. Missios, *et al.*, Scaled Cortical Impact in Immature Swine: Effect of Age and Gender on Lesion Volume. *J. Neurotrauma* **26**, 1943 (2009).
199. S. L. Craner, R. H. Ray, Somatosensory cortex of the neonatal pig: I. Topographic organization of the primary somatosensory cortex (SI). *J. Comp. Neurol.* **306**, 24–38 (1991).
200. A. C. Duhaime, *et al.*, Maturation-dependent response of the piglet brain to scaled cortical impact. *J. Neurosurg.* **93**, 455–462 (2000).
201. J.-J. Chiu, S. Chien, Effects of disturbed flow on vascular endothelium: pathophysiological basis and clinical perspectives. *Physiol. Rev.* **91**, 327–387 (2011).
202. M. Das, K. Mayilsamy, S. S. Mohapatra, S. Mohapatra, Mesenchymal stem cell therapy for the treatment of traumatic brain injury: progress and prospects. *Rev. Neurosci.* **30** (2019).
203. S. S. Bedi, *et al.*, Autologous bone marrow mononuclear cells therapy attenuates activated microglial/macrophage response and improves spatial learning after traumatic brain injury. *J. Trauma Acute Care Surg.* **75**, 410 (2013).
204. H. W. Caplan, *et al.*, Human cord blood-derived regulatory T-cell therapy modulates the central and peripheral immune response after traumatic brain injury. *Stem Cells Transl. Med.* **9**, 903–916 (2020).
205. H. MT, *et al.*, Cell therapies for traumatic brain injury. *Neurosurg. Focus* **24** (2008).
206. R. G. Mira, M. Lira, W. Cerpa, Traumatic Brain Injury: Mechanisms of Glial Response. *Front. Physiol.* **12**, 1748 (2021).
207. S. Heindl, *et al.*, Automated morphological analysis of microglia after stroke. *Front. Cell. Neurosci.* **12**, 106 (2018).
208. A. Joseph, *et al.*, Nanoparticle-microglial interaction in the ischemic brain is modulated by injury duration and treatment. *Bioeng. Transl. Med.* **5** (2020).
209. C. Kozlowski, R. M. Weimer, An automated method to quantify microglia morphology and application to monitor activation state longitudinally in vivo. *PLoS One* **7** (2012).
210. M. A. Mir, Developing costimulatory molecules for immunotherapy of diseases. *Dev. Costimulatory Mol. Immunother. Dis.*, 1–322 (2015).
211. S. Gyoneva, R. M. Ransohoff, Inflammatory reaction after traumatic brain injury: therapeutic potential of targeting cell-cell communication by chemokines. *Trends Pharmacol. Sci.* **36**, 471–480 (2015).
212. G. Olmos, J. Lladó, Tumor necrosis factor alpha: a link between neuroinflammation and excitotoxicity. *Mediators Inflamm.* **2014** (2014).
213. A. Abdelhak, *et al.*, Blood GFAP as an emerging biomarker in brain and spinal cord disorders. *Nat. Rev. Neurol.* **18**, 158–172 (2022).
214. T. Woodcock, M. C. Morganti-Kossmann, The role of markers of inflammation in traumatic brain injury. *Front. Neurol.* **4** (2013).

215. J. Xin Yu, V. M. Hubbard-Lucey, J. Tang, The global pipeline of cell therapies for cancer. *Nat. Rev. Drug Discov.* **18**, 821–822 (2019).
216. S. S. Neelapu, *et al.*, Axicabtagene Ciloleucel CAR T-Cell Therapy in Refractory Large B-Cell Lymphoma. *N. Engl. J. Med.* **377**, 2531–2544 (2017).
217. S. L. Maude, *et al.*, Tisagenlecleucel in Children and Young Adults with B-Cell Lymphoblastic Leukemia. *N. Engl. J. Med.* **378**, 439–448 (2018).
218. D. P. Schuster, ARDS: Clinical lessons from the oleic acid model of acute lung injury. *Am. J. Respir. Crit. Care Med.* (1994) https:/doi.org/10.1164/ajrccm.149.1.8111590.
219. S. J. Schuster, *et al.*, Chimeric Antigen Receptor T Cells in Refractory B-Cell Lymphomas. *N. Engl. J. Med.* **377**, 2545–2554 (2017).
220. N. Gagelmann, F. Ayuk, D. Atanackovic, N. Kröger, B cell maturation antigen-specific chimeric antigen receptor T cells for relapsed or refractory multiple myeloma: A meta-analysis. *Eur. J. Haematol.* **104**, 318–327 (2020).
221. A. J. Hou, L. C. Chen, Y. Y. Chen, Navigating CAR-T cells through the solid-tumour microenvironment. *Nat. Rev. Drug Discov. 2021 207* **20**, 531–550 (2021).
222. K. G. Anderson, I. M. Stromnes, P. D. Greenberg, Obstacles posed by the tumor microenvironment to T cell activity: a case for synergistic therapies. *Cancer Cell* **31**, 311 (2017).
223. Y. Zhang, X. Y. Guan, P. Jiang, Cytokine and Chemokine Signals of T-Cell Exclusion in Tumors. *Front. Immunol.* **11**, 3093 (2020).
224. A. Mantovani, P. Allavena, F. Marchesi, C. Garlanda, Macrophages as tools and targets in cancer therapy. *Nat. Rev. Drug Discov. 2022 2111* **21**, 799–820 (2022).
225. Z. Duan, Y. Luo, Targeting macrophages in cancer immunotherapy. *Signal Transduct. Target. Ther.* **6**, 1–21 (2021).
226. L. Cassetta, J. W. Pollard, Targeting macrophages: Therapeutic approaches in cancer. *Nat. Rev. Drug Discov.* **17**, 887–904 (2018).
227. S. T. Barry, D. I. Gabrilovich, O. J. Sansom, A. D. Campbell, J. P. Morton, Therapeutic targeting of tumour myeloid cells. *Nat. Rev. Cancer* **23** (2023).
228. D. M. Mosser, J. P. Edwards, Exploring the full spectrum of macrophage activation. *Nat. Rev. Immunol.* **8**, 958–69 (2008).
229. L. Cassetta, J. W. Pollard, A timeline of tumour-associated macrophage biology. *Nat. Rev. Cancer* **23** (2023).
230. C. B. Williams, E. S. Yeh, A. C. Soloff, Tumor-associated macrophages: unwitting accomplices in breast cancer malignancy. *npj Breast Cancer 2016 21* **2**, 1–12 (2016).
231. R. Andreesen, B. Hennemann, S. W. Krause, Adoptive immunotherapy of cancer using monocyte-derived macrophages: rationale, current status, and perspectives. *J. Leukoc. Biol.* **64**, 419–426 (1998).
232. S. Lee, S. Kivimäe, A. Dolor, F. C. Szoka, Macrophage-based cell therapies: The long and winding road. *J. Control. Release* **240**, 527–540 (2016).
233. M. Klichinsky, *et al.*, Human chimeric antigen receptor macrophages for cancer immunotherapy. *Nat. Biotechnol. 2020 388* **38**, 947–953 (2020).
234. O. Adebowale, J. Guerriero, S. Mitragotri, Dynamics of Macrophage Tumor Infiltration. *Submitted*.
235. C. Shi, E. G. Pamer, Monocyte recruitment during infection and inflammation. *Nat. Rev. Immunol.* **11**, 762–774 (2011).
236. L. Tang, *et al.*, Enhancing T cell therapy through TCR-signaling-responsive nanoparticle

drug delivery. *Nat. Biotechnol. 2018 368* **36**, 707–716 (2018).
237. J. P. Böttcher, C. Reis e Sousa, The Role of Type 1 Conventional Dendritic Cells in Cancer Immunity. *Trends in Cancer* **4**, 784 (2018).
238. T. F. Gajewski, K. R. Cron, CDC1 dysregulation in cancer: An opportunity for intervention. *J. Exp. Med.* **217** (2020).
239. K. Wang, T. Shen, G. P. Siegal, S. Wei, The CD4/CD8 ratio of tumor-infiltrating lymphocytes at the tumor-host interface has prognostic value in triple-negative breast cancer. *Hum. Pathol.* **69**, 110–117 (2017).
240. D. Jorgovanovic, M. Song, L. Wang, Y. Zhang, Roles of IFN-γ in tumor progression and regression: a review. *Biomark. Res. 2020 81* **8**, 1–16 (2020).
241. H. Dillekås, M. S. Rogers, O. Straume, Are 90% of deaths from cancer caused by metastases? *Cancer Med.* **8**, 5574–5576 (2019).
242. R. Deng, *et al.*, Inhibition of tumor growth and alteration of associated macrophage cell type by an HO-1 inhibitor in breast carcinoma-bearing mice. *Oncol. Res.* **20**, 473–482 (2013).
243. A. Pusuluri, *et al.*, Role of synergy and immunostimulation in design of chemotherapy combinations: An analysis of doxorubicin and camptothecin. *Bioeng. Transl. Med.* **4** (2019).
244. R. L. Siegel Mph, *et al.*, Cancer statistics, 2023. *CA. Cancer J. Clin.* **73**, 17–48 (2023).
245. A. Shimabukuro-Vornhagen, *et al.*, Cytokine release syndrome. *J. Immunother. cancer* **6** (2018).
246. D. W. Lee, *et al.*, Current concepts in the diagnosis and management of cytokine release syndrome. *Blood* **124**, 188–195 (2014).
247. T. Tanaka, M. Narazaki, T. Kishimoto, IL-6 in Inflammation, Immunity, and Disease. *Cold Spring Harb. Perspect. Biol.* **6**, 16295–16296 (2014).
248. , CAR T Cells: Engineering Immune Cells to Treat Cancer - NCI (April 3, 2023).
249. A. V. Finck, T. Blanchard, C. P. Roselle, G. Golinelli, C. H. June, Engineered cellular immunotherapies in cancer and beyond. *Nat. Med.* **28**, 678–689 (2022).
250. C. H. June, *et al.*, Engineered T cells for cancer therapy. *Cancer Immunol. Immunother.* **63**, 969–975 (2014).
251. B. Santomasso, C. Bachier, J. Westin, K. Rezvani, E. J. Shpall, The Other Side of CAR T-Cell Therapy: Cytokine Release Syndrome, Neurologic Toxicity, and Financial Burden. *Am. Soc. Clin. Oncol. Educ. book. Am. Soc. Clin. Oncol. Annu. Meet.* **39**, 433–444 (2019).
252. M. Abou-El-Enein, *et al.*, Scalable Manufacturing of CAR T cells for Cancer Immunotherapy. *Blood cancer Discov.* **2**, 408–422 (2021).
253. Y. Zheng, L. Tang, L. Mabardi, S. Kumari, D. J. Irvine, Enhancing Adoptive Cell Therapy of Cancer through Targeted Delivery of Small-Molecule Immunomodulators to Internalizing or Noninternalizing Receptors. *ACS Nano* **11**, 3089–3100 (2017).
254. A. J. Kwiatkowski, *et al.*, Treatment with an antigen-specific dual microparticle system reverses advanced multiple sclerosis in mice. *Proc. Natl. Acad. Sci. U. S. A.* **119**, 1–11 (2022).
255. N. Pishesha, *et al.*, Induction of antigen-specific tolerance by nanobody–antigen adducts that target class-II major histocompatibility complexes. *Nat. Biomed. Eng.* **5**, 1389–1401 (2021).

9. Appendix

9.1. Appendix A: Text

9.1.1. Dexamethasone Quantification

Dexamethasone concentrations were measured by HPLC-MS, using a similar method as previously reported (197). Briefly, dexamethasone standards and samples were dissolved in acetonitrile. Using an HPLC (Agilent 1290 Infinity II) with a single quadrupole mass analyzer detector (Agilent MSD XT), 5 uL of standard or sample was injected onto a 2.1 x 50 mm C18 column (Agilent Poroshell 120) using an isocratic 60:40 0.1% formic acid:acetonitrile containing 0.1% formic acid. Dexamethasone was detected at 393.3 Da in positive ion mode at a capillary voltage of 4000V. Drying gas was 300°C at 10 L/min, sheath gas was 250°C at 7 L/min, and a nebulizer pressure of 45 psig was used. Dexamethasone eluted at 1.6 min and was linearly detected between 0.25 – 1000 ng/mL.

9.1.2. Atomic Force Microscopy (AFM)

Backpacks (BPs) were adhered to glass slides, mounted on the AFM (JPK Nanowizard, Bruker) and imaged in Qi (single point contact) mode using All-In-One-Al cantilever D with a stiffness of ~40Nm^{-1}. 10µm X 10µm regions were scanned for quantifying BP topography, followed by a 2µm X 2µm scan on BP surface for probing stiffness. Topography and stiffness were recovered using JPK DP data processing software; stiffness was obtained by fitting corrected deflection curves to a Hertz model assuming a pyramid tip.

9.1.3. F(ab') Digestion

Anti-mouse CD45 antibody (Biolegend) was digested with pepsin using the Pierce™ F(ab')2 Preparation Kit (ThermoFisher) following the vendor's instructions to yield F(ab')2 fragments. The F(ab')2 fragments were purified by preparing an AminoLink™ Plus Immobilization Column (ThermoFisher) with Goat anti-Rat IgG Fc Secondary Antibody (ThermoFisher) coupled to the column following the vendor's instructions. The solution of F(ab')2 was incubated with the functionalized column for 30 minutes to allow Fc debris to bind to the column. The F(ab')2 solution was subsequently washed through the column and concentrated using Amicon Ultra-4 30 kDa Centrifugal Filters (MilliporeSigma) to a concentration of 0.5-2mg/mL. The purified CD45 F(ab')2 was reduced with an equal volume of 1.8mM DTT solution for 20 minutes and washed 4 times sequentially with Zeba desalting columns to yield CD45 F(ab') fragments with free thiol groups, as described previously (253).

9.1.4. EAE Induction

EAE was induced in female C57BL/6 mice (9-14 weeks) using the EK-2110 kit (Hooke Laboratories). Emulsion containing myelin oligodendrocyte glycoprotein 35-55 (MOG_{35-55}) and Complete Freund's Adjuvant was injected subcutaneously, 0.1mL/site on the upper and lower back for a total of 0.2mL/mouse. 2 and 24 hours after, a solution of pertussis toxin was prepared (1.1µg/mL) and injected intraperitoneally (0.1mL/dose, 1 dose per mouse).

9.1.5. EAE Scoring Rubric

7 days after EAE induction, mice were weighed and scored daily according to the following established rubric (157, 254, 255): 0- no obvious changes in motor function. 0.5- tip of tail is limp. 1.0- entire tail is limp; when picked up by base of tail, the whole tail drapes over finger from the

base. 1.5- when picked up by base of tail, whole tail drapes over finger and when the mouse is dropped on a wire rack, at least one hind leg falls through consistently. 2.0- the animal has both a limp tail and weakness of one or both the hind limbs. When picked up by base of tail, the legs are now clasped and held close together. 2.5- Limp tail and dragging of both hind legs and/or complete paralysis of 1 hind limb at the hip; both hind legs still have some movement, but both feet flip during ambulation resulting in the tops of feet dragging. 3.0- Mouse has a limp tail and complete paralysis of both hind legs; animal can still right itself from lateral recumbence. 3.5- Limp tail, complete paralysis of hind legs, and when placed on its side, animal is unable to right itself from lateral recumbence. 4.0- Limp tail, complete hind leg paralysis, and partial front leg paralysis; animal is still alert and feeding when gel is placed nearby. 4.5- Complete hind and partial front leg paralysis, no movement around the cage; mouse is not alert. 5.0- moribund or death.

9.2. Appendix B: Tables

Appendix Table 9.1. Resolution limits, advantages, and limitations of non-spherical particle characterization methods.

Literature frequency values are presented as a percentage of all (156) identified studies.

Method	Measurement	Frequency in Literature	Key Advantages and Resolution	Limitations	Throughput
Microscopy					
Scanning Electron Microscopy	Size and morphology	100 Studies (64%)	5 nm resolution, <1 nm with specialized instrument. Large field of view.	Sample preparation, including drying and coating. Cryogenic conditions needed for biological samples and gels	Low
Transmission Electron Microscopy	Size and morphology	49 Studies (31%)	0.2 nm resolution, and as low as 0.5 A with specialized instrument. Large field of view and detailed structural information.	Sample preparation and staining, which can lead to artifacts. Cryogenic conditions needed for biological samples and gels	Very Low
Fluorescence Microscopy	Size, morphology, cell interaction	15 Studies (10%)	150 nm resolution.	Fluorescent labeling of samples.	Moderate
Confocal Microscopy	Size, morphology, cell interaction	18 Studies (12%)	150 nm (lateral), 500 nm (axial) resolution.	Fluorescent labeling of samples.	Low
Phase Contrast / Optical Microscopy	Size, morphology, cell interaction	18 Studies (12%)	400 nm resolution.	Extent of sample / specimen contrast	Moderate
Atomic Force Microscopy	Size, morphology, elastic modulus, molecular interactions	15 Studies (10%)	1 nm (lateral), 0.1 nm (axial). Does not require vacuum or extensive sample prep.	Smaller field of view, higher noise, and slower than other methods.	Very Low
Optical Surface Profilometry	Size, morphology, surface roughness	2 Studies (1%)	500 nm (lateral), 0.1 nm (axial)	Greater speed and field of view than AFM, with a resolution tradeoff.	Low
Particle Sizing					
Dynamic Light Scattering	Diameter	55 Studies (35%)	1 nm to 1 µm	Relies on an assumption of uniform, spherical particles	High
Static Light Scattering	Diameter, Structural information such as shape and degree of branching for small particles.	4 Studies (3%)	100 nm – 10 µm	Sensitive to sample impurities. Best used in combination with a separation technique (chromatography, ultracentrifugation, AF4 etc.)	High
Light Obscuration	Diameter	3 Studies (2%)	1 – 100 µm. Advantageous for monitoring and measurement of particles under flow conditions	Tends to overestimate the diameter of non-spherical particles due to alignment under flow.	Moderate
Other Particle Characterization Methods					
Zeta Potential / Electrophoretic Mobility	Electrical potential of the particle – media interface	29 Studies (19%)	Relative extent of repulsion / stability for colloids and particles	Highly sensitive to the surrounding media (pH, presence of ions, etc.). Often extrapolated as a measure of particle surface chemistry.	Moderate
Ellipsometry	Thin film thickness	1 Study (<1%)	Generally less than 50 nm	Limited usefulness for particle suspensions.	Moderate
Small Angle Neutron Scattering	Polymer chain, crystal, and pore structures. Particle sizing	1 Study (<1%)	1 nm to 1 µm	Larger sample volume and acquisition time than SAXS. Expensive instrument, typically present only in specialized facilities.	Low
Small Angle X-Ray Scattering	Polymer chain, crystal, and pore structures. Particle sizing	3 Studies (2%)	1 nm to 1µm	Lower contrast between components of organic composites, as compared to SANS. Radiation damage to sample.	High
BET / Nitrogen Adsorption	Surface area and pore size	4 Studies (3%)	Pore size from 2-100 nm.	Large mass (gram scale) of dried sample is required	Low
Rheology / DMA	Elastic and Shear Modulus	2 Studies (1%)	Monitoring mechanical changes to particle suspensions in response to a stimulus.	Large sample volume and concentration often required.	Low

Appendix Table 9.2. Macrophage and backpack counts for treated TBI pigs

Pig Number	469	471	475	479	486	487	491	497	508	521	524
Injected Macrophages (million)	114.5	126	157.5	110	132	128.5	84	174.5	51.87	208.5	262
% BP+ Macrophages	ND	17.5	15	25	10	20	13	12	25	20	20

ND: not determined

Appendix Table 9.3. The rate of adverse events was not different for saline and treated piglets.

Apnea, unscheduled deaths, and neck swelling were not different between treatment groups. There was one case of infection at the neck incision site in a piglet receiving saline. The most serious concern was apnea at the time of backpack-macrophage or saline administration, which was assumed to be an anesthetic effect as it occurred in both groups. Apnea occurred in a subset of piglets when re-anesthetized 4 h after injury (3 h after recovery from surgical anesthesia). One piglet (saline) was successfully resuscitated, and one was unable to be resuscitated (treated). In the case where the piglet was unable to be resuscitated, the duration of apnea was unknown as staff failed to use a pulse oximeter during anesthesia and recovery. To avoid this complication, we initiated administration of backpack-macrophages or saline via catheter in awake piglets with staff present who were able to resuscitate piglets. One awake piglet collapsed and was apneic when backpack-macrophages and buprenorphine were administered at the same time. Ventilation was achieved by positioning the epiglottis up and exposing the larynx with a laryngoscope followed by administration of 100% oxygen. The piglet eventually recovered without further incident. Collapse was not observed in piglets receiving saline and buprenorphine awake and the final piglet received backpack-macrophages awake without incident. The collapsing incident is thought to be due to a vasovagal syncope. Young piglets are sensitive to both anesthetics and restraint, and perhaps, restraint with an intramuscular injection 4 h after general anesthesia was enough to induce a transient loss of blood pressure and consciousness.

Complication	Saline	Treated	P value
Apnea at macrophage administration with or without unscheduled death	492	514 (unscheduled death), 521	$p = 0.53$, $X^2 = .386$
Swollen neck at incision sites/ catheter placement	498 (infection), 525	469, 524	Not different

Appendix Table 9.4. Organ toxicology was not different between treatment groups. (n = 4 treated, n = 5 saline).

Organ	Pathological Findings via H&E	Saline Count	Treated Count
Kidney	No specific abnormalities	2	2
	Rare sclerotic glomeruli	1	2
	Focal vacuolization renal tubular epithelium Rare necrotic amorphous debris within tubules	1	3
Liver	No specific abnormalities	0	0
	Rare perivenular eosinophils Very occasional neutrophils within sinusoids Mild increase in neutrophils within sinusoids	5	6
Lung	No specific abnormalities	1	1
	Rare intra-alveolar eosinophils Rare intra-alveolar and interstitial neutrophils and eosinophils Focal peribronchiolar small lymphocytes	2	3
	Patchy intra-alveolar necrosis with reactive pneumocytes	1	2
Spleen	No specific abnormalities	5	6
	Sum of no specific abnormalities	7	9
	Sum of mild findings	3	11
	Sum of medium to significant findings	2	5

Appendix Table 9.5. Piglet exclusions for lesion analyses.

Total Piglets During the Period (N = 24)
Exclusions (N = 5)
Events that prevented the piglet from completing the study: • n = 1: Staff availability was limited due to pervasive COVID infections followed by a formalin spill and delayed response from our institution prevented perfusion of a piglet (488, vehicle). • n = 1: Piglet (514, backpack-macrophage) was apneic during second anesthesia, ~3h after recovery from anesthesia for the surgery for the administration of saline and was unable to be resuscitated. At necropsy, the piglet had pre-existing, condition where extensive abdominal fluid (40 mL) and pericardial fluid was present that was negative for bacterial culture.
Problems with backpack-macrophages injected (post-hoc decisions) • n = 2: piglets (475, 486) received backpack-macrophages where the culture media of the cells was indicated to be acidic indicating that cells were overcrowded, and growth and health was limited. One of these piglets (475) had a larger lesion than most backpack-macrophages, 486 had a typical lesion size, but was treated the same for this criterion. • n = 1: piglet (508) received backpack-macrophages that were 1 standard deviation from mean backpack-macrophage number (mean: 140.5 million, SD: 58; mean – 1 SD = 82.6; piglet received 51.87 million backpack-macrophages). There tended to be an inverse correlation between lesion volume and the number of backpack-macrophages injected.
Total Included in the Study: n = 19 Vehicle piglets: n = 11 Macrophage-backpack piglets: n = 8

9.3. Appendix C: Figures

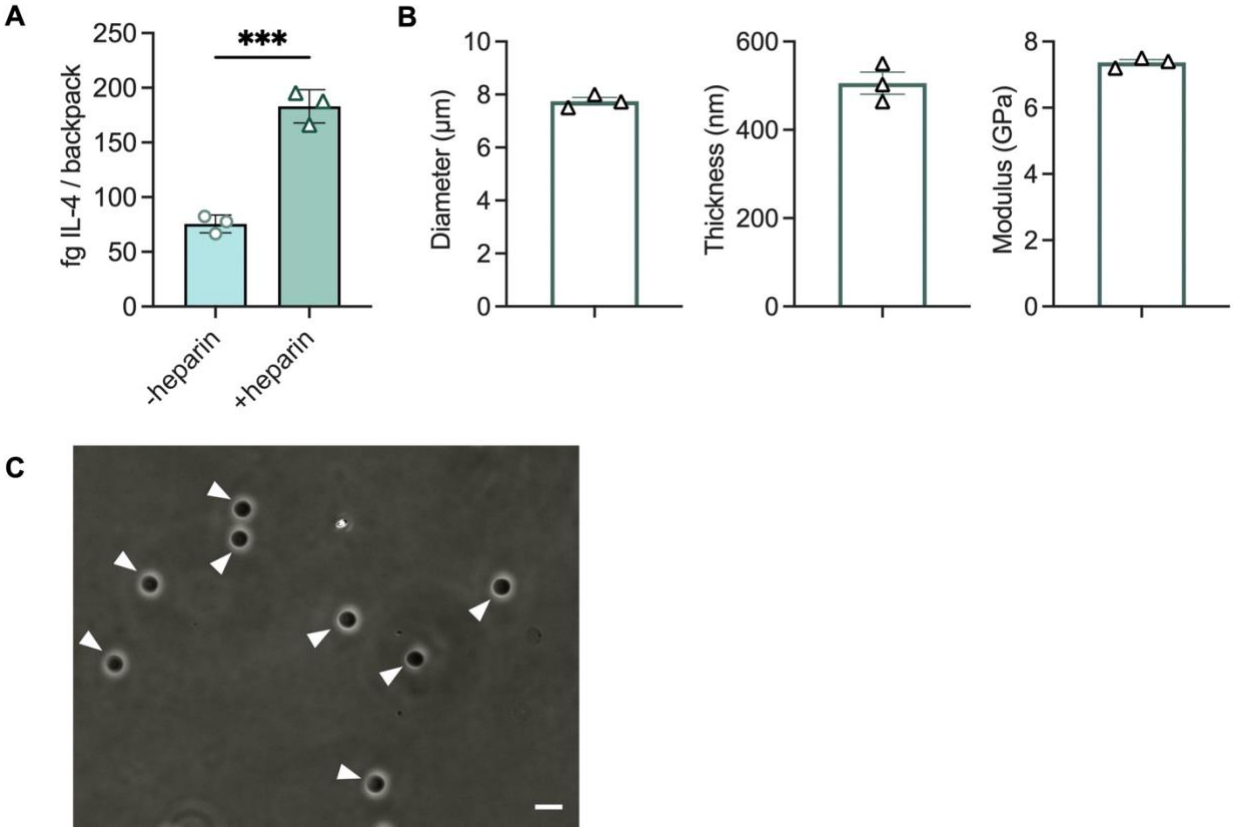

Appendix Figure 9-1. Material properties of IL-4/Dexamethasone backpacks.
A) Loading of IL-4 in backpacks with (+) and without (-) heparin was quantified by analyzing cumulative IL-4 release from backpacks over 14 days via ELISA; mean ± SD (n=3). B) Backpacks were characterized via atomic force microscopy (AFM). Backpack diameter; mean ± SD (n=3); backpack thickness; mean ± SD (n=3); Young's modulus; mean ± SD (n=3). C) Representative brightfield microscope image of resuspended backpacks in aqueous solution after 24 hours. Scale bar represents 10 µm.

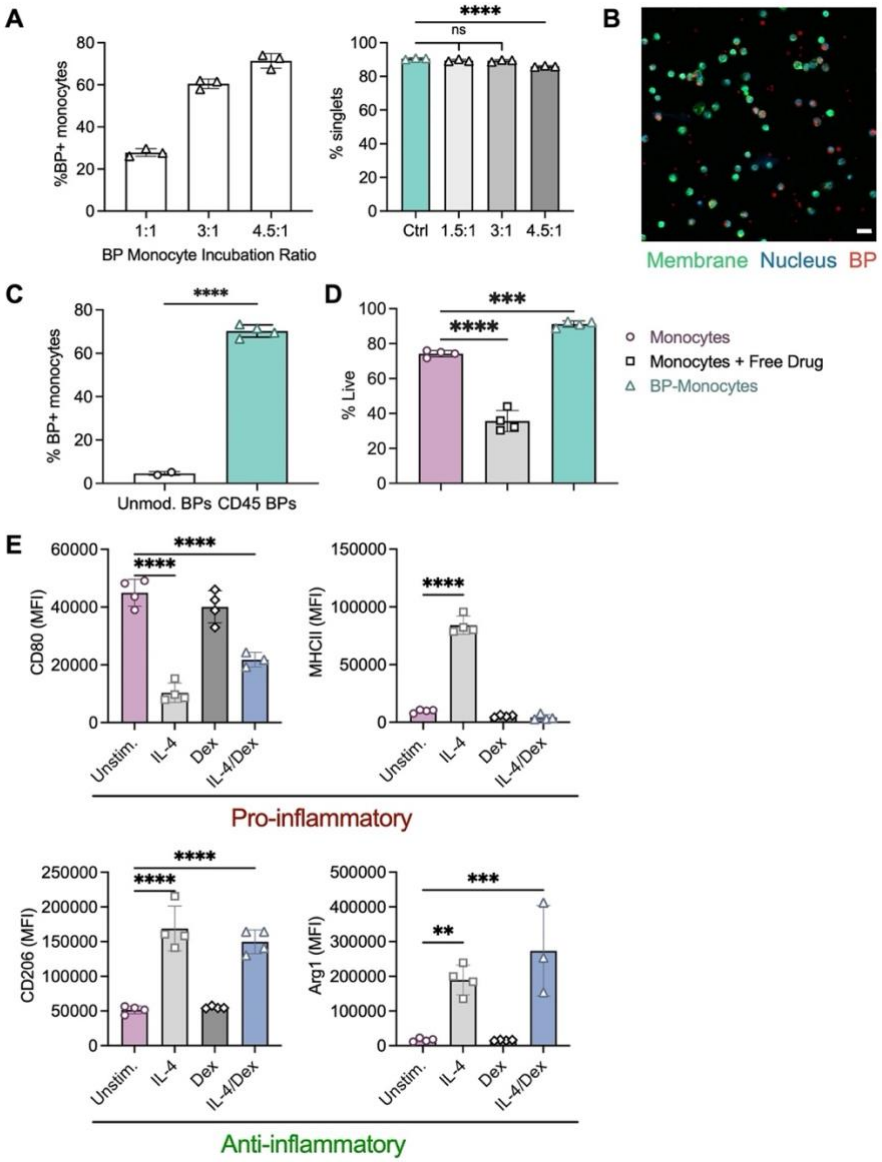

Appendix Figure 9-2. IL-4/Dexamethasone Backpack-monocyte design validation.
A) CD45-functionalized backpacks were adhered to primary bone marrow murine monocytes. Left, percentage of monocytes with >1 backpack as a function of backpack:monocyte incubation ratio (assessed by flow cytometry); mean ± SD (n=3) Right, percent of singlets of all cells for monocytes alone (Ctrl.) or backpack-monocytes at increasing BP:Monocyte incubation ratios; mean ± SD (n=3) . B) Confocal micrograph of monocyte (membrane: green, nucleus: blue) with backpack (red). Scale bar represents 20µm. Data in A analyzed by two-tailed student's t test; **P<0.01. C) Backpacks (BPs) were adhered to human blood-derived monocytes. Percentage of monocytes with >1 backpack (unmodified BP or CD45-modified BP), as determined by flow cytometry; mean ± SD (n=2-4). d) Monocytes, monocytes with free IL-4/dexamethasone (20ng/mL IL-4, 1 µg/mL dexamethasone), or backpack-laden monocytes (BP-Mo.) were cultured for 72 hours and analyzed for viability via flow cytometry; mean ± SD (n=4). E) Monocytes were plated for differentiation into macrophages with unstimulated media or media supplemented with IL-4 (10ng/mL), dexamethasone (Dex, 50ng/mL), or a combination of the two. After 48 hours,

cells were harvested and analyzed for expression of pro-inflammatory (MHCII, CD80) and anti-inflammatory (CD206, Arg1) markers by flow cytometry; mean ± SD (n=4). Data in A were analyzed by two-tailed student's t test; ns, not significant, ****P<0.0001. Data in B, C analyzed by one-way ANOVA with Tukey's HSD test. **p<0.01, ***p<0.001, ****p<0.0001.

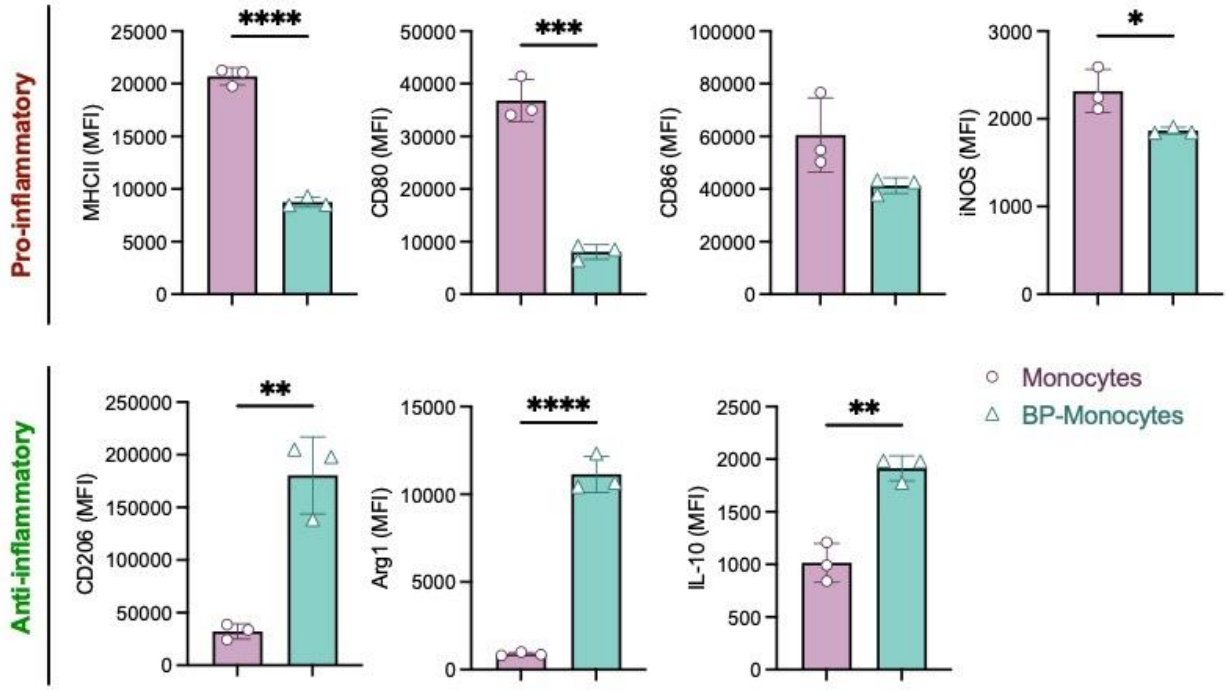

Appendix Figure 9-3. Backpacks polarize monocytes in unstimulated media over 48h.
Monocytes or backpack-laden monocytes were cultured and analyzed for expression of pro-inflammatory (MHCII, CD80, CD86, and iNOS) and anti-inflammatory (CD206, Arg1, IL-10) markers via flow cytometry; mean ± SD (n=3). Data were analyzed by two-tailed student's t test; *P<0.05, **P<0.01, ***P<0.001, ****P<0.0001.

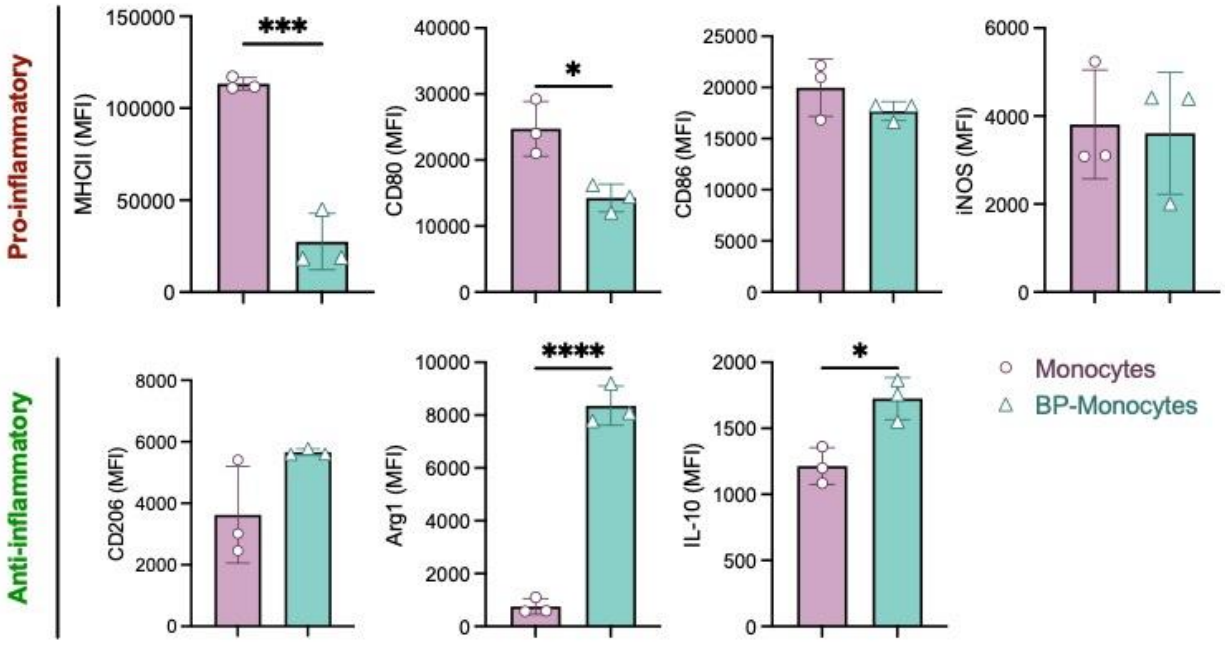

Appendix Figure 9-4. Backpacks polarize monocytes in pro-inflammatory media over 48h. Monocytes or backpack-laden monocytes were cultured in media supplemented with 1 ng/mL of IFNγ and analyzed for expression of pro-inflammatory (MHCII, CD80, CD86, and iNOS) and anti-inflammatory (CD206, Arg1, IL-10) markers; mean ± SD (n=3). Data were analyzed by two-tailed student's t test; *P<0.05, **P<0.01, ***P<0.001, ****P<0.0001.

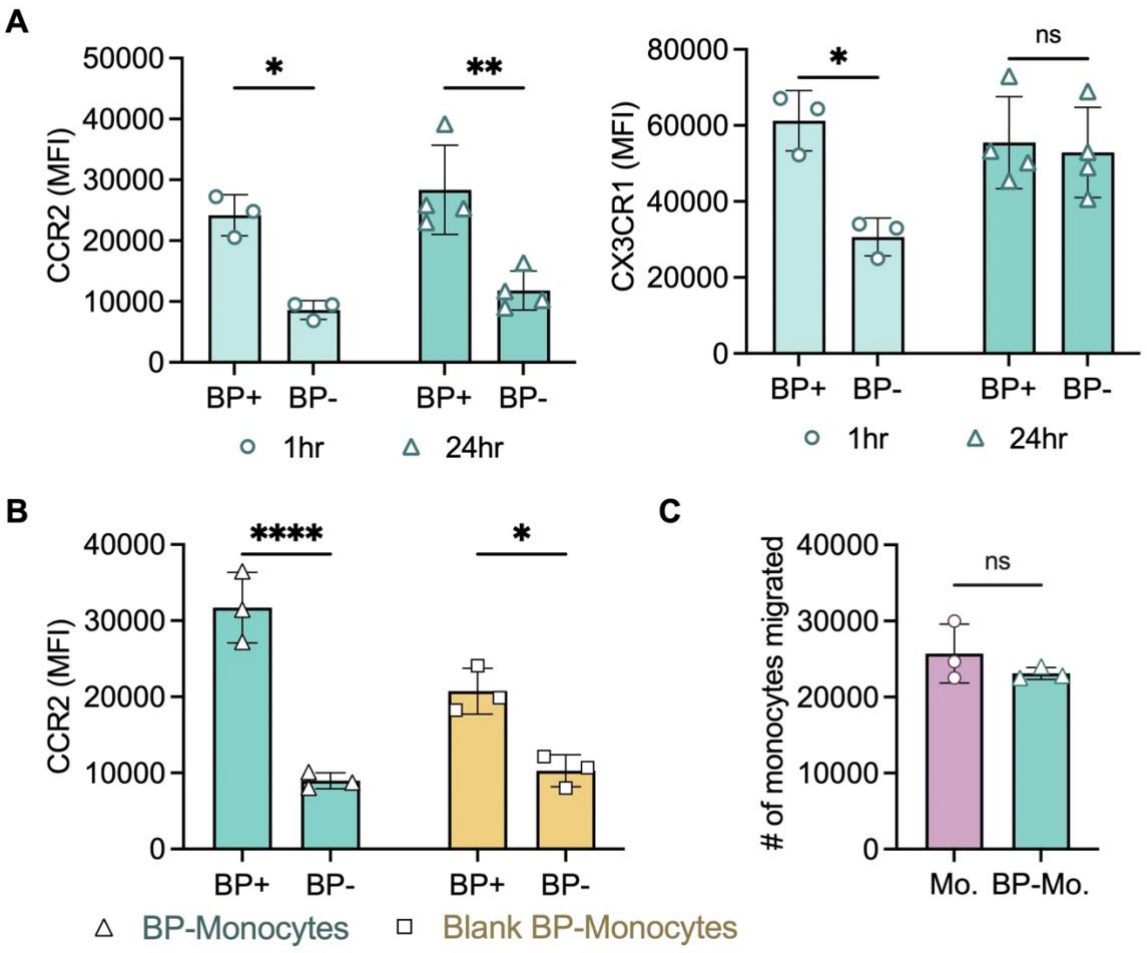

Appendix Figure 9-5. Characterization of backpack design for promoting monocyte migration.

A) Chemokine receptor expression (CCR2, CX3CR1) of the backpack+ and backpack- subpopulations of backpack monocytes at 1 and 24 hr, quantified by flow cytometry; mean ± SD (n=3-4). B) Chemokine receptor expression (CCR2) of the backpack+ and backpack- subpopulations of backpack-monocytes (monocytes with drug-loaded backpacks) and monocytes with unloaded backpacks at 24 hours; mean ± SD (n=3). C) Migration of backpacks adhered to primary human monocytes was assessed using a Transwell assay, with endothelial cells seeded on 5µm inserts, and media containing 10ng/mL CCL2 added to the lower chamber. 200k monocytes or backpack-monocytes were added into the upper chamber. The number of monocytes or backpack-monocytes in the lower chamber after 24 hours was counted; mean ± SD (n=3). Data in A, B, were analyzed by two-tailed student's t test; ns, not significant, *P<0.05, **P<0.01, ***P<0.001, ****P<0.0001. Data in C analyzed by two-tailed student's t test; ns, not significant.

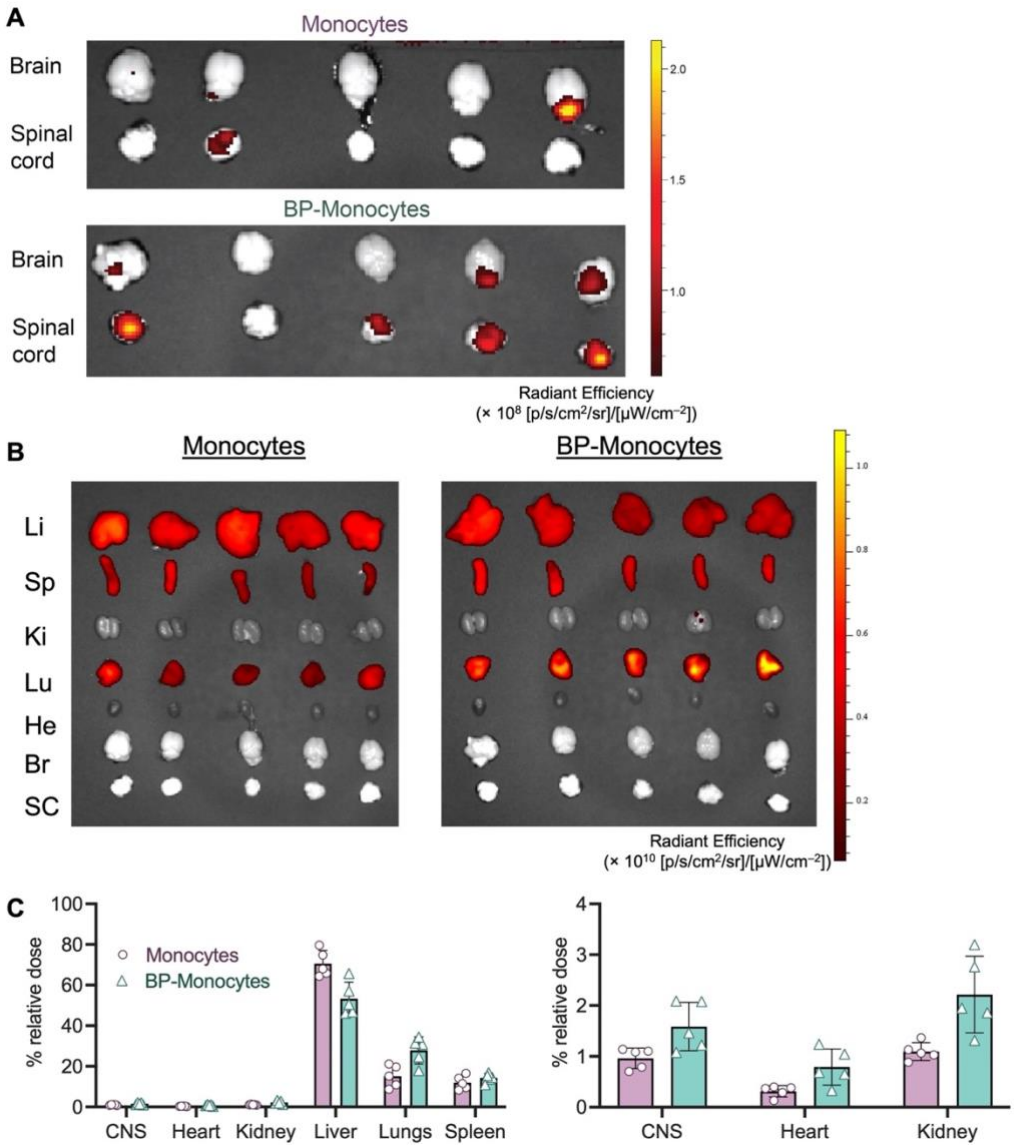

Appendix Figure 9-6. Biodistribution characterization of monocytes and monocyte backpacks 24hours after administration.

EAE was induced in female C57BL/6J mice. Mice were administered $3x10^6$ monocytes or backpack-laden monocytes (BP-monocytes) intravenously via tail vein on day 11, at the onset of clinical signs, and sacrificed 24 hours after. Monocytes were labeled with DiR 750 prior to injection. A) *In vivo* imaging system (IVIS) imaging of fluorescence signal (DiR 750) from adoptively transferred cells in CNS (brain and spinal cord). B) IVIS imaging of fluorescence signal (DiR 750) from adoptively transferred cells in organs (Liver, Li; Spleen, Sp; Kidney, Ki; Lungs, Lu; Heart, He; Brain, Br; Spinal cord, SC). C) Fluorescence quantification of relative accumulated dose for monocytes and backpack-monocytes; mean ± SD (n=5).

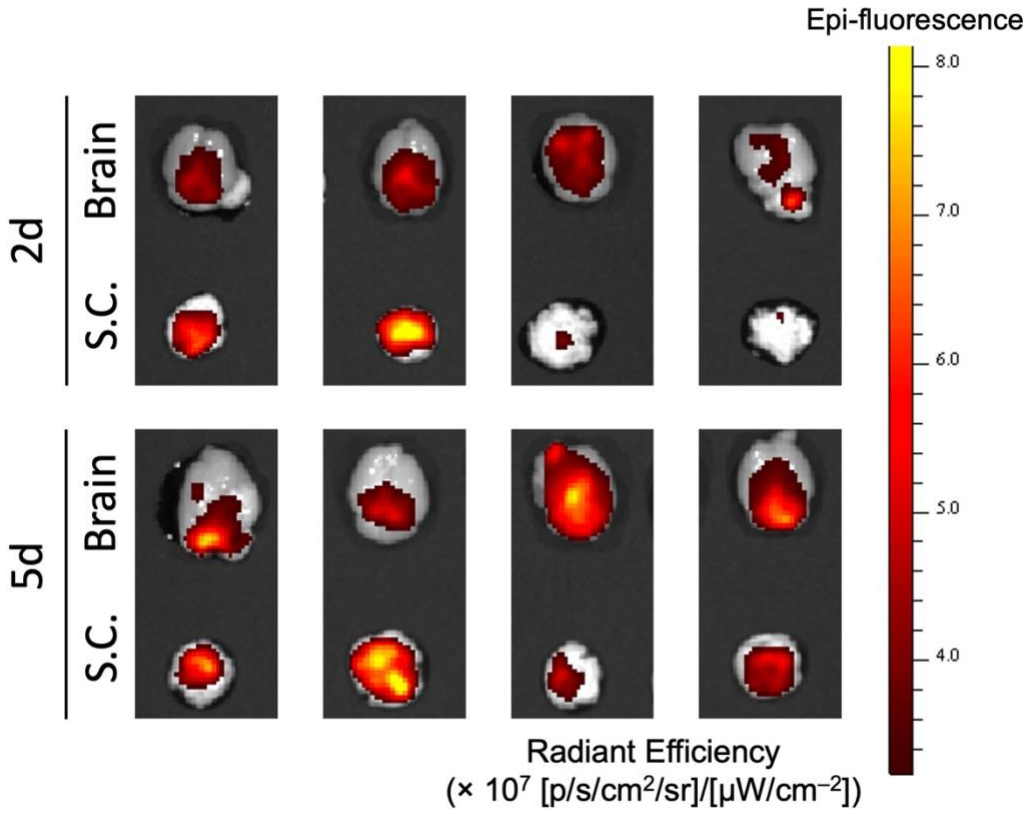

Appendix Figure 9-7. Backpack-monocytes persist in the CNS of EAE for up to 5 days. EAE was induced in female C57BL/6J mice. Mice were treated with monocytes or backpack-monocytes at the onset of clinical signs on Day 11 (i.v., tail vein), with the adoptively transferred monocytes stained with DiR 750. The mice were sacrificed after 2 days or 5 days, and the CNS was harvested. *In vivo* system imaging (IVIS) of brain and spinal cord displaying DiR 750 signal.

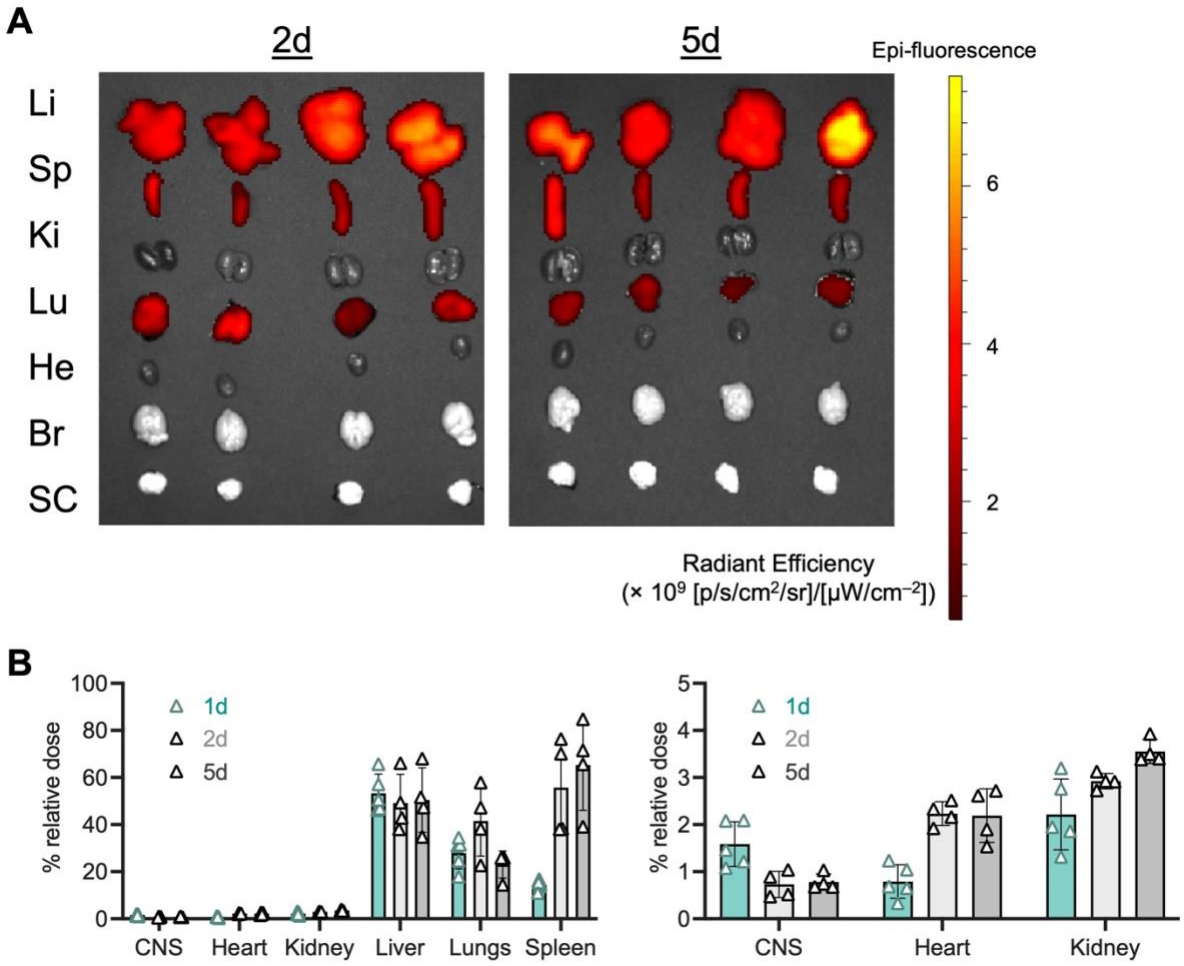

Appendix Figure 9-8. Biodistribution characterization of monocytes and monocyte backpacks two and five days after administration.
EAE was induced in female C57BL/6J mice. Mice were treated with monocytes or backpack-monocytes at the onset of clinical signs on Day 11 (i.v., tail vein), with the adoptively transferred monocytes stained with DiR 750. The mice were sacrificed after 2 days or 5 days, and the CNS was harvested. A) IVIS imaging of fluorescence signal (DiR 750) from adoptively transferred cells in organs (Liver, Li; Spleen, Sp; Kidney, Ki; Lungs, Lu; Heart, He; Brain, Br; Spinal cord, SC). B) Fluorescence quantification of relative accumulated dose for monocytes and backpack-monocytes; mean ± SD (n=4-5).

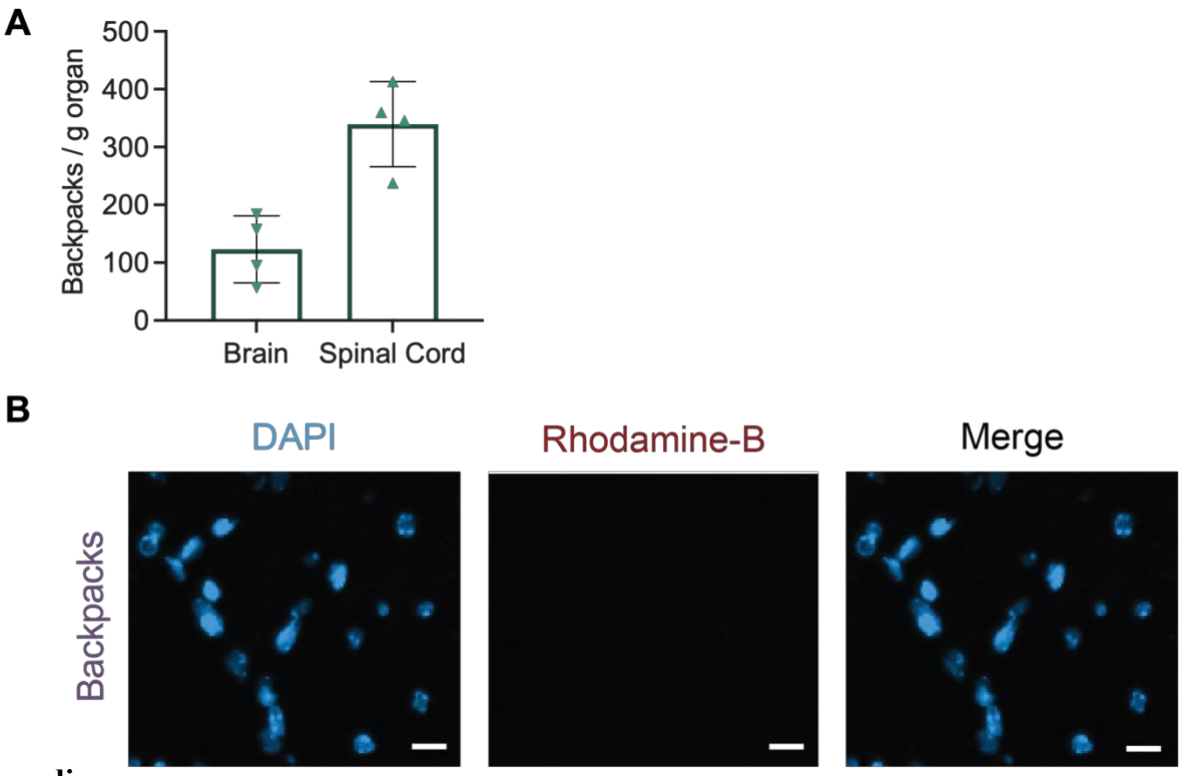

Appendix

Figure 9-9. Free backpacks do not substantially accumulate in the CNS of EAE mice.
EAE was induced in female C57BL/6J mice. EAE mice were administered $3x10^6$ free backpacks intravenously via tail vein on day 11, at the onset of clinical signs. Mice were sacrificed 24 hours after for CNS harvest. A) After single cell suspension processing of the brain and spinal cord, infiltrating backpacks per mass organ was quantified via flow cytometry; mean ± SD (n=4). B) Fluorescence imaging of lumbar spinal cord stained for DAPI (nucleus, blue) and Rhodamine-B (backpacks, red). Scale bar represents 10µm.

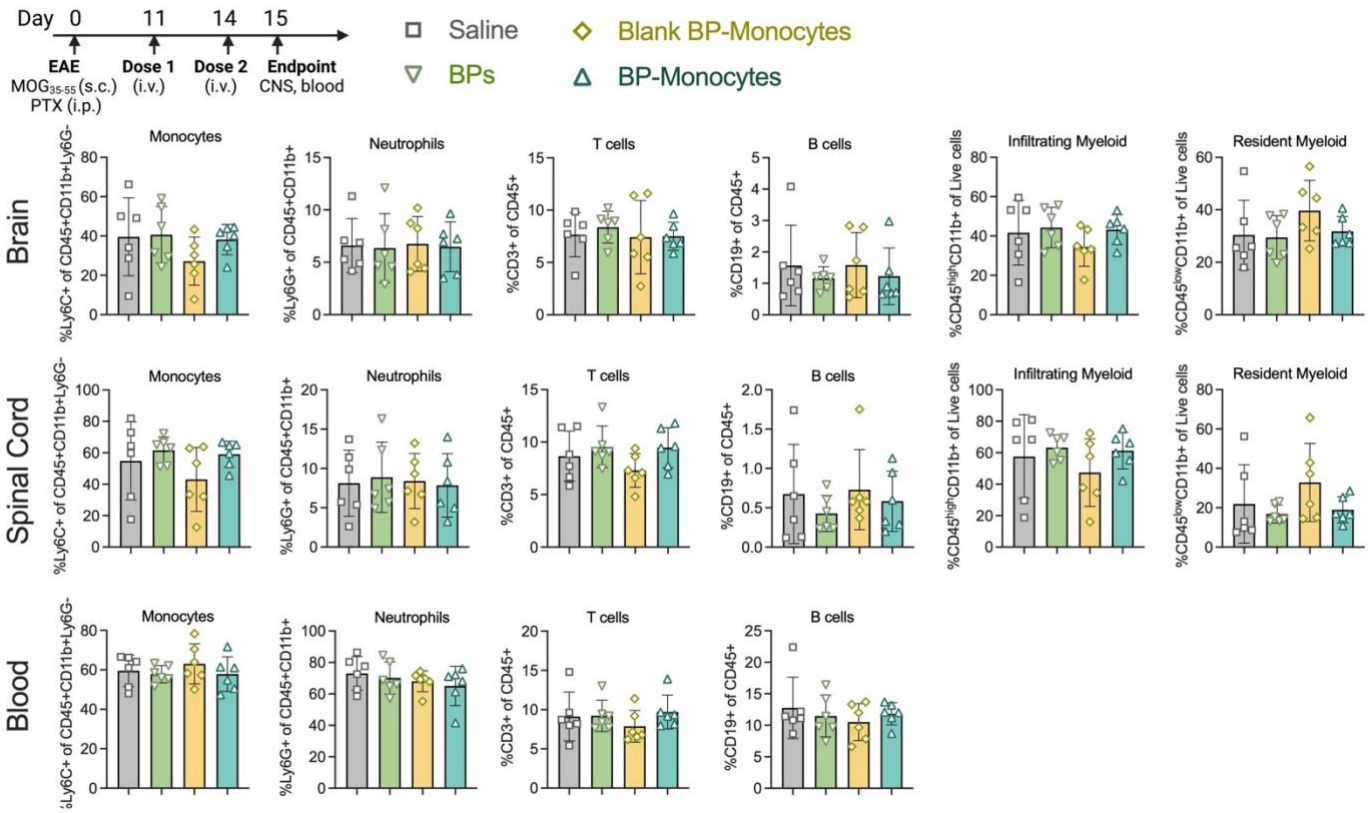

Appendix Figure 9-10. General immune cell abundances in CNS and blood at Day 15.
EAE was induced in female C57BL/6J mice. Mice were administered $3x10^6$ backpacks (BPs), blank backpack-carrying monocytes, BP-monocytes, or saline intravenously via tail vein on days 11 and 14 and sacrificed on day 15. The CNS and blood were harvested, processed into single cell suspensions, and analyzed via flow cytometry for immune cell populations. Percentages of monocytes (%$Ly6C^+$ of $Ly6G^-CD11b^+CD45^+$), neutrophils (%$Ly6G^+$ of $CD11b^+CD45^+$), T cells (% $CD3^+$ of $CD45^+$), B cells (%$CD19^+$ of $CD45^+$), infiltrating myeloid cells ($CD45^{high}CD11b^+$ of live cells), resident myeloid cells ($CD45^{low}CD11b^+$ of live cells); mean ± SD (n=6). Statistical analysis: one-way ANOVA with Tukey's HSD test.

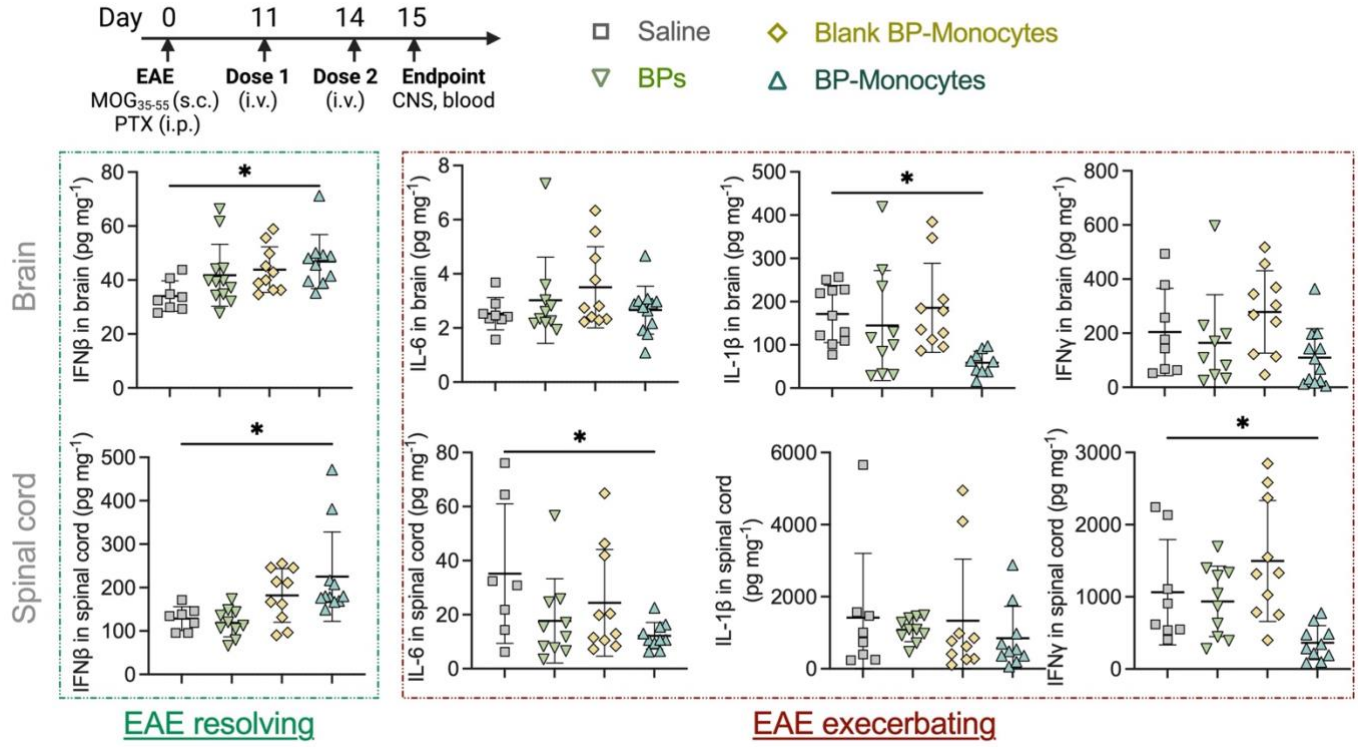

Appendix Figure 9-11. Cytokine content in brain and spinal cord at Day 15.
EAE was induced in female C57BL/6J mice. Mice were administered $3x10^6$ backpacks (BPs), blank backpack-carrying monocytes, BP-monocytes, or saline intravenously via tail vein on days 11 and 14 and sacrificed on day 15. The CNS was harvested the tissue homogenate was analyzed for concentrations of anti-/pro-inflammatory mediators at day 15; mean ± SD (n=7-10). Statistical analysis: one-way ANOVA with Tukey's HSD test; ns, not significant, *P<0.05.

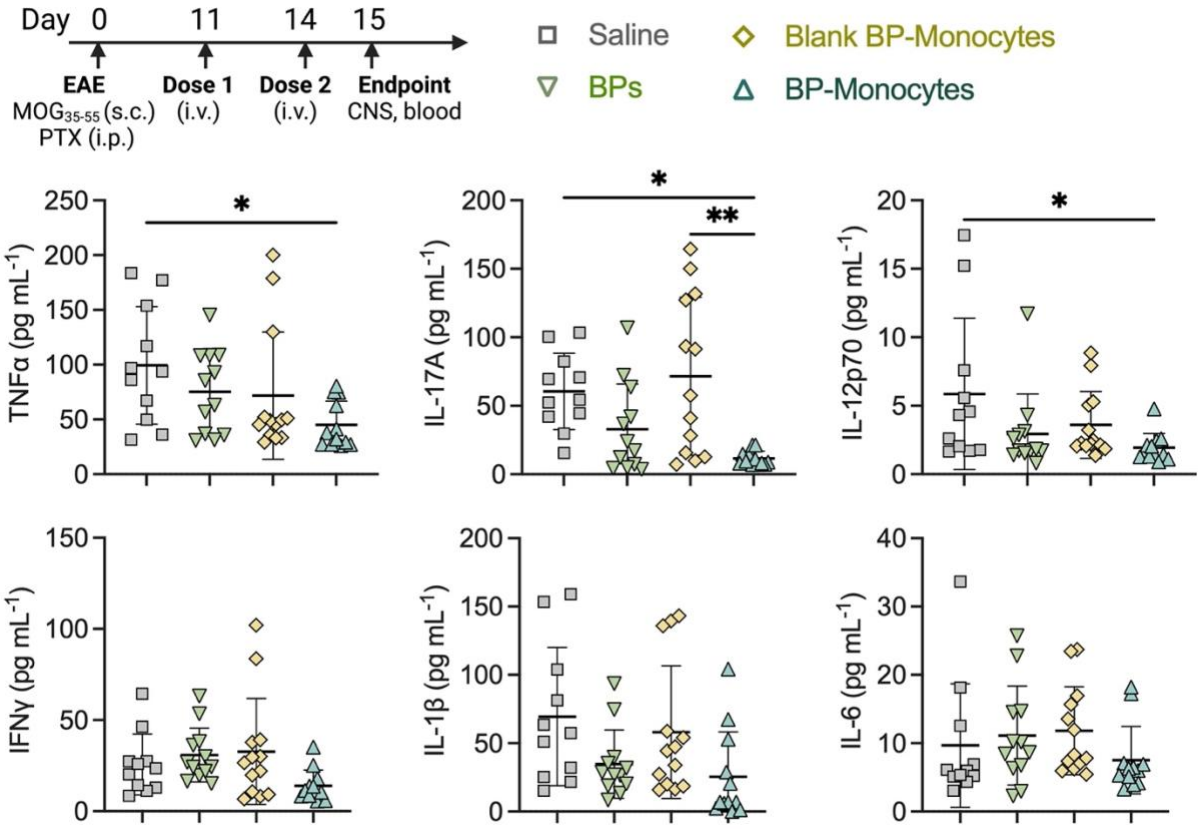

Appendix Figure 9-12. Serum cytokine content at Day 15.
EAE was induced in female C57BL/6J mice. Mice were administered $3x10^6$ backpacks (BPs), blank backpack-carrying monocytes, BP-monocytes, or saline intravenously via tail vein on days 11 and 14 and sacrificed on day 15. Blood was drawn, processed into serum, and analyzed for concentrations of pro-inflammatory mediators at day 15; mean ± SD (n=10-13). Statistical analysis: one-way ANOVA with Tukey's HSD test; ns, not significant, *P<0.05.

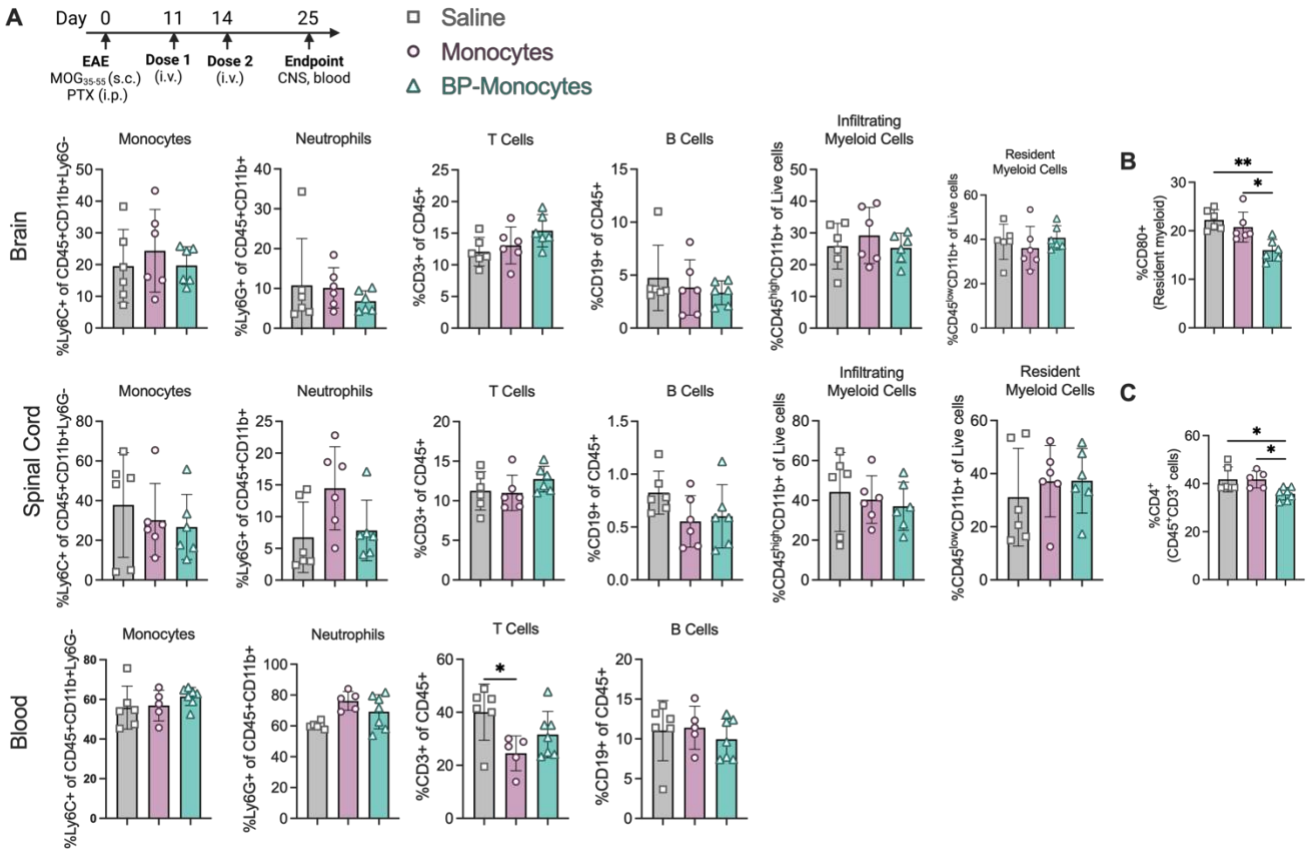

Appendix Figure 9-13. General immune cell abundances in CNS and blood at Day 25.
EAE was induced in female C57BL/6J mice. Mice were administered $3x10^6$ monocytes, backpack (BP)-carrying monocytes or saline intravenously via tail vein on days 11 and 14 and sacrificed on day 25. The CNS and blood were harvested, processed into single cell suspensions, and analyzed via flow cytometry for immune cell profile. A) Percentages of monocytes (%$Ly6C^+$ of $Ly6G^-$ $CD11b^+CD45^+$), neutrophils (%$Ly6G^+$ of $CD11b^+CD45^+$), T cells (% $CD3^+$ of $CD45^+$), B cells (%$CD19^+$ of $CD45^+$), infiltrating myeloid cells ($CD45^{high}CD11b^+$ of live cells), resident myeloid cells ($CD45^{low}CD11b^+$ of live cells); mean ± SD (n=5-7). B) %$CD80^+$ of resident myeloid cells of the brain ($CD45^{low}CD11b^+$); mean ± SD (n=6). C)%$CD4^+$ T cells (of $CD3^+CD45^+$ T cells) of the blood; mean ± SD (n=6). Statistical analysis: one-way ANOVA with Tukey's HSD test; ns, not significant, *P<0.05, **P<0.01.

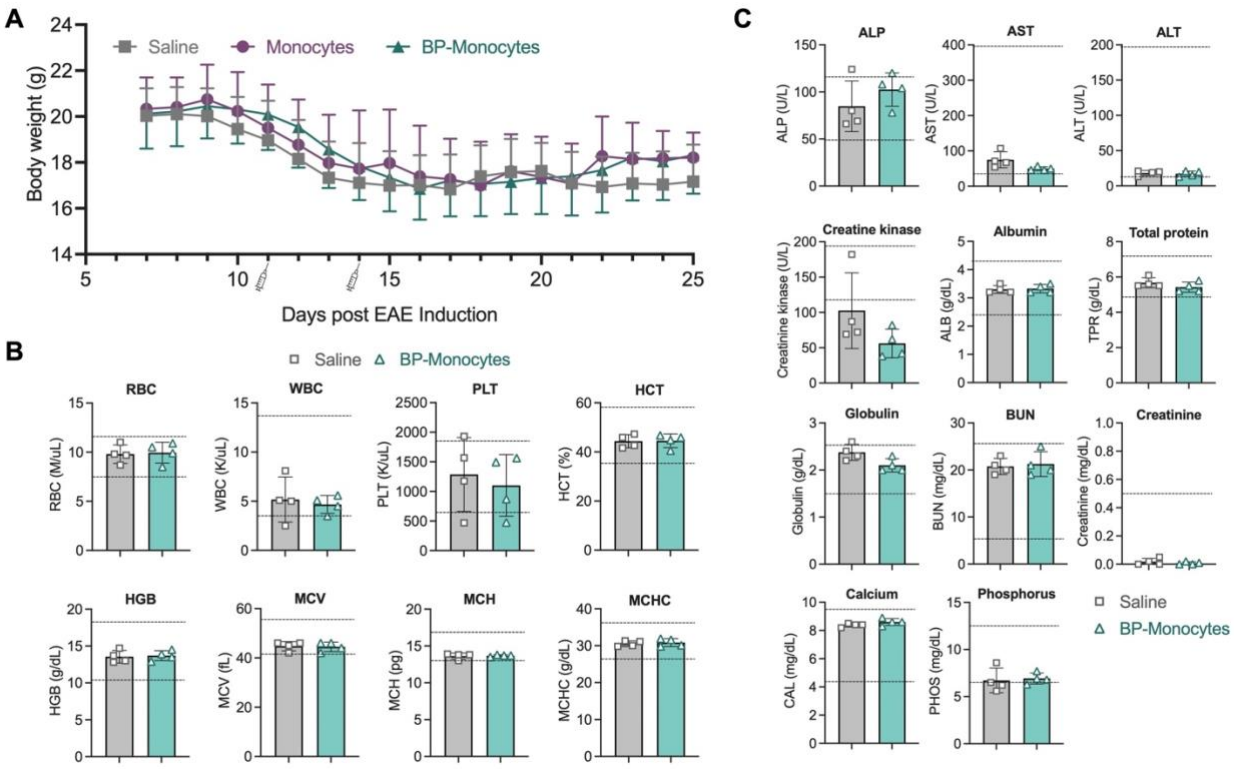

Appendix Figure 9-14. Safety assessment of backpack-monocyte treatment.
EAE was induced in female C57BL/6J mice. Mice were administered $3x10^6$ monocytes, backpack (BP)-carrying monocytes or saline intravenously via tail vein on days 11 and 14 and monitored until day 25. A) Body weight over time following two doses of treatment from Figure 5B; mean ± SE (n=11-14). B). Hematology analysis of EAE mice treated with saline or monocyte backpacks. No significant differences between saline group and monocyte backpack group were detected. RBC: red blood cell, WBC: white blood cell, PLT: platelet, HCT: hematocrit, HBG: hemoglobin, MCV: mean corpuscular volume, MCH: mean corpuscular hemoglobin, MCHC: mean corpuscular hemoglobin concentration; mean ± SD (n=4). C) Serum chemistry analysis of EAE mice treated with saline or monocyte backpacks. No significant differences between saline group and monocyte backpack group were detected. ALP: alkaline phosphatase, AST: aspartate aminotransferase, ALT: alanine aminotransferase, BUN: blood urine nitrogen; mean ± SD (n=4). Data were analyzed by two-tailed student's t test. Dashed Lines indicate established normal range.

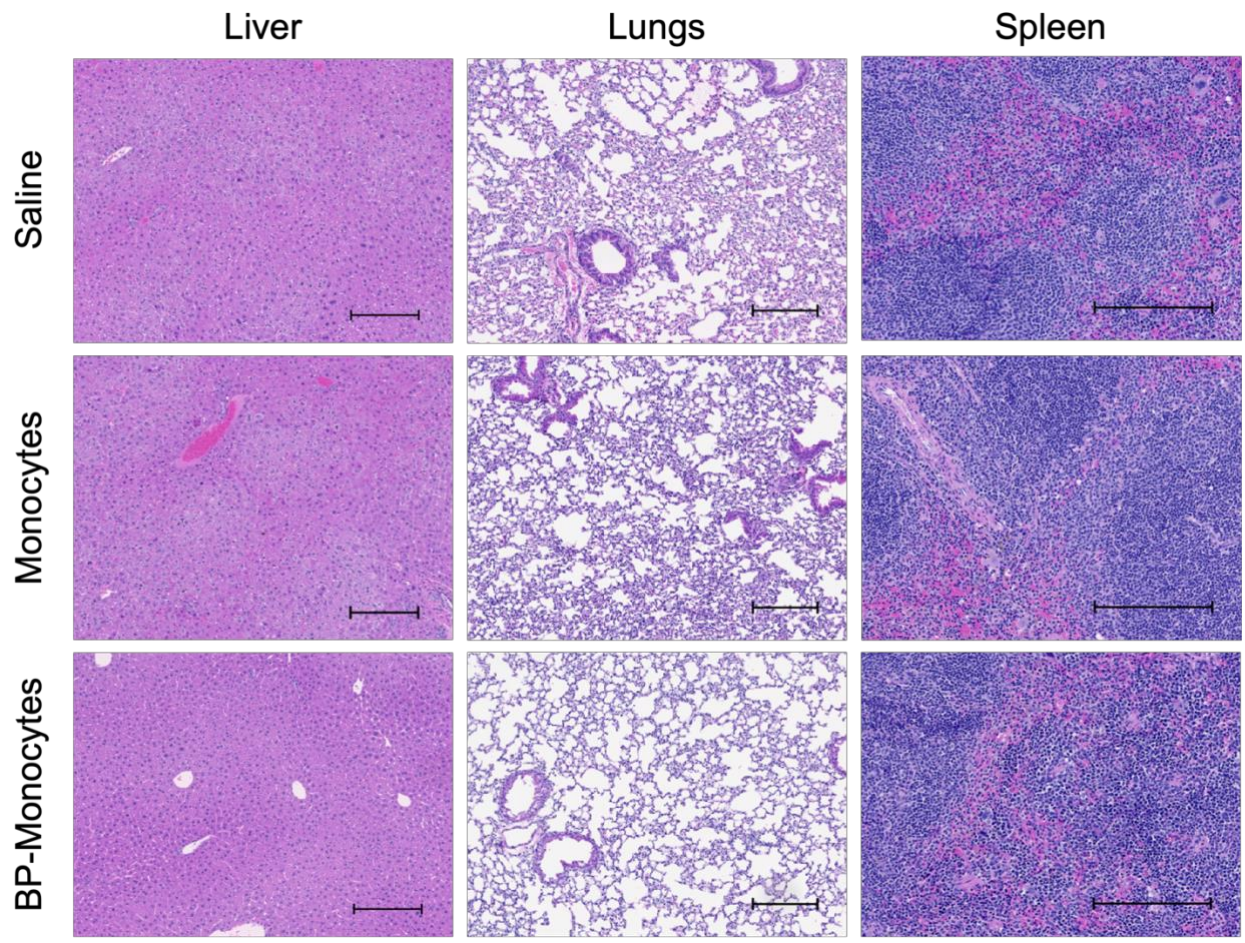

Appendix Figure 9-15. H&E of major mouse organs following different treatments in EAE model.

Mice received same doses as in efficacy study (Fig. 5). Organs of mice were analyzed by H&E staining. Representative of n = 3 biologically independent animals per group. Scale bar = 200µm.

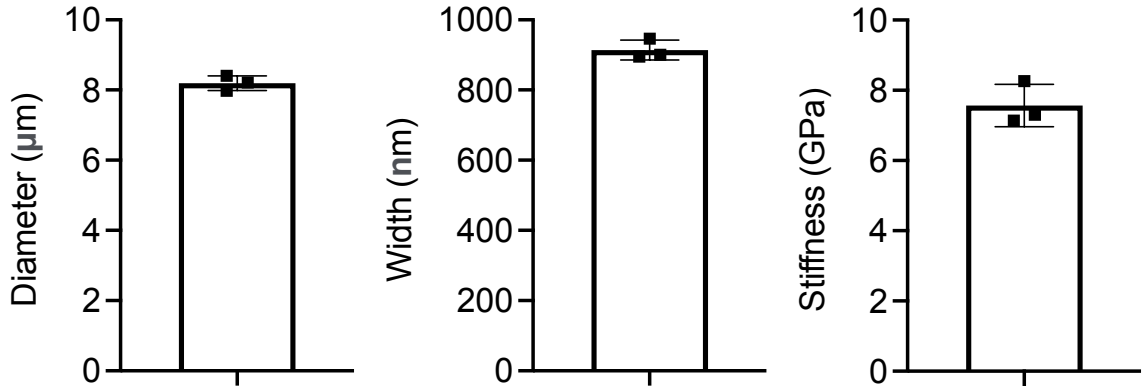

Appendix Figure 9-16. Backpack characteristics.
The diameter, width, and stiffness of backpacks were determined by AFM (JPK Nanowizard, Bruker). Backpacks had a diameter or 8.2 um, width of 913.67 nm, and stiffness of 7.57 GPa.

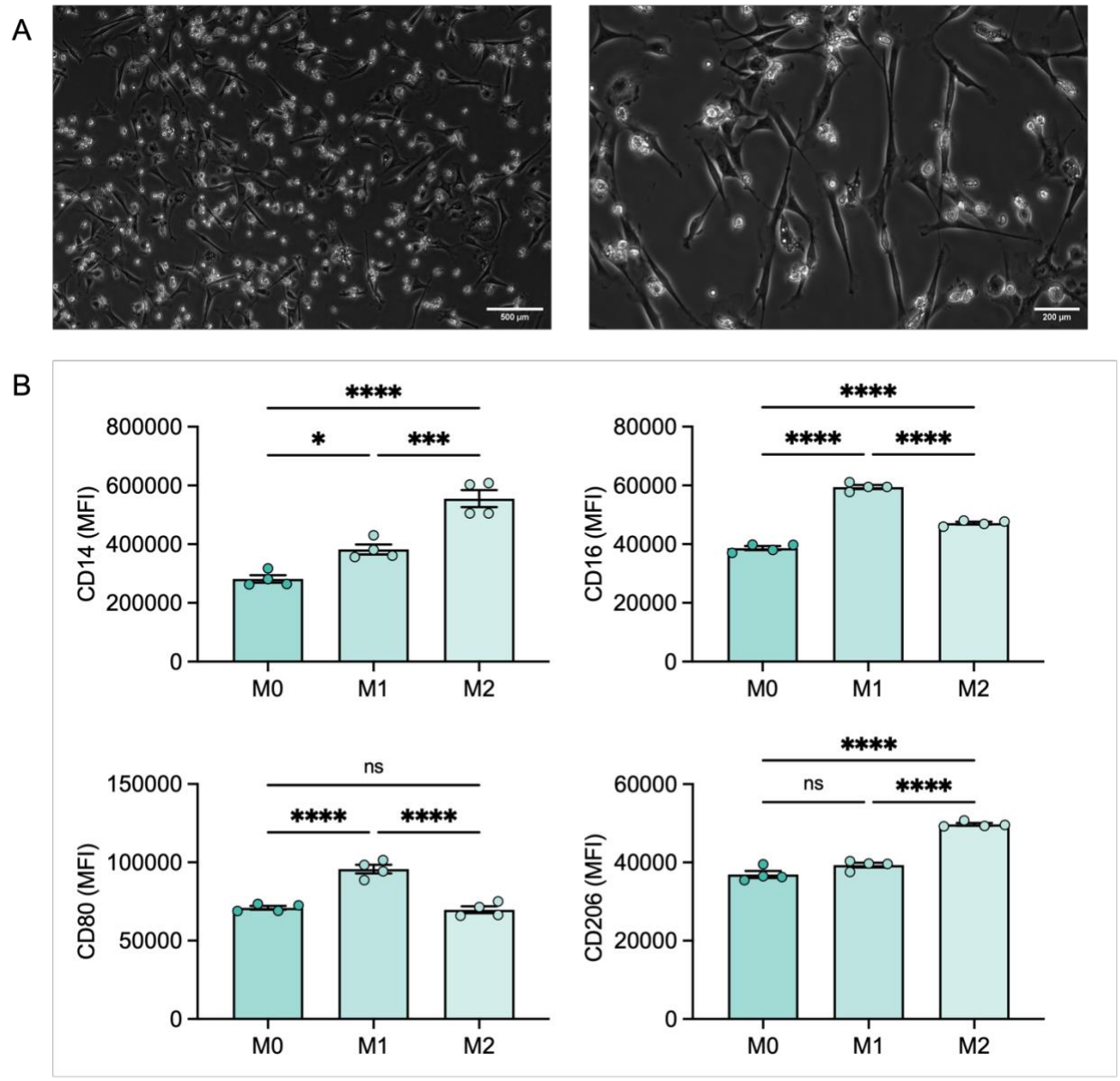

Appendix Figure 9-17. Characterization of porcine macrophages.
Brightfield microphotographs display representative M2 porcine macrophages at A) 10x and B) 20x magnification. After 6DIV culturing with 20 ng/mL M-CSF, macrophages were replated and cultured in different media for 3DIV for polarization into M0 (20 ng/mL M-CSF), M1 (20 ng/mL M-CSF + 20 ng/mL IFN-γ), and M2 (20 ng/mL M-CSF + 20 ng/mL IL-4) phenotypes. C) CD14, CD16, CD80, and CD206 expression of M0, M1, and M2 macrophages. Data were analyzed by one-way ANOVA with Tukey's HSD test (ns = not significant, *p < 0.5, ***p < 0.005, ****p < 0.0001).

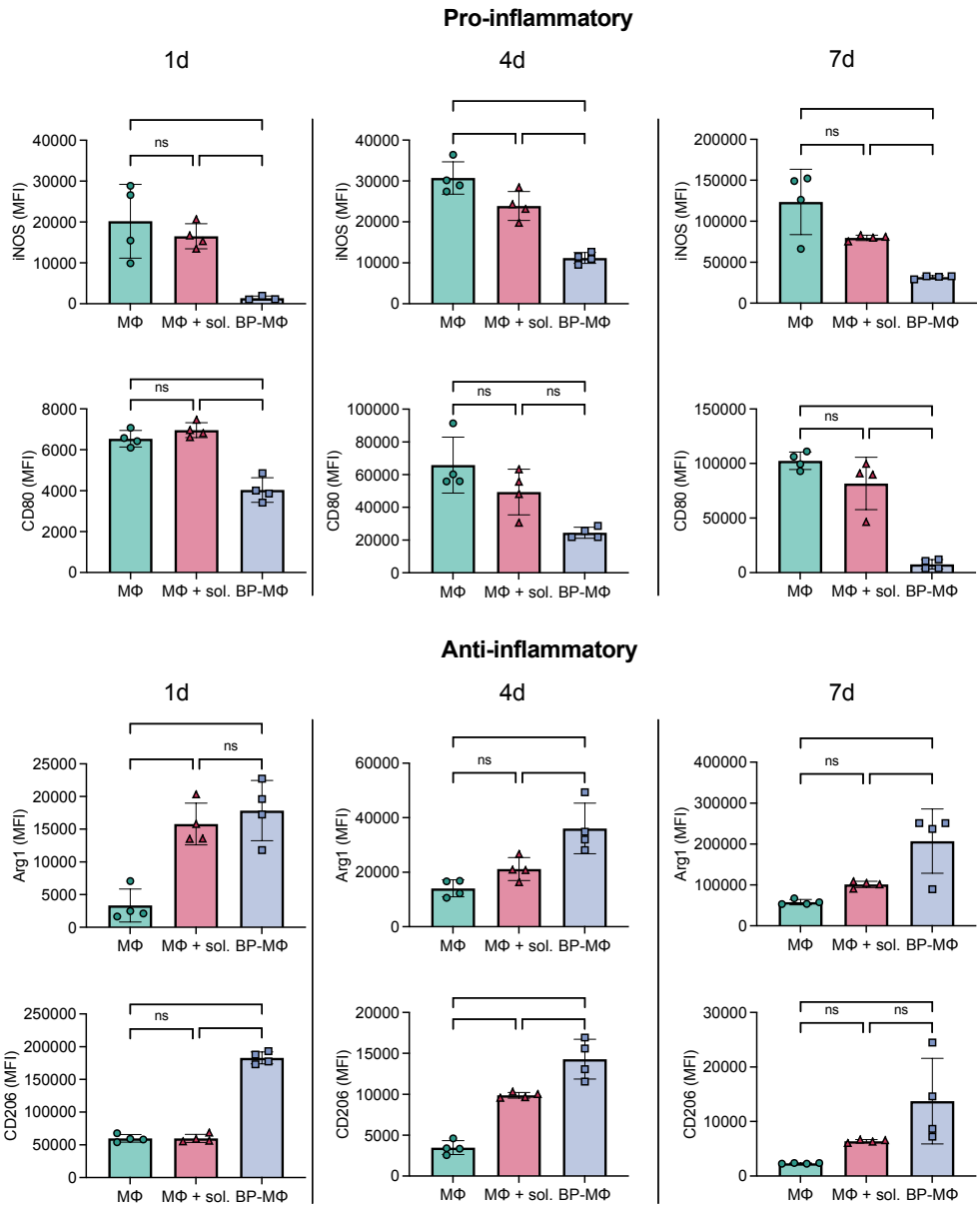

Appendix Figure 9-18. Backpacks polarize porcine macrophages in unstimulated media over 7 days.

Macrophages, macrophages with free IL-4/Dexamethasone, or backpack-macrophages were cultured and analyzed for expression of pro-inflammatory (iNOS, CD80) and anti-inflammatory (Arg1, CD206) markers via flow cytometry; mean ± SD (n=5). Data were analyzed by two-tailed student's t test; ns = not significant, *P<0.05, **P<0.01, ***P<0.001, ****P<0.0001.

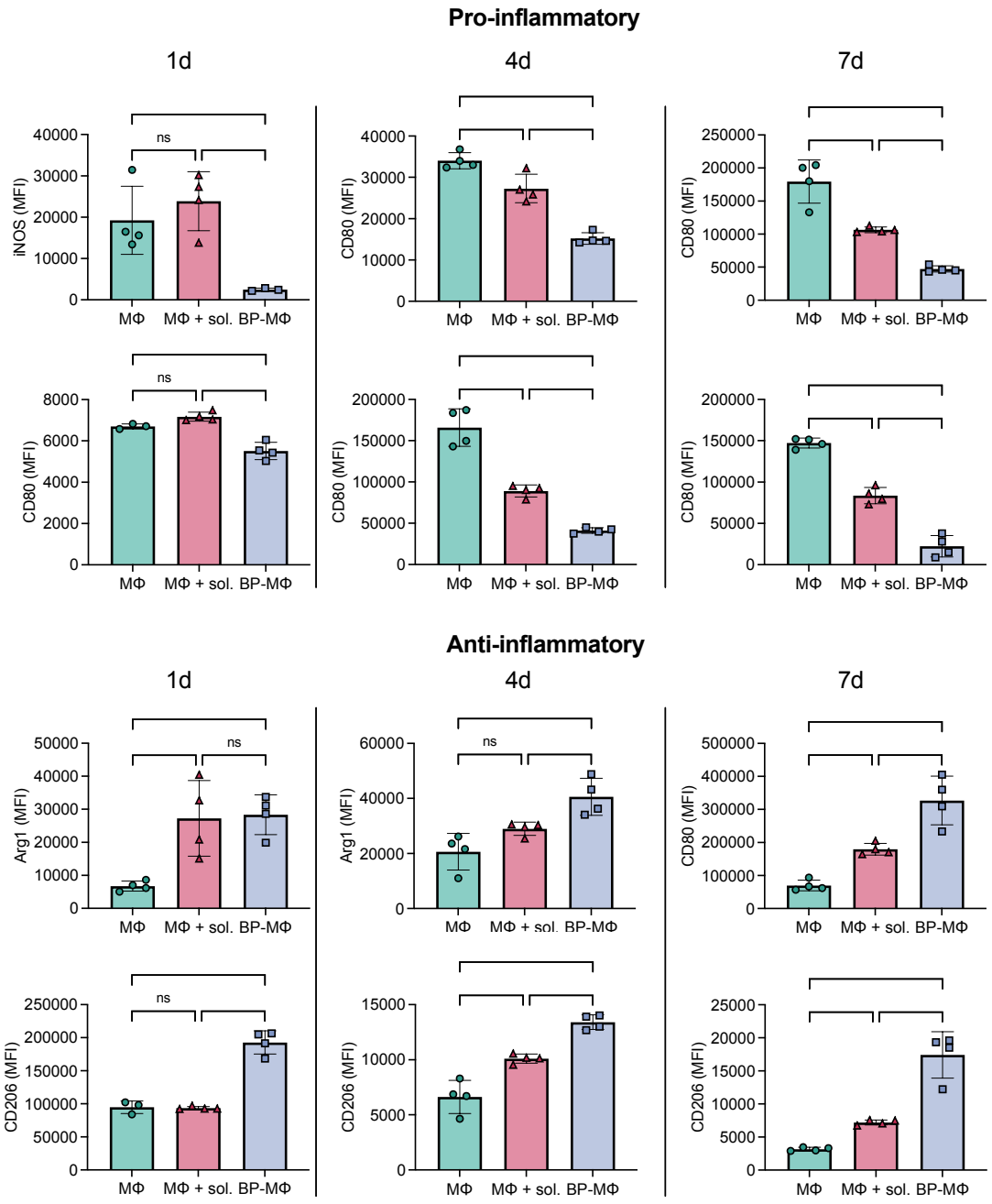

Appendix Figure 9-19. Backpacks polarize porcine macrophages in unstimulated media over 7 days.

Macrophages, macrophages with free IL-4/Dexamethasone, or backpack-macrophages were cultured and analyzed for expression of pro-inflammatory (iNOS, CD80) and anti-inflammatory (Arg1, CD206) markers via flow cytometry; mean ± SD (n=5). Data were analyzed by two-tailed student's t test; ns = not significant, *P<0.05, **P<0.01, ***P<0.001, ****P<0.0001.

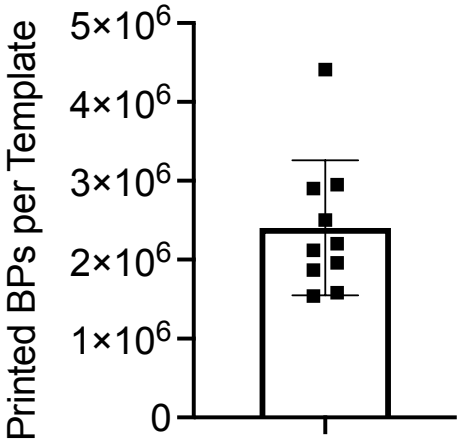

Appendix Figure 9-20. Backpack printing at scale.
Number of recovered backpacks per PDMS template after microcontact printing.

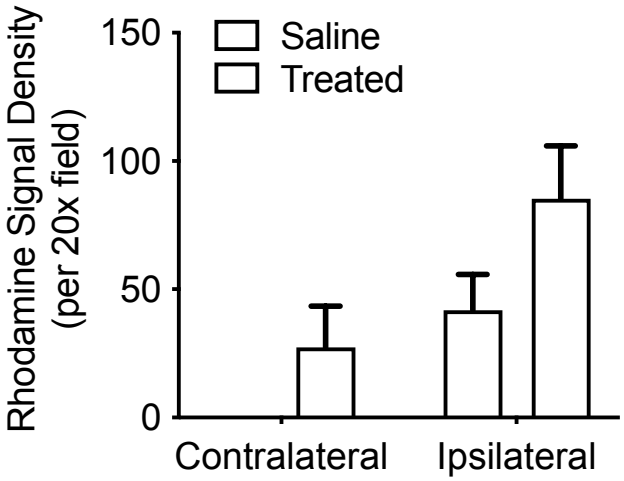

Appendix Figure 9-21. Rhodamine signal density in brain hemispheres.
Backpacks were labelled with Rhodamine and visualized in the peri-contusional area of the rostral gyrus. Some rhodamine signal were detected in the saline treated pigs via automated analysis as red blood cells auto-fluoresced at the contusion site from hemorrhage and were similarly sized to backpacks.

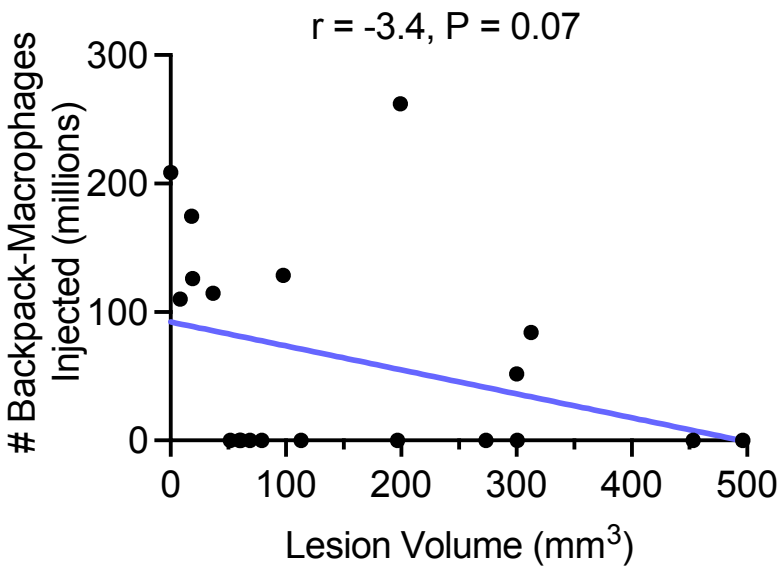

Appendix Figure 9-22. One-sided Pearson Correlation.
There was an inverse correlation between backpack-macrophage number injected and lesion volume.

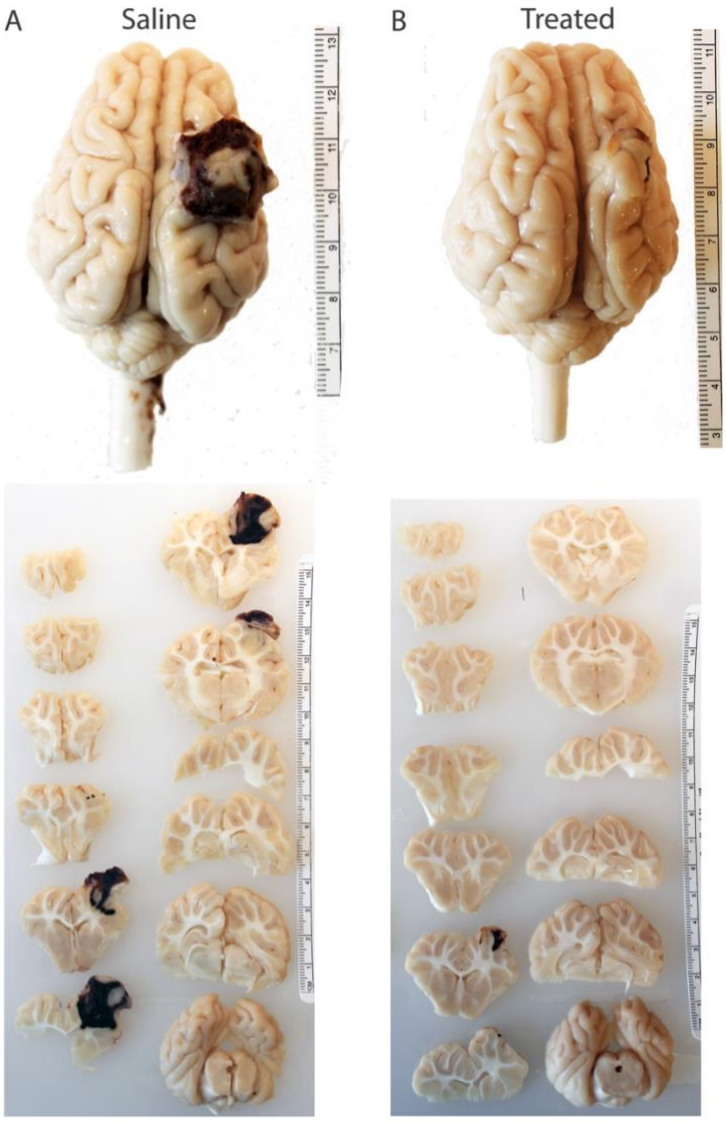

Appendix Figure 9-23. Whole brain sections.
The whole brain and coronal sections (5 mm thick, rostral facing down) of a piglet A) receiving saline or B) treated with backpack-macrophages (ruler = cm).

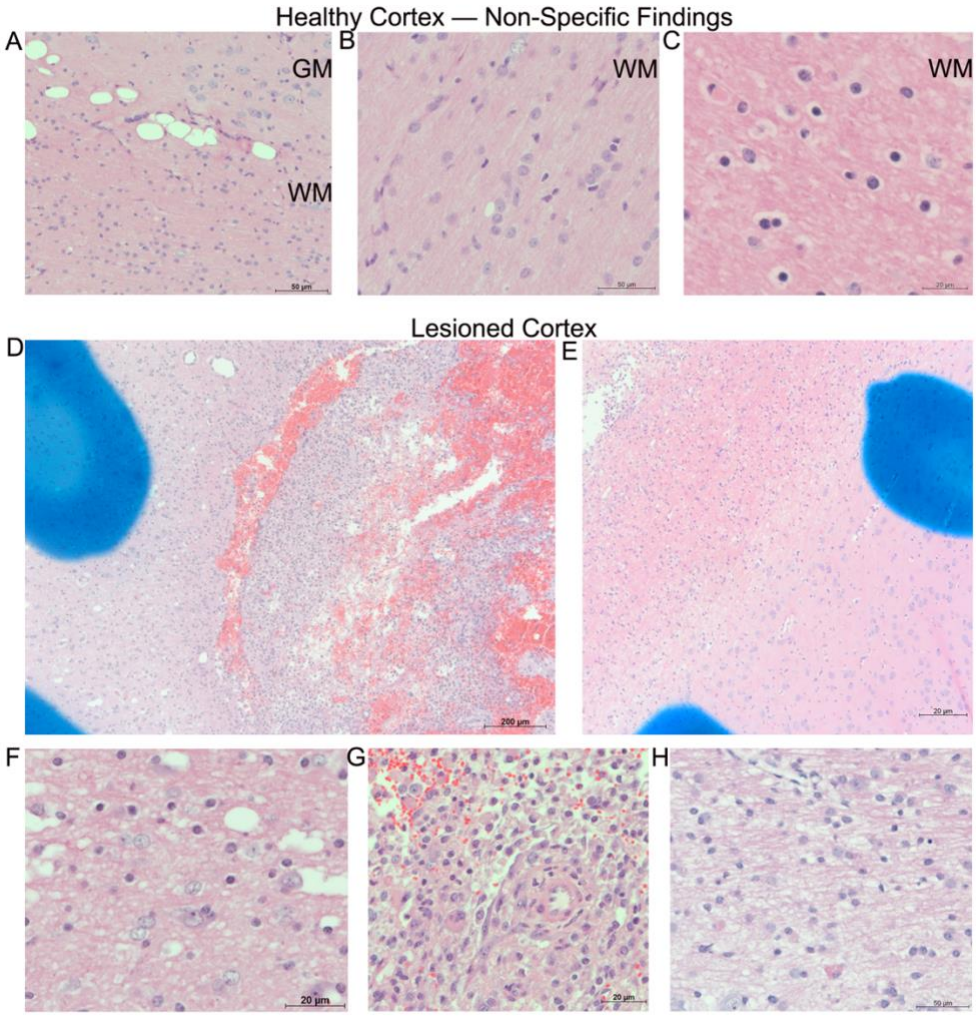

Appendix Figure 9-24. Photomicrographs demonstrating healthy and lesioned cortex 7 days after cortical impact.

A-C) Tissue that was healthy had intact gray matter (GM) and white matter (WM). A) Non-specific vacuolization at the gray-white matter interface considered to be normal tissue. B) Healthy, normal appearing white matter. C) White matter with vacuolization around oligodendrocytes that was considered non-specific (potential perfusion artifact) with white matter fibers still appearing tightly packed. D) Low power view of demarcated lesion (with blue mark) of the gray matter. Lesion includes tissue with lost structural integrity, hemorrhage (red = red blood cells), and an infiltration of immune cells (small purple nuclei). E) Lower power view of demarcated lesion in the white matter with lesioned white matter, including a white matter cavity, adjacent to normal appearing gray matter. F) High power view of lesioned gray matter with vacuolization of neuropil, vacuolization of neurons and oligodendrocytes, pyknotic cells, tissue loss but with most neuron cell bodies still normal appearing. G) High power view of advanced lesion with red blood cells infiltrated throughout, pyknotic cells, cell drop out, tissue loss, and remodeling. H) Lesioned white matter often extended beyond the area of gray matter lesion. Here, the white matter tract exhibit rarefication and some pyknotic cells.

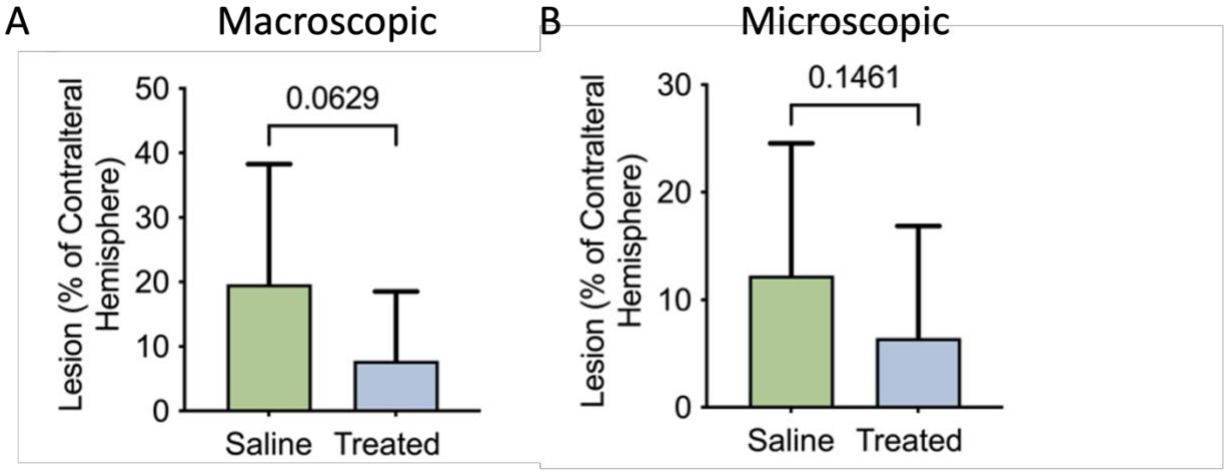

Appendix Figure 9-25. Piglets were treated with saline or backpack-macrophages, as described in Fig. 4.

When the area of the lesion size was expressed as a ratio of the area of the contralateral hemisphere either A) macroscopically or B) microscopically, lesion size decreased or tended to decrease in treated piglets vs. saline piglets (one-sided, unpaired, student's t-test).

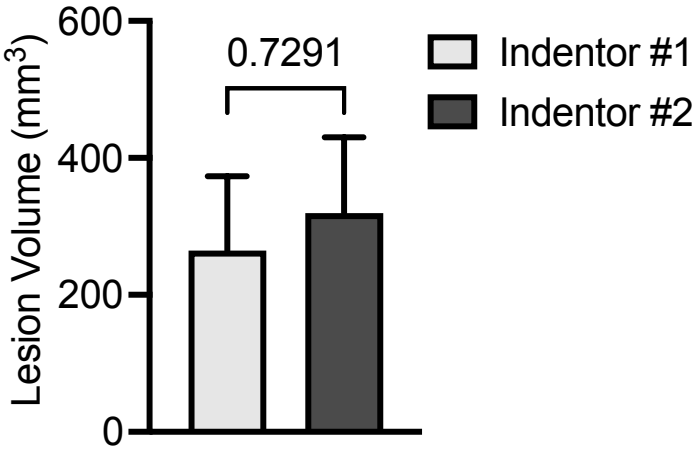

Appendix Figure 9-26. Comparison of Indentors.

Two indentors were used to induce cortical impact and alternated among subjects. There was no difference in the lesion size resulting from impact between indentors (unpaired, two tailed student's t-test).

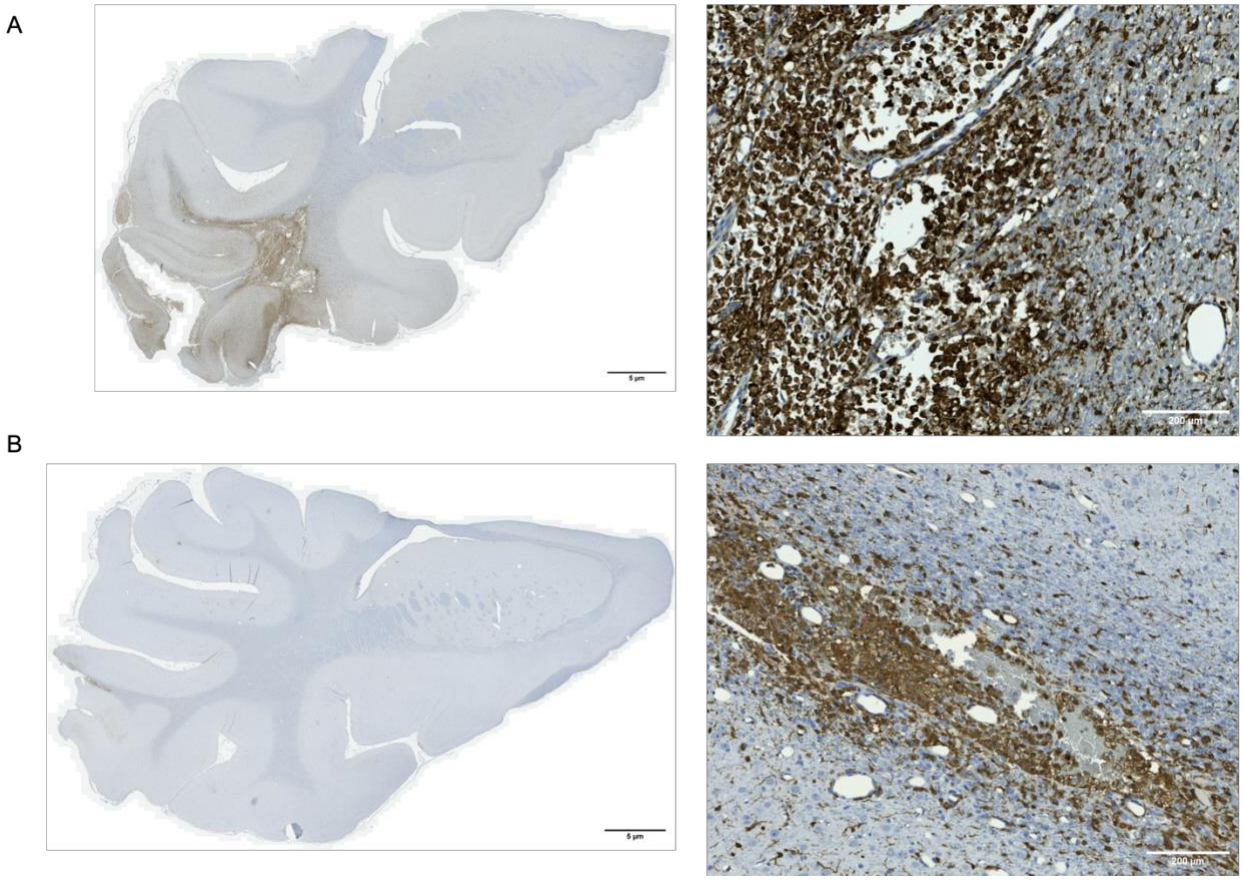

Appendix Figure 9-27. Iba1 immunohistochemistry of ipsilateral hemispheres.
Brightfield microphotographs depict representative whole hemisphere and 20x images of A) saline and B) treated ipsilateral hemispheres 7 days after cortical impact. Slices were stained with rabbit anti-Iba1 primary antibody, HRP-antibody, and DAB chromogen staining and counterstained with hematoxylin to assess Iba1 positivity (brown). Whole hemisphere scale bar = 5 mm. 20x image scale bar = 200 µm.

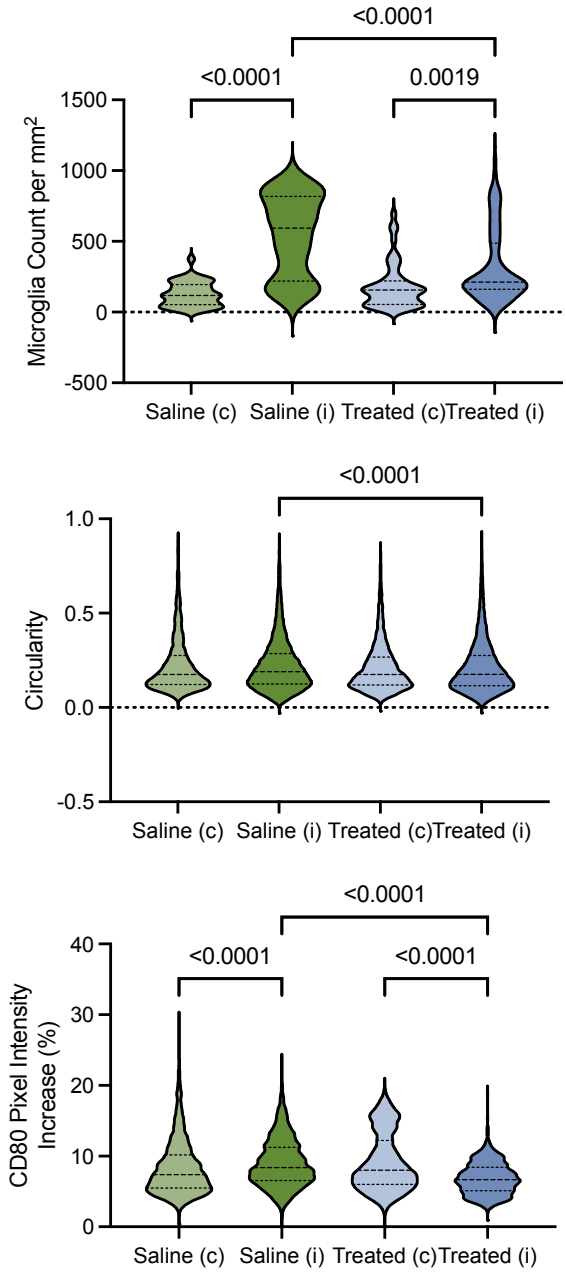

Appendix Figure 9-28. ImageJ microglia analysis of ipsilateral and contralateral hemispheres.

Images in the peri-contusion region were analyzed to determine A) Iba1+ microglia count per mm^2, B) individual Iba1+ microglia circularity, and C) individual microglia CD80 pixel intensity increase for both ipsilateral (i) and contralateral (c) hemispheres for saline and treated pigs.

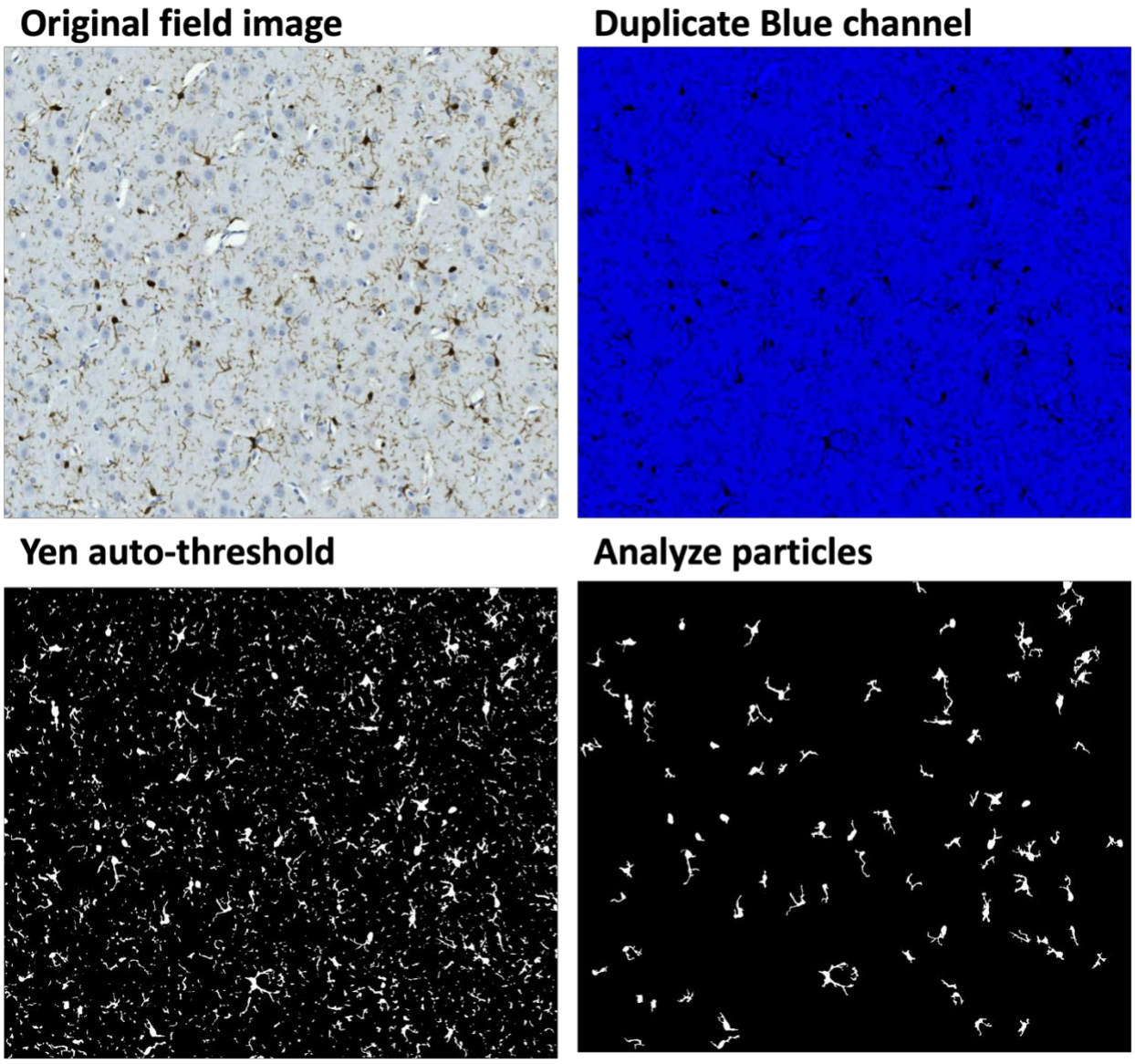

Appendix Figure 9-29. ImageJ image analysis for determining microglia count per mm^2 and circularity.
Representative images depict the ImageJ image processing steps each image underwent to determine microglia count and circularity, as described in the *Microscopic evaluation of Iba-1 and CD80* section of the Materials and Methods.

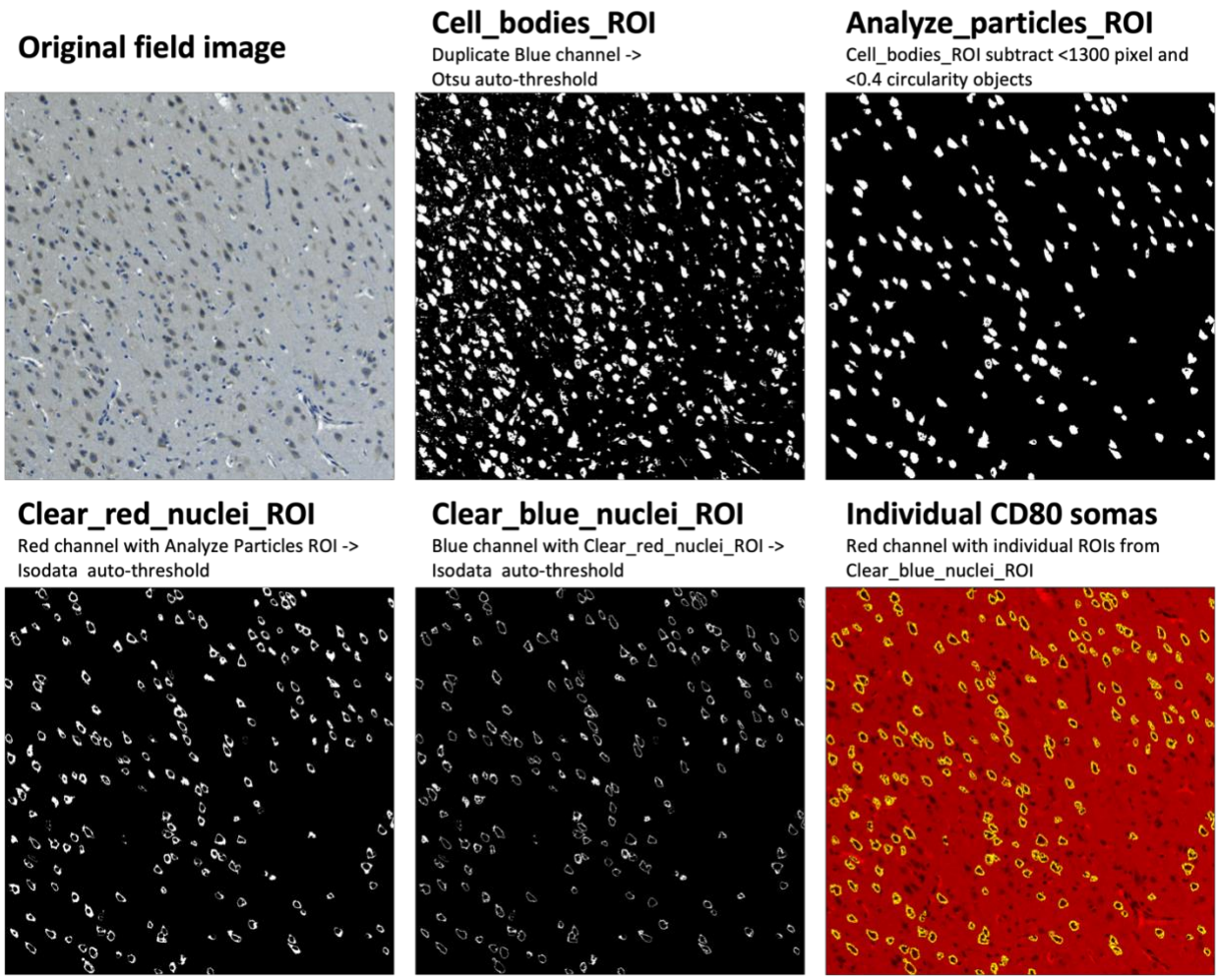

Appendix Figure 9-30. ImageJ image analysis for determining soma CD80 pixel intensity. Representative images depict the ImageJ image processing steps each image underwent to determine soma CD80 pixel intensity, as described in the *Microscopic evaluation of Iba-1 and CD80* section of the Materials and Methods.

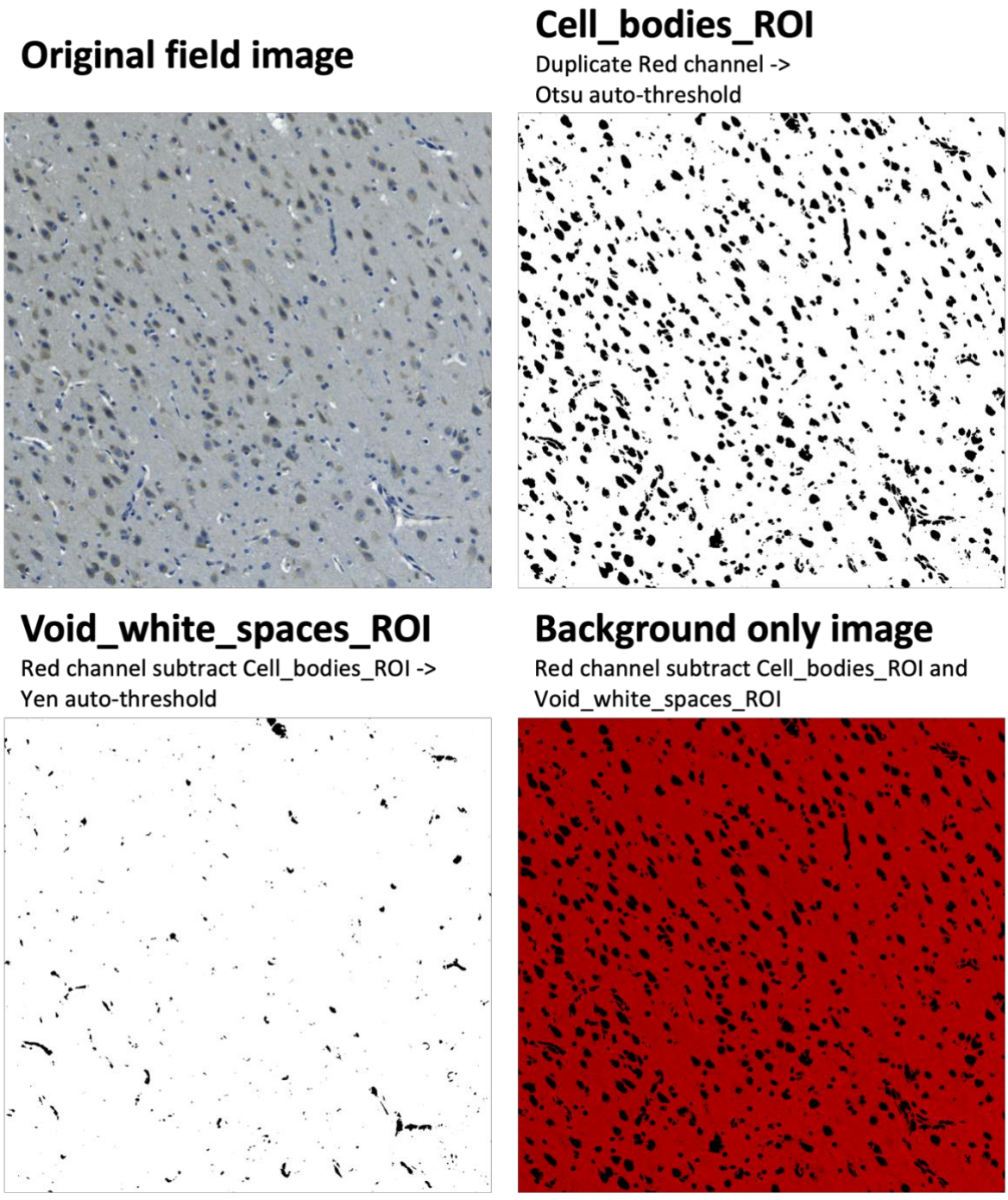

Appendix Figure 9-31. ImageJ image analysis for determining background CD80 pixel intensity.
Representative images depict the ImageJ image processing steps each image underwent to determine background CD80 pixel intensity, as described in the *Microscopic evaluation of Iba-1 and CD80* section of the Materials and Methods.

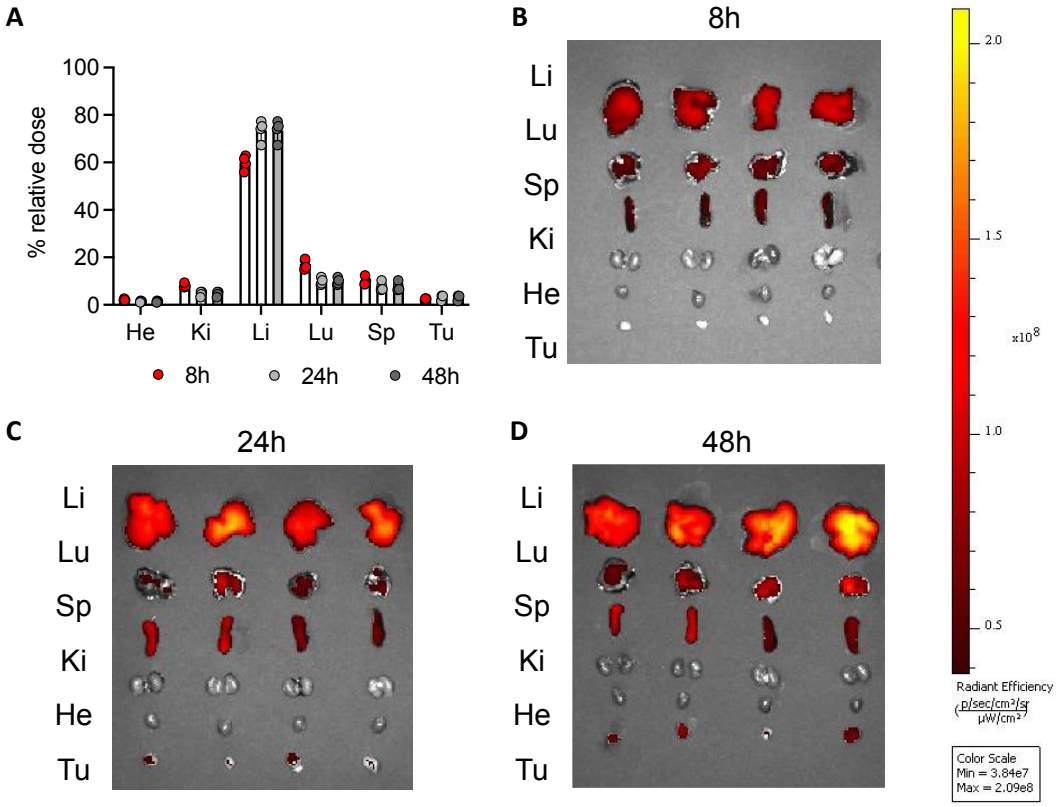

Appendix Figure 9-32. Biodistribution of adoptively transferred monocytes.
Tumors were inoculated with 4T1 in the mammary fat pad. Mice were administered $4x10^6$ monocyte intravenously via tail-vein on Day 5. A) Biodistribution data for fluorescently labelled monocytes. Animals were sacrificed at 8, 24, 48 h following monocyte injection; organs (liver, lungs, spleen, kidneys, heart, and tumor) were resected and monocyte concentration determined by fluorescent imaging. Representative IVIS images at B) 8 hours, C) 24 hours, and D) 48 hours.

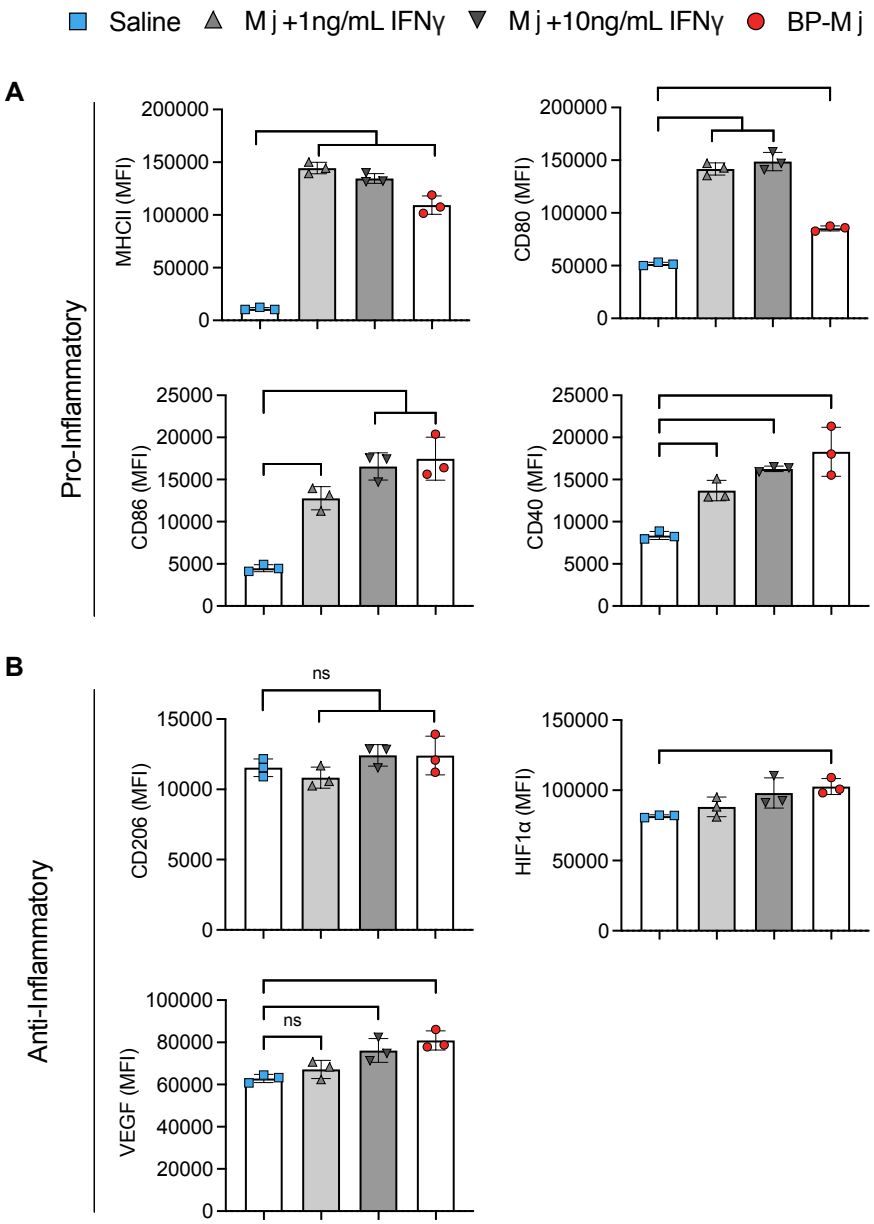

Appendix Figure 9-33. IFNγ-backpacks polarize monocytes in unstimulated media over 24h. Monocytes, monocytes with 1ng/mL or 10 ng/mL of free IFNγ, or IFNγ backpack-laden monocytes were cultured and analyzed for expression of pro-inflammatory (MHCII, CD80, CD86, and CD40) and anti-inflammatory (CD206, HIF1 α, VEGF) markers via flow cytometry; mean ± SD (n=3). Data were analyzed by one-way ANOVA with Tukey's HSD test; *P<0.05, **P<0.01, ***P<0.001, ****P<0.0001.

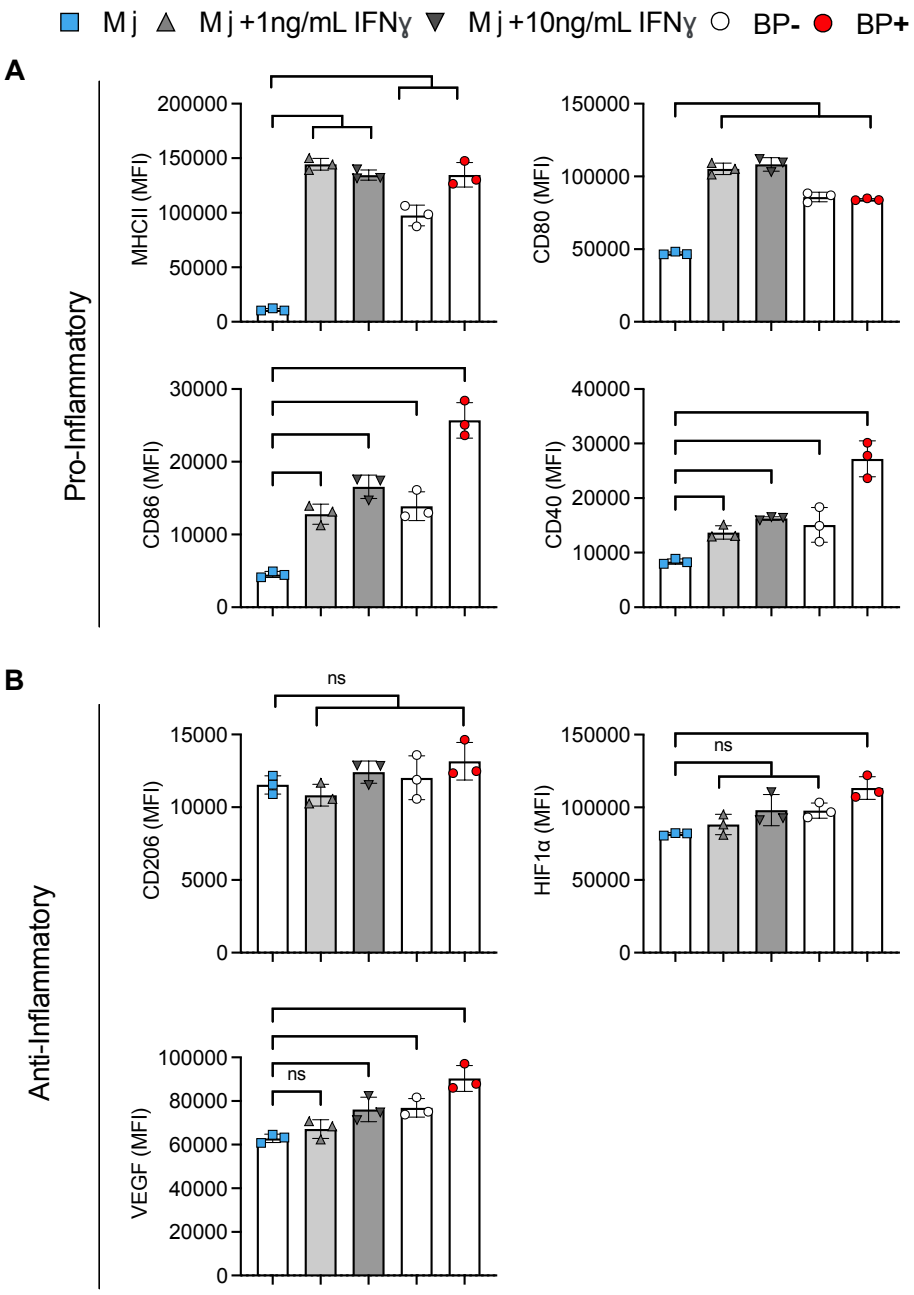

Appendix Figure 9-34. Comparison of IFNγ-backpacks+ and IFNγ-backpacks- monocytes within the IFNγ-backpack group in unstimulated media over 24h.
Monocytes, monocytes with 1ng/mL or 10 ng/mL of free IFNγ, or IFNγ backpack-laden monocytes were cultured and analyzed for expression of pro-inflammatory (MHCII, CD80, CD86, and CD40) and anti-inflammatory (CD206, HIF1 α, VEGF) markers via flow cytometry. BP- and BP+ represent monocytes without and with backpacks in the BP-monocyte group; mean ± SD (n=3). Data were analyzed by one-way ANOVA with Tukey's HSD test; *P<0.05, **P<0.01, ***P<0.001, ****P<0.0001.

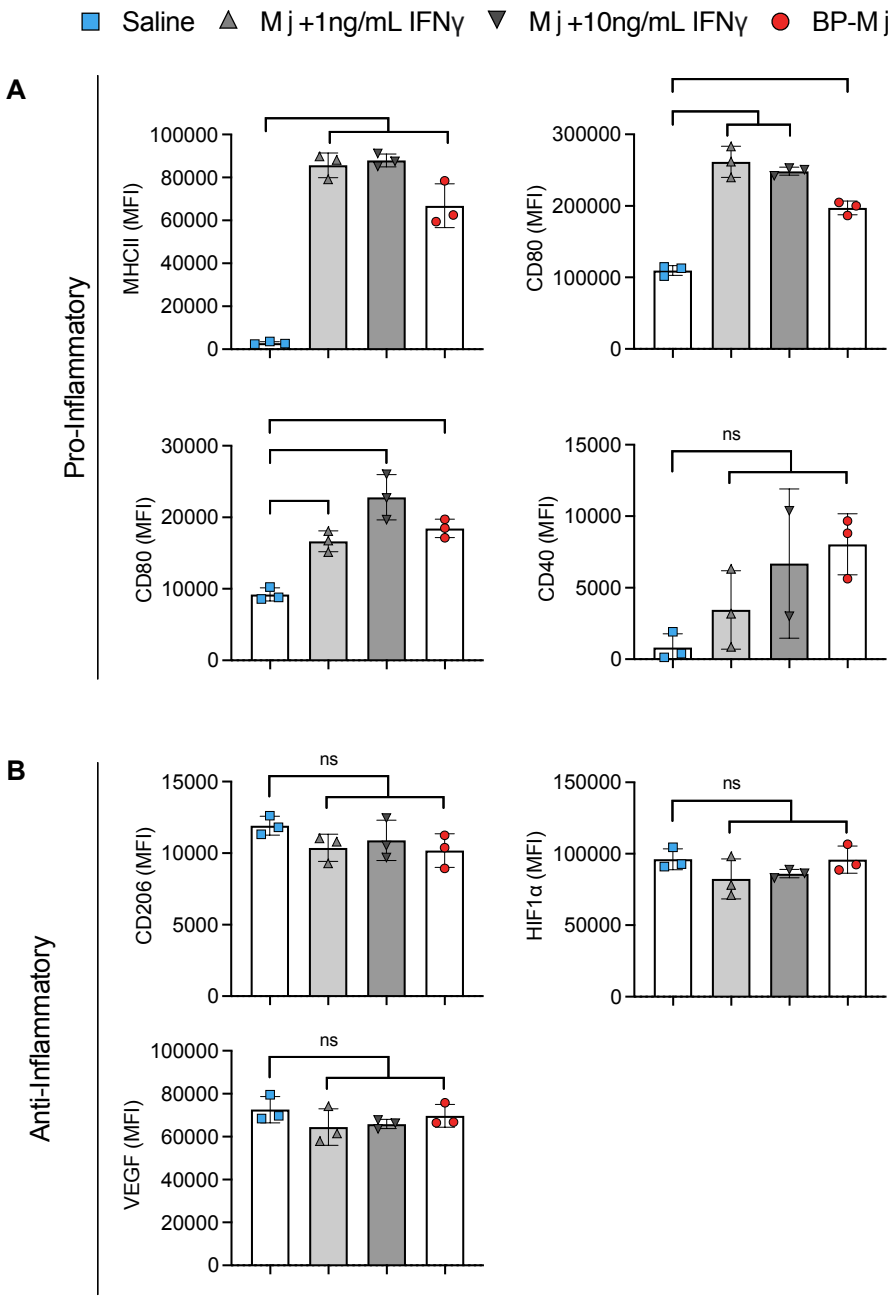

Appendix Figure 9-35. IFNγ-backpacks polarize monocytes in 4T1-media over 24h.
Monocytes, monocytes with 1ng/mL or 10 ng/mL of free IFNγ, or IFNγ backpack-laden monocytes were cultured and analyzed for expression of pro-inflammatory (MHCII, CD80, CD86, and CD40) and anti-inflammatory (CD206, HIF1 α, VEGF) markers via flow cytometry; mean ± SD (n=3). Data were analyzed by one-way ANOVA with Tukey's HSD test; *P<0.05, **P<0.01, ***P<0.001, ****P<0.0001.

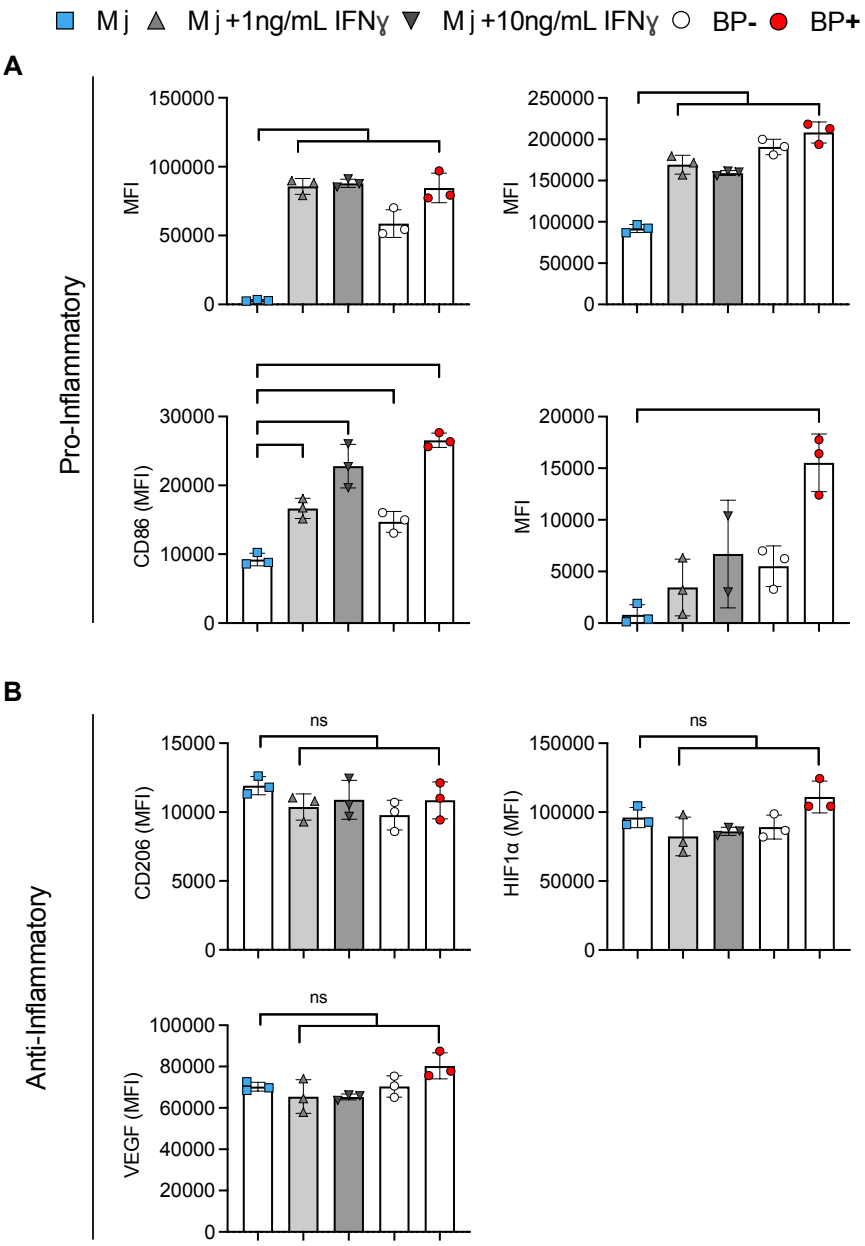

Appendix Figure 9-36. Comparison of IFNγ-backpacks+ and IFNγ-backpacks- monocytes within the IFNγ-backpack group in unstimulated media over 24h.
Monocytes, monocytes with 1ng/mL or 10 ng/mL of free IFNγ, or IFNγ backpack-laden monocytes were cultured and analyzed for expression of pro-inflammatory (MHCII, CD80, CD86, and CD40) and anti-inflammatory (CD206, HIF1 α, VEGF) markers via flow cytometry. BP- and BP+ represent monocytes without and with backpacks in the BP-monocyte group; mean ± SD (n=3). Data were analyzed by one-way ANOVA with Tukey's HSD test; *P<0.05, **P<0.01, ***P<0.001, ****P<0.0001.

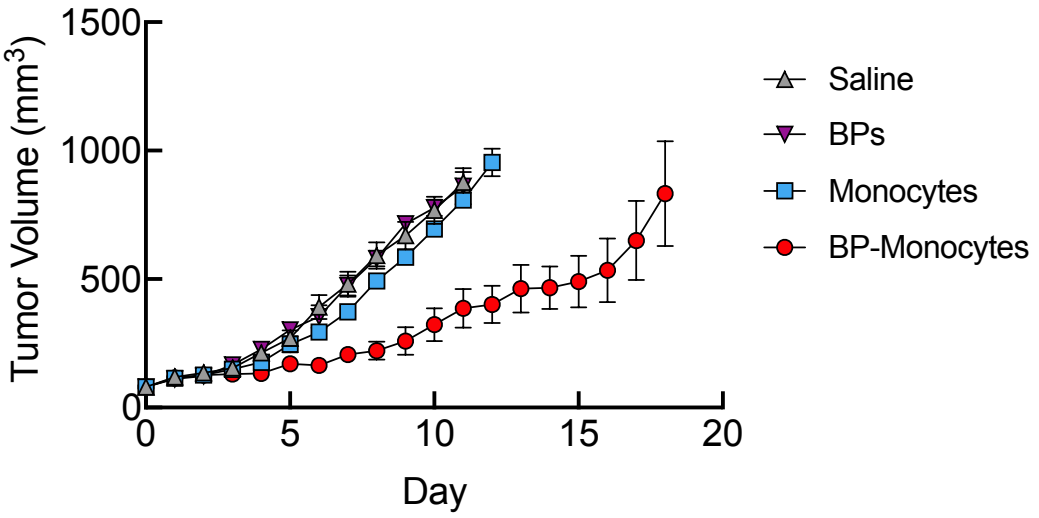

Appendix Figure 9-37. Full tumor growth curve.
Tumor volume over time until the mice reached ethical endpoints. Tumor volume is plotted as mean ± SEM with n=7 mice per group.

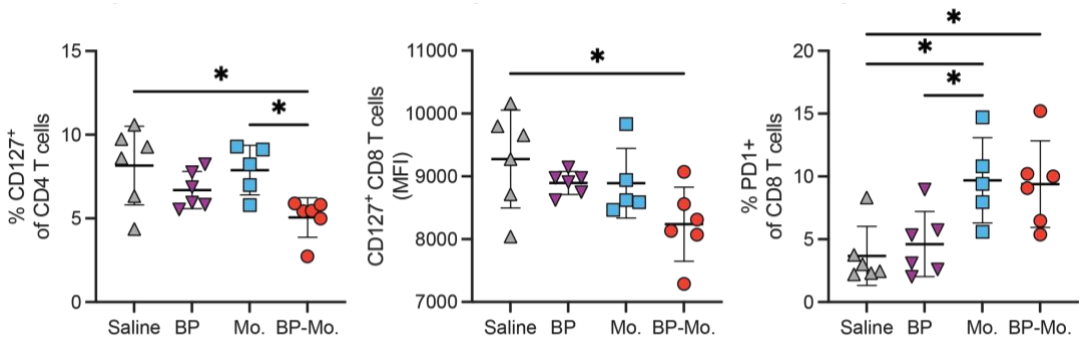

Appendix Figure 9-38. Blood markers panel.
Blood from mice treated as described in Figure 5 was processed into single suspensions and the T cell profile of the blood was analyzed; mean ± SD (n=7). Data were analyzed using one-way ANOVA with Tukey's HSD test; ns, not significant, *P<0.05.

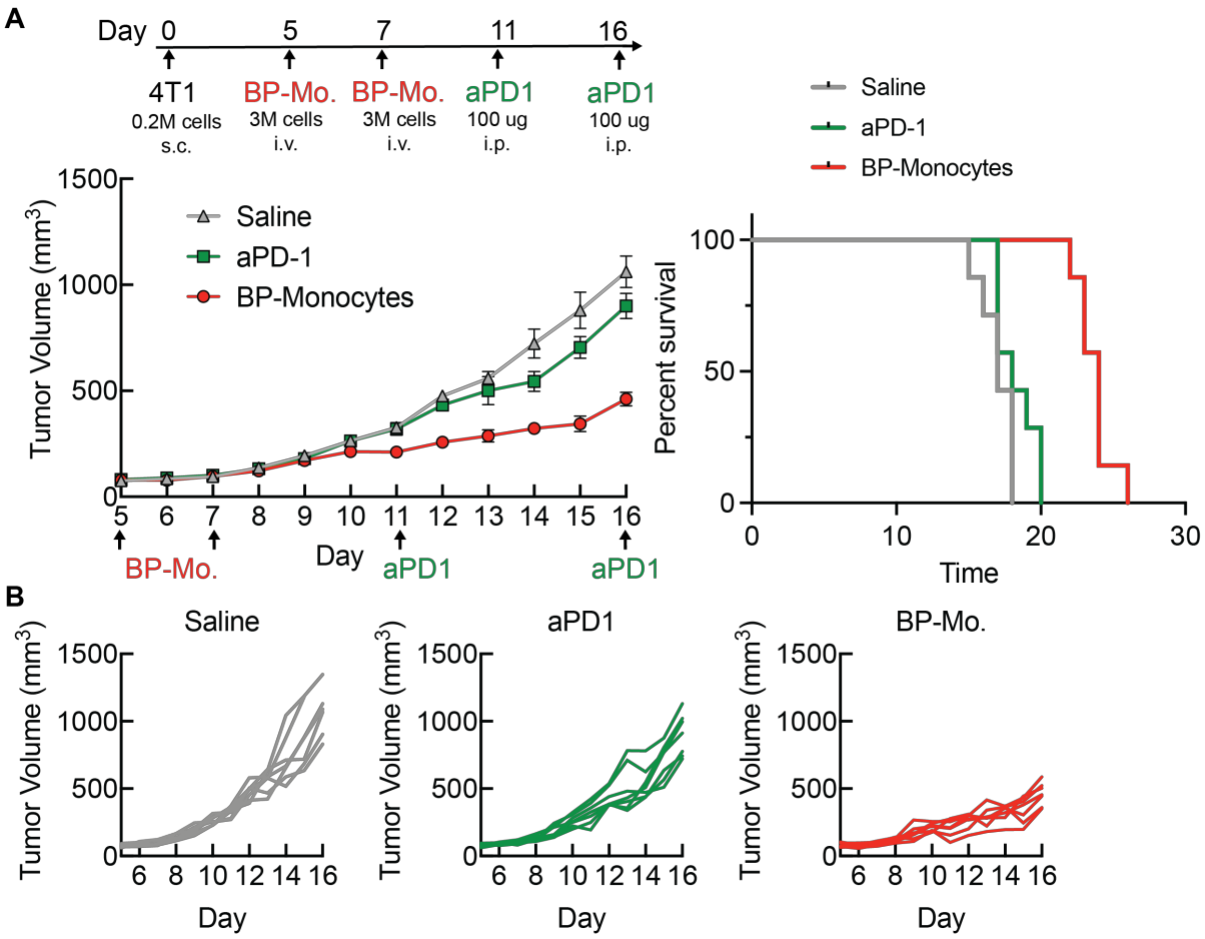

Appendix Figure 9-39. IFNγ backpacks adhered to monocytes display enhanced therapeutic efficacy in compared to checkpoint inhibitor.

(A) All mice were injected with 4T1 cancer cells in the mammary fat pad on day 0 and cell therapy or saline was administered intravenously on days 5 and 7. Mice treated with anti-PD1 intraperitoneally (100ug) on days 11 and 16. Tumor volume and time until the mice reached ethical endpoints are shown in panel A. Tumor volume is plotted as mean ± SEM with n=7 mice per group. (B) Tumor volumes are plotted for the seven individual mice in each treatment group.

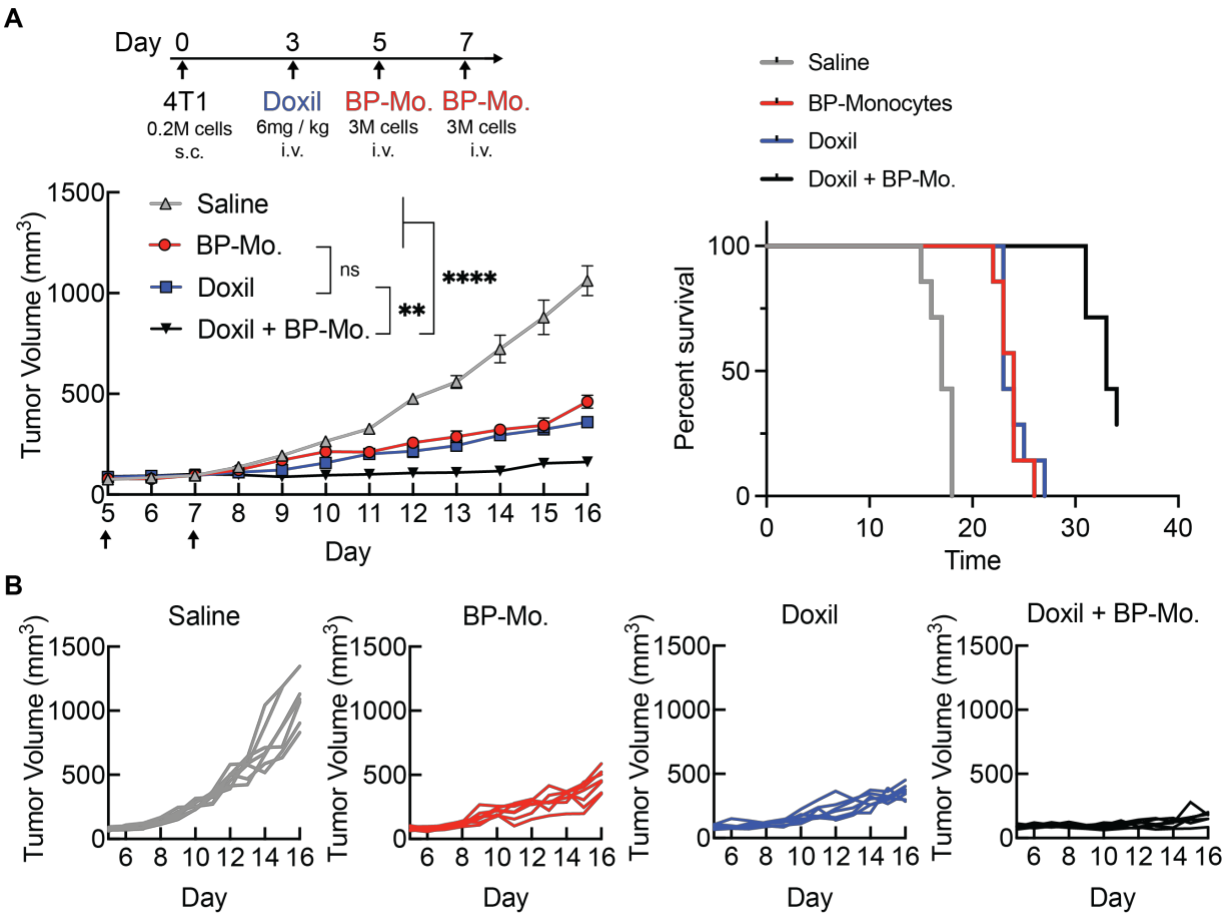

Appendix Figure 9-40. IFNγ backpacks adhered to monocytes display enhanced therapeutic efficacy in combination with Doxil.

(A) All mice were injected with 4T1 cancer cells in the mammary fat pad on day 0 and cell therapy or saline was administered intravenously on days 5 and 7. Mice treated with PLD received 6mg/kg doxorubicin intravenously two days prior to the first dose of cell therapy. Tumor volume and time until the mice reached ethical endpoints are shown in panel A. Tumor volume is plotted as mean ± SEM with n=7 mice per group. (B) Tumor volumes are plotted for the seven individual mice in each treatment group. For A, Data were analyzed by one-way ANOVA with Tukey's HSD; **p<0.01, ****p<0.0001.

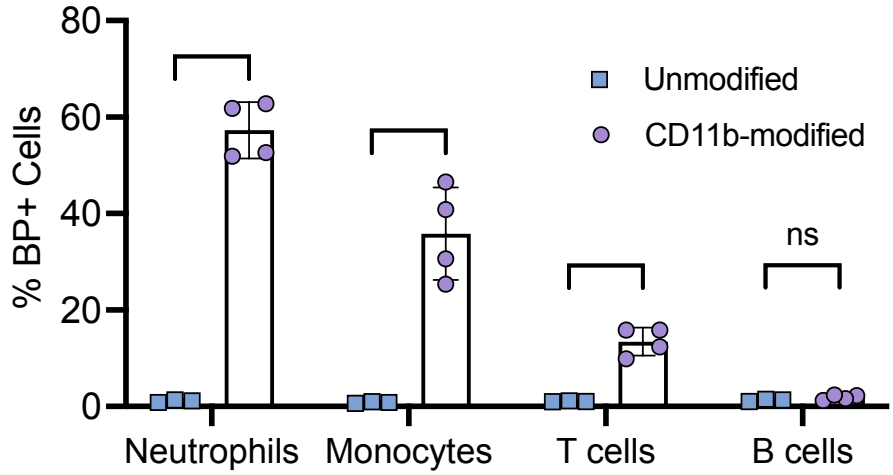

Appendix Figure 9-41. Antibody functionalization modulates specific cell-backpack interactions.
Unmodified or CD11b modified backpacks were incubated in whole blood for 1 hour at a concentration of 1 million backpacks/mL. Blood was then lysed and stained for different markers to determine backpack attachment to immune cell subsets, as assessed by flow cytometry. Data were analyzed by two-way ANOVA; **$p<0.01$, ****$p<0.0001$.